ACS OMEGA

http://pubs.acs.org/journal/acsodf

Article

How Reliable Is the Ideal Adsorbed Solution Theory for the Estimation of Mixture Separation Selectivities in Microporous Crystalline Adsorbents?

Rajamani Krishna* and Jasper M. van Baten

Cite This: *ACS Omega* 2021, 6, 15499−15513

Read Online

ACCESS | Metrics & More | Article Recommendations | Supporting Information

ABSTRACT: Microporous crystalline adsorbents such as zeolites and metal−organic frameworks (MOFs) have potential use in a wide variety of separation applications. The adsorption selectivity S_{ads} is a key metric that quantifies the efficacy of any microporous adsorbent in mixture separations. The Ideal Adsorbed Solution Theory (IAST) is commonly used for estimating the value of S_{ads}, with unary isotherms of the constituent guests as data inputs. There are two basic tenets underlying the development of the IAST. The first tenet mandates a homogeneous distribution of adsorbates within the pore landscape. The second tenet requires the surface area occupied by a guest molecule in the mixture to be the same as that for the corresponding pure component. Configurational-bias Monte Carlo (CBMC) simulations are employed in this article to highlight several scenarios in which the IAST fails to provide a quantitatively correct description of mixture adsorption equilibrium due to a failure to conform to either of the two tenets underpinning the IAST. For CO_2 capture with cation-exchanged zeolites and MOFs with open metal sites, there is congregation of CO_2 around the cations and unsaturated metal atoms, resulting in failure of the IAST due to an inhomogeneous distribution of adsorbates in the pore space. Thermodynamic non-idealities also arise due to the preferential location of CO_2 molecules at the window regions of 8-ring zeolites such as DDR and CHA or within pockets of MOR and AFX zeolites. Thermodynamic non-idealities are evidenced for water/alcohol mixtures due to molecular clustering engendered by hydrogen bonding. It is also demonstrated that thermodynamic non-idealities can be strong enough to cause selectivity reversals, which are not anticipated by the IAST.

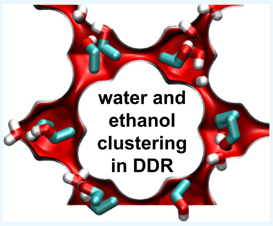

1. INTRODUCTION

Microporous adsorbents such as zeolites and metal−organic frameworks (MOFs) offer energy-efficient alternatives to conventional separation technologies such as distillation. There has been a tremendous upsurge in research on the development of MOFs for a variety of applications such as CO_2 capture and alkene/alkane, alkyne/alkene, and water/alcohol mixture separations. In industrial practice, there are two alternative configurations for utilizing the microporous materials: (i) as crystallites in fixed-bed devices that are operated in transient mode in pressure swing adsorption (PSA) technologies and (ii) as thin perm-selective layers in membrane constructs. A key metric that quantifies the separation performance of both fixed-bed adsorbers and membrane permeation units is the adsorption selectivity S_{ads}. Intracrystalline diffusional influences serve to either enhance or diminish the separation efficacy dictated by mixture adsorption equilibrium. For n-component mixture adsorption, the selectivity of guest constituent i with respect to another guest constituent j in that mixture, $S_{ads,\,ij}$, is defined by

$$S_{ads,ij} = \frac{q_i/q_j}{f_i/f_j} = \frac{q_i/q_j}{y_i/y_j} \tag{1}$$

where q_i and q_j are the molar loadings of the constituents i and j in the adsorbed phase in equilibrium, respectively, with the bulk fluid phase mixture having partial fugacities f_i and f_j and mole fractions $y_i = f_i/f_t$; $f_t = (\sum_{k=1}^{n} f_k)$. For the estimation of the component loadings and selectivity $S_{ads,\,ij}$, it is a common practice to use the Ideal Adsorbed Solution Theory (IAST)[1,2] that requires the unary isotherm data as inputs. The IAST approach has been used in a number of published works for evaluating and ranking microporous crystalline adsorbents for separating a wide variety of mixtures, including CO_2/CH_4,[3,4] CO_2/N_2,[3,5] CO_2/H_2,[6,7] $SO_2/CO_2/N_2$,[8] C_2H_2/C_2H_4,[9−11] C_2H_2/CO_2,[12] C_2H_4/C_2H_6,[13−17] C_3H_4/C_3H_6,[18−20] C_3H_6/C_3H_8,[16,21] Xe/Kr,[22,23] water/alcohol,[24−27] pentane isomers,[28] hexane isomers,[29−31] xylene isomers,[32−34] and ethylbenzene/styrene.[35,36]

Of these cited references, the validity of the use of the IAST for providing quantitatively accurate estimates of selectivities

Received: April 22, 2021
Accepted: May 25, 2021
Published: June 2, 2021

https://doi.org/10.1021/acsomega.1c02136
ACS Omega 2021, 6, 15499−15513

has been established by resorting to configurational-bias Monte Carlo (CBMC) simulations in the following limited number of cases: C_2H_2/C_2H_4 in ZUL-100 and ZUL-200,[11] hexane isomers in $Fe_2(BDP)_3$[30] and ZIF-77,[31] and xylene isomers in MAF-X8.[34]

Despite the widespread usage of the IAST, a limited number of investigations have found that IAST estimates of component loadings for mixture adsorption are not in quantitative agreement with experimental data. These studies include the adsorption of CO_2/N_2,[37] CO_2/CH_4,[38−41] CO_2/C_3H_8,[42−44] CO_2/C_2H_4,[45−47] CO_2/H_2S,[48] and H_2S/C_3H_8[48] mixtures in cation-exchanged zeolites such as NaX (commonly known by its trade name 13X), LTA-5A, ZSM-5, and H-MOR.

The primary objective of this article is to investigate the reliability of IAST estimates of mixture adsorption equilibrium. We aim to highlight a variety of scenarios that would enable researchers to anticipate the possibility of the failure of the IAST to provide quantitative estimates of the component loadings in the adsorbed phase. To meet with the objectives, we resort to configurational-bias Monte Carlo (CBMC) simulations of the unary and mixture adsorption equilibrium for a wide variety of guest/host combinations. The CBMC simulations are performed using the methodology that is firmly established in the literature; details are provided in the Supporting Information accompanying this publication, which also includes (a) structural details of host materials, (b) CBMC data for unary and mixture adsorption, and (c) unary isotherm data fits.

2. RESULTS AND DISCUSSION

2.1. The IAST and Its Prescriptions. In the Myers−Prausnitz development of the IAST,[1] the partial fugacities in the bulk fluid mixture are related to the mole fractions x_i in the adsorbed phase mixture

$$x_i = q_i/q_t; \quad q_t = q_1 + q_2 + ... + q_n; \quad i = 1, 2, ..., n \tag{2}$$

by the analogue of Raoult's law for vapor−liquid equilibrium, i.e.,

$$f_i = P_i^0 x_i; \quad i = 1, 2, ..., n \tag{3}$$

where P_i^0 is the pressure for sorption of every component i, which yields the same spreading pressure π for each of the pure components, as that for the mixture:

$$\frac{\pi A}{RT} = \int_0^{P_1^0} \frac{q_1^0(f)}{f} df = \int_0^{P_2^0} \frac{q_2^0(f)}{f} df = \int_0^{P_3^0} \frac{q_3^0(f)}{f} df = ... \tag{4}$$

In eq 4, A represents the surface area per kg of framework, and $q_i^0(f)$ is the pure component adsorption isotherm; the superscript 0 is used to emphasize that $q_i^0(f)$ relates the pure component loading to the bulk fluid fugacity. Since the surface area A is not directly accessible from experimental data, the surface potential,[40,43] $\frac{\pi A}{RT} \equiv \Phi$, with the unit mol kg^{-1}, serves as a convenient and practical proxy for the spreading pressure π; the surface potential has also been termed the adsorption potential in several recent publications.[49−52]

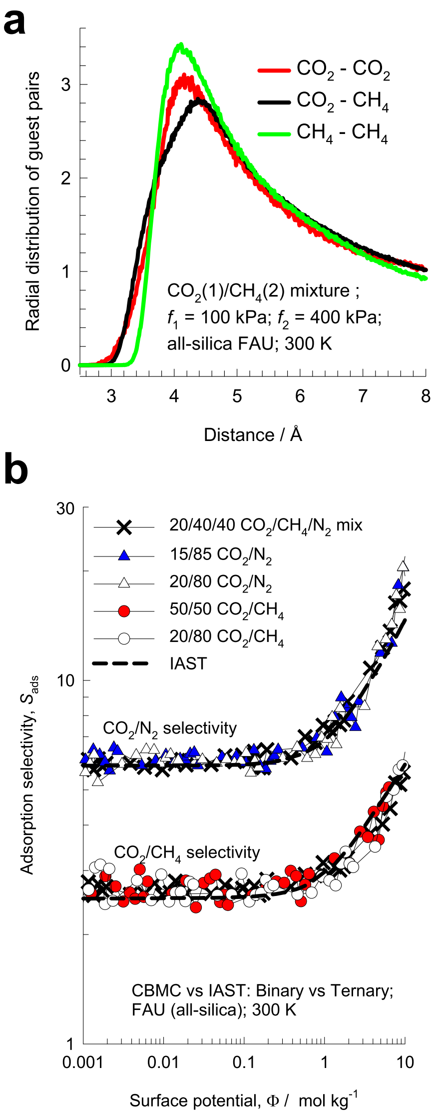

Figure 1. (a) Radial distribution of guest pairs determined from CBMC simulations for the adsorption of CO_2/CH_4 mixtures in all-silica FAU zeolite at 300 K and total fugacity f_t = 500 kPa and y_1 = 0.2. (b) CBMC data for adsorption selectivity for 50/50 CO_2/CH_4, 20/80 CO_2/CH_4, 15/85 CO_2/N_2, 20/80 CO_2/N_2, and 20/40/40 $CO_2/CH_4/N_2$ mixtures in all-silica FAU. The x-axis represents the surface potential Φ. The dashed lines are the IAST estimations. All calculation details and input data are provided in the Supporting Information accompanying this publication.

For multicomponent mixture adsorption, each of the equalities on the right side of eq 4 must be satisfied. These constraints may be solved using a suitable equation solver to yield the set of values of P_1^0, P_2^0, P_3^0, ..., P_n^0, all of which satisfy eq 4. The corresponding values of the integrals using P_i^0 as upper limits of integration must yield the same value of the surface potential Φ for each component; this ensures that the obtained solution is the correct one.

The adsorbed phase mole fractions x_i are then determined from

$$x_i = f_i/P_i^0; \quad i = 1, 2, ..., n \tag{5}$$

The applicability of eq 5 mandates that all of the adsorption sites within the microporous material are equally accessible to each of the guest molecules, implying a homogeneous

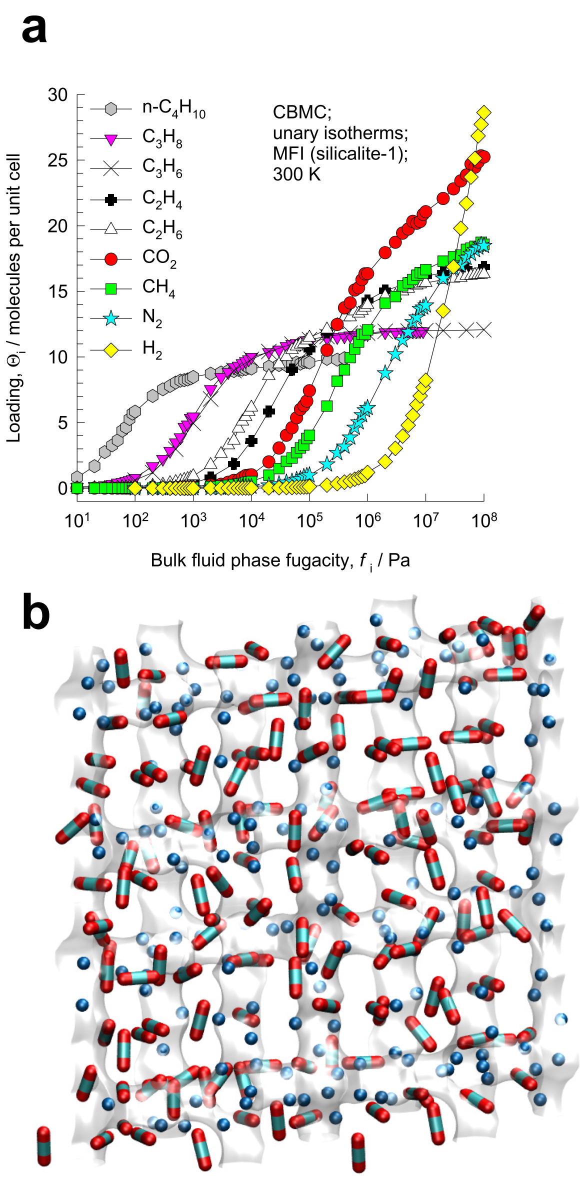

Figure 2. (a) CBMC simulations of unary isotherms for light gaseous molecules H_2, N_2, CO_2, CH_4, C_2H_4, C_2H_6, C_3H_6, C_3H_8, and *n*-C_4H_{10} in MFI zeolite at 300 K. (b) Computational snapshots showing the location of CO_2 and CH_4 for binary mixture adsorption in MFI.

distribution of guest adsorbates within the pore landscape, with no preferential locations of any guest species.

In view of eqs 2 and 5, we rewrite eq 1 as the ratio of the sorption pressures

$$S_{\mathrm{ads},ij} = P_j^0/P_i^0 \tag{6}$$

Applying the restriction specified by eq 4, it follows that $S_{\mathrm{ads},\,ij}$ is uniquely determined by the surface potential Φ. It is important to note that eq 6 is valid irrespective of the total number of components in the mixture. In other words, the presence of component 3 in the ternary mixture has no direct influence on the adsorption selectivity $S_{\mathrm{ads},12} = P_2^0/P_1^0$ for the 1−2 pair, except for the fact that the surface potential Φ that satisfies eq 4 is altered due to the presence of component 3.

A further key assumption of the IAST is that the adsorption enthalpies and surface areas of the adsorbed molecules do not change upon mixing with other guests. If the total mixture loading is q_t, the area covered by the adsorbed mixture is $\frac{A}{q_t}$ with the unit m^2 (mole mixture)$^{-1}$. Therefore, the assumption of no surface area change due to mixture adsorption translates as $\frac{A}{q_t} = \frac{Ax_1}{q_1^0(P_1^0)} + \frac{Ax_2}{q_2^0(P_2^0)} + \cdots + \frac{Ax_n}{q_n^0(P_n^0)}$; the total mixture loading is $q_t = q_1 + q_2 + \ldots + q_n$, which is calculated from

$$\frac{1}{q_t} = \frac{x_1}{q_1^0(P_1^0)} + \frac{x_2}{q_2^0(P_2^0)} + \ldots + \frac{x_n}{q_n^0(P_n^0)} \tag{7}$$

in which $q_1^0(P_1^0)$, $q_2^0(P_2^0)$, ..., $q_n^0(P_n^0)$ are determined from the unary isotherm fits, using the sorption pressures for each component P_1^0, P_2^0, P_3^0, ..., P_n^0, that are available from the solutions to eq 4. The occurrence of molecular clustering and hydrogen bonding should be expected to invalidate the applicability of eq 7 because the surface area occupied by a molecular cluster is different from that of each of the unclustered guest molecules in the adsorbed phase.

The ratio of the total mixture loading, q_t, to the saturation capacity of the mixture, $q_{\mathrm{sat,\,mix}}$, is the fractional pore occupancy, θ, which is relatable to Φ as follows (see the Supporting Information for the complete derivation)

$$\theta \equiv q_t/q_{\mathrm{sat,mix}} = 1 - \exp(-\Phi/q_{\mathrm{sat,mix}}) \tag{8}$$

where the saturation capacity $q_{\mathrm{sat,\,mix}}$ is calculated from the saturation capacities of the constituent guests

$$\frac{1}{q_{\mathrm{sat,mix}}} = \sum_{k=1}^{n} \frac{x_k}{q_{k,\mathrm{sat}}} \tag{9}$$

The surface potential Φ is therefore also interpretable as a proxy for the pore occupancy.

Armed with these concepts, let us compare the CBMC simulation data for mixture adsorption with the IAST predictions. Further details of the CBMC simulations (force fields used and host structures) and IAST (unary isotherm data fits) are provided in the Supporting Information.

2.2. Homogeneously Distributed Guests: Fulfilling the IAST Prescription. A quantitative procedure to verify the IAST precept of homogeneous distribution of guest adsorbates within the pore space is to perform CBMC simulations to determine the spatial locations of the guest molecules and to determine the intermolecular distances. As an illustration, we consider CO_2/CH_4 mixture adsorption in all-silica FAU zeolite with a total fugacity f_t = 500 kPa and y_1 = 0.2 at 300 K. FAU zeolite has a large "open" structure that consists of cages with a volume of 786 Å^3, separated by 12-ring windows with a size of 7.4 Å. By sampling a total of 10^5 simulation steps, the radial distribution of the separation distances between the molecular pairs CO_2−CO_2, CO_2−CH_4, and CH_4−CH_4 were determined. The data on the distances between the molecular pairs CO_2−CO_2, CO_2−CH_4, and CH_4−CH_4 are shown in Figure 1a; such plots are commonly termed radial distribution functions (RDFs). We note that the peaks occur at practically the same intermolecular distances. This indicates that there are no congregation or segregation effects and that the guest molecules are homogeneously distributed within the pore landscape, adequately fulfilling the precept of the IAST. Consequently, we should expect the IAST to provide a good quantitative description of CO_2/CH_4 mixture adsorption in all-silica FAU zeolite. As confirmation, Figure 1b presents CBMC data for CO_2/CH_4, and CO_2/N_2 adsorption selectivities for 50/50 CO_2/CH_4, 20/80 CO_2/CH_4, 15/85 CO_2/N_2, 20/80

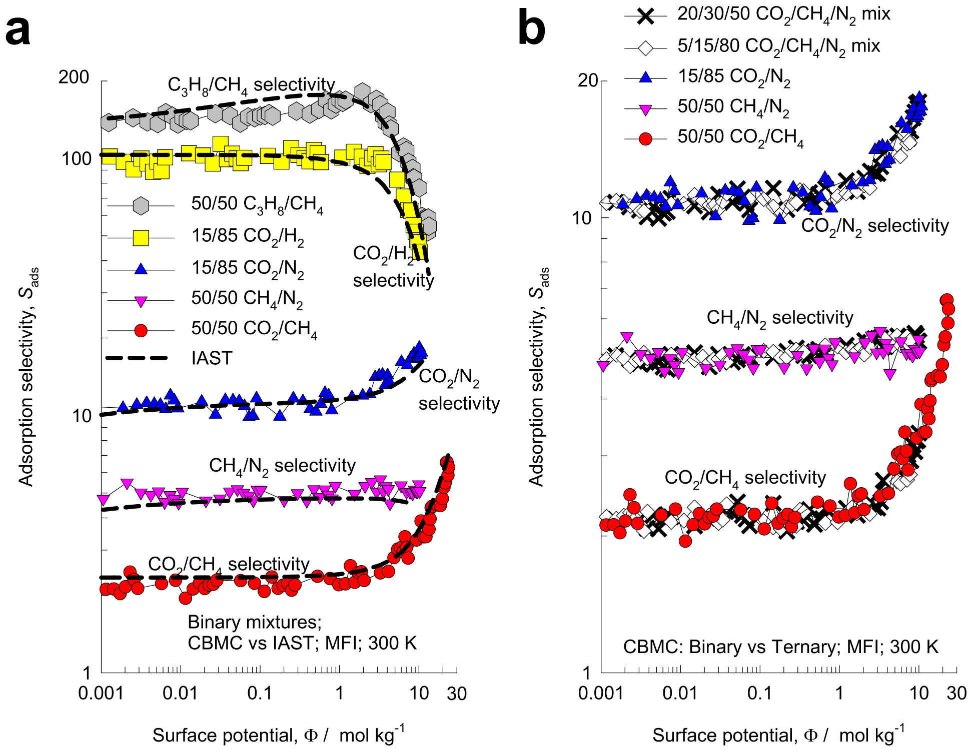

Figure 3. (a) CBMC simulations (indicated by symbols) of the adsorption selectivity S_{ads} for five different binary mixtures: CO_2/CH_4, CO_2/N_2, CH_4/N_2, CO_2/H_2, and C_3H_8/CH_4 in MFI zeolite at 300 K. The dashed lines are the IAST calculations for corresponding S_{ads} values using the dual-site Langmuir−Freundlich fits of unary isotherms. (b) Comparison of CO_2/CH_4, CO_2/N_2, and CH_4/N_2 adsorption selectivities determined from binary mixtures, with the corresponding values in two different ternary mixtures: 5/15/80 $CO_2/CH_4/N_2$ and 20/30/50 $CO_2/CH_4/N_2$. The *x*-axes represent the surface potential Φ. All calculation details and input data are provided in the Supporting Information accompanying this publication.

CO_2/N_2, and 20/40/40 $CO_2/CH_4/N_2$ mixtures in all-silica FAU. The CO_2/CH_4 and CO_2/N_2 selectivities are uniquely determined by the surface potential Φ, irrespective of the composition of the bulk fluid phase mixture and the presence of the third component. The IAST estimations, shown by the dashed lines, are in good agreement with the CBMC-simulated values of S_{ads}.

Let us turn to mixture adsorption in MFI zeolite, a host structure in which the guest molecules are more strongly constrained. MFI (also called silicalite-1) has a topology consisting of a set of intersecting straight channels and zig-zag (or sinusoidal) channels with sizes of 5.4 Å × 5.5 Å and 5.4 Å × 5.6 Å. The IAST prescription demanding the homogeneous distribution of guest molecules within MFI zeolite is fulfilled only for light gaseous guest molecules such as H_2, N_2, CO_2, CH_4, C_2H_4, C_2H_6, C_3H_6, C_3H_8, and *n*-C_4H_{10}. These light gaseous guests can locate anywhere along the straight channels and zig-zag channels, and there are no perceptible isotherm inflections, as evidenced in the unary isotherms in Figure 2a. The saturation capacities follow the hierarchy $H_2 > CO_2 > N_2 \approx CH_4 > C_2H_4 \approx C_2H_6 > C_3H_6 \approx C_3H_8 > n\text{-}C_4H_{10}$. Figure 2b shows computational snapshots for the adsorption of CO_2 and CH_4 within the intersecting channel topology of MFI zeolite. It is noticeable that neither guest species show any preferential location and there is no visual indication of segregated adsorption. The Coulombic interactions of CO_2 with the negatively charged oxygen atoms in the zeolite framework are not strong enough to cause segregation between CO_2 and CH_4. We should therefore expect the mixture adsorption characteristics to be adequately well described by the IAST.

The IAST calculations for the adsorption selectivity S_{ads} for five different binary mixtures CO_2/CH_4, CO_2/H_2, CO_2/N_2, CH_4/N_2, and C_3H_8/CH_4 are compared with the corresponding S_{ads} values determined from CBMC simulations in Figure 3a. For all five mixtures, the IAST estimations are in good agreement with the CBMC-simulated data, plotted as a function of the surface potential Φ. For CO_2/CH_4 and CO_2/N_2 mixtures, the S_{ads} increases as pore saturation conditions are approached, i.e., $\Phi > 10$ mol kg^{-1}; $\theta > 0.5$, because of entropy effects that favor the guest CO_2 with the higher saturation capacity (cf. Figure 2a); the explanation of entropy effects is provided in the published literature.[33,53] For CO_2/H_2 and C_3H_8/CH_4 mixtures, the S_{ads} decreases as pore saturation conditions are approached because entropy effects favor the smaller guests H_2 and CH_4, respectively, that have significantly higher saturation capacities. For CH_4/N_2 mixtures, the S_{ads} is practically independent of occupancy because the saturation capacities of CH_4 and N_2 are nearly the same, as evidenced in Figure 2a.

Figure 3b presents a comparison of CO_2/CH_4, CO_2/N_2, and CH_4/N_2 adsorption selectivities determined from binary mixtures in MFI, with the corresponding values determined from CBMC simulations using two different ternary mixtures: 5/15/80 $CO_2/CH_4/N_2$ and 20/30/50 $CO_2/CH_4/N_2$. Each of the three selectivities shows a unique dependence on Φ, as prescribed by eqs 5 and 6. In other words, the presence of component 3 in the ternary mixture has no direct influence on the adsorption selectivity for the 1−2 pair other than via Φ, as is anticipated on the basis of the development of the IAST.

Results analogous to those presented in Figures 1b and 3b, demonstrating the unique dependence of S_{ads} on Φ, and the

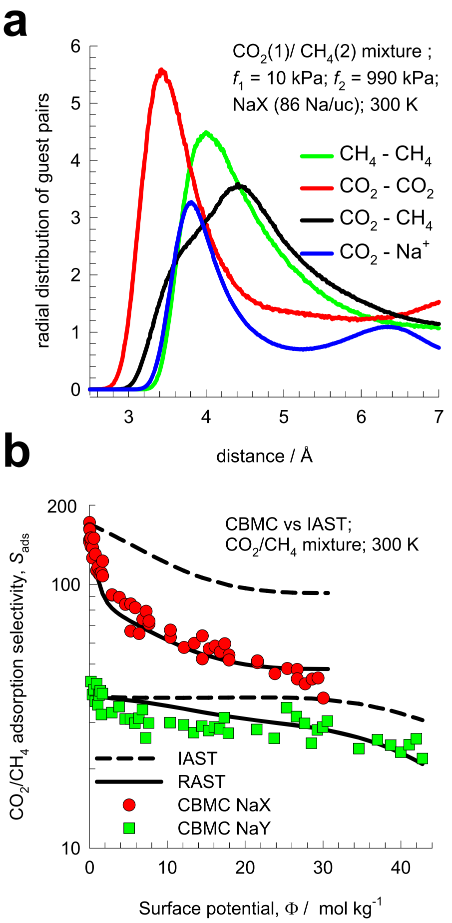

Figure 4. (a) Radial distribution of guest pairs determined from CBMC simulations for the adsorption of CO_2/CH_4 mixtures in NaX zeolite at 300 K and total fugacity f_t = 1 MPa, and y_1 = 0.01. (b) Comparison CO_2/CH_4 adsorption selectivities determined from CBMC simulations for NaY (138 Si, 54 Al, 54 Na^+, and Si/Al = 2.56) and NaX (106 Si, 86 Al, 86 Na^+, and Si/Al = 1.23) zeolites at 300 K. The CBMC-simulated values (indicated by symbols) are compared with RAST (continuous solid lines) and IAST (dashed lines) estimates. All calculation details and input data are provided in the Supporting Information accompanying this publication.

concomitant accuracy of IAST estimates are found for (i) $CO_2/CH_4/N_2$ mixture adsorption in ISV that has intersecting channel structures of 6 Å (see Figure S28), (ii) $CO_2/CH_4/N_2$ mixture adsorption in all-silica LTA zeolite that has cages separated by 4.11 Å × 4.47 Å 8-ring windows (see Figure S77), (iii) adsorption of ternary and quinary mixtures of hexane isomers in Mg_2(dobdc), which has 1D hexagonal channels of 11 Å (see Figure S102a), and (iv) adsorption of ternary and quinary mixtures of hexane isomers in Co(BDP), which has 1D square channels of 10 Å (see Figure S102b). In all these cases, the IAST prescription is met because the guest molecules are homogeneously distributed within the pore landscape, allowing the guest species to compete equitably with one another.

2.3. Congregation of Charged Guests around Cations. Let us consider CO_2/CH_4 mixture adsorption in cation-exchanged NaX zeolite that has the same pore topology as FAU zeolite; per unit cell NaX zeolite has 106 Si, 86 Al, and 86 Na^+ with Si/Al = 1.23. Figure 4a presents the RDF data determined from CBMC simulations. If we compare the first peaks, it is noteworthy that the CO_2-CO_2 and CO_2-Na^+ pairs are close together, indicating that the major proportion of CO_2 congregates around the cations. A further point to note is that the CO_2-CH_4 separation distance is significantly larger than the CO_2-CO_2 and CH_4-CH_4 separation distances. This implies that the CH_4 molecules face less severe competitive adsorption with CO_2 than is anticipated by the IAST. Consequently, as seen in Figure 4b, the values of S_{ads} estimated by the IAST are significantly higher, by about a factor of two, than those determined by CBMC. Also shown in Figure 4b are the CBMC data for CO_2/CH_4 mixture adsorption in NaY zeolite (138 Si, 54 Al, 54 Na^+, and Si/Al = 2.56); the IAST estimates are also in excess of the CBMC data, but the departures are less than that experienced with NaX because congregation effects are reduced due to the presence of fewer cations in NaY. Of course, in the total absence of cations, the IAST estimates are in excellent agreement with CBMC data, as already witnessed in Figure 1b.

The inhomogeneous distribution of adsorbates is a common feature of mixtures of charged and neutral guests in cation-exchanged zeolites. Figure 5a shows the RDF data for CO_2/C_3H_8 mixture adsorption in NaX zeolite. The $CO_2-C_3H_8$ separation distance is significantly higher than between the CO_2-CO_2 and CO_2-Na^+ pairs, indicating that C_3H_8 experiences reduced competition with CO_2 partners. The consequences of this reduced competition is reflected by the CBMC data for $CO_2(1)/C_3H_8(2)$ mixture adsorption in three different CBMC campaigns: (i) equimolar mixtures, $y_1 = y_2 = 0.5$, with varying $f_t = f_1 + f_2$, (ii) f_t = 1 MPa with varying y_1, and (iii) f_t = 50 kPa with varying y_1. The assumption of an ideal adsorbed mixture anticipates all three data sets to follow a unique $S_{ads} - \Phi$ dependence, as shown by the dashed line in Figure 5b. However, the CBMC data (indicated by symbols) show that the $CO_2(1)/C_3H_8(2)$ adsorption selectivity S_{ads} does not follow a unique dependence on Φ.

To quantify non-ideality effects and departures from the IAST, we need to abandon Raoult's law assumption in eq 3 and introduce activity coefficients γ_i

$$\gamma_i = f_i / x_i P_i^0; \quad i = 1, 2 ..., n \tag{10}$$

Figure 5c presents the activity coefficients calculated from the CBMC data for campaign (i) for equimolar mixtures of CO_2 and C_3H_8 with varying f_t. As $\Phi \rightarrow 0$, both activity coefficients tend to unity $\gamma_i \rightarrow 1$; this corresponds with the Henry regime of adsorption. In other words, at vanishing small values of pore occupancy, non-ideality effects can be ignored, as should be expected. With increasing pore occupancy, the activity coefficient of C_3H_8 steadily decreases below unity, whereas the activity coefficient of CO_2 remains close to unity over the entire range of Φ values.

Figure 5d presents the activity coefficients calculated from the CBMC data for campaign (ii) with f_t = 1 MPa and varying bulk fluid mixture composition; in this campaign, the variation of Φ is minimal and falls in the range $24 < \Phi < 30$ mol kg^{-1}. Both activity coefficients are strongly dependent on the composition of the adsorbed phase mixture, x_1, and satisfy the requirement $x_i \rightarrow 1$; $\gamma_i \rightarrow 1$.

Following the approaches of Myers, Talu, and Sieperstein,[43,48,54] we model the excess Gibbs free energy for binary mixture adsorption as follows

$$\frac{G^{\text{excess}}}{RT} = x_1 \ln(\gamma_1) + x_2 \ln(\gamma_2) \tag{11}$$

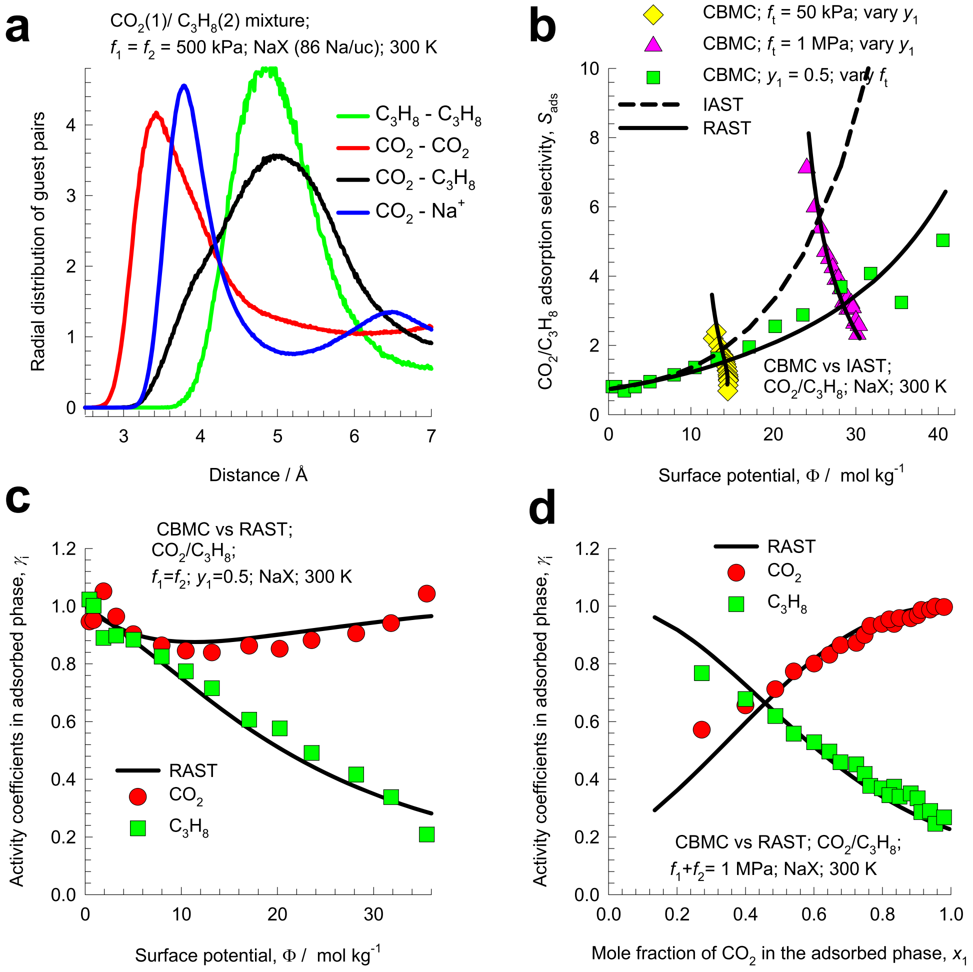

Figure 5. (a) Radial distribution of guest pairs determined from CBMC simulations for the adsorption of CO_2/C_3H_8 mixtures in NaX zeolite at 300 K and total fugacity f_t = 1 MPa and y_1 = 0.5. (b) Adsorption selectivity S_{ads} for $CO_2(1)/C_3H_8(2)$ mixture adsorption in NaX zeolite at 300 K for three different CBMC campaigns, plotted as a function of the surface potential Φ: (i) constant composition y_1 = 0.5 with varying $f_t = f_1 + f_2$, (ii) f_t = 1 MPa with varying composition y_1, and (iii) f_t = 50 kPa with varying y_1. The CBMC-simulated values (indicated by symbols) are compared with RAST (continuous solid lines) and IAST (dashed lines) estimates. (c) Activity coefficients for $CO_2(1)$ and $C_3H_8(2)$, determined from campaign (i). (d) Activity coefficients for $CO_2(1)$ and $C_3H_8(2)$ determined from campaign (ii). The continuous solid lines in panels (b) and (c) are RAST/Margules model calculations. All calculation details and input data are provided in the Supporting Information accompanying this publication.

For the calculation of the total mixture loading $q_t = q_1 + q_2$, we need to replace eq 7 by

$$\frac{1}{q_t} = \frac{x_1}{q_1^0(P_1^0)} + \frac{x_2}{q_2^0(P_2^0)} + \left(\frac{1}{q_t}\right)^{\text{excess}} \tag{12}$$

The excess reciprocal loading for the mixture can be related to the partial derivative of the Gibbs free energy with respect to the surface potential at constant composition

$$\left(\frac{1}{q_t}\right)^{\text{excess}} = \left.\frac{\partial\left(\frac{G^{\text{excess}}}{RT}\right)}{\partial\Phi}\right|_{T,x} \tag{13}$$

For quantitative modeling of the data on activity coefficients, a variety of models such as regular solution,[43] Wilson,[50,51,55] NRTL,[56] SPD,[48] and Margules[52,57] have been used. For example, the Margules model takes the following form

$$\ln(\gamma_1) = x_2^2(A_{12} + 2(A_{21} - A_{12})x_1)(1 - \exp(-C\Phi))$$
$$\ln(\gamma_2) = x_1^2(A_{21} + 2(A_{12} - A_{21})x_2)(1 - \exp(-C\Phi)) \tag{14}$$

In eq 14, C is a constant with the unit kg mol^{-1}. The introduction of $(1 - \exp(-C\Phi))$ imparts the correct limiting behaviors for the activity coefficients in the Henry regime: $\Phi \to 0$; $\gamma_i \to 1$. As pore saturation conditions are approached, this correction factor tends to unity: $(1 - \exp(-C\Phi)) \to 1$.

Combining eqs 11−14, we derive

$$\frac{1}{q_t} = \frac{x_1}{q_1^0(P_1^0)} + \frac{x_2}{q_2^0(P_2^0)} + x_1x_2[A_{12}x_2 + A_{21}x_1]C\exp(-C\Phi) \tag{15}$$

The parameters A_{12}, A_{21}, and C can be fitted to match the CBMC data on activity coefficients; the fitting procedure is detailed in the Supporting Information accompanying this publication. The continuous solid lines in Figure 5c,d are calculations following the Real Adsorbed Solution Theory

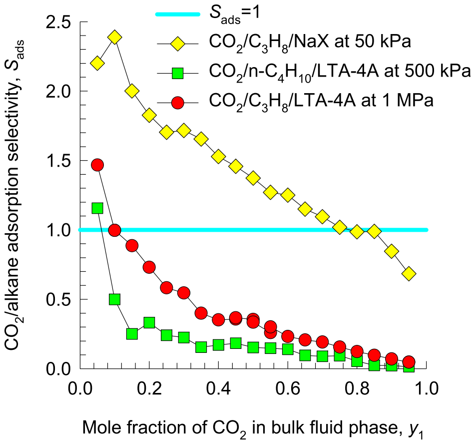

Figure 6. CBMC simulation data for CO_2/alkane selectivities determined from three different CBMC campaigns: (i) $CO_2(1)/C_3H_8(2)$ mixture adsorption in NaX with f_t = 50 kPa and varying y_1, (ii) $CO_2(1)/C_3H_8(2)$ mixture adsorption in LTA-4A with f_t = 1 MPa and varying y_1, and (iii) $CO_2(1)/n\text{-}C_4H_{10}(2)$ mixture adsorption in LTA-4A with f_t = 500 kPa and varying y_1. The CO_2/alkane selectivity values in each case are plotted against the mole fraction in the bulk fluid mixture, y_1. All calculation details and input data are provided in the Supporting Information accompanying this publication.

(RAST) with fitted Margules parameters $A_{12} = -3.082$, $A_{21} = -2.170$, and $C = 0.038$ kg mol^{-1}.

With the introduction of activity coefficients, eq 6 needs to be replaced by the more generalized expression for the adsorption selectivity for the i−j pair

$$S_{ads,ij} = \frac{P_j^0 \gamma_j}{P_i^0 \gamma_i} \qquad (16)$$

Equations 14 and 16 imply that the $S_{ads,\,ij}$ depends on both Φ and the composition of the adsorbed mixture; this point is underscored in the RAST calculations (indicated by the continuous solid lines) of the selectivity for the three campaigns in Figure 5b. An important consequence of this complex dependence is the occurrence of selectivity reversal phenomena. Figure 6 presents CBMC data on the CO_2/C_3H_8 and $CO_2/n\text{-}C_4H_{10}$ selectivities for cation-exchanged zeolites NaX and LTA-4A; in the simulations, the total mixture fugacity f_t is maintained at a fixed value. With increasing proportion of CO_2 in the bulk fluid mixture, selectivity reversals in favor of the alkane occur; all such reversals are not anticipated by the IAST (see Figures S69, S75, S76, and S86). Experimental evidence of such selectivity reversals, attributable to congregation of CO_2 around cations, has been reported for CO_2/C_3H_8[42−44] and CO_2/C_2H_4[45] in cation-exchanged zeolites.

For the adsorption of the CO_2-bearing mixture in Mg_2(dobdc), the preponderance of CO_2 around the unsaturated Mg^{2+} sites causes quantitative failure of the IAST; see CBMC data in Figures S95 and S96.

Other examples of the failure of the IAST, along with alternative approaches to RAST modeling of non-idealities, are available in the literature.[2,58−62]

2.4. Preferential Location of Guests at Channel Intersections of MFI Zeolite. Due to configurational considerations, branched alkanes prefer to locate at the channel intersections of MFI zeolite because of the extra "leg room" that is available here. An extra "push" is required to locate these molecules within the channel interiors. This extra push results in an inflection in the pure component isotherms at a loading of four molecules per unit cell because per unit cell of MFI, there are four channel intersection sites;[63−66] see Figure 7a. Cyclic hydrocarbons, such as cyclohexane, benzene, and ethylbenzene, also prefer to locate at the intersections; the unary isotherm for benzene also exhibits a strong inflection at a loading of four molecules per unit cell (cf. Figure 7a). For

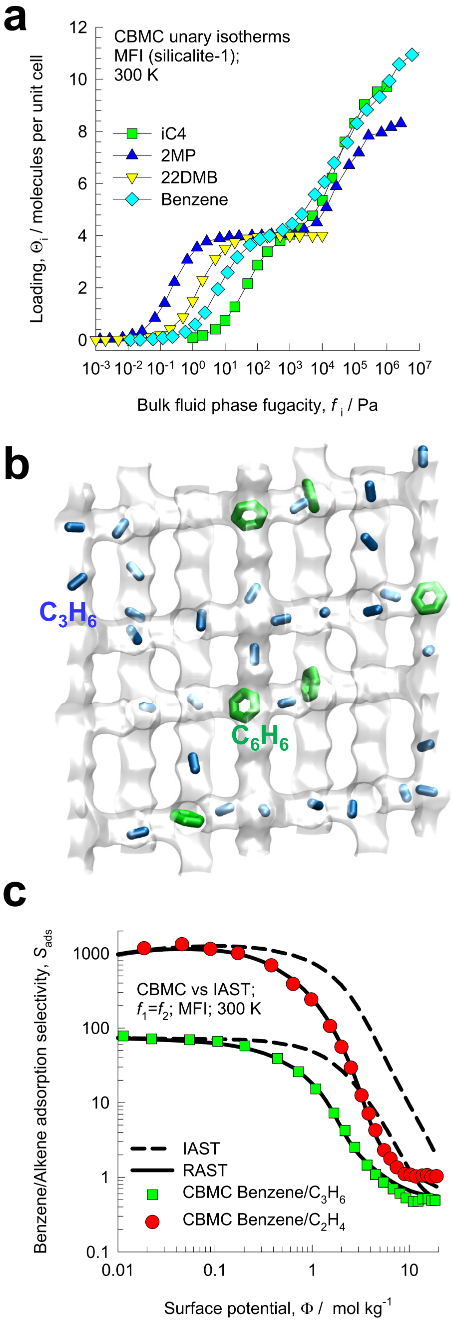

Figure 7. (a) CBMC simulations of unary isotherms for branched alkanes and benzene in MFI zeolite at 300 K. (b) Computational snapshots showing the location of guest molecules for $C_3H_6(1)$/benzene(2) mixture adsorption in MFI zeolite at 300 K. (c) Adsorption selectivity S_{ads} for benzene/C_2H_4 and benzene/C_3H_6 mixtures in MFI zeolite, plotted as a function of the surface potential Φ. The CBMC-simulated values (indicated by symbols) are compared with RAST (continuous solid lines) and IAST (dashed lines) estimates. All calculation details and input data are provided in the Supporting Information accompanying this publication.

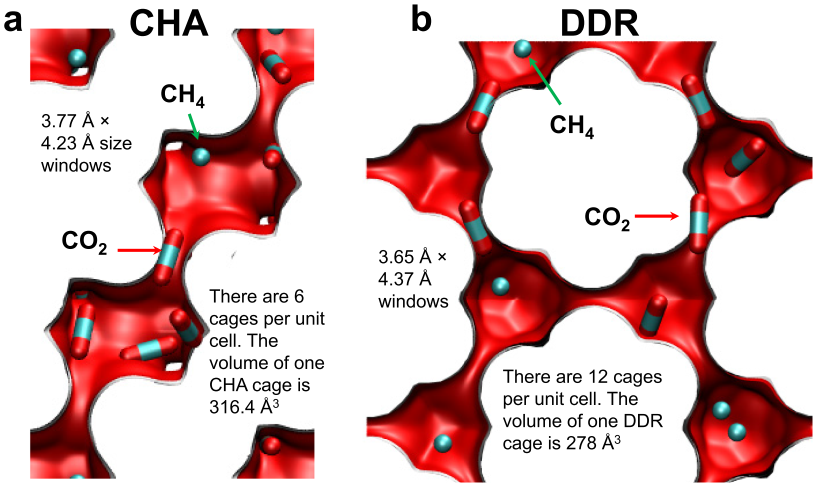

Figure 8. Computational snapshots for $CO_2(1)/CH_4(2)$ mixture adsorption in (a) CHA and (b) DDR zeolites at 300 K.

$C_3H_6(1)$/benzene(2) mixture adsorption in MFI, the computational snapshots in Figure 7b clearly show that the aromatics are exclusively located at the channel intersections, whereas the linear propene can locate anywhere along either the straight or zig-zag channels. Figure 7c plots the CBMC data for adsorption selectivity S_{ads} of $C_2H_4(1)$/benzene(2) and $C_3H_6(1)$/benzene(2) mixtures as functions of Φ. For both mixtures, the IAST (indicated by the dashed lines) significantly overestimates the S_{ads} value in favor of benzene, except for the limiting case of low pore occupancy $\Phi \rightarrow 0$, $\theta \rightarrow 0$. The IAST calculation assumes that alkene molecules (C_2H_4 or C_3H_6) compete with all of the benzene molecules, making no allowance for segregation and preferential adsorption of benzene at the intersections. Due to segregation effects, the competition faced by alkene molecules within the channels is lower than that in the entire pore space. In other words, the IAST anticipates a stiffer competition between benzene and alkenes as it assumes a uniform distribution of adsorbates; consequently, the separation selectivity is overestimated. Due to the preferential location of benzene at the intersections, some alkene molecules are farther removed from benzene and suffer diminished competition.

A further point to be noted is that the benzene/alkene selectivity reduces significantly with increasing values of Φ; this reduction in S_{ads} is a direct consequence of entropy effects that favor alkene because of significantly higher saturation capacity. The CBMC data for C_3H_6/benzene mixtures and entropy effects are strong enough to cause selectivity reversals in favor of propene, for $\Phi > 5$ mol kg^{-1}, corresponding to $\theta > 0.93$. Such selectivity reversal is not quantitatively matched by the IAST; the use of the RAST is necessary for a good quantitative description of $S_{ads} - \Phi$ characteristics.

For precisely analogous reasons, adsorption of C_3H_8/iso-C_4H_{10}, n-C_4H_{10}/iso-C_4H_{10}, and n-hexane/2-methylpentane mixtures in MFI zeolite shows significant deviations from IAST estimates of component loadings and selectivities; see Figures S19−S25 of the Supporting Information.

2.5. Preferential Location of CO_2 at Window Regions of Cage-Type Zeolites.

For the separation of CO_2 from gaseous mixtures with CH_4, cage-type zeolites such as CHA, DDR, LTA, and ERI are of practical interest;[67−69] these materials consist of cages separated by narrow windows in the 3.3−4.5 Å range. For adsorption of CO_2/CH_4 mixtures, CBMC simulations[67] show that the window regions of cage-type zeolites have a significantly higher proportion of CO_2 than within the cages; see computational snapshots in Figure 8 for (a) CHA and (b) DDR zeolites.

In Figure 9a, the CBMC-simulated values of the adsorption selectivity S_{ads} for CO_2/CH_4 mixture adsorption in CHA, determined from three different CBMC campaigns, are plotted as a function of Φ. For all three sets of CBMC data, the IAST calculations overestimate the values of S_{ads} because the competition faced by CH_4, which locates predominantly within the cages, is less severe than anticipated because of the preferential location of CO_2 in the window regions. The deviations of IAST estimates from CBMC-simulated values increase with increasing pore occupancies.

Precisely analogous results are obtained for CO_2/CH_4 mixture adsorption in DDR, determined from two different CBMC campaigns; see Figure 9b. The CBMC-simulated S_{ads} values for the two sets of campaigns are not uniquely related to Φ, as is anticipated by the IAST; the non-unique $S_{ads} - \Phi$ characteristics are quantitatively captured by the RAST. As pore saturation conditions are approached, the IAST predictions of selectivities become increasingly optimistic.

2.6. Preferential Location of CO_2 within Pockets of AFX and MOR.

Earlier works have shown that AFX zeolite is particularly effective for CO_2 capture applications.[70−72] Figure 10a shows snapshots for adsorption of the binary mixture of CO_2 and CH_4. In one unit cell of AFX, there are four 490 Å^3-sized cages, connected to four small pockets each of 98 Å^3. The 8-ring windows separating two cages are 3.44 Å × 3.88 Å in size. Guests such as CH_4, N_2, or H_2 are preferentially located within the cages. The competition experienced by CH_4, N_2, or H_2 from coadsorption with CO_2 should be expected to be significantly lowered because the window regions and the small pockets are preferred locations for CO_2.[67,70,71,73] Consequently, the IAST should be expected to overestimate the CO_2/CH_4 selectivity. The CBMC data for CO_2/CH_4 mixture adsorption in AFX confirms this expectation; see Figure 11a. Figure 11a also shows that the IAST overestimates the CO_2/CH_4 selectivity values in MOR zeolite because CO_2 gets firmly ensconced in the side pockets (cf. snapshots in Figure 10b), far removed from the CH_4 partners that preferentially reside in the main 12-ring 1D channels.

The segregation between CO_2 and its partners in MOR also results in selectivity reversals. Figure 11b shows CBMC data for $CO_2(1)/C_3H_8(2)$ mixture adsorption in all-silica MOR

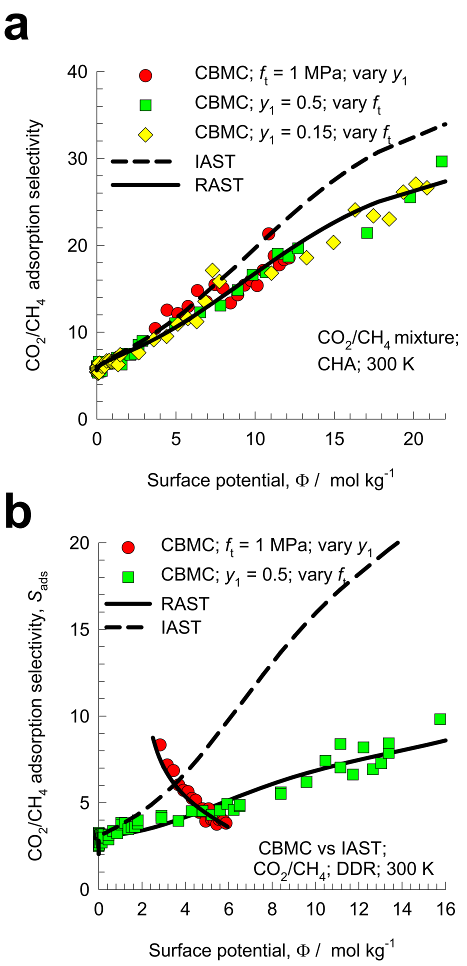

Figure 9. (a) CBMC data for adsorption selectivity S_{ads} for CO$_2$(1)/CH$_4$(2) mixture adsorption in CHA zeolite, determined for three different campaigns: (i) constant composition y_1 = 0.5 with varying $f_t = f_1 + f_2$, (ii) constant composition y_1 = 0.15 with varying f_t, and (iii) f_t = 1 MPa with varying y_1. (b) CBMC data for adsorption selectivity S_{ads} for CO$_2$(1)/CH$_4$(2) mixture adsorption in DDR, determined for two different campaigns: (i) constant composition y_1 = 0.5 with varying f_t and (ii) f_t = 1 MPa with varying composition y_1. The x-axes represent the surface potential Φ. The CBMC-simulated values (indicated by symbols) are compared with RAST (continuous solid lines) and IAST (dashed lines) estimates. All calculation details and input data are provided in the Supporting Information accompanying this publication.

zeolite for a campaign in which the total fluid phase fugacity f_t = 40 kPa and the bulk fluid phase mixture composition $y_1 = f_1/f_t$ is varied. For $y_1 < 0.6$, $S_{ads} > 1$, and the selectivity is in favor of CO$_2$. The CBMC simulations show that the adsorption selectivity S_{ads} is increasingly lowered below unity, i.e., in favor of alkane, with increasing proportion of CO$_2$ in the bulk gas phase. The IAST anticipates S_{ads} to be virtually independent of y_1 and does not anticipate the selectivity reversal phenomena. Experimental evidence is available for such selectivity reversals, which require the use of the RAST for quantification.[48,50]

2.7. Hydrogen Bonding in Water/Alcohol Mixtures.

For water/alcohol mixture adsorption in zeolites and MOFs, the manifestation of hydrogen bonding between water and alcohol molecules can be demonstrated by sampling the spatial locations of the guest molecules to determine the O····H distances of various pairs of molecular distances. For water(1)/ethanol(2) mixture adsorption in DDR zeolite at 300 K, the RDFs of O····H distances for water−water, water−ethanol, and ethanol−ethanol pairs are shown in Figure 12. We note that the first peaks in the RDFs occur at a distance less than 2 Å, which is characteristic of hydrogen bonding.[74,75] The heights of the first peaks are a direct reflection of the degree of hydrogen bonding between the molecular pairs. The degree of H-bonding between water−ethanol pairs is significantly larger, by about an order of magnitude, than for water−water and ethanol−ethanol pairs.

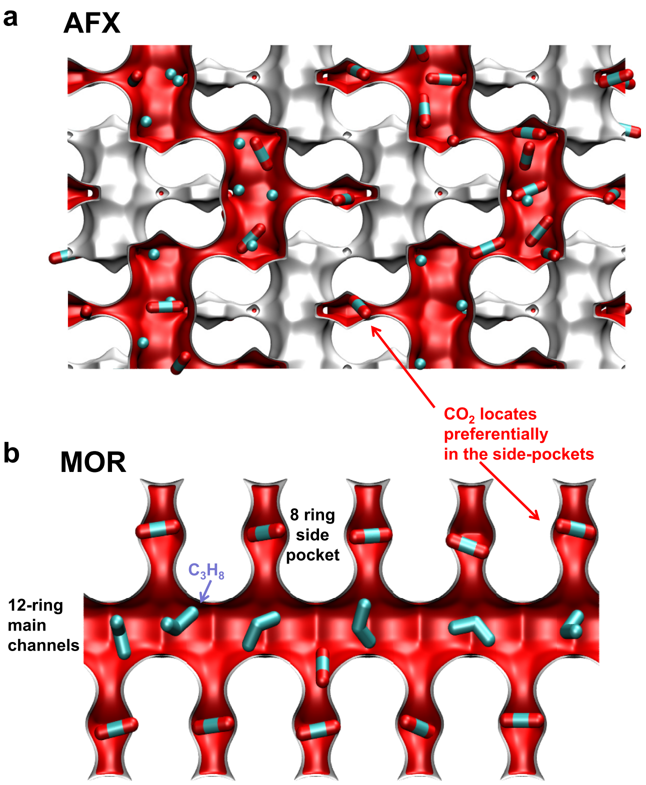

Figure 10. (a) Snapshots showing the location of guest molecules for CO$_2$(1)/CH$_4$(2) mixture adsorption in AFX zeolite at 300 K. (b) Snapshots showing the location of guest molecules for CO$_2$(1)/C$_3$H$_8$(2) mixture adsorption in MOR zeolite at 300 K.

Figure 13a presents CBMC data on the ethanol/water selectivity in DDR for mixtures in which the partial fugacities are maintained equal for both guests, i.e., $f_1 = f_2$. With increasing values of the surface potential, the selectivity increasingly favors water adsorption due to its smaller size. For Φ ≈ 10 mol kg^{-1}, corresponding to a pore occupancy $\theta \approx 0.9$, the mixture adsorption is water-selective. Although the IAST calculations (dashed lines) correctly anticipate the selectivity reversal phenomenon, the quantitative agreement of IAST estimates with CBMC data is poor. For Φ < 10 mol kg^{-1}, the IAST overestimates S_{ads} due to enhanced water uptake resulting from molecular clustering. A further, distinct consequence of molecular clustering effects induced by hydrogen bonding is that the effective size difference between the guest molecules is reduced. Consequently, entropy effects are moderated by clustering phenomena. The IAST that does not account for clustering anticipates an exaggerated influence of entropy effects. In other words, for Φ > 10 mol kg^{-1}, cluster formation tends to moderate entropy effects, and the IAST anticipates stronger water selectivity than found in CBMC simulations.

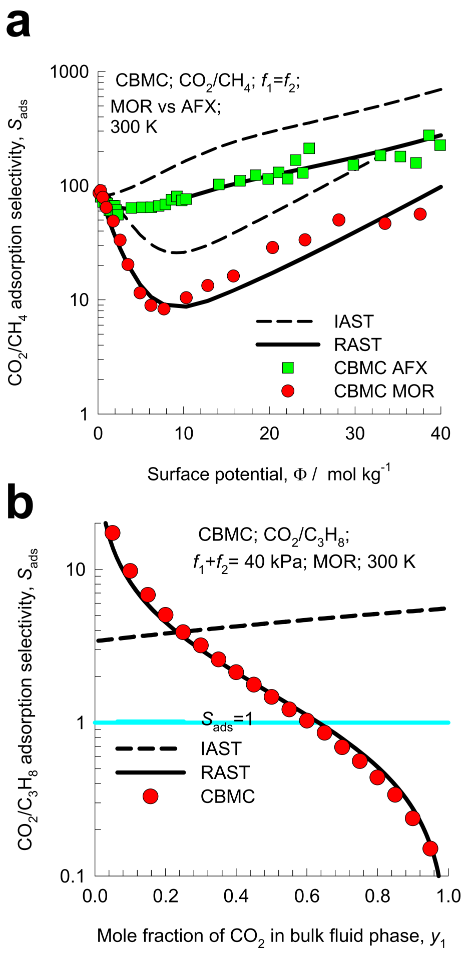

Figure 11. (a) CBMC simulation data on the adsorption selectivity S_{ads} for equimolar $f_1 = f_2$ $CO_2(1)/CH_4(2)$ mixture adsorption in AFX and MOR zeolites at 300 K, plotted as a function of the surface potential Φ. (b) CBMC simulation data on the adsorption selectivity for $CO_2(1)/C_3H_8(2)$ mixture adsorption in MOR zeolite at 300 K. The total fluid phase fugacity is f_t = 1 MPa, and the composition y_1 is varied. In panels (a) and (b), the CBMC-simulated values (indicated by symbols) are compared with RAST (continuous solid lines) and IAST (dashed lines) estimates. All calculation details and input data are provided in the Supporting Information accompanying this publication.

Figure 13b presents CBMC data for ethanol/water selectivity in DDR zeolite for a campaign in which the bulk fluid composition is varied while holding the total bulk mixture fugacity constant at f_t = 10 kPa. The CBMC data show that for water-rich mixtures, $y_1 > 0.5$, the adsorption is ethanol-selective; this is desired of adsorbents, say, in recovery of bioethanol from fermentation broths. However, for feed mixtures that are richer in ethanol, $y_1 < 0.5$, the adsorption is water-selective; this is a desirable feature, say, for use of DDR in membrane constructs for water-selective pervaporation processes.[76] The IAST (dashed line) anticipates ethanol-selective adsorption over the entire range of compositions y_1.

The combined set of component loadings in the two CBMC campaigns was used to determine the set of Margules parameters $A_{12} = -5.325$, $A_{21} = -1.665$, and C = 1.868 kg mol^{-1} to quantify the non-idealities. Figure 13c presents the RAST calculations of the activity coefficients for equimolar water/ethanol mixtures with varying f_t. As the surface potential $\Phi \rightarrow 0$, both activity coefficients tend to unity $\gamma_1 \rightarrow 1$, $\gamma_2 \rightarrow 1$, as is expected in the Henry regime. The water activity coefficient exhibits a deep minimum for $0.01 < \Phi < 10$ mol kg^{-1}; under these conditions, there is significant enhancement in the water ingress that is caused by hydrogen bonding. With increasing pore occupancy, there is a monotonous decrease in the activity coefficient of ethanol below unity.

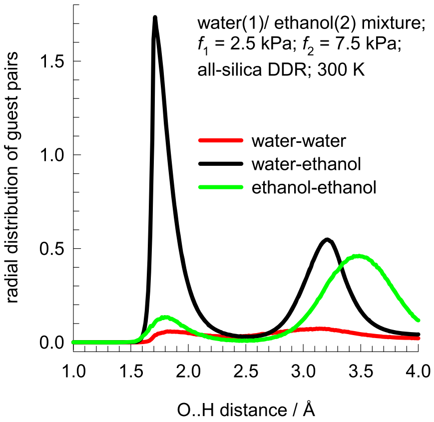

Figure 12. RDF of O····H distances for molecular pairs of water(1)/ethanol(2) mixture adsorption in DDR zeolite at 300 K. The partial fugacities of components 1 and 2 are f_1 = 2.5 kPa and f_2 = 7.5 kPa. The magnitudes of the first peaks are a direct reflection of the degree of hydrogen bonding between the molecular pairs.

Figure 13c presents the activity coefficients for the campaign in which f_t = 10 kPa and the bulk fluid mixture composition is varied. In this campaign, the variation of the surface potential is minimal and $\Phi \approx 7$ mol kg^{-1}. Both activity coefficients are strongly dependent on the composition of the adsorbed phase mixture, x_1, and satisfy the requirement $x_i \rightarrow 1$; $\gamma_i \rightarrow 1$. The use of the RAST is essential for quantitative modeling the selectivity reversals observed in Figure 13a,b.

Precisely analogous results are obtained for water/alcohol mixture adsorption in CHA; see Figures S36−S38. The adsorption of alcohol-rich feed mixtures in CHA is water-selective; therefore, CHA membranes are used for the purification of alcohols by membrane pervaporation because diffusion through 3.8 Å × 4.2 Å 8-ring windows of CHA also favors water.[29,75,77−79]

2.8. Segregated Adsorption Due to the Selective Size Exclusion of Guest Molecules.

One scenario in which it is evident that the mandate of homogeneous distribution of adsorbates is not fulfilled is the one in which one of the guest molecules is effectively excluded from the pore space on the basis of molecular size. We discuss below three examples of mixture separations exploiting size exclusion; in all these cases, CBMC simulations of mixture adsorption are not feasible.

For reducing the nitrogen content of natural gas, consisting predominantly of CH_4, one practical solution is to choose materials such as Ba-ETS-4 (ETS = Engelhard titano-silicate; ETS-4 is also named as CTS-1 = contracted titano-silicate-1) with pore size ≈ 3.7 Å so as to effectively exclude the spherical CH_4 molecule (3.7 Å) while allowing entry for the pencil-like nitrogen molecule (4.4 Å × 3.3 Å).[80−84] The experimental data of Bhadra[85] for the binary mixture adsorption equilibrium of CH_4/N_2 mixtures in Ba-ETS-4 demonstrate the failure of the IAST due to the segregated nature of adsorption.[86]

For C_3H_6/C_3H_8 mixture separations, a potent strategy is to employ NbOFFIVE-1-Ni (KAUST-7)[87] or Co-gallate,[88] which almost completely excludes the saturated alkane from the

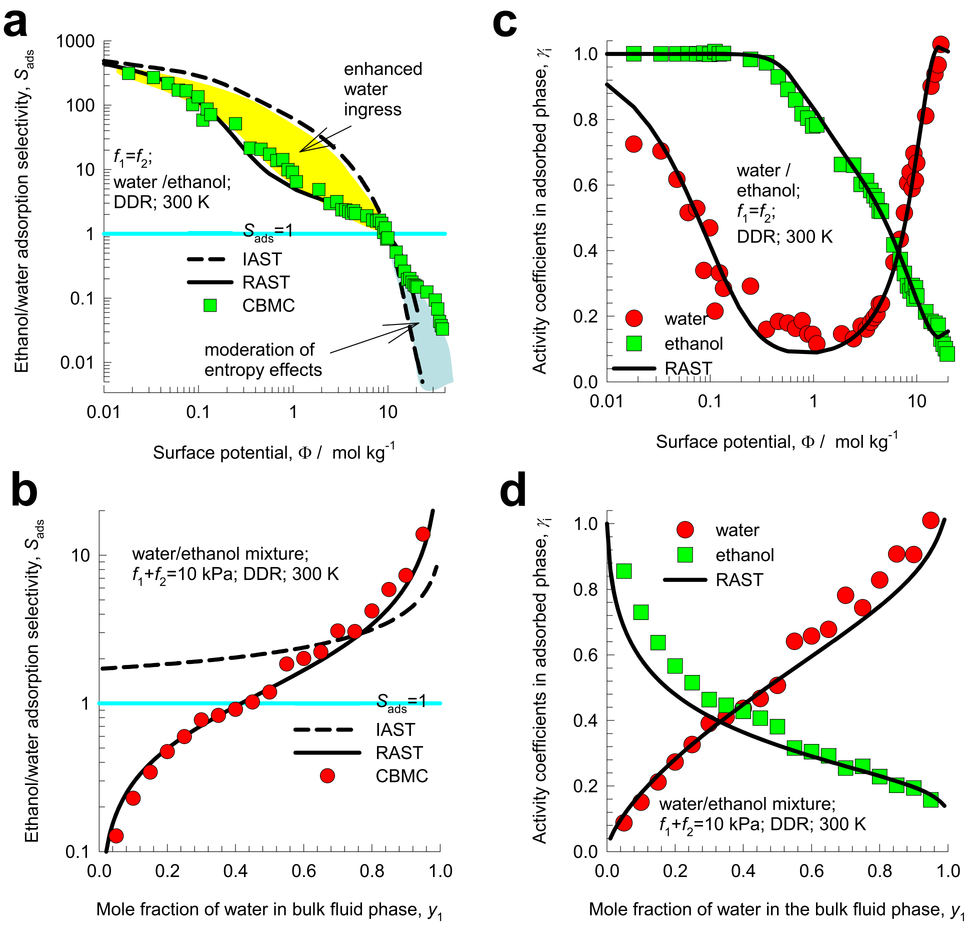

Figure 13. (a, b) CBMC simulation data for the ethanol/water selectivity S_{ads} for water(1)/ethanol(2) mixture adsorption in DDR at 300 K for two different campaigns. (a) In this campaign, the total fugacity f_t is varied, maintaining equal partial fugacities, $f_1 = f_2$, in the bulk fluid phase mixture. (b) In the second campaign, the total bulk fluid phase fugacity $f_t = f_1 + f_2 = 10$ kPa; the water composition in the bulk fluid mixture, y_1, is varied from 0 to 1. The CBMC-simulated values (indicated by symbols) are compared with RAST (continuous solid lines) and IAST (dashed lines) estimates. (c, d) RAST calculations of the activity coefficients, using fitted Margules parameters, for the two campaigns shown in panels (a) and (b). All calculation details and input data are provided in the Supporting Information accompanying this publication.

pores. For C_2H_4/C_2H_6 separations, near total exclusion of C_2H_6 is achieved by use of an ultramicroporous metal−organic framework UTSA-280 [$Ca(C_4O_4)(H_2O)$], which possesses rigid one-dimensional channels.[14] The 1D channels are of a similar size to C_2H_4 molecules (all of atoms of which lie on the same plane) but, owing to the size, shape, and rigidity of the pores, practically exclude the C_2H_6. The applicability of the IAST to describe the mixture adsorption equilibrium for the aforementioned MOFs for alkene/alkane separations is clearly open to question.

3. CONCLUSIONS

The derivation of the IAST is based on two tenets: (i) homogeneous distribution of guest adsorbates in the pore space, allowing for equitable competition for the occupation of adsorption sites, and (ii) the surface area occupied by a guest molecule in the mixture that is essentially the same as for unary adsorption, implying no occurrence of clustering with partners. An important implication of the IAST is that the adsorption selectivity for the i−j pair, $S_{ads,\ ij}$, is uniquely determined by the surface potential Φ, irrespective of the mixture composition and the presence of additional partners in the mixture. CBMC simulations of mixture adsorption in a wide variety of host materials have been used to investigate and highlight scenarios in which the IAST tenets are violated.

(1) For the adsorption of CO_2-bearing mixtures, an inhomogeneous distribution of adsorbates is engendered due to congregation of CO_2 around the extra-framework cations in zeolites and exposed "open" charged metal sites of MOFs. Due to the inhomogeneous distribution of adsorbates, the partner molecules endure a reduced degree of competition with CO_2 than is presumed in the IAST. Consequently, the IAST generally tends to anticipate a higher selectivity of CO_2 with respect to partner species. The IAST also fails to anticipate reversals in the selectivity of CO_2-bearing mixtures of varying composition.

(2) For the adsorption of CO_2-bearing mixtures in cage-type zeolites such as CHA and DDR, the CO_2 molecules prefer to perch at the window regions; partner molecules such as CH_4 prefer to locate within the cages and enjoy reduced competition with partner CO_2 molecules. The IAST estimates of S_{ads} are overly optimistic. The preferential location of CO_2 within the side pockets of zeolites MOR and AFX leads to quantitative failure of the IAST for analogous regions. In severe cases, such as for CO_2/C_3H_8 adsorption in MOR, the IAST fails to

https://doi.org/10.1021/acsomega.1c02136
ACS Omega 2021, 6, 15499−15513

anticipate selectivity reversals; such failure has been confirmed by experiments.[48]

(3) The IAST mandate of homogeneous distribution of guest adsorbates is clearly violated for MOFs and zeolites that rely on the principle of size exclusion to enable separations.

(4) For separations of linear and branched alkanes using MFI zeolite, thermodynamic non-ideality effects arise due to the preferential location of the branched alkanes at the channel intersections that offer more “leg room”. Aromatic molecules such as benzene also prefer to locate at the intersections, and consequently, the IAST estimates of component loadings and selectivities of adsorption of benzene/alkene and benzene/alkane mixtures are not of acceptable accuracy.

(5) For water/ethanol adsorption, molecular clustering occurs due to strong hydrogen bonding between water and ethanol. The IAST fails to provide quantitative predictions of selectivities for two separate reasons depending on the value of the surface potential Φ and pore occupancy θ. At relatively low values of Φ, water/ethanol clusters tend to increase the uptake of water, far in excess of the values anticipated by the IAST. Consequently, the IAST overestimates the ethanol/water selectivity. For large values of Φ, close to pore saturation, the occurrence of water/ethanol clusters has the effect of moderating entropy effects that normally favor the smaller water molecule with the higher saturation capacity. The IAST overestimates entropy effects and anticipates a higher degree of water selectivity than found in the CBMC simulations. The IAST does not also anticipate reversals that favor water in ethanol-rich mixtures.

(6) For quantification of non-ideality effects, activity coefficients γ_i need to be introduced as shown in eq 10. While the γ_i can be backed out from CBMC data on mixture adsorption, there are no reliable procedures for estimating these *a priori*. Streb and Mazzotti[40,41] discuss a procedure for the estimation of the RAST model parameters from cyclic experiments for CO_2/CH_4 mixture adsorption in 13X zeolite.

■ ASSOCIATED CONTENT

Supporting Information

The Supporting Information is available free of charge at https://pubs.acs.org/doi/10.1021/acsomega.1c02136.

Structural details of zeolites and MOFs, details of the CBMC simulation methodology, details of the IAST and Real Adsorbed Solution Theory (RAST) calculations for mixture adsorption equilibrium, unary isotherm fits for all the guest/host combinations, Margules and Wilson parameter fits for thermodynamic non-idealities, and plots of CBMC simulation data and comparisons with IAST/RAST estimates for all guest/host combinations (PDF)

■ AUTHOR INFORMATION

Corresponding Author

Rajamani Krishna – *Van't Hoff Institute for Molecular Sciences, University of Amsterdam, 1098 XH Amsterdam, The Netherlands;* orcid.org/0000-0002-4784-8530; Email: r.krishna@contact.uva.nl

Author

Jasper M. van Baten – *Van't Hoff Institute for Molecular Sciences, University of Amsterdam, 1098 XH Amsterdam, The Netherlands*

Complete contact information is available at: https://pubs.acs.org/10.1021/acsomega.1c02136

Notes

The authors declare no competing financial interest.

■ ACKNOWLEDGMENTS

The authors acknowledge Dr. Richard Baur for helpful discussions.

■ NOMENCLATURE

Latin alphabet

A	surface area per kg of framework, $m^2\ kg^{-1}$
A_{12}, A_{21}	Margules parameters, dimensionless
C	constant used in eq 14, $kg\ mol^{-1}$
f_i	partial fugacity of species i, Pa
f_t	total fugacity of the bulk fluid mixture, Pa
G^{excess}	excess Gibbs free energy, $J\ mol^{-1}$
n	number of species in the mixture, dimensionless
P_i^0	sorption pressure, Pa
q_i	molar loading of species i, $mol\ kg^{-1}$
$q_i^0(f)$	pure component adsorption isotherm for i, $mol\ kg^{-1}$
q_t	total molar loading of the mixture, $mol\ kg^{-1}$
$q_{sat,\ mix}$	saturation capacity of the mixture, $mol\ kg^{-1}$
R	gas constant, 8.314 $J\ mol^{-1}\ K^{-1}$
S_{ads}	adsorption selectivity, dimensionless
T	absolute temperature, K
x_i	mole fraction of species i in the adsorbed phase, dimensionless
y_i	mole fraction of species i in the bulk fluid mixture, dimensionless

Greek alphabet

γ_i	activity coefficient of component i in the adsorbed phase, dimensionless
θ	fractional occupancy, dimensionless
Θ_i	loading of species i, molecules per unit cell
π	spreading pressure, $N\ m^{-1}$
Φ	surface potential, $mol\ kg^{-1}$

Subscripts

i,j	components in mixture
t	referring to the total mixture
sat	referring to saturation con

Superscripts

0	referring to pure component loading
excess	referring to excess parameter

■ REFERENCES

(1) Myers, A. L.; Prausnitz, J. M. Thermodynamics of Mixed Gas Adsorption. *AIChE. J.* **1965**, *11*, 121−130.

(2) Walton, K. S.; Sholl, D. S. Predicting Multicomponent Adsorption: 50 years of the Ideal Adsorbed Solution Theory. *AIChE. J.* **2015**, *61*, 2757−2762.

(3) Xiang, S.; He, Y.; Zhang, Z.; Wu, H.; Zhou, W.; Krishna, R.; Chen, B. Microporous Metal-Organic Framework with Potential for Carbon Dioxide Capture at Ambient Conditions. *Nat. Commun.* **2012**, *3*, 954 http://dx.doi.org/doi:10.1038/ncomms1956.

(4) Krishna, R. Methodologies for Evaluation of Metal-Organic Frameworks in Separation Applications. *RSC Adv.* **2015**, *5*, 52269−52295.

(5) Krishna, R. Methodologies for Screening and Selection of Crystalline Microporous Materials in Mixture Separations. *Sep. Purif. Technol.* **2018**, *194*, 281−300.

(6) Herm, Z. R.; Swisher, J. A.; Smit, B.; Krishna, R.; Long, J. R. Metal-Organic Frameworks as Adsorbents for Hydrogen Purification and Pre-Combustion Carbon Dioxide Capture *J. Am. Chem. Soc.* **2011**, *133*, 5664−5667.

(7) Wu, H.; Yao, K.; Zhu, Y.; Li, B.; Shi, Z.; Krishna, R.; Li, J. Cu-TDPAT, an *rht*-type Dual-Functional Metal−Organic Framework Offering Significant Potential for Use in H_2 and Natural Gas Purification Processes Operating at High Pressures. *J. Phys. Chem. C* **2012**, *116*, 16609−16618.

(8) Yin, M. J.; Xiong, X. H.; Feng, X. F.; Xu, W. Y.; Krishna, R.; Luo, F. A Robust Cage-Based Metal−Organic Framework Showing Ultrahigh SO_2 Uptake for Efficient Removal of Trace SO_2 from SO_2/CO_2 and $SO_2/CO_2/N_2$ Mixtures. *Inorg. Chem.* **2021**, *60*, 3447−3451.

(9) Cui, X.; Chen, K.; Xing, H.; Yang, Q.; Krishna, R.; Bao, Z.; Wu, H.; Zhou, W.; Dong, X.; Han, Y.; Li, B.; Ren, Q.; Zaworotko, M. J.; Chen, B. Pore Chemistry and Size Control in Hybrid Porous Materials for Acetylene Capture from Ethylene. *Science* **2016**, *353*, 141−144.

(10) Li, B.; Cui, X.; O'Nolan, D.; Wen, H.-M.; Jiang, M.; Krishna, R.; Wu, H.; Lin, R.-B.; Chen, Y.-S.; Yuan, D.; Xing, H.; Zhou, W.; Ren, Q.; Qian, G.; Zaworotko, M. J.; Chen, B. An Ideal Molecular Sieve for Acetylene Removal from Ethylene with Record Selectivity and Productivity. *Adv. Mater.* **2017**, *29*, 1704210.

(11) Shen, J.; He, X.; Ke, T.; Krishna, R.; van Baten, J. M.; Chen, R.; Bao, Z.; Xing, H.; Dincǎ, M.; Zhang, Z.; Yang, Q.; Ren, Q. Simultaneous interlayer and intralayer space control in two-dimensional metal−organic frameworks for acetylene/ethylene separation. *Nat. Commun.* **2020**, *11*, 6259.

(12) Zhang, Y.; Hu, J.; Krishna, R.; Wang, L.; Yang, L.; Cui, X.; Duttwyler, S.; Xing, H. Rational design of microporous MOFs with anionic boron cluster functionality and cooperative dihydrogen binding sites for highly selective capture of acetylene. *Angew. Chem., Int. Ed.* **2020**, *59*, 17664−17669.

(13) Li, L.; Lin, R.-B.; Krishna, R.; Li, H.; Xiang, S.; Wu, H.; Li, J.; Zhou, W.; Chen, B. Ethane/ethylene Separation in a Metal-Organic Framework with Iron-Peroxo Sites. *Science* **2018**, *362*, 443−446.

(14) Lin, R.-B.; Li, L.; Zhou, H.-L.; Wu, H.; He, C.; Li, S.; Krishna, R.; Li, J.; Zhou, W.; Chen, B. Molecular Sieving of Ethylene from Ethane using a Rigid Metal-Organic Framework. *Nat. Mater.* **2018**, *17*, 1128−1133.

(15) Krishna, R. Screening Metal-Organic Frameworks for Mixture Separations in Fixed-Bed Adsorbers using a Combined Selectivity/Capacity Metric. *RSC Adv.* **2017**, *7*, 35724−35737.

(16) He, Y.; Krishna, R.; Chen, B. Metal-Organic Frameworks with Potential for Energy-Efficient Adsorptive Separation of Light Hydrocarbons. *Energy Environ. Sci.* **2012**, *5*, 9107−9120.

(17) Yang, H.; Wang, Y.; Krishna, R.; Jia, X.; Wang, Y.; Hong, A. N.; Dang, C.; Castillo, H. E.; Bu, X.; Feng, P. Pore-Space-Partition-Enabled Exceptional Ethane Uptake and Ethane-Selective Ethane−Ethylene Separation. *J. Am. Chem. Soc.* **2020**, *142*, 2222−2227.

(18) Peng, Y.-L.; Wang, T.; Jin, C.; Li, P.; Suepaul, S.; Beemer, G.; Chen, Y.; Krishna, R.; Cheng, P.; Pham, T.; Space, B.; Zaworotko, M. J.; Zhang, Z. A Robust Heterometallic Ultramicroporous MOF with Ultrahigh Selectivity for Propyne/Propylene Separation. *J. Mater. Chem. A* **2021**, *9*, 2850−2856.

(19) Peng, Y.-L.; He, C.; Pham, T.; Wang, T.; Li, P.; Krishna, R.; Forrest, K. A.; Hogan, A.; Suepaul, S.; Space, B.; Fang, M.; Chen, Y.; Zaworotko, M. J.; Li, J.; Li, L.; Zhang, Z.; Cheng, P.; Chen, B. Robust Microporous Metal-Organic Frameworks for Highly Efficient and Simultaneous Removal of Propyne and Propadiene from Propylene. *Angew. Chem., Int. Ed.* **2019**, *58*, 10209−10214.

(20) Li, L.; Wen, H.-M.; He, C.; Lin, R.-B.; Krishna, R.; Wu, H.; Zhou, W.; Li, J.; Li, B.; Chen, B. A Metal−Organic Framework with Suitable Pore Size and Specific Functional Site for Removal of Trace Propyne from Propylene. *Angew. Chem., Int. Ed.* **2018**, *57*, 15183−15188.

(21) Krishna, R. Metrics for Evaluation and Screening of Metal-Organic Frameworks for Applications in Mixture Separations. *ACS Omega* **2020**, *5*, 16987−17004.

(22) Banerjee, D.; Cairns, A. J.; Liu, J.; Krishna, R.; Thallapally, P. K.; Strachan, D. M. Potential of Metal-Organic Frameworks for Capture of Noble Gases. *Acc. Chem. Res.* **2015**, *48*, 211−219.

(23) Tao, Y.; Fan, Y.; Xu, Z.; Feng, X.; Krishna, R.; Luo, F. Boosting Selective Adsorption of Xe over Kr by Double-Accessible Open-Metal Site in Metal−Organic Framework: Experimental and Theoretical Research. *Inorg. Chem.* **2020**, *59*, 11793−11800.

(24) Motkuri, R. K.; Thallapally, P. K.; Annapureddy, H. V. R.; Dang, L.; Krishna, R.; Nune, S. K.; Fernandes, C. A.; Liu, J.; McGrail, B. P. Separation of Polar Compounds using a Flexible Metal-Organic Framework. *Chem. Commun.* **2015**, *51*, 8421−8424.

(25) Plessius, R.; Kromhout, R.; Ramos, A. L. D.; Ferbinteanu, M.; Mittelmeijer-Hazeleger, M. C.; Krishna, R.; Rothenberg, G.; Tanase, S. Highly Selective Water Adsorption in a Lanthanum Metal-Organic Framework. *Chem. − Eur. J.* **2014**, *20*, 7922−7925.

(26) He, C.-T.; Jiang, L.; Ye, Z.-M.; Krishna, R.; Zhong, Z.-S.; Liao, P.-Q.; Xu, J.; Ouyang, G.; Zhang, J.-P.; Chen, X.-M. Exceptional hydrophobicity of a large-pore metal-organic zeolite. *J. Am. Chem. Soc.* **2015**, *137*, 7217−7223.

(27) Zhang, K.; Lively, R. P.; Zhang, C.; Koros, W. J.; Chance, R. R. Investigating the Intrinsic Ethanol/Water Separation Capability of ZIF-8: An Adsorption and Diffusion Study. *J. Phys. Chem. C* **2013**, *117*, 7214−7225.

(28) Krishna, R.; van Baten, J. M. Screening Metal-Organic Frameworks for Separation of Pentane Isomers. *Phys. Chem. Chem. Phys.* **2017**, *19*, 8380−8387.

(29) Krishna, R. The Maxwell-Stefan Description of Mixture Diffusion in Nanoporous Crystalline Materials. *Microporous Mesoporous Mater.* **2014**, *185*, 30−50.

(30) Herm, Z. R.; Wiers, B. M.; Van Baten, J. M.; Hudson, M. R.; Zajdel, P.; Brown, C. M.; Maschiocchi, N.; Krishna, R.; Long, J. R. Separation of Hexane Isomers in a Metal-Organic Framework with Triangular Channels. *Science* **2013**, *340*, 960−964.

(31) Dubbeldam, D.; Krishna, R.; Calero, S.; Yazaydın, A. Ö. Computer-Assisted Screening of Ordered Crystalline Nanoporous Adsorbents for Separation of Alkane Isomers. *Angew. Chem., Int. Ed.* **2012**, *51*, 11867−11871.

(32) Yoon, J. W.; Lee, J. S.; Piburn, G. W.; Cho, K. H.; Jeon, K.; Lim, H.-K.; Kim, H.; Jun, C.-H.; Humphrey, S. M.; Krishna, R.; Chang, J.-S. Highly Selective Adsorption of p-Xylene over other C8 Aromatic Hydrocarbons by Co-CUK-1: A Combined Experimental and Theoretical Assessment. *Dalton Trans.* **2017**, *46*, 16096−16101.

(33) Krishna, R. Separating Mixtures by Exploiting Molecular Packing Effects in Microporous Materials. *Phys. Chem. Chem. Phys.* **2015**, *17*, 39−59.

(34) Torres-Knoop, A.; Krishna, R.; Dubbeldam, D. Separating Xylene Isomers by Commensurate Stacking of p-Xylene within Channels of MAF-X8. *Angew. Chem., Int. Ed.* **2014**, *53*, 7774−7778.

(35) Torres-Knoop, A.; Heinen, J.; Krishna, R.; Dubbeldam, D. Entropic Separation of Styrene/Ethylbenzene Mixtures by Exploitation of Subtle Differences in Molecular Configurations in Ordered Crystalline Nanoporous Adsorbents. *Langmuir* **2015**, *31*, 3771−3778.

(36) Mukherjee, S.; Joarder, B.; Desai, A. V.; Manna, B.; Krishna, R.; Ghosh, S. K. Exploiting Framework Flexibility of a Metal-Organic Framework for Selective Adsorption of Styrene over Ethylbenzene. *Inorg. Chem.* **2015**, *54*, 4403−4408.

(37) Wilkins, N. S.; Rajendran, A. Measurement of competitive CO_2 and N_2 adsorption on Zeolite 13X for post-combustion CO_2 capture. *Adsorption* **2019**, *25*, 115−133.

(38) Gholipour, F.; Mofarahi, M. Adsorption Equilibrium of Methane and Carbon Dioxide on Zeolite13X: Experimental and Thermodynamic Modeling. *J. Supercritical Fluids* **2016**, *111*, 47−54.

(39) Hefti, M.; Marx, D.; Joss, L.; Mazzotti, M. Adsorption Equilibrium of Binary Mixtures of Carbon Dioxide and Nitrogen on Zeolites ZSM-5 and 13X. *Microporous Mesoporous Mater.* **2015**, *215*, 215−228.

(40) Streb, A.; Mazzotti, M. Adsorption for efficient low carbon hydrogen production: part 1—adsorption equilibrium and breakthrough studies for $H_2/CO_2/CH_4$ on zeolite 13X. *Adsorption* **2021**, *27*, 541−558.

(41) Streb, A.; Mazzotti, M. Adsorption for efficient low carbon hydrogen production: part 2—Cyclic experiments and model predictions. *Adsorption* **2021**, *27*, 559−575.

(42) Costa, E.; Calleja, G.; Jimenez, A.; Pau, J. Adsorption Equilibrium of Ethylene, Propane, Propylene, Carbon Dioxide, and Their Mixtures in 13X Zeolite. *J. Chem. Eng. Data* **1991**, *36*, 218−224.

(43) Siperstein, F. R.; Myers, A. L. Mixed-Gas Adsorption. *AIChE. J.* **2001**, *47*, 1141−1159.

(44) Calleja, G.; Pau, J.; Calles, J. A. Pure and Multicomponent Adsorption Equilibrium of Carbon Dioxide, Ethylene, and Propane on ZSM-5 Zeolites with Different Si/Al Ratios. *J. Chem. Eng. Data* **1998**, *43*, 994−1003.

(45) Basmadjian, D.; Hsieh, S. T. Isothermal Column Sorption of Ethylene-Carbon Dioxide Mixtures with Azeotropic Behaviour. *Can. J. Chem. Eng.* **1980**, *58*, 185−189.

(46) van Zandvoort, I.; Ras, E.-J.; de Graaf, R.; Krishna, R. Using Transient Breakthrough Experiments for Screening of Adsorbents for Separation of C_2H_4/CO_2 Mixtures *Sep. Purif. Technol.* **2020**, *241*, 116706.

(47) van Zandvoort, I.; van der Waal, J. K.; Ras, E.-J.; de Graaf, R.; Krishna, R. Highlighting non-idealities in C_2H_4/CO_2 mixture adsorption in 5A zeolite. *Sep. Purif. Technol.* **2019**, *227*, 115730.

(48) Talu, O.; Zwiebel, I. Multicomponent Adsorption Equilibria of Nonideal Mixtures. *AIChE. J.* **1986**, *32*, 1263−1276.

(49) Krishna, R.; Van Baten, J. M. Using Molecular Simulations to Unravel the Benefits of Characterizing Mixture Permeation in Microporous Membranes in Terms of the Spreading Pressure. *ACS Omega* **2020**, *5*, 32769−32780.

(50) Krishna, R.; Van Baten, J. M. Elucidation of Selectivity Reversals for Binary Mixture Adsorption in Microporous Adsorbents. *ACS Omega* **2020**, *5*, 9031−9040.

(51) Krishna, R.; Van Baten, J. M. Using Molecular Simulations for Elucidation of Thermodynamic Non-Idealities in Adsorption of CO_2-containing Mixtures in NaX Zeolite. *ACS Omega* **2020**, *5*, 20535−20542.

(52) Krishna, R.; Van Baten, J. M. Water/Alcohol Mixture Adsorption in Hydrophobic Materials: Enhanced Water Ingress caused by Hydrogen Bonding. *ACS Omega* **2020**, *5*, 28393−28402.

(53) Krishna, R. Elucidation and Characterization of Entropy Effects in Mixture Separations with Micro-porous Crystalline Adsorbents. *Sep. Purif. Technol.* **2019**, *215*, 227−241.

(54) Talu, O.; Myers, A. L. Rigorous Thermodynamic Treatment of Gas-Adsorption. *AIChE. J.* **1988**, *34*, 1887−1893.

(55) Krishna, R.; Van Baten, J. M. Investigating the Non-idealities in Adsorption of CO_2-bearing Mixtures in Cation-exchanged Zeolites. *Sep. Purif. Technol.* **2018**, *206*, 208−217.

(56) Sochard, S.; Fernandes, N.; Reneaume, J.-M. Modeling of Adsorption Isotherm of a Binary Mixture with Real Adsorbed Solution Theory and Nonrandom Two-Liquid Model. *AIChE. J.* **2010**, *56*, 3109−3119.

(57) Mittal, N.; Bai, P.; Siepmann, J. I.; Daoutidis, P.; Tsapatsis, M. Bioethanol Enrichment using Zeolite Membranes: Molecular Modeling, Conceptual Process Design and Techno-Economic Analysis. *J. Membr. Sci.* **2017**, *540*, 464−476.

(58) Cessford, N. F.; Seaton, N. A.; Düren, T. Evaluation of Ideal Adsorbed Solution Theory as a Tool for the Design of Metal-Organic Framework Materials. *Ind. Eng. Chem. Res.* **2012**, *51*, 4911−4921.

(59) Gamba, G.; Rota, R.; Storti, G.; Carr, S.; Morbidelli, M. Absorbed Solution Theory Models for Multicomponent Adsorption Equilibria. *AIChE. J.* **1989**, *35*, 959−966.

(60) Zhang, H.; Wang, S. Modeling Bisolute Adsorption of Aromatic Compounds Based on Adsorbed Solution Theories. *Environ. Sci. Technol.* **2017**, *51*, 5552−5562.

(61) Erto, A.; Lancia, A.; Musmarra, D. Real Adsorbed Solution Theory model for competitive multicomponent liquid adsorption onto granular activated carbon. *Microporous Mesoporous Mater.* **2012**, *154*, 45−50.

(62) Bartholdy, S.; Bjørner, M. G.; Solbraa, E.; Shapiro, A.; Kontogeorgis, G. M. Capabilities and Limitations of Predictive Engineering Theories for Multicomponent Adsorption. *Ind. Eng. Chem. Res.* **2013**, *52*, 11552−11563.

(63) Vlugt, T. J. H.; Zhu, W.; Kapteijn, F.; Moulijn, J. A.; Smit, B.; Krishna, R. Adsorption of linear and branched alkanes in the silicalite-1. *J. Am. Chem. Soc.* **1998**, *120*, 5599−5600.

(64) Vlugt, T. J. H.; Krishna, R.; Smit, B. Molecular Simulations of Adsorption Isotherms for Linear and Branched Alkanes and Their Mixtures in Silicalite. *J. Phys. Chem. B* **1999**, *103*, 1102−1118.

(65) Krishna, R.; Smit, B.; Calero, S. Entropy effects during sorption of alkanes in zeolites. *Chem. Soc. Rev.* **2002**, *31*, 185−194.

(66) Schenk, M.; Vidal, S. L.; Vlugt, T. J. H.; Smit, B.; Krishna, R. Separation of alkane isomers by exploiting entropy effects during adsorption on silicalite-1: A configurational-bias Monte Carlo simulation study. *Langmuir* **2001**, *17*, 1558−1570.

(67) Krishna, R.; van Baten, J. M. Segregation effects in adsorption of CO_2 containing mixtures and their consequences for separation selectivities in cage-type zeolites. *Sep. Purif. Technol.* **2008**, *61*, 414−423.

(68) Krishna, R.; van Baten, J. M. A molecular dynamics investigation of the diffusion characteristics of cavity-type zeolites with 8-ring windows. *Microporous Mesoporous Mater.* **2011**, *137*, 83−91.

(69) Krishna, R.; van Baten, J. M. Onsager coefficients for binary mixture diffusion in nanopores. *Chem. Eng. Sci.* **2008**, *63*, 3120−3140.

(70) Krishna, R.; van Baten, J. M. A comparison of the CO_2 capture characteristics of zeolites and metal-organic frameworks. *Sep. Purif. Technol.* **2012**, *87*, 120−126.

(71) Krishna, R.; van Baten, J. M. In silico screening of metal-organic frameworks in separation applications. *Phys. Chem. Chem. Phys.* **2011**, *13*, 10593−10616.

(72) Bui, M.; Adjiman, C. S.; Bardow, A.; Anthony, E. J.; Boston, A.; Brown, S.; Fennell, P. S.; Fuss, S.; Galindo, A.; Hackett, L. A.; Hallett, J. P.; Herzog, H. J.; Jackson, G.; Kemper, J.; Krevor, S.; Maitland, G. C.; Matuszewski, M.; Metcalfe, I. S.; Petit, C.; Puxty, G.; Reimer, J.; Reiner, D. M.; Rubin, E. S.; Scott, S. A.; Shah, N.; Smit, B.; Trusler, J. P. M.; Webley, P.; Wilcox, J.; Mac Dowell, N. Carbon capture and storage (CCS): the way forward. *Energy Environ. Sci.* **2018**, *11*, 1062−1176.

(73) Krishna, R.; van Baten, J. M. Investigating cluster formation in adsorption of CO_2, CH_4, and Ar in zeolites and metal organic frameworks at sub-critical temperatures. *Langmuir* **2010**, *26*, 3981−3992.

(74) Zhang, C.; Yang, X. Molecular dynamics simulation of ethanol/water mixtures for structure and diffusion properties. *Fluid Phase Equilib.* **2005**, *231*, 1−10.

(75) Krishna, R.; van Baten, J. M. Hydrogen Bonding Effects in Adsorption of Water-alcohol Mixtures in Zeolites and the Consequences for the Characteristics of the Maxwell-Stefan Diffusivities. *Langmuir* **2010**, *26*, 10854−10867.

(76) Kuhn, J.; Castillo-Sanchez, J. M.; Gascon, J.; Calero, S.; Dubbeldam, D.; Vlugt, T. J. H.; Kapteijn, F.; Gross, J. Adsorption and Diffusion of Water, Methanol, and Ethanol in All-Silica DD3R: Experiments and Simulation. *J. Phys. Chem. C* **2009**, *113*, 14290−14301.

(77) Hasegawa, Y.; Abe, C.; Nishioka, M.; Sato, K.; Nagase, T.; Hanaoka, T. Formation of high flux CHA-type zeolite membranes and

their application to the dehydration of alcohol solutions. *J. Membr. Sci.* **2010**, *364*, 318−324.

(78) Krishna, R.; van Baten, J. M. Highlighting Pitfalls in the Maxwell-Stefan Modeling of Water-Alcohol Mixture Permeation across Pervaporation Membranes. *J. Membr. Sci.* **2010**, *360*, 476−482.

(79) Krishna, R.; van Baten, J. M. Mutual slowing-down effects in mixture diffusion in zeolites. *J. Phys. Chem. C* **2010**, *114*, 13154−13156.

(80) Bhadra, S. J.; Farooq, S. Separation of MethaneNitrogen Mixture by Pressure Swing Adsorption for Natural Gas Upgrading. *Ind. Eng. Chem. Res.* **2011**, *50*, 14030−14045.

(81) Majumdar, B.; Bhadra, S. J.; Marathe, R. P.; Farooq, S. Adsorption and Diffusion of Methane and Nitrogen in Barium Exchanged ETS-4. *Ind. Eng. Chem. Res.* **2011**, *50*, 3021−3034.

(82) Jayaraman, A.; Hernandez-Maldonado, A. J.; Yang, R. T.; Chinn, D.; Munson, C. L.; Mohr, D. H. Clinoptilolites for Nitrogen/Methane Separation. *Chem. Eng. Sci.* **2004**, *59*, 2407−2417.

(83) Yang, R. T. *Adsorbents: Fundamentals and Applications*. John Wiley & Sons, Inc.: Hoboken, New Jersey, 2003; pp 1−410.

(84) Habgood, H. W. The Kinetics of Molecular Sieve Action. Sorption of Nitrogen-Methane Mixtures by Linde Molecular Sieve 4A. *Canad. J. Chem* **1958**, *36*, 1384−1397.

(85) Bhadra, S. J. *Methane-Nitrogen Separation by Pressure Swing Adsorption*. Ph.D. Dissertation, National University of Singapore, Singapore, 2007.

(86) Krishna, R.; van Baten, J. M.; Baur, R. Highlighting the Origins and Consequences of Thermodynamic Nonidealities in Mixture Separations using Zeolites and Metal-Organic Frameworks. *Microporous Mesoporous Mater.* **2018**, *267*, 274−292.

(87) Cadiau, A.; Adil, K.; Bhatt, P. M.; Belmabkhout, Y.; Eddaoudi, M. A Metal-Organic Framework−Based Splitter for Separating Propylene from Propane. *Science* **2016**, *353*, 137−140.

(88) Liang, B.; Zhang, X.; Xie, Y.; RB, L.; Krishna, R.; Cui, H.; Li, Z.; Shi, Y.; Wu, H.; Zhou, W.; Chen, B. An Ultramicroporous Metal−Organic Framework for High Sieving Separation of Propylene from Propane. *J. Am. Chem. Soc.* **2020**, *142*, 17995−17801.

Supporting Information

How Reliable is the Ideal Adsorbed Solution Theory for Estimation of Mixture Separation Selectivities in Microporous Crystalline Adsorbents?

Rajamani Krishna* and Jasper M. van Baten

Van 't Hoff Institute for Molecular Sciences
University of Amsterdam
Science Park 904
1098 XH Amsterdam, The Netherlands
email: r.krishna@contact.uva.nl

Table of Contents

1 Preamble

The Supporting Information accompanying our article *How Reliable is the Ideal Adsorbed Solution Theory for Estimation of Mixture Separation Selectivities in Microporous Crystalline Adsorbents?* Provides (a) structural details of zeolites, and MOFs, (b) details of the CBMC simulation methodology, (b) details of the IAST, and Real Adsorbed Solution Theory (RAST) calculations for mixture adsorption equilibrium, (c) unary isotherm fits for all the guest/host combinations, (d) Margules and Wilson parameter fits for thermodynamic non-idealities, (e) Plots of CBMC simulation data and comparisons with IAST/RAST estimates for all guest/host combinations.

For ease of reading, the Supporting Information is written as a stand-alone document; as a consequence, there is some overlap of material with the main manuscript.

2 Structural details of microporous crystalline materials

The investigated host materials fall into five broad classes.

1. One-dimensional (1D) channels (Mg_2(dobdc), JBW, Co(BDP)).
2. One-dimensional channels with side pockets (MOR)
3. Intersecting channels (MFI, ISV)
4. Cages separated by narrow windows (CHA, DDR, ZIF-8, AFX, LTA-4A)
5. Cavities with large windows (FAU (all-silica), NaY (144 Si, 48 Al, 48 Na^+, Si/Al=3), NaX (106 Si, 86 Al, 86 Na^+, Si/Al=1.23))

The crystallographic data are available on the zeolite atlas website of the International Zeolite Association (IZA).[1, 2] Further details on the structure, landscape, pore dimensions of a very wide variety of micro-porous materials are available in the published literature.[3-10] Table S1, and Table S2 provide some salient structural information on various zeolites and MOFs of interest.

2.1 List of Tables for Structural details of microporous crystalline materials

Table S1. Salient structural information.

Structure	Topology	Fractional pore volume, ϕ	Pore volume/ cm^3/g	Framework density/ kg/m^3
Mg_2(dobdc)	1D hexagonal-shaped channels of 11 Å	0.708	0.782	905
IRMOF-1	Two alternating, inter-connected, cavities of 10.9 Å and 14.3 Å with window size of 8 Å.	0.812	1.369	593
Co(BDP)	10 Å square-shaped 1D channels	0.669	0.927	721.55
JBW	1D channels	0.161	0.086	1873.80
CHA	316 $Å^3$ cages separated by 3.77 Å × 4.23 Å size windows	0.382	0.264	1444
MOR	12-ring (7.0 Å × 6.5 Å) 1D channels, connected to 8-ring (5.7 Å × 2.6 Å) pockets	0.285	0.166	1714.69
DDR	277.8 $Å^3$ cages separated by 3.65 Å × 4.37 Å size windows	0.245	0.139	1760
LTA-4A	cages of 743 $Å^3$ volume, separated by 4.11 Å × 4.47 Å 8-ring windows	0.375	0.245	1529.6
AFX	490 $Å^3$ size cages connected to pockets of 98 $Å^3$ in size. Cages are separated by 3.4 Å × 3.9 Å size windows.	0.359	0.246	1463.71
ZIF-8	1168 $Å^3$ cages separated by 3.26 Å size windows	0.476	0.515	924
MFI	10-ring intersecting channels of 5.4 Å – 5.5 Å and 5.4 Å – 5.6 Å size	0.297	0.165	1796
ISV	Intersecting channels of two sizes: 12-ring of 6.1 Å -6.5 Å and 12-ring of 5.9 Å - 6.6 Å	0.426	0.278	1533
FAU (all silica)	786 $Å^3$ cages separated by 7.4 Å size windows	0.439	0.328	1338
NaY	786 $Å^3$ cages separated by 7.4 Å size windows	0.41	0.303	1347
NaX	786 $Å^3$ cages separated by 7.4 Å size windows	0.40	0.280	1421

Table S2. Pore volumes, surface areas, and characteristic (Delaunay) dimensions

Structure	**Pore volume** / cm^3 g^{-1}	**Surface area** / m^2 g^{-1}	**Delaunay diameter**/ Å
MFI	0.165	487.2	5.16
ISV	0.278	911.4	5.96
FAU (all silica)	0.328	1086	7.4
NaY	0.303	950	7.4
NaX	0.280	950	7.4
CHA	0.264	757.5	3.98
DDR	0.139	350	4.02
AFX	0.246	674.5	3.8
ZIF-8	0.515	1164.7	3.26
LTA-4A	0.245	896	4
Mg_2(dobdc)	0.782	1640.0	10.7
Co(BDP)	0.927	2148.8	10
JBW	0.086	25	3.66
MOR	0.166	417	6.44

3 Configurational-Bias Monte Carlo Simulation Methodology

The simulation methodologies and the force field information used are the same as detailed in the Supplementary Materials accompanying our earlier publications.[3, 5, 9, 11-14] A short summary is provided hereunder.

3.1 Zeolites (all silica)

CH_4 molecules are described with a united atom model, in which each molecule is treated as a single interaction center.[15] The interaction between adsorbed molecules is described with Lennard-Jones terms; see Figure S1. The Lennard-Jones parameters for CH_4-zeolite interactions are taken from Dubbeldam et al.[16]. The force field for H_2 corresponds to that given by Kumar et al.[17] In implementing this force field, quantum effects for H_2 have been ignored because the work of Kumar et al.[17] has shown that quantum effects are of negligible importance for temperatures above 200 K; all our simulations were performed at 300 K. The Lennard-Jones parameters for CO_2-zeolite and N_2-zeolite are essentially those of Makrodimitris et al.[18]; see also García-Pérez et al.[19] and García-Sanchez et al.[20] For simulations with linear alkanes with two or more C atoms, the beads in the chain are connected by harmonic bonding potentials. A harmonic cosine bending potential models the bond bending between three neighboring beads, a Ryckaert-Bellemans potential controls the torsion angle. The beads in a chain separated by more than three bonds interact with each other through a Lennard-Jones potential; see schematic in Figure S1. The force fields of Dubbeldam et al.[16] was used for the variety of potentials. The Lennard-Jones potentials are shifted and cut at 12 Å.

The zeolite frameworks were considered to be rigid in all the simulation results reported in the article.

3.2 Force fields and CBMC simulation methodology for water/alcohol mixtures

For simulations of adsorption of guest molecules water, methanol, and ethanol, the force field implementation follows earlier publications.[21-24] Water is modeled using the Tip5pEw potential.[25] The alcohols are described with the TraPPE force field.[26] Intramolecular potentials are included to describe the flexibility of alcohols, while the water molecules are kept rigid. The bond lengths are fixed for all molecules. Bond bending potentials are considered for methanol and ethanol, and a torsion potential is used for ethanol.[26] The force field parameters are summarized in Table S3.

All simulations are performed in the grand canonical ensemble; the chemical potentials of each component in the bulk fluid phase equal that of the corresponding guest adsorbate within the microporous framework. In our simulations, the partial fugacities in the bulk fluid mixture as specified; this fixes the values of the chemical potentials.

Following Kiselev and co-workers,[27] the zeolite is modeled as a rigid crystal. The interactions of the guest (pseudo) atoms with the host zeolite atoms aredominated by the dispersive interactions with the oxygen atoms, these interactions are described with a Lennard-Jones potential; see Table S4.

The Lorentz-Berthelot mixing rules were applied for calculating the Lennard-Jones parameters describing guest-host interactions

$$\begin{aligned} \sigma_{guest-host} &= \frac{\left(\sigma_{guest} + \sigma_{host}\right)}{2} \\ \frac{\varepsilon_{guest-host}}{k_B} &= \sqrt{\frac{\varepsilon_{guest}}{k_B} \times \frac{\varepsilon_{host}}{k_B}} \end{aligned} \tag{S1}$$

The Lennard-Jones potentials are shifted and cut at 12 Å. Periodic boundary conditions were employed. The Configurational-Bias Monte Carlo (CBMC) simulation technique used is identical to that used by Kuhn et al.,[24] and is described in detail by Frenkel and Smit.[28]

3.3 Cation-exchanged zeolites

The following two cation-exchanged structures were investigated

NaX (106 Si, 86 Al, 86 Na^+, Si/Al=1.23)

NaY (144 Si, 48 Al, 48 Na^+, Si/Al=3)

The presence of cations reduces the accessible pore volume. The location of the cations are pictured in Figure S2, and Figure S3.

The force field information for the simulations with cations are taken from García-Sanchez et al.[20] In the MC simulations, the cations were allowed to move within the framework and both Lennard-Jones and Coulombic interactions are taken into consideration.

In the CBMC simulations both Lennard-Jones and Coulombic interactions are taken into consideration; see schematic sketch in Figure S4.

3.4 MOFs

The metal organic framework structures were considered to be rigid in the simulations. For the atoms in the host metal organic framework, the generic UFF[29] and DREIDING[30] force fields were used. The Lorentz-Berthelot mixing rules were applied for calculating σ and ε/k_B for guest-host interactions.

The structural information on MgMOF-74 (= Mg_2(dobdc) = Mg\(dobdc) with dobdc = (dobdc^{4-} = 1,4-dioxido-2,5-benzenedicarboxylate)) was obtained from a variety of references.[31-36] The simulations for MgMOF-74 were carried out with the force field information provided by Yazaydin et al.[36]

The structural information for Co(BDP) with (BDP^{2-} = 1,4-benzenedipyrazolate) is from Choi et al. [37] and Salles et al. [38].

3.5 CBMC code

All simulations reported in this work were carried out using an in-house BIGMAC code, originally developed by T.J.H. Vlugt. This code was modified to handle rigid molecular structures and charges. The calculation of the accessible pore volume using the Widom insertion of He probe atoms is implemented within the BIGMAC code.

All CBMC simulations reported in this work were conducted at a temperature T = 300 K.

3.6 List of Tables for Configurational-Bias Monte Carlo Simulation Methodology

Table S3. Lennard-Jones parameters for guest pseudo-atoms. as provided in Table 1 of Kuhn et al.[24] The water model has two off-center charges that are labeled M in the Table. The name "alcohol" refers to both methanol and ethanol molecules.

Molecule	(pseudo-) atom	σ / Å	ε/k_B / K	charge
water	O	3.097	89.516	0
water	H	0	0	0.241
water	M	0	0	-0.241
methanol	CH3	3.75	98	0.265
ethanol	CH3	3.75	98	0
ethanol	CH2	3.95	46	0.265
alcohol	O	3.02	93	-0.7
alcohol	H	0	0	0.435

Table S4. Lennard-Jones parameters for host atoms in all-silica zeolites.

(pseudo-) atom	σ / Å	ε/k_B / K	charge
Si			2.05
O	3	93.53	-1.025

3.7 List of Figures for Configurational-Bias Monte Carlo Simulation Methodology

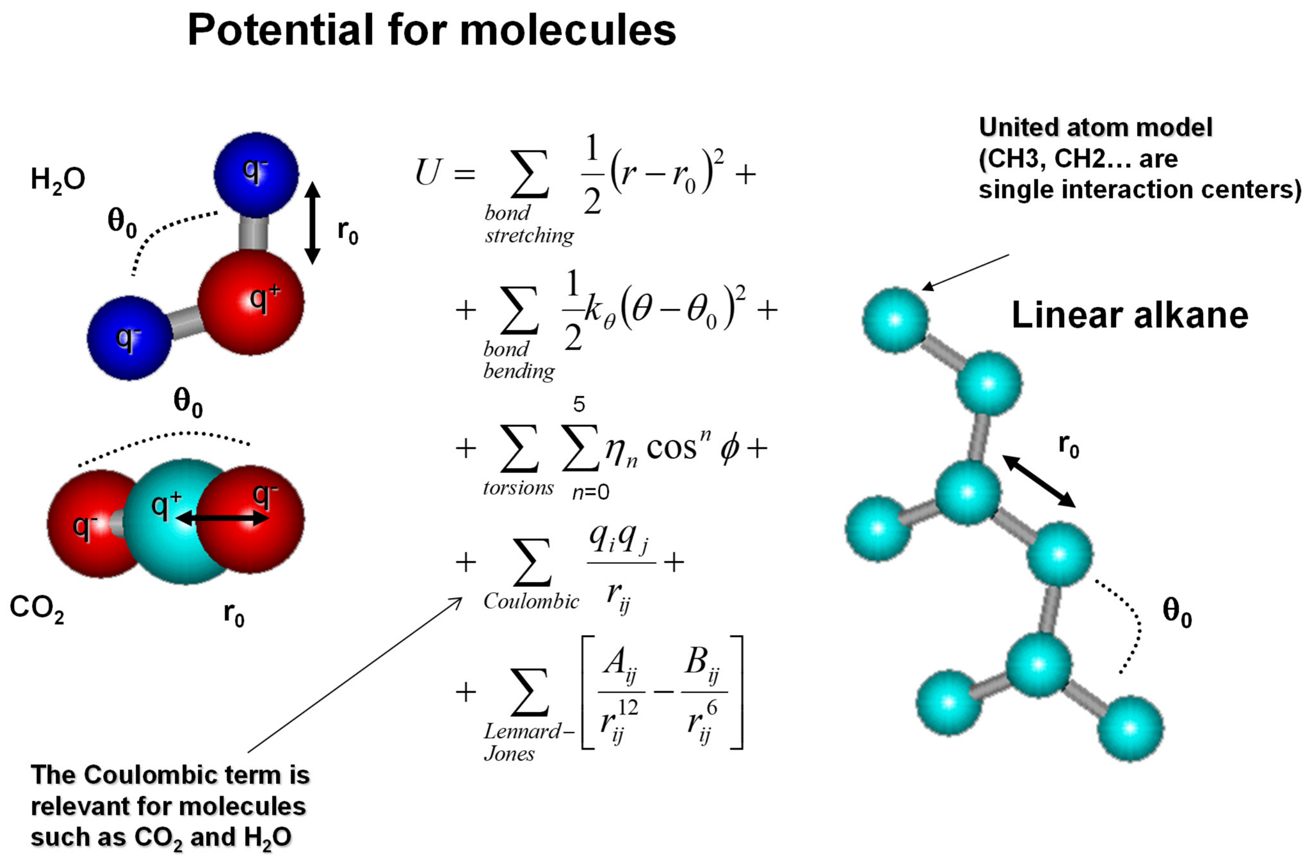

Potential for molecules

$$U = \sum_{\substack{\text{bond}\\ \text{stretching}}} \frac{1}{2}\left(r-r_0\right)^2 + \sum_{\substack{\text{bond}\\ \text{bending}}} \frac{1}{2}k_\theta\left(\theta-\theta_0\right)^2 + \sum_{\text{torsions}} \sum_{n=0}^{5} \eta_n \cos^n \phi + \sum_{\text{Coulombic}} \frac{q_i q_j}{r_{ij}} + \sum_{\substack{\text{Lennard-}\\ \text{Jones}}} \left[\frac{A_{ij}}{r_{ij}^{12}} - \frac{B_{ij}}{r_{ij}^{6}}\right]$$

United atom model (CH3, CH2… are single interaction centers)

Linear alkane

The Coulombic term is relevant for molecules such as CO_2 and H_2O

Figure S1. Potential for molecules.

NaX (106 Si, 86 Al, 86 Na+, Si/Al=1.23)

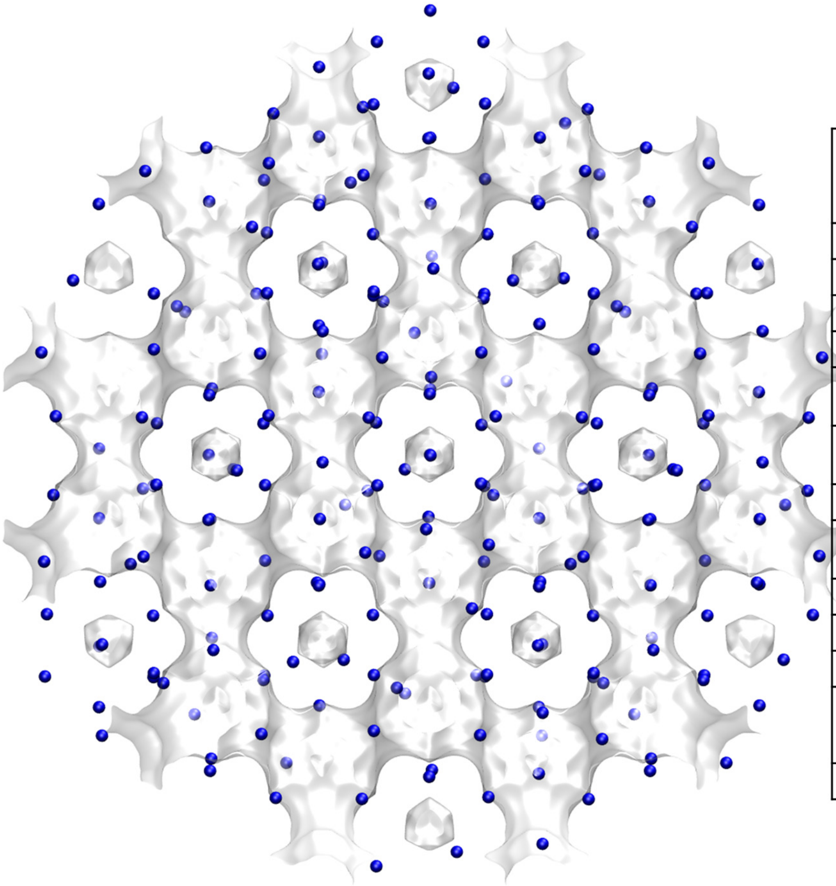

	FAU 86 Na/uc
a /Å	25.028
b /Å	25.028
c /Å	25.028
Cell volume / Å^3	15677.56
conversion factor for [molec/uc] to [mol per kg Framework]	0.0745
conversion factor for [molec/uc] to [kmol/m^3]	0.2658
ρ [kg/m3] (with cations)	1421.277
MW unit cell [g/mol(framework+cations)]	13418.42
ϕ, fractional pore volume	0.399
open space / Å^3/uc	6248.0
Pore volume / cm^3/g	0.280
Surface area /m^2/g	
DeLaunay diameter /Å	7.37

Figure S2. Location of cations for NaX zeolite (106 Si, 86 Al, 86 Na$^+$, Si/Al=1.23)

NaY (144 Si, 48 Al, 48 Na+, Si/Al=3)

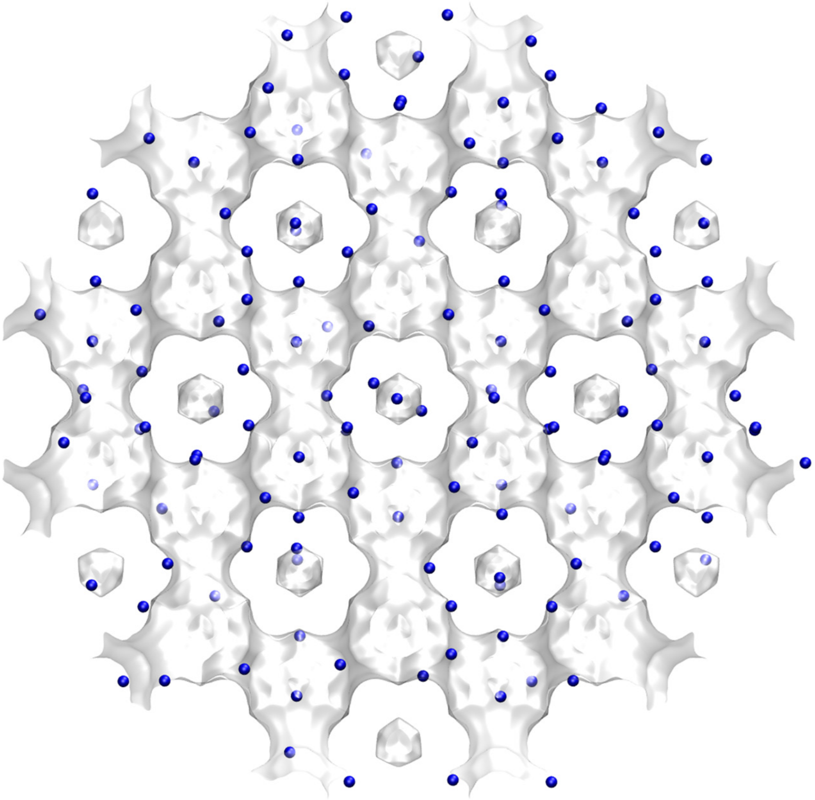

	FAU 48 Na/ucl
a /Å	25.028
b /Å	25.028
c /Å	25.028
Cell volume / Å^3	15677.56
conversion factor for [molec/uc] to [mol per kg Framework]	0.0794
conversion factor for [molec/uc] to [kmol/m^3]	0.2596
ρ [kg/m3] (with cations)	1333.19
MW unit cell [g/mol(framework+cations)]	12586.78
ϕ, fractional pore volume	0.408
open space / Å^3/uc	6396.6
Pore volume / cm^3/g	0.306
Surface area /m^2/g	
DeLaunay diameter /Å	7.37

Figure S3. Location of cations for NaY zeolite (144 Si, 48 Al, 48 Na$^+$, Si/Al=3)

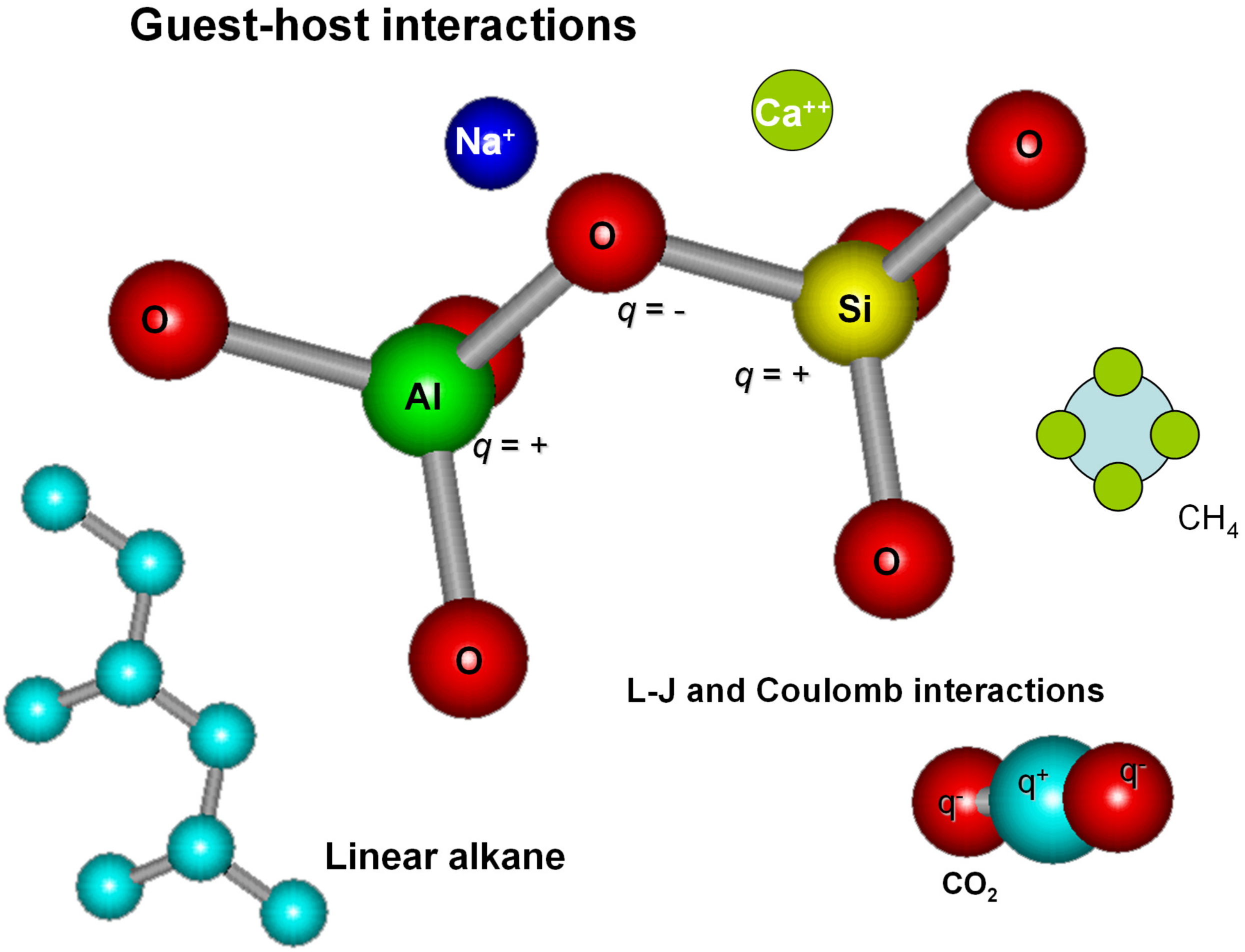

Figure S4. Guest-host interactions.

4 RDFs of O···H distances

In order to demonstrate the occurrence of hydrogen bonding in water/methanol, and water/ethanol mixtures CBMC simulation data on the spatial locations of the guest molecules were sampled to determine the O···H distances of various pairs of molecules. distances. By sampling a total of 10^6 simulation steps, the radial distribution functions (RDF) of O···H distances were determined for water-water, water-alcohol, and alcohol-alcohol pairs. Figure S5 shows the RDF of O…H distances for molecular pairs of water(1)/ethanol(2) mixture adsorption in CHA zeolite at 300 K. The partial fugacities of components 1 and 2 are f_1= 2.5 kPa, f_2= 7.5 kPa. We note the first peaks in the RDFs occur at a distance less than 2 Å, that is characteristic of hydrogen bonding.[21, 39] The heights of the first peaks are a direct reflection of the degree of hydrogen bonding between the molecular pairs. We may conclude, therefore that for water/methanol mixtures the degree of H-bonding between water-methanol pairs is significantly larger, by about an order of magnitude, than for water-water, and methanol-methanol pairs.

A visual appreciation of hydrogen bonding is gleaned from the snapshots in Figure S6 for water/ethanol mixture adsorption in CHA.

Figure S7 shows the corresponding results for RDF of O···H distances for molecular pairs of water(1)/ethanol(2) mixture adsorption in DDR zeolite at 300 K. The H-bonding between water/ethanol pairs is much stronger than for water/water and ethanol/ethanol pairs; these conclusions are in line with those for CHA zeolite. A visual appreciation of hydrogen bonding is gleaned from the snapshots in Figure S8 for water/ethanol mixture adsorption in DDR.

4.1 List of Figures for RDFs of O····H distances

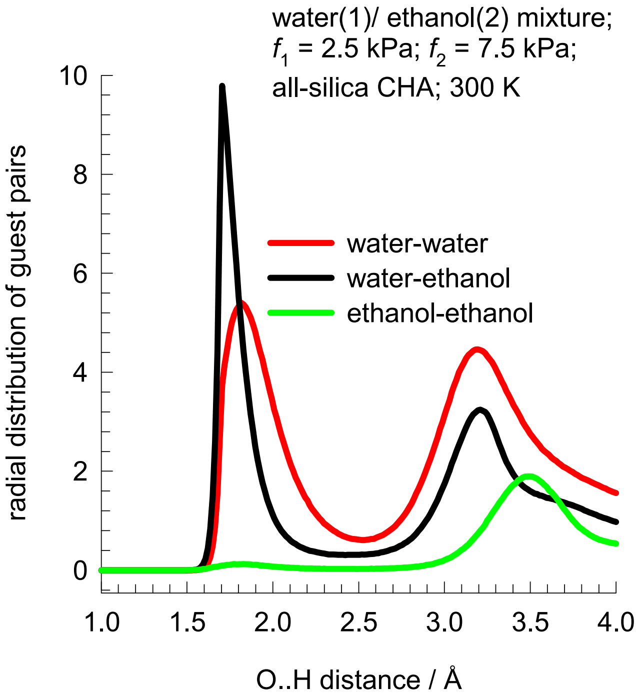

Figure S5. RDF of O····H distances for molecular pairs of water(1)/ethanol(2) mixture adsorption in CHA zeolite at 300 K. The partial fugacities of components 1 and 2 are f_1= 2.5 kPa, f_2= 7.5 kPa. The magnitudes of the first peaks is a direct reflection of the degree of hydrogen bonding between the molecular pairs.

RDFs of O···H distances

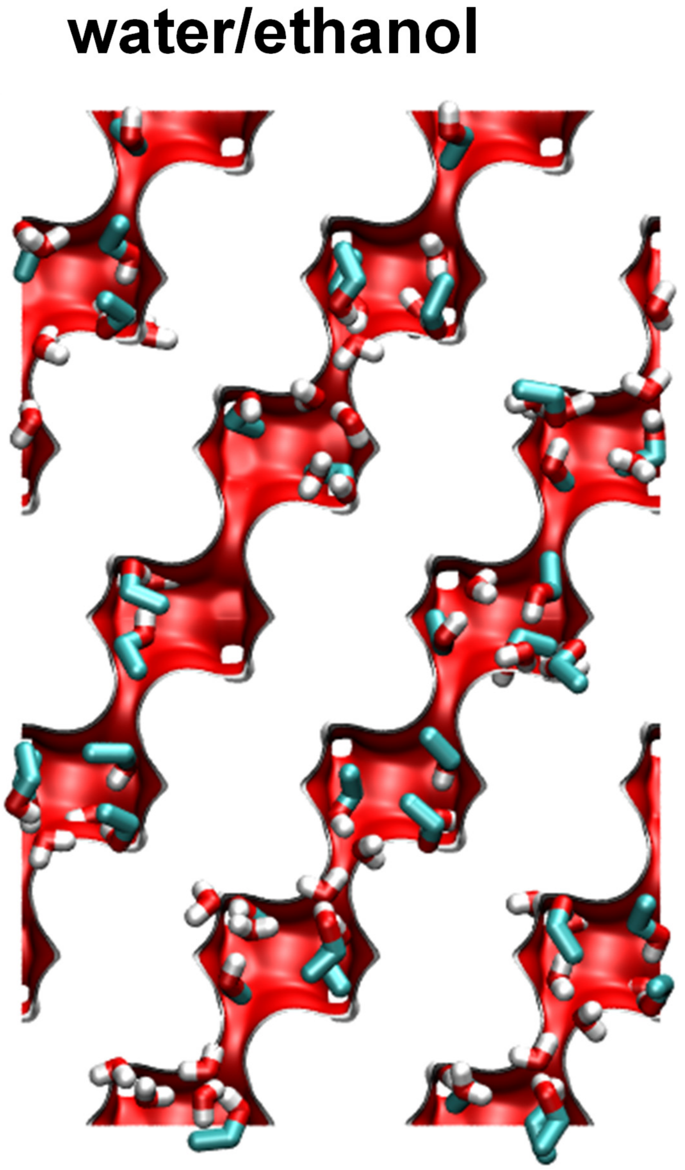

Figure S6. Snapshots showing location and conformations of guest molecules for adsorption of water(1)/ethanol(2) mixture adsorption in CHA zeolite at 300 K. The partial fugacities of components 1 and 2 are f_1= 2.5 kPa, f_2= 7.5 kPa.

RDFs of O····H distances

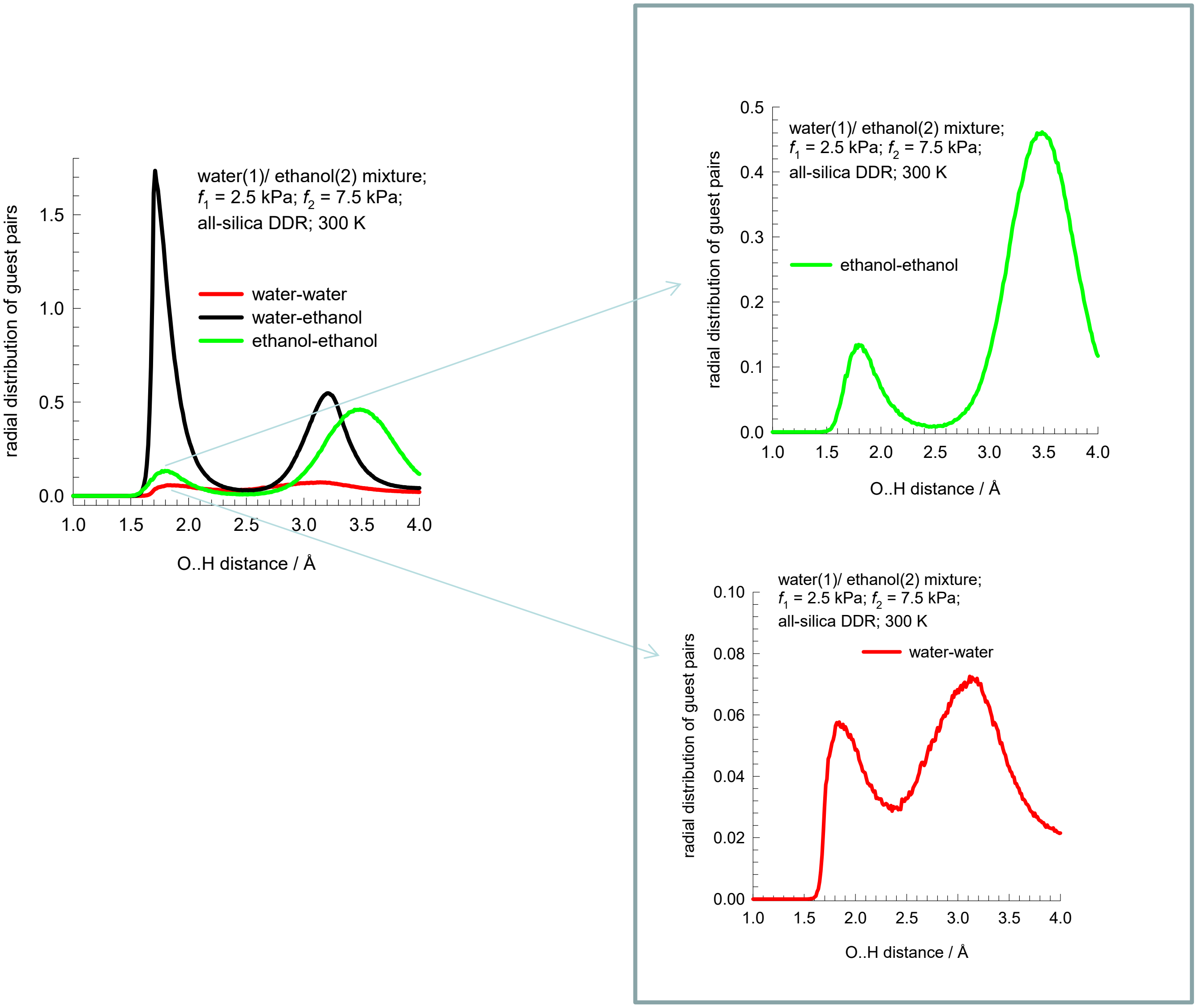

Figure S7. RDF of O····H distances for molecular pairs of water(1)/ethanol(2) mixture adsorption in DDR zeolite at 300 K. The partial fugacities of components 1 and 2 are f_1= 2.5 kPa, f_2= 7.5 kPa. The inset plots the RDF for water-water pairs with different scale on the y-axis.

RDFs of O···H distances

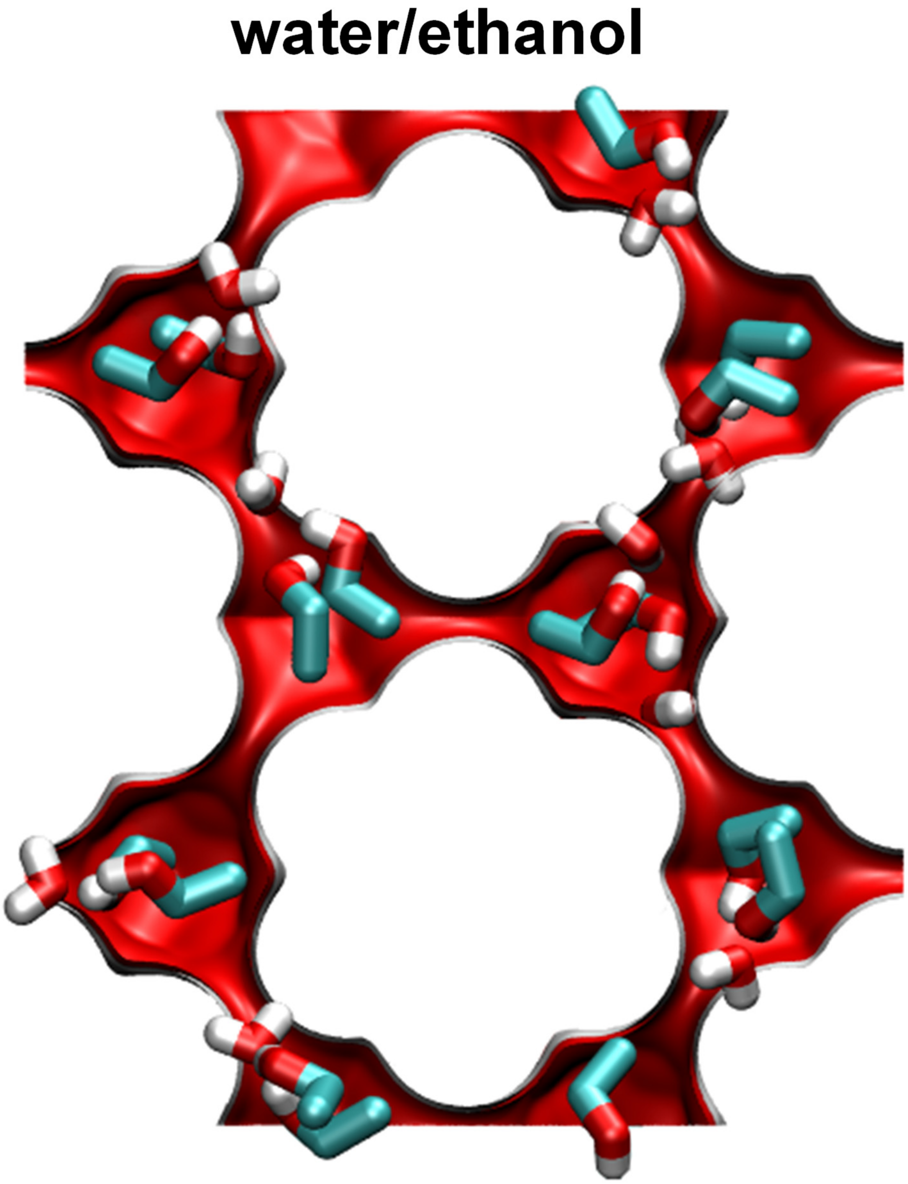

Figure S8. Snapshots showing location and conformations of guest molecules for adsorption of water(1)/ethanol(2) mixture adsorption in DDR zeolite at 300 K. The partial fugacities of components 1 and 2 are f_1= 2.5 kPa, f_2= 7.5 kPa.

5 IAST calculations of mixture adsorption equilibrium

5.1 Brief outline of theory

Within microporous crystalline materials such as zeolites and metal-organic frameworks (MOFs), the guest molecules exist in the adsorbed phase. The Gibbs adsorption equation[40] in differential form is

$$Ad\pi = \sum_{i=1}^{n} q_i d\mu_i \tag{S2}$$

The quantity A is the surface area per kg of framework, with units of m^2 per kg of the framework of the crystalline material; q_i is the molar loading of component i in the adsorbed phase with units moles per kg of framework; μ_i is the molar chemical potential of component i. The spreading pressure π has the same units as surface tension, i.e. N m^{-1}.

The chemical potential of any component in the adsorbed phase, μ_i, equals that in the bulk fluid phase. If the partial fugacities in the bulk fluid phase are f_i, we have

$$d\mu_i = RTd\ln f_i \tag{S3}$$

where R is the gas constant (= 8.314 J mol^{-1} K^{-1}).

Briefly, the basic equation of Ideal Adsorbed Solution Theory (IAST) theory of Myers and Prausnitz[41] is the analogue of Raoult's law for vapor-liquid equilibrium, i.e.

$$f_i = P_i^0 x_i; \quad i = 1,2,...n \tag{S4}$$

where x_i is the mole fraction in the adsorbed phase

$$x_i = \frac{q_i}{q_1 + q_2 + ...q_n} \tag{S5}$$

and P_i^0 is the pressure for sorption of every component i, which yields the same spreading pressure, π for each of the pure components, as that for the mixture:

IAST calculations of mixture adsorption equilibrium

$$\frac{\pi A}{RT} = \int_0^{P_1^0} \frac{q_1^0(f)}{f} df = \int_0^{P_2^0} \frac{q_2^0(f)}{f} df = \int_0^{P_3^0} \frac{q_3^0(f)}{f} df = ... \tag{S6}$$

where $q_i^0(f)$ is the *pure* component adsorption isotherm. The units of $\frac{\pi A}{RT} \equiv \Phi$, also called the surface potential,[42, 43] are mol kg^{-1}; the surface potential has also been called the adsorption potential in several recent publications.[44-47]

The unary isotherm may be described by say the 1-site Langmuir isotherm

$$q^0(f) = q_{sat}\frac{bf}{1+bf}; \quad \theta = \frac{bf}{1+bf} \tag{S7}$$

where we define the fractional *occupancy* of the adsorbate molecules, $\theta = q^0(f)/q_{sat}$. The superscript 0 is used to emphasize that $q^0(f)$ relates the *pure component* loading to the bulk fluid fugacity. More generally, the unary isotherms may need to be described by, say, the dual-site Langmuir-Freundlich model

$$q^0(f) = q_{A,sat}\frac{b_A f^{\nu_A}}{1+b_A f^{\nu_A}} + q_{B,sat}\frac{b_B f^{\nu_B}}{1+b_B f^{\nu_B}} \tag{S8}$$

Each of the integrals in Eq (S6) can be evaluated analytically:

$$\begin{aligned}
\Phi &= \int_{f=0}^{P_i^0} \frac{q^0(f)}{f} df = \frac{q_{A,sat}}{\nu_A}\ln\left(1+b_A\left(P_i^0\right)^{\nu_A}\right) + \frac{q_{B,sat}}{\nu_B}\ln\left(1+b_B\left(P_i^0\right)^{\nu_B}\right) \\
\Phi &= \int_{f=0}^{P_i^0} \frac{q^0(f)}{f} df = \frac{q_{A,sat}}{\nu_A}\ln\left(1+b_A\left(\frac{f_i}{x_i}\right)^{\nu_A}\right) + \frac{q_{B,sat}}{\nu_B}\ln\left(1+b_B\left(\frac{f_i}{x_i}\right)^{\nu_B}\right)
\end{aligned} \tag{S9}$$

The right members of eq (S9) is a function of P_i^0. For multicomponent mixture adsorption, each of the equalities on the right side of eq (S6) must be satisfied. These constraints may be solved using a suitable equation solver, to yield the set of values of P_1^0, P_2^0, P_3^0,.. P_n^0, all of which satisfy eq (S6). The corresponding values of the integrals using these as upper limits of integration must yield the same value of the surface potential $\frac{\pi A}{RT} \equiv \Phi$ for each component; this ensures that the obtained solution is the correct one.

The adsorbed phase mole fractions x_i are then determined from eq (S4)

$$x_i = \frac{f_i}{P_i^0}; \quad i = 1,2,...n \tag{S10}$$

The applicability of eq (S10) mandates that all of the adsorption sites within the microporous material are equally accessible to each of the guest molecules, implying a homogeneous distribution of guest adsorbates within the pore landscape, with no preferential locations of any guest species. The circumstances in which this mandate is not fulfilled are highlighted in recent works.[45-48]

A further key assumption of the IAST is that the adsorption enthalpies and surface areas of the adsorbed molecules do not change upon mixing. If the total mixture loading is q_t, the area covered by the adsorbed mixture is $\frac{A}{q_t}$ with units of m^2 (mole mixture)$^{-1}$. Therefore, the assumption of no surface area change due to mixture adsorption translates as $\frac{A}{q_t} = \frac{Ax_1}{q_1^0\left(P_1^0\right)} + \frac{Ax_2}{q_2^0\left(P_2^0\right)} + \cdots \frac{Ax_n}{q_n^0\left(P_n^0\right)}$; the total mixture loading is $q_t = q_1 + q_2 ... + q_n$ is calculated from

$$\frac{1}{q_t} = \frac{x_1}{q_1^0(P_1^0)} + \frac{x_2}{q_2^0(P_2^0)} + ... + \frac{x_n}{q_n^0(P_n^0)} \tag{S11}$$

in which $q_1^0(P_1^0)$, $q_2^0(P_2^0)$,... $q_n^0(P_n^0)$ are determined from the unary isotherm fits, using the sorption pressures for each component P_1^0, P_2^0, P_3^0,.. P_n^0 that are available from the solutions to eqs (S6), and (S9). The occurrence of molecular clustering and hydrogen bonding should be expected to applicability of eq (S11) because the surface area occupied by a molecular cluster is different from that of each of the un-clustered guest molecules in the adsorbed phase.

The entire set of eqs (S4) to (S11) need to be solved numerically to obtain the loadings, q_i of the individual components in the mixture.

5.2 Selectivity for mixture adsorption

For *n*-component mixture adsorption, the selectivity of guest constituent *i* with respect to another guest constituent *j*, in that mixture, $S_{ads,ij}$, is defined by

$$S_{ads,ij} = \frac{q_i/q_j}{f_i/f_j} = \frac{x_i/f_i}{x_j/f_j} \tag{S12}$$

where q_i, q_j are the molar loadings of the constituents *i* and *j*, in the adsorbed phase in equilibrium with a bulk fluid phase mixture with partial fugacities f_i, f_j, and mole fractions $y_i = f_i/f_t$; $f_t = \left(\sum_{k=1}^{n} f_k\right)$. In view of eqs (S10), and (S11), we may re-write eq (S12) as the ratio of the sorption pressures

$$S_{ads,ij} = \frac{P_j^0}{P_i^0} \tag{S13}$$

Applying the restriction specified by eq (S6), it follows that $S_{ads,ij}$ is uniquely determined by the surface potential Φ. It is important to note that eq (S13) is valid irrespective of the total number of components in the mixture. Put another way, the presence of component 3 in the ternary mixture has no influence of the adsorption selectivity $S_{ads,12} = \frac{P_2^0}{P_1^0}$ for the 1-2 pair, except insofar as the presence of component 3 alters the value of the surface potential Φ for the 1-2-3 mixture. Therefore, for an ideal adsorbed phase mixture, the presence of additional guest constituents, say species 3, 4, 5, etc. do not influence the selectivity of the 1-2 pair. We use CBMC simulations to seek verification of this important feature of the IAST.

5.3 Fractional occupancy related to the surface potential

For the general case, from knowledge of the surface potential, $\frac{\pi A}{RT}$, the fractional occupancy for mixture adsorption is then calculated using

$$\theta \equiv \frac{q_t}{q_{sat,mix}} = 1 - \exp\left(-\Phi/q_{sat,mix}\right) \tag{S14}$$

For a binary mixture, the saturation capacity $q_{sat,mix}$ is calculated from the saturation capacities of the constituent guests

IAST calculations of mixture adsorption equilibrium

$$q_{sat,mix} = \frac{1}{\dfrac{x_1}{q_{1,sat}} + \dfrac{x_2}{q_{2,sat}}}; \quad q_{1,sat} = q_{1,A,sat} + q_{1,B,sat}; \quad q_{2,sat} = q_{2,A,sat} + q_{2,B,sat} \tag{S15}$$

where

$$x_1 = \frac{q_1}{q_1 + q_2}; \quad x_2 = \frac{q_2}{q_1 + q_2} \tag{S16}$$

are the mole fractions in the adsorbed mixture. For equimolar mixtures, $x_1 = x_2 = 0.5$, eq (S16) simplifies to yield $q_{sat,mix} = \dfrac{2}{\dfrac{1}{q_{1,sat}} + \dfrac{1}{q_{2,sat}}}$.

The fundamental justification of Eq (S15) is provided by applying eq (S11) to pore saturation conditions.

Equation (S14) is the appropriate generalization of eq (S29), derived in the following section for the mixed-gas Langmuir model. It is also to be noted that eq (15) of our earlier publication[49] has a typographical error in the calculation of $q_{sat,mix}$; the correct form is given by eq (S15).

5.4 IAST model: 1-site Langmuir isotherms

The IAST procedure will be applied for binary mixture adsorption in which the unary isotherms are described by the 1-site Langmuir model in which the saturation capacities of components 1 and 2 are identical to each other, i.e. $q_{1,sat} = q_{2,sat} = q_{sat}$:

$$q^0(f) = q_{sat}\frac{bf}{1+bf}; \quad \theta = \frac{bf}{1+bf} \tag{S17}$$

where we define the fractional *occupancy* of the adsorbate molecules, $\theta = q^0(f)/q_{sat}$. The superscript 0 is used to emphasize that $q^0(f)$ relates the *pure component* loading to the bulk fluid fugacity.

For unary adsorption, the surface potential for a 1-site Langmuir isotherm can be calculated analytically

$$\Phi = q_{sat}\ln\left(1 + bP^0\right) \tag{S18}$$

The objective is to determine the molar loadings, q_1, and q_2, in the adsorbed phase.

IAST calculations of mixture adsorption equilibrium

Performing the integration of eq (S6) results in an expression relating the sorption pressures P_i^0 of the two species

$$\begin{aligned} &\Phi = q_{sat} \ln\left(1+b_1 P_1^0\right) = q_{sat} \ln\left(1+b_2 P_2^0\right) \\ &b_1 P_1^0 = b_2 P_2^0 = \exp\left(\frac{\Phi}{q_{sat}}\right) - 1 \end{aligned} \tag{S19}$$

In view of eq (S13), we may derive the following expression for $S_{ads,12}$

$$S_{ads,12} = \frac{P_2^0}{P_1^0} = \frac{b_1}{b_2} \tag{S20}$$

The adsorbed phase mole fractions of component 1, and component 2 are given by eq (S10)

$$x_1 = \frac{f_1}{P_1^0}; \quad x_2 = 1 - x_1 = \frac{f_2}{P_2^0} \tag{S21}$$

Combining eqs (S19), and (S21):

$$\begin{aligned} &\exp\left(\frac{\pi A}{q_{sat} RT}\right) - 1 = b_1 \frac{f_1}{x_1} = b_2 \frac{f_2}{1-x_1} \\ &\frac{\pi A}{q_{sat} RT} = \ln\left(1 + b_1 \frac{f_1}{x_1}\right) = \ln\left(1 + b_2 \frac{f_2}{x_2}\right) \end{aligned} \tag{S22}$$

The adsorbed phase mole fractions can be determined

$$\frac{x_1}{x_2} = \frac{q_1}{q_2} = \frac{b_1 f_1}{b_2 f_2}; \quad x_1 = \frac{q_1}{q_t} = \frac{b_1 f_1}{b_1 f_1 + b_2 f_2}; \quad x_2 = \frac{q_2}{q_t} = \frac{b_2 f_2}{b_1 f_1 + b_2 f_2} \tag{S23}$$

Once x_1, and $x_2 = 1 - x_1$ are determined, the sorption pressures can be calculated:

$$P_1^0 = \frac{f_1}{x_1}; \quad P_2^0 = \frac{f_2}{x_2} = \frac{f_2}{1-x_1} \tag{S24}$$

From eqs (S19), (S23), and (S24) we get

$$\begin{aligned} &b_i P_1^0 = \frac{b_1 f_1}{x_1} = b_2 P_2^0 = \frac{b_2 f_2}{x_2} = b_1 f_1 + b_2 f_2 \\ &1 + b_i P_1^0 = 1 + b_2 P_2^0 = 1 + b_1 f_1 + b_2 f_2 \end{aligned} \tag{S25}$$

Combining eqs (S22), and (S25) we get the following expression for the surface potential for the mixture

$$\Phi = q_{sat} \ln\left(1 + b_1 f_1 + b_2 f_2\right) \tag{S26}$$

The total amount adsorbed, $q_t = q_1 + q_2$ can be calculated from Eq (S11)

$$q_t = q_1 + q_2 = q_{sat} \frac{b_1 P_1^0}{1 + b_1 P_1^0} = q_{sat} \frac{b_2 P_2^0}{1 + b_2 P_2^0} = q_{sat} \frac{b_1 f_1 + b_2 f_2}{1 + b_1 f_1 + b_2 f_2} \tag{S27}$$

Combining eqs (S23), and (S27) we obtain the following explicit expressions for the component loadings, and fractional occupancies

$$\theta_1 = \frac{q_1}{q_{sat}} = \frac{b_1 f_1}{1 + b_1 f_1 + b_2 f_2}; \quad \theta_2 = \frac{q_2}{q_{sat}} = \frac{b_2 f_2}{1 + b_1 f_1 + b_2 f_2} \tag{S28}$$

Equation (S28) is commonly referred to as the mixed-gas Langmuir model.

From eqs (S19), (S27), and (S28) we derive the following expression for the total occupancy of the mixture

$$\theta = \theta_1 + \theta_2 = \frac{q_t}{q_{sat}} = 1 - \exp\left(-\frac{\Phi}{q_{sat}}\right) = \frac{b_1 f_1 + b_2 f_2}{1 + b_1 f_1 + b_2 f_2} \tag{S29}$$

For *unary* adsorption of component *i*, say, $f_i = P_i^0$, the occupancy of component 1 is

$$\theta_i = 1 - \exp\left(-\frac{\Phi}{q_{sat}}\right) = \frac{b_i f_i}{1 + b_i f_i}; \quad \text{unary adsorption of species i} \tag{S30}$$

From eqs (S29), and (S30) we may also conclude the *occupancy* may be considered to be the appropriate *proxy* for the spreading pressure. The conclusion that we draw from the foregoing analysis is that the equalities of spreading pressures for unary adsorption of component 1, unary adsorption of component 2, and binary 1-2 mixture adsorption also implies the corresponding equalities of the corresponding *occupancies* for unary adsorption of component 1, unary adsorption of component 2, and binary 1-2 mixture adsorption.

IAST calculations of mixture adsorption equilibrium

6 The Real Adsorbed Solution Theory (RAST)

To account for non-ideality effects in mixture adsorption, we introduce activity coefficients γ_i into Eq (S4) [41]

$$f_i = P_i^0 x_i \gamma_i \tag{S31}$$

Following the approaches of Myers, Talu, and Sieperstein[42, 50, 51] we model the excess Gibbs free energy for binary mixture adsorption as follows

$$\frac{G^{excess}}{RT} = x_1 \ln\left(\gamma_1\right) + x_2 \ln\left(\gamma_2\right) \tag{S32}$$

For calculation of the total mixture loading $q_t = q_1 + q_2$ we need to replace eq (S11) by

$$\frac{1}{q_t} = \frac{x_1}{q_1^0(P_1^0)} + \frac{x_2}{q_2^0(P_2^0)} + \left(\frac{1}{q_t}\right)^{excess} \tag{S33}$$

The excess reciprocal loading for the mixture can be related to the partial derivative of the Gibbs free energy with respect to the surface potential at constant composition

$$\left(\frac{1}{q_t}\right)^{excess} = \left.\frac{\partial\left(\dfrac{G^{excess}}{RT}\right)}{\partial \Phi}\right|_{T,x} \tag{S34}$$

6.1 Margules model for activity coefficients

The Margules model for activity coefficients is

$$\begin{aligned}
\ln(\gamma_1) &= x_2^2\left(A_{12} + 2\left(A_{21} - A_{12}\right)x_1\right)\left(1 - \exp\left(-C\Phi\right)\right) \\
\ln(\gamma_2) &= x_1^2\left(A_{21} + 2\left(A_{12} - A_{21}\right)x_2\right)\left(1 - \exp\left(-C\Phi\right)\right)
\end{aligned} \tag{S35}$$

In eq (S35) C is a constant with the units kg mol^{-1}. The introduction of $\left(1 - \exp\left(-C\Phi\right)\right)$ imparts the correct limiting behaviors $\gamma_i \to 1;\ \Phi \to 0$ for the activity coefficients in the Henry regime,

$f_t \to 0; \quad \Phi \to 0$. As pore saturation conditions are approached, this correction factor tends to unity $\left(1-\exp\left(-C\Phi\right)\right) \to 1$. The choice of A_{12} = A_{21} = 0 in eq (S35), yields unity values for the activity coefficients.

For calculation of the total mixture loading $q_t = q_1 + q_2$ we need to replace eq (S11) by

$$\frac{1}{q_t} = \frac{x_1}{q_1^0(P_1^0)} + \frac{x_2}{q_2^0(P_2^0)} + x_1 x_2 \left[A_{12} x_2 + A_{21} x_1 \right] C \exp\left(-C\Phi\right) \tag{S36}$$

6.2 Wilson model for activity coefficients

The Wilson model for activity coefficients are given for binary mixtures by

$$\begin{aligned} \ln(\gamma_1) &= \left(1 - \ln(x_1\Lambda_{11} + x_2\Lambda_{12}) - \frac{x_1\Lambda_{11}}{x_1\Lambda_{11} + x_2\Lambda_{12}} - \frac{x_2\Lambda_{21}}{x_2 + x_1\Lambda_{21}} \right) \left(1-\exp\left(-C\Phi\right)\right) \\ \ln(\gamma_2) &= \left(1 - \ln(x_1\Lambda_{21} + x_2\Lambda_{22}) - \frac{x_1\Lambda_{12}}{x_1\Lambda_{11} + x_2\Lambda_{12}} - \frac{x_2\Lambda_{22}}{x_1\Lambda_{21} + x_2\Lambda_{22}} \right) \left(1-\exp\left(-C\Phi\right)\right) \end{aligned} \tag{S37}$$

In Eq (S37), $\Lambda_{11} \equiv 1; \quad \Lambda_{22} \equiv 1$, and C is a constant with the units kg mol^{-1}. The choice of $\Lambda_{12} = \Lambda_{21} = 1$ in Eq (S37), yields unity values for the activity coefficients.

The excess reciprocal loading for the mixture can be related to the partial derivative of the Gibbs free energy with respect to the surface potential at constant composition

$$\left(\frac{1}{q_t}\right)^{excess} = \left.\frac{\partial\left(\frac{G^{excess}}{RT}\right)}{\partial\Phi}\right|_{T,x} = \left[-x_1 \ln(x_1 + x_2\Lambda_{12}) - x_2 \ln\left(x_2 + x_1\Lambda_{21}\right) \right] C \exp\left(-C\Phi\right) \tag{S38}$$

For calculation of the total mixture loading we need to replace Eq (S11) by

$$\frac{1}{q_t} = \frac{x_1}{q_1^0(P_1^0)} + \frac{x_2}{q_2^0(P_2^0)} + \left[-x_1 \ln(x_1 + x_2\Lambda_{12}) - x_2 \ln\left(x_2 + x_1\Lambda_{21}\right) \right] C \exp\left(-C\Phi\right) \tag{S39}$$

The parameters Λ_{12}, Λ_{21}, and C can be fitted to match the experimental data on mixture adsorption. The implementation of the activity coefficients is termed as the Real Adsorbed Solution Theory (RAST).

The Real Adsorbed Solution Theory (RAST)

With the introduction of activity coefficients, the expression for the adsorption selectivity for binary mixtures is

$$S_{ads}=\frac{q_1/q_2}{y_1/y_2}=\frac{q_1/y_1}{q_2/y_2}=\frac{x_1/f_1}{x_2/f_2}=\frac{P_2^0\gamma_2}{P_1^0\gamma_1} \tag{S40}$$

7 CBMC data for mixture adsorption and RAST analysis

7.1 CBMC simulation campaigns

A comprehensive campaign of CBMC simulations for adsorption of a variety of binary mixtures in several host materials were carried out. Two types of mixture adsorption campaigns were conducted.

Campaign A. The bulk fluid phase composition held constant at a value say $y_1 = y_2 = 0.5$, $y_1 = 0.1$, $y_1 = 0.15$, or $y_1 = 0.9$ and the bulk fluid phase fugacity $f_t = f_1 + f_2$ was varied over a wide range from the Henry regime of adsorption, $f_t \to 0; \quad \Phi \to 0$, to pore saturation conditions, typically $\Phi > 30$.

Campaign B. The bulk fluid phase fugacity $f_t = f_1 + f_2$ was held at a constant value, and the bulk fluid phase mixture composition y_1 was varied $0 < y_1 < 1$.

Each CBMC simulation data point, for specified partial fugacities in the bulk fluid phase, f_1, f_2, yields the component loadings, $q_{1,CBMC}; q_{2,CBMC}$, and the total mixture loading $q_{t,CBMC} = q_{1,CBMC} + q_{2,CBMC}$.

For each guest/host combination, CBMC simulations of the unary isotherms of the constituent guest molecules were also carried out.

7.2 Determination of activity coefficients from CBMC mixture adsorption data

For each CBMC mixture simulation campaign (Campaign A, or Campaign B), the mole fractions of the adsorbed phase, $x_1 = \frac{q_{1,CBMC}}{q_{t,CBMC}}; x_2 = \frac{q_{2,CBMC}}{q_{t,CBMC}}; q_{t,CBMC} = q_{1,CBMC} + q_{2,CBMC}$ are determined. The sorption pressures P_1^0, P_2^0, each of which satisfying eq (S6), can be determined from using the unary isotherm fits for each of the components in the binary mixture.

The activity coefficients of the two components $\gamma_{1,CBMC}; \gamma_{2,CBMC}$ are determined from eq (S31):

$$\gamma_{1,CBMC} = \frac{f_1}{P_1^0 x_{1,CBMC}}; \gamma_{2,CBMC} = \frac{f_2}{P_2^0 x_{2,CBMC}} \tag{S41}$$

The activity coefficients of the two components $\gamma_{1,CBMC};\gamma_{2,CBMC}$, determined using eq (S41) are subject to a degree of scatter that is inherent in the CBMC mixture simulation data.

7.3 Determination of Margules and Wilson fit parameters from mixture adsorption data

For each mixture/host combination, the set of three Margules parameters A_{12}, A_{21}, C that yield the minimum value for the objective function calculated as the sum of the mean-squared deviations between the CBMC simulated activity coefficients, and those predicted using RAST

$$\text{Objective Function} = \left(\frac{\gamma_{1,CBMC} - \gamma_{1,RAST}}{\gamma_{1,CBMC}}\right)^2 + \left(\frac{\gamma_{2,CBMC} - \gamma_{2,RAST}}{\gamma_{2,CBMC}}\right)^2 \tag{S42}$$

An alternative objective function used for some data sets is to seek the minimum value for the objective function calculated as the sum of the mean-squared deviations between the CBMC simulated component loadings and those predicted using RAST

$$\text{Objective Function} = \left(q_{1,CBMC} - q_{1,RAST}\right)^2 + \left(q_{2,CBMC} - q_{2,RAST}\right)^2 \tag{S43}$$

The A_{12}, A_{21}, C were determined using the Excel solver function. For determination of the Margules parameters A_{12}, A_{21}, C, the CBMC data for both Campaigns A, and B were employed.

A similar procedure is applied to determine the set of Wilson parameters.

8 Mixture adsorption in all-silica MFI zeolite

MFI zeolite (also called silicalite-1) has a topology consisting of a set of intersecting straight channels, and zig-zag (or sinusoidal) channels of 5.4 Å × 5.5 Å and 5.4 Å × 5.6 Å size. The pore landscapes and structural details are provided in Figure S9, and Figure S10. The crystal framework density $\rho = 1796$ kg m^{-3}. The pore volume $V_p = 0.165$ cm^3/g.

8.1 Adsorption of mixtures of light gaseous molecules in MFI zeolite

The applicability of Raoult's law analog, eq (S4), mandates that all of the adsorption sites within the microporous material are equally accessible to each of the guest molecules, implying a homogeneous distribution of guest adsorbates within the pore landscape, with no preferential locations of any guest species.[46, 48] This requirement of homogeneous distribution of guest molecules within MFI zeolite is fulfilled for light gaseous molecules such as H_2, N_2, CO_2, CH_4, C_2H_4, C_2H_6, C_3H_6, C_3H_8, and n-C_4H_{10}. Figure S11a shows computational snapshots for the adsorption of CO_2, and CH_4 within the intersecting channel topology of MFI zeolite. It is noticeable that neither guest species shows any preferential location and there is no visual indication of segregated adsorption. The only charged species is CO_2; the coulombic interactions with the negatively charged oxygen atoms in the zeolite framework are not strong enough to cause segregation between CO_2, and CH_4. We should therefore expect the mixture adsorption characteristics to be adequately well described by the IAST. Figure S11b shows CBMC simulations for the unary isotherms of light gaseous molecules in MFI zeolite at 300 K. The light gaseous guests can locate anywhere along the straight channels and zig-zag channels, and there are no perceptible isotherm inflections. The loadings, plotted on the y-axis are expressed in units of molecules per unit cell, Θ. To obtain the loading q, with units of mol kg^{-1}, the conversion factor is 1 molecule uc^{-1} = 0.173366 mol kg^{-1}. These unary isotherms were each fitted with the dual-site Langmuir-Freundlich model, eq (S8); the parameter values are defined in Table S5. The IAST calculations for the adsorption selectivity, S_{ads}, for five different binary mixtures CO_2/CH_4, CO_2/H_2, CO_2/N_2, CH_4/N_2, C_3H_8/CH_4, are compared with the corresponding S_{ads} values determined from CBMC simulations in Figure S12a,b. In Figure S12a the S_{ads} values are plotted as function of the surface potential, Φ. In Figure S12b the S_{ads} values are plotted as function of the pore occupancy, θ, determined from eq (S14). For all five mixtures the IAST estimations are in good agreement with the CBMC simulations. For CO_2/CH_4 and CO_2/N_2 mixtures, the S_{ads} increases as pore saturation conditions are approached, i.e. $\Phi > 10$ mol kg^{-1}; $\theta > 0.5$ because of entropy effects that favor the guest CO_2 with the higher saturation capacity (cf. Figure S11b); the explanation of entropy effects are provided in the published literature.[52, 53]

For CO_2/H_2 and C_3H_8/CH_4 mixtures, the S_{ads} decreases as pore saturation conditions are approached, i.e. $\Phi > 10$ mol kg^{-1}; $\theta > 0.5$ because entropy effects favor the smaller guests H_2 and CH_4, respectively.

The use of the mixed-gas Langmuir model, eq (S28), with equal saturation capacities is unable to cater for entropy effects as evidenced for the aforementioned four CO_2/CH_4, CO_2/N_2, CO_2/H_2 and C_3H_8/CH_4 mixtures.

For CH_4/N_2 mixtures, the S_{ads} is practically independent of occupancy because the saturation capacities of CH_4, and N_2 are nearly the same, as evidenced in Figure S11b.

A further important point to note is that for the adsorption selectivity as defined in eq (S13) for component 1 with respect to component 2, also holds for the same guest components in the presence of other guest species, 3, 4, 5, ..etc. Equation (S6) implies that if the comparisons are made at the same surface potential Φ, the value of S_{ads} for component 1 with respect to component 2, remains the same irrespective of the presence of additional guest components in the same host.

Figure S13 presents a comparison of CO_2/CH_4, CO_2/N_2, and CH_4/N_2 adsorption selectivities determined from binary mixtures, with the corresponding values determined from CBMC simulations two different ternary mixtures: 5/15/80 $CO_2/CH_4/N_2$, and 20/30/50 $CO_2/CH_4/N_2$ in MFI zeolite at 300 K. Each of the three selectivities shows a unique dependence on Φ, as prescribed by eq (S13). Put another way, the presence of component 3 in the ternary mixture has no influence of the adsorption selectivity for the 1-2 pair other than via the surface potential.

8.2 Preferential location of guest molecules at intersections of MFI zeolite

Due to configurational considerations, branched alkanes prefer to locate at the channel intersections because of the extra "leg room" that is available here. An extra "push" is required to locate these molecules within the channel interiors. This extra push results in an inflection in the pure component isotherms at a loading of 4 molecules per unit cell because per unit cell of MFI, there are four channel intersection sites.[54-57] See CBMC simulation data for iso-butane (iC4), 2-methylpentane (2MP), and 2,2 dimethylbutane (22DMB) in Figure S14a. Figure S14b shows computational snapshots for the location of iC4 within the channel topology of MFI zeolite. Cyclic hydrocarbons, such as cyclohexane, Benzene (Bz), and ethylbenzene (EthBz) also prefer to locate at the intersections; the unary isotherm for benzene also exhibits a strong inflection at a loading, $\Theta = 4$ molecules per unit cell; see snapshots for location of benzene in Figure S14c.

Due to the preferential location of branched and cyclic hydrocarbons at the channel intersections, the adsorption of mixtures containing these types of hydrocarbons along with linear alkanes, exhibit entropy effects that favor the linear alkanes and alkenes. We illustrate these effects by considering the adsorption of five different binary mixtures: C_2H_4(1)/benzene(2), C_3H_6(1)/benzene(2), C_3H_8/iso-butane(iC4), nC4/iC4, n-hexane(nC6)/2-methylpentane(2MP).

8.3 Adsorption of C_2H_4/benzene and C_3H_6/benzene mixtures in MFI zeolite

Figure S15a,b show computational snapshots of the location of guest molecules for (a) C_2H_4(1)/benzene(2) and (b) C_3H_6(1)/benzene(2) mixture adsorption in MFI zeolite at 300 K. The benzene molecules are located at the intersections whereas the alkenes can locate anywhere along the straight and zig-zag channels. It is also evident from the snapshots that some of the alkene guest molecules are located remotely from the benzene; consequently, the competition faced by the alkenes is less severe than that anticipated by IAST that mandates a homogeneous distribution of adsorbates. We should therefore expect the IAST to overestimate the nature of competitive adsorption. To confirm this expectations, CBMC simulations of adsorption of C_2H_4(1)/benzene(2) and C_3H_6(1)/benzene(2) mixture with equal partial fugacitites $f_1 = f_2; \quad y_1 = f_1/(f_1 + f_2) = 0.5$ were performed. These results are presented in Figure S16, and Figure S17; in these figures CBMC data are represented by symbols. The dashed lines are IAST estimations.

First, let us consider C_2H_4(1)/benzene(2) mixture adsorption in MFI. Figure S16a shows the unary isotherms of C_2H_4 and benzene in MFI zeolite at 300 K. Benzene is more strongly adsorbed than ethene at fluid phase fugacities $f_i < 10^4$ Pa. The continuous solid lines are unary isotherm dual-Langmuir-Freundlich fits with the parameters provided in Table S5. Figure S16b compares the component loadings in C_2H_4(1)/benzene(2) mixtures with CBMC simulations of unary isotherms, where the comparison is made on the basis of partial fugacities in the bulk fluid phase. Figure S16c presents CBMC data for benzene(2)/C_2H_4(1) adsorption selectivity (indicated by symbols) compared with IAST (dashed lines) and RAST (continuous solid lines) estimates. In the RAST calculations, the Margules parameters (specified in Table S6) are fitted to match the component loadings for mixture adsorption. The IAST overestimates the adsorption selectivity because of the implicit assumption of homogeneous distribution of adsorbates. The IAST calculation assumes that C_2H_4 molecules compete with *all* of the benzene molecules, making no allowance for segregation and preferential adsorption of benzene at the intersections. Due to segregation effects the competition faced by C_2H_4 molecules within the channels is *smaller* than that in the entire pore space. In other words, the IAST anticipates a stiffer competition between benzene and C_2H_4 as it assumes a uniform distribution of composition; consequently, the separation selectivity is *over*estimated. Due to preferential location of benzene at the intersections, some ethene molecules are farther removed from benzene and suffer diminished competition.

In Figure S16d, the CBMC data for component loadings in mixture compared with IAST and RAST estimates. The IAST severely underestimates the alkene component loadings in the mixture.

In Figure S16e,f the activity coefficients determined from CBMC simulated data are compared with RAST model calculations. It is noteworthy that the activity coefficient of ethene falls significantly below unity with increasing bulk fluid phase fugacities, $f_t = f_1 + f_2$.

Precisely analogous results are obtained from the analysis of CBMC data for C_3H_6(1)/Benzene(2) mixture adsorption in MFI; the corresponding data are presented in Figure S17.

Figure S18a compare the CBMC data for adsorption selectivity S_{ads} of C_2H_4(1)/Benzene(2) C_3H_6(1)/Benzene(2) mixtures, plotted as a function of the surface potential, Φ . For both mixtures, the IAST overestimates S_{ads} value in favor of benzene.

8.4 Adsorption of mixtures of linear and branched alkanes in MFI zeolite

Figure S19, and Figure S20 show the computational snapshots for adsorption of C_3H_8/iC4, nC4/iC4, and nC6/2MP mixtures MFI zeolite at 300 K. Due to configurational considerations, the branched alkanes demand more "leg-room" and, consequently, are predominantly located at the channel intersections. The linear alkanes are able to locate at either the straight channels or zig-zag channels. Due to the segregated nature of adsorption, the competition between the linear and branched alkanes is less severe than anticipated by the IAST.

To confirm this expectation, the CBMC data for C_3H_8/iC4, nC4/iC4, and nC6/2MP mixture adsorption are presented in Figure S21, Figure S22, Figure S23, Figure S24, and Figure S25.

First, let us consider equimolar C_3H_8(1)/iC4(2) mixture adsorption in MFI with equal partial fugacitites $f_1 = f_2; \quad y_1 = f_1/(f_1+f_2) = 0.5$. Figure S21a shows the unary isotherms of C_3H_8(1), and iC4(2) in MFI zeolite at 300 K. The branched alkane is more strongly adsorbed than C_3H_8 at fluid phase fugacities $f_i < 10^3$ Pa. Due to configurational considerations, iC4 molecules prefer to locate at the channel intersections because of the extra "leg room" that is available here. An extra "push" is required to locate iC4 within the channel interiors. This extra push results in an inflection in the iC4 at a loading of 4 molecules per unit cell.[54-57] However, for $f_t > 10^3$ Pa, the loadings of C_3H_8 exceed that of iC4 because the alkane can locate anywhere within the channels, whilst the adsorption of iC4 is restricted to the intersection sites. The continuous solid lines are unary isotherm dual-Langmuir-Freundlich fits with the parameters provided in Table S5.

Figure S21b compares the component loadings in C_3H_8(1)/iC4(2) mixtures with CBMC simulations of unary isotherms, where the comparison is made on the basis of partial fugacities in the bulk fluid phase. Figure S21c presents CBMC data for C_3H_8(1)/iC4(2) adsorption selectivity (indicated by symbols) compared with IAST (dashed lines) and RAST (continuous solid lines) estimates. In the RAST calculations, the Margules parameters (specified in Table S6) are fitted to match the component loadings for mixture adsorption. The increase in the C_3H_8(1)/iC4(2) adsorption selectivity with increased pore occupancy is the direct consequence of entropy effects that favor the guest with the higher saturation capacity, i.e. C_3H_8. The IAST overestimates the adsorption selectivity at pore saturation conditions because of the implicit assumption of homogeneous distribution of adsorbates. The IAST calculation assumes that C_3H_8 molecules compete with *all* of the iC4 molecules, making no allowance for segregation and preferential adsorption of iC4e at the intersections. Due to segregation effects the competition faced by C_3H_8 molecules within the channels is *smaller* than that in the entire pore space. In other words, the IAST anticipates a stiffer competition between iC4 and C_3H_8 as it assumes a uniform distribution of composition; consequently, the separation selectivity is *over*estimated. A different way of viewing this is to state that entropy effects are moderated due to the occurrence of segregated adsorption.

In Figure S21d, the CBMC data for component loadings in mixture compared with IAST and RAST estimates. It is noteworthy that propane loading nearly coincides with that of iC4 at $f_t \approx 5\times10^3$ Pa. It is noteworthy that propane loading nearly coincides with that of iC4 at $f_t \approx 5\times10^3$ Pa. Entropy effects cause the loadings of propane to exceed that of iso-butane for $f_t > 5\times10^3$ Pa. For $f_t > 5\times10^3$ Pa, the IAST severely overestimates the C_3H_8 loadings in the mixture, whilst underestimating the iC4 loading.

In Figure S21e,f the activity coefficients determined from CBMC simulated data are compared with RAST model calculations. It is noteworthy that the activity coefficient of iC4 falls significantly below unity as pore saturation conditions are approached.

Analogous results are obtained from the analysis of CBMC data for nC4(1)/iC4(2) mixture adsorption in MFI; the corresponding data are presented in Figure S22.

Mixture adsorption in all-silica MFI zeolite

Figure S23 presents CBMC simulation data for Campaign B $\left(f_t = f_1 + f_2 = 100 \text{ Pa}; \quad \text{vary } y_1\right)$ for nC4(1)/iC4(2) mixture adsorption in MFI zeolite at 300 K in which the bulk fluid phase composition y_1 is varied from 0 to 1. At the chosen total fugacity $f_t = f_1 + f_2 = 100$ Pa, the IAST estimates are of adequate accuracy and the activity coefficients are close to unity.

Figure S18b compare the CBMC data for adsorption selectivity S_{ads} of C_3H_8(1)/iC4(2) nC4(1)/iC4(2) mixtures, plotted as a function of the surface potential, Φ . For both mixtures, the IAST overestimates S_{ads} value in favor of the linear alkane.

Figure S24 presents the CBMC data for nC6/2MP adsorption corresponding, respectively, to Campaign A $\left(f_1 = f_2; \quad y_1 = f_1/\left(f_1 + f_2\right) = 0.5\right)$. Due to configurational considerations, the branched isomer 2MP is practically excluded due to mixture adsorption at saturation conditions in Campaign A. The experimental data of Titze et al. [58] using Infra-Red Microscopy (IRM) are in good agreement with CBMC simulations; these provide experimental verification of the entropy effects that favor nC6.

Figure S25 present the CBMC data for nC6/2MP adsorption corresponding to Campaign B $\left(f_t = f_1 + f_2 = 1 \text{ Pa}; \quad \text{vary } y_1\right)$. At the chosen total fugacity $f_t = f_1 + f_2 =$ 1 Pa, the IAST estimates are of adequate accuracy and the activity coefficients are close to unity.

Figure S18a compare the CBMC data for adsorption selectivity S_{ads} of C_2H_4(1)/Benzene(2) C_3H_6(1)/Benzene(2) mixtures, plotted as a function of the surface potential, Φ . For both mixtures, the IAST overestimates S_{ads} value in favor of benzene.

8.5 List of Tables for Mixture adsorption in all-silica MFI zeolite

Table S5. Dual-site Langmuir-Freundlich parameters for guest molecules in MFI at 300 K. To convert from molecules uc^{-1} to mol kg^{-1}, multiply by 0.173367.

	Site A			Site B		
	$\Theta_{A,sat}$ molecules uc^{-1}	b_A $\mathrm{Pa}^{-\nu A}$	ν_A dimensionless	$\Theta_{B,sat}$ molecules uc^{-1}	b_B $\mathrm{Pa}^{-\nu B}$	ν_B dimensionless
H_2	30	3.57E-08	1	42	1.39E-09	1
N_2	16	6.37E-07	1	16	3.82E-07	0.7
CO_2	19	6.12E-06	1	11	1.73E-08	1
CH_4	7	5.00E-09	1	16	3.10E-06	1
C_2H_6	3.3	4.08E-07	1	13	7.74E-05	1
C_2H_4	6.9	1.988E-04	0.65	10.1	6.959E-06	1.2
C_3H_8	1.4	3.35E-04	0.67	10.7	6.34E-04	1.06
C_3H_6	0.6	2.912E-06	1	11.4	6.534E-04	1
nC_4H_{10}	1.5	2.24E-03	0.57	8.7	9.75E-03	1.12
iso-C_4H_{10}	4	2.29E-02	1	6	2.87E-05	1
nC_6H_{14}	6.6	7.08E-01	0.83	1.4	1.66E+01	1.5
2MP	4	4.513	1.05	4	7.92E-05	1.13
Benzene	4	1.359E-01	1.06	8	2.339E-03	0.52

Table S6. Margules non-ideality parameters for binary mixtures in all-silica MFI zeolite at 300 K.

	C / kg mol^{-1}	A_{12}	A_{21}
C_2H_4/Benzene	0.433	-3.107	-8.369
C_3H_6/Benzene	0.271	-2.001	-9.149
C_3H_8/iso-C_4H_{10}	0.322	-2.814	-3.859
n-C_4H_{10}/iso-C_4H_{10}	0.190	0.578	-3.175
n-C_6H_{12}/2MP	0.386	1.340	1.580

8.6 List of Figures for Mixture adsorption in all-silica MFI zeolite

MFI **pore landscape**

	MFI
a /Å	20.022
b /Å	19.899
c /Å	13.383
Cell volume / Å^3	5332.025
conversion factor for [molec/uc] to [mol per kg Framework]	0.1734
conversion factor for [molec/uc] to [kmol/m^3]	1.0477
ρ [kg/m3]	1796.386
MW unit cell [g/mol(framework)]	5768.141
ϕ, fractional pore volume	0.297
open space / Å^3/uc	1584.9
Pore volume / cm^3/g	0.165
Surface area /m^2/g	487.0
DeLaunay diameter /Å	5.16

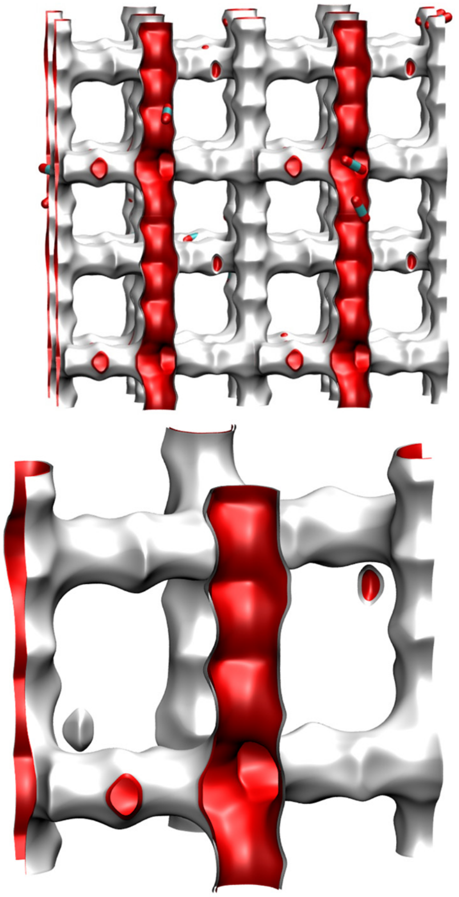

Figure S9. Pore landscape and structural data for MFI zeolite.

MFI channel dimensions

10 ring channel
of MFI viewed
along [100]

10 ring channel
of MFI viewed
along [010]

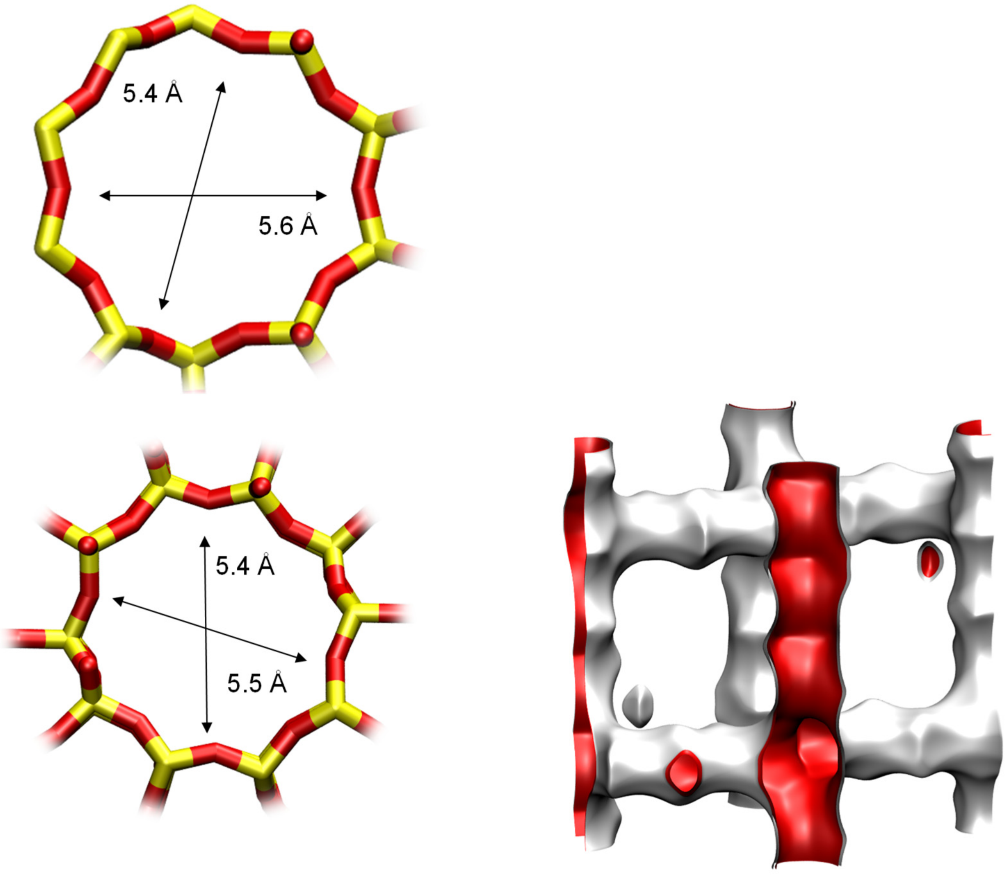

Figure S10. Pore landscape and structural data for MFI zeolite.

Mixture adsorption in all-silica MFI zeolite

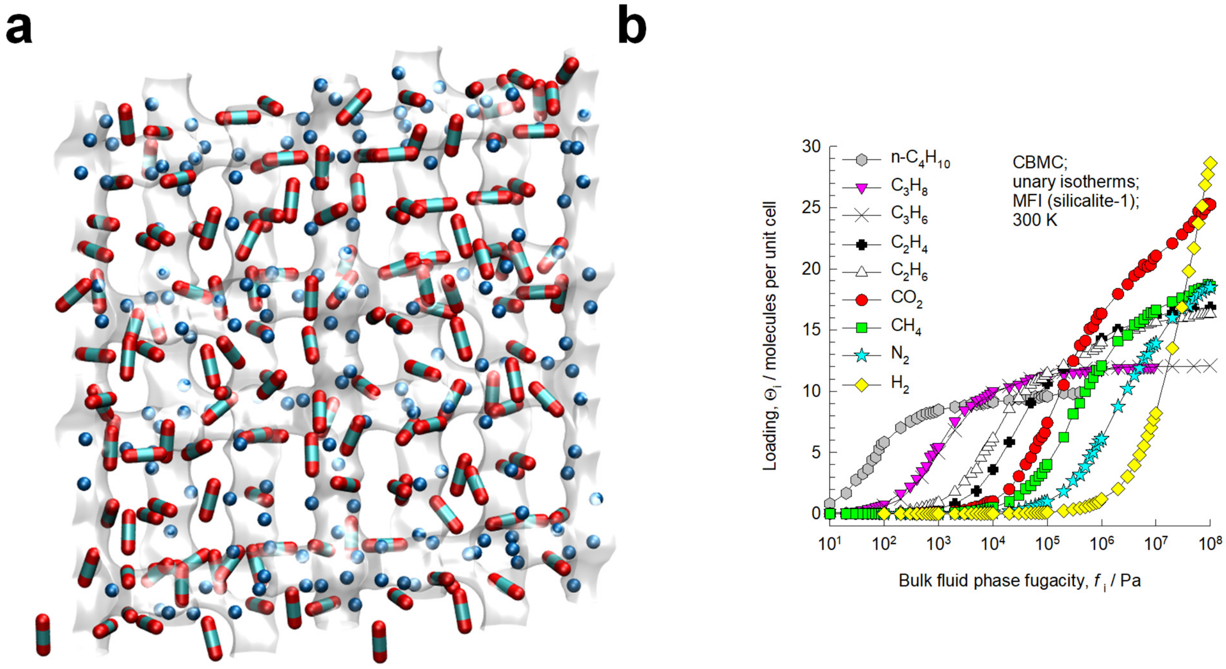

Figure S11. (a) Computational snapshots showing the distribution of. CO_2 and CH_4 for binary mixture adsorption. (b) CBMC simulations of unary isotherms for light gaseous molecules H_2, N_2, CO_2, CH_4, C_2H_4, C_2H_6, C_3H_6, C_3H_8, and n-C_4H_{10} in MFI zeolite at 300 K.

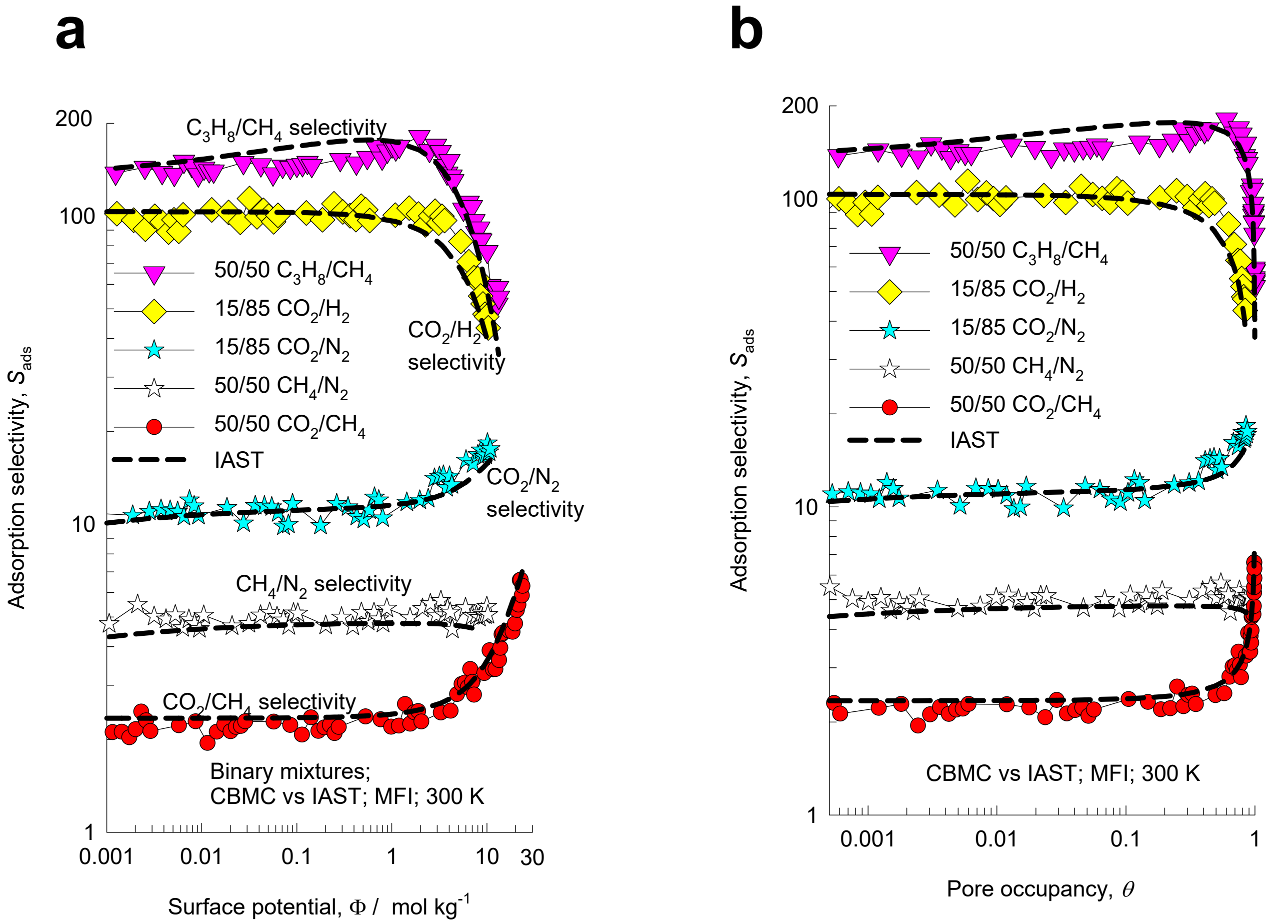

Figure S12. (a, b) CBMC simulations (indicated by symbols) of the adsorption selectivity, S_{ads} , for five different binary CO_2/CH_4, CO_2/H_2, CO_2/N_2, CH_4/N_2, C_3H_8/CH_4 mixtures compared with the IAST calculations (indicated by dashed lines) for corresponding S_{ads} values using the Dual-site Langmuir-Freundlich fits of unary isotherms. In (a) the S_{ads} values are plotted as function of the surface potential, Φ . In (b) the S_{ads} values are plotted as function of the pore occupancy, θ, determined from eq (S14).

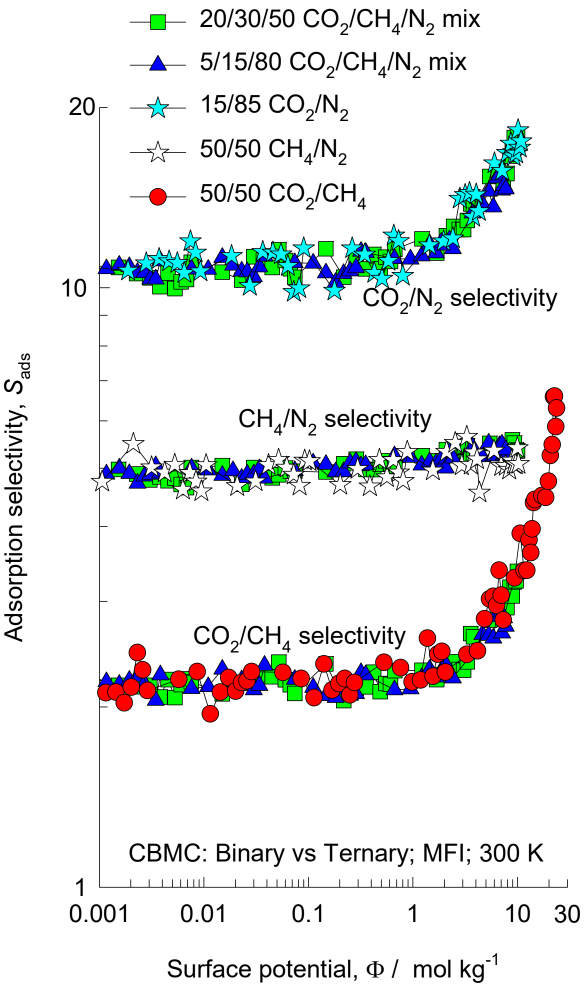

Figure S13. Comparison of CO_2/CH_4, CO_2/N_2, and CH_4/N_2 adsorption selectivities determined from binary mixtures, with the corresponding values in two different ternary mixtures: 5/15/80 $CO_2/CH_4/N_2$, and 20/30/50 $CO_2/CH_4/N_2$. The *x*-axis represents the surface potential, Φ .

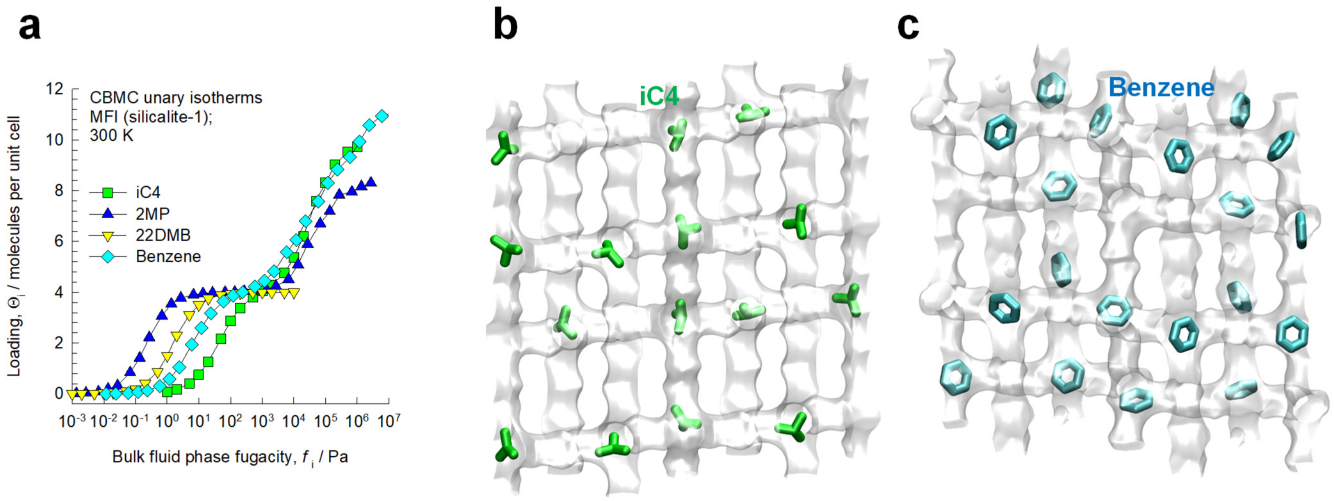

Figure S14. (a) CBMC simulations of unary isotherms for branched alkanes and benzene in MFI zeolite at 300 K. (b, c) Computational snapshots showing the preferential location of (b) iC4 and (c) benzene at the channel intersections of MFI zeolite.

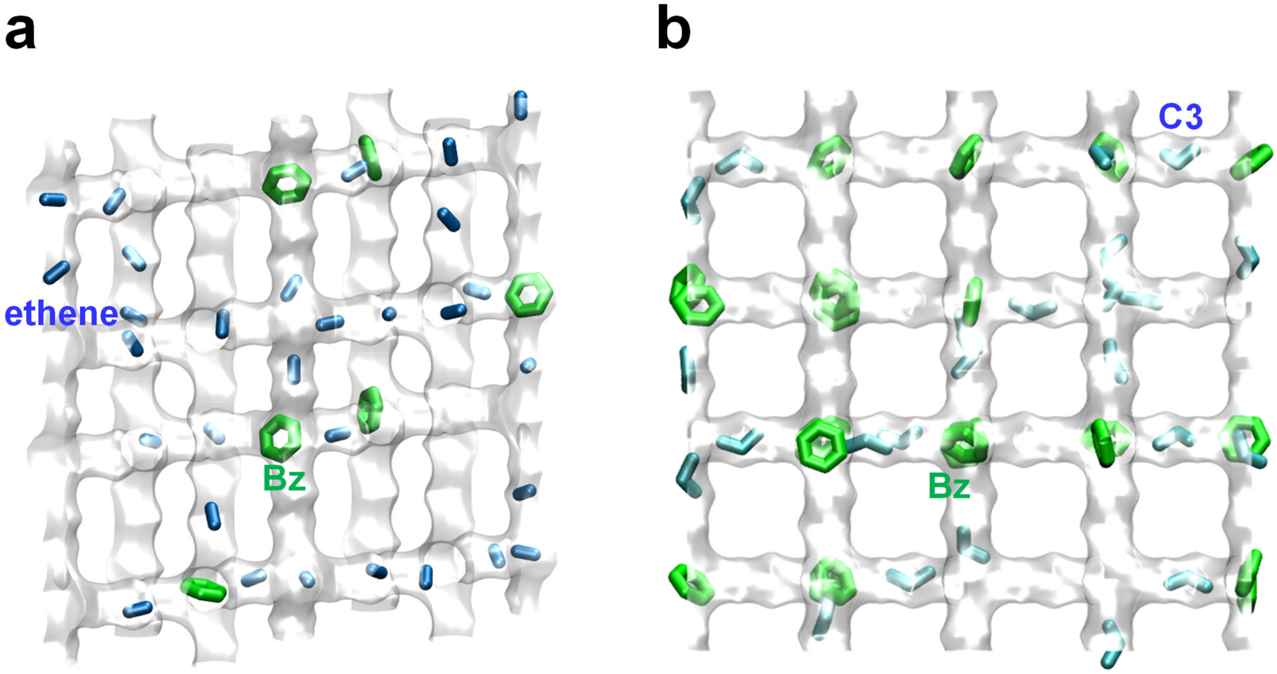

Figure S15. (a, b) Computational snapshots showing the location of guest molecules for (a) C_2H_4(1)/Benzene(2) and (b) C_3H_6(1)/Benzene(2) mixture adsorption in MFI zeolite at 300 K.

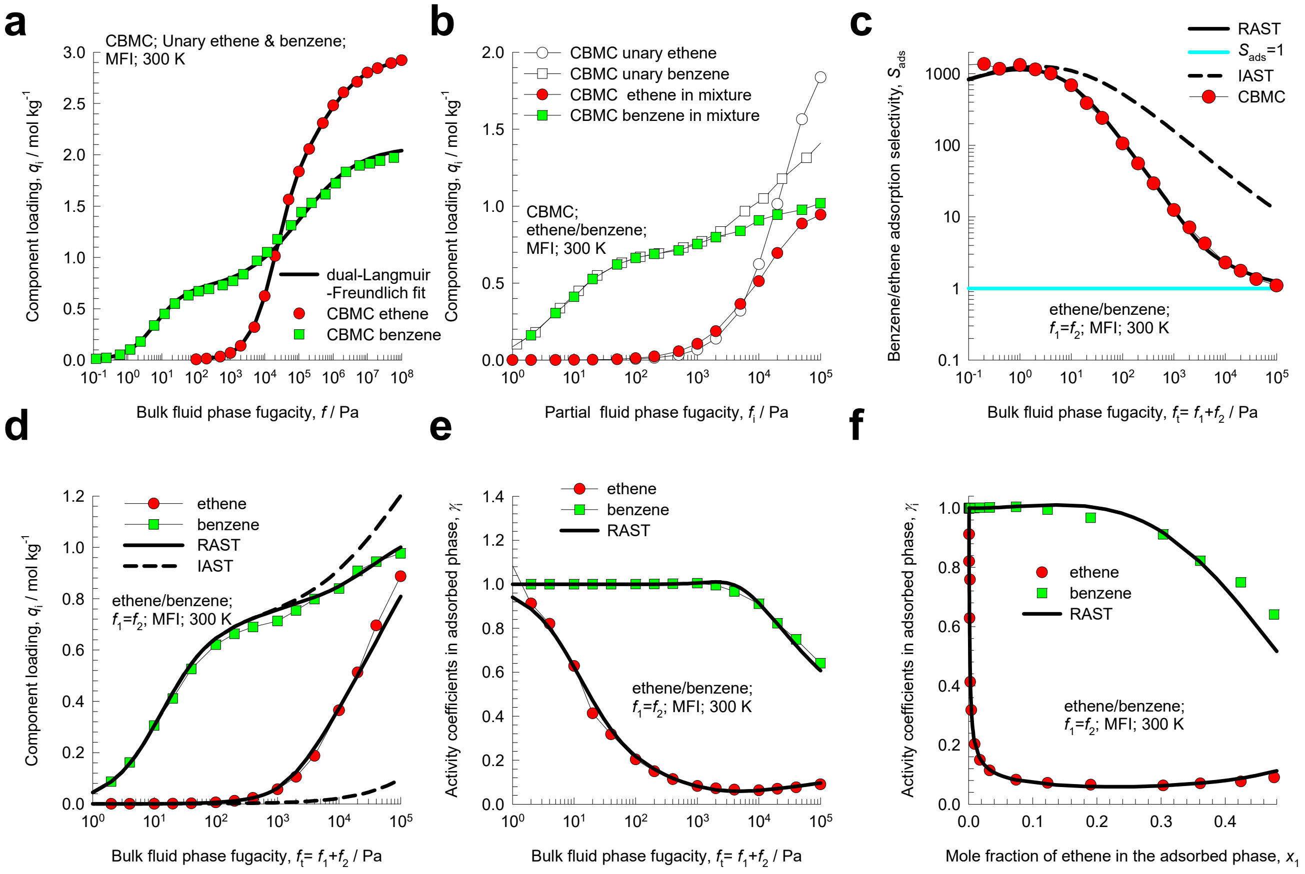

Figure S16. CBMC simulation data and analysis for Campaign A (y_1= 0.5) for C_2H_4(1)/Benzene(2) mixture adsorption in MFI zeolite at 300 K. (a) Unary isotherms and fits. (b) Component loadings in mixture compared with CBMC simulations of unary isotherms. (c) CBMC data for Benzene(2)/C_2H_4(1) adsorption selectivity compared with IAST and RAST estimates. (d) CBMC data for component loadings in mixture compared with RAST estimates. (e, f) Activity coefficients from CBMC compared with RAST model calculations. The unary isotherm data fits and Margules parameters are provided in Table S5, and Table S6.

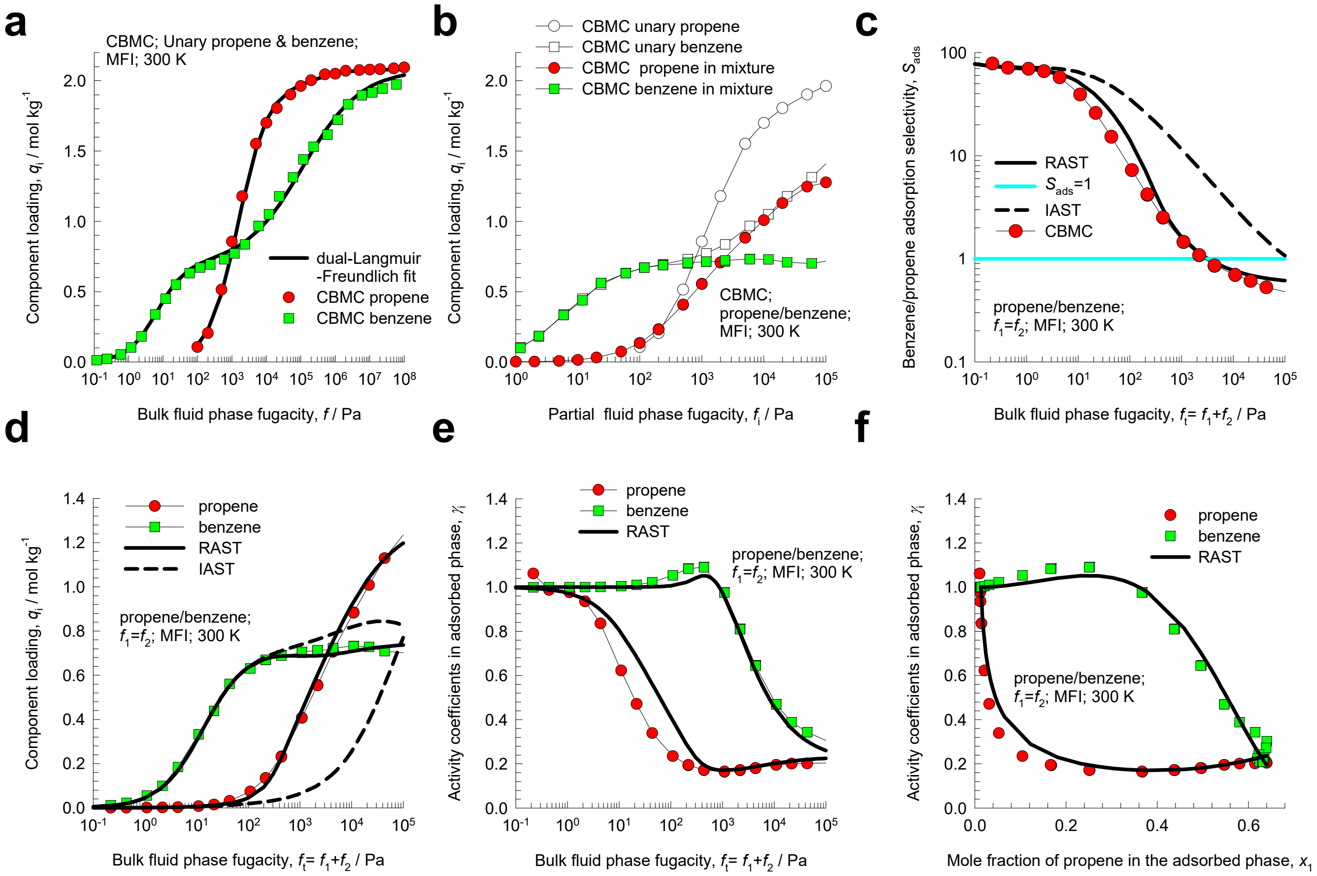

Figure S17. CBMC simulation data and analysis for Campaign A (y_1= 0.5) for C_3H_6(1)/Benzene(2) mixture adsorption in MFI zeolite at 300 K. (a) Unary isotherms and fits. (b) Component loadings in mixture compared with CBMC simulations of unary isotherms. (c) CBMC data for Benzene(2)/C_3H_6(1) adsorption selectivity compared with IAST and RAST estimates. (d) CBMC data for component loadings in mixture compared with RAST estimates. (e, f) Activity coefficients from CBMC compared with RAST model calculations. The unary isotherm data fits and Margules parameters are provided in Table S5, and Table S6.

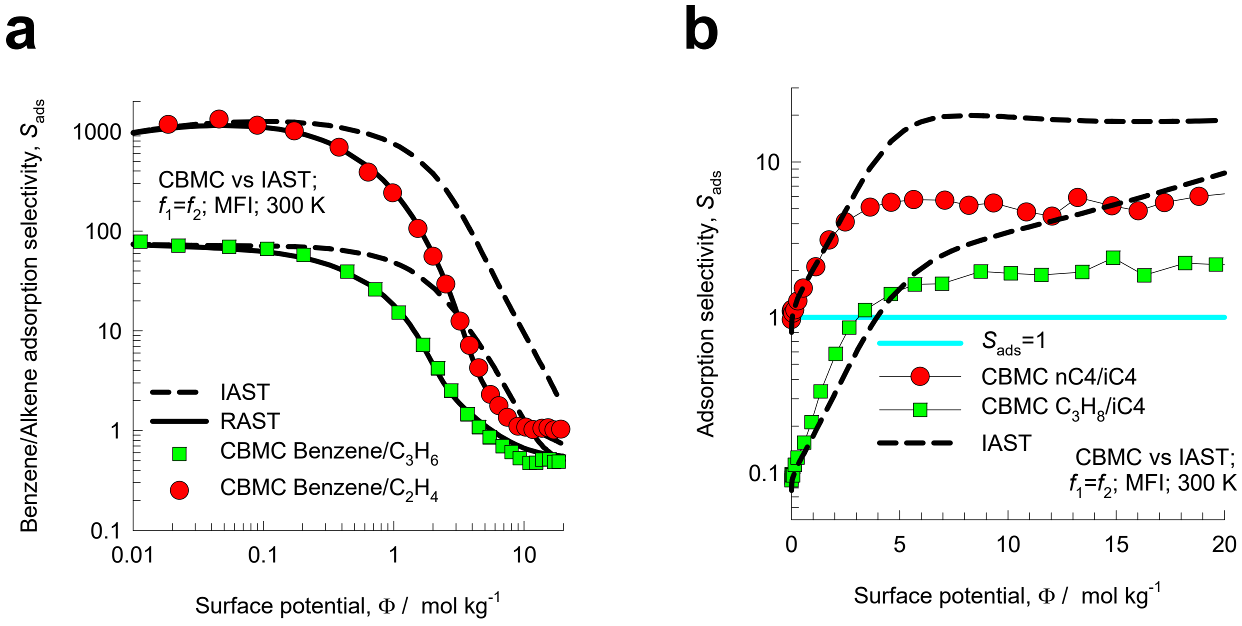

Figure S18. Adsorption selectivity S_{ads} for (a) benzene/C_2H_4, and benzene/C_3H_6 mixtures and (b) C_3H_8/iC4, and nC4/iC4 mixtures plotted as function of the surface potential Φ. The CBMC simulated values (indicated by symbols) are compared with RAST (continuous solid lines), and IAST (dashed lines) estimates.

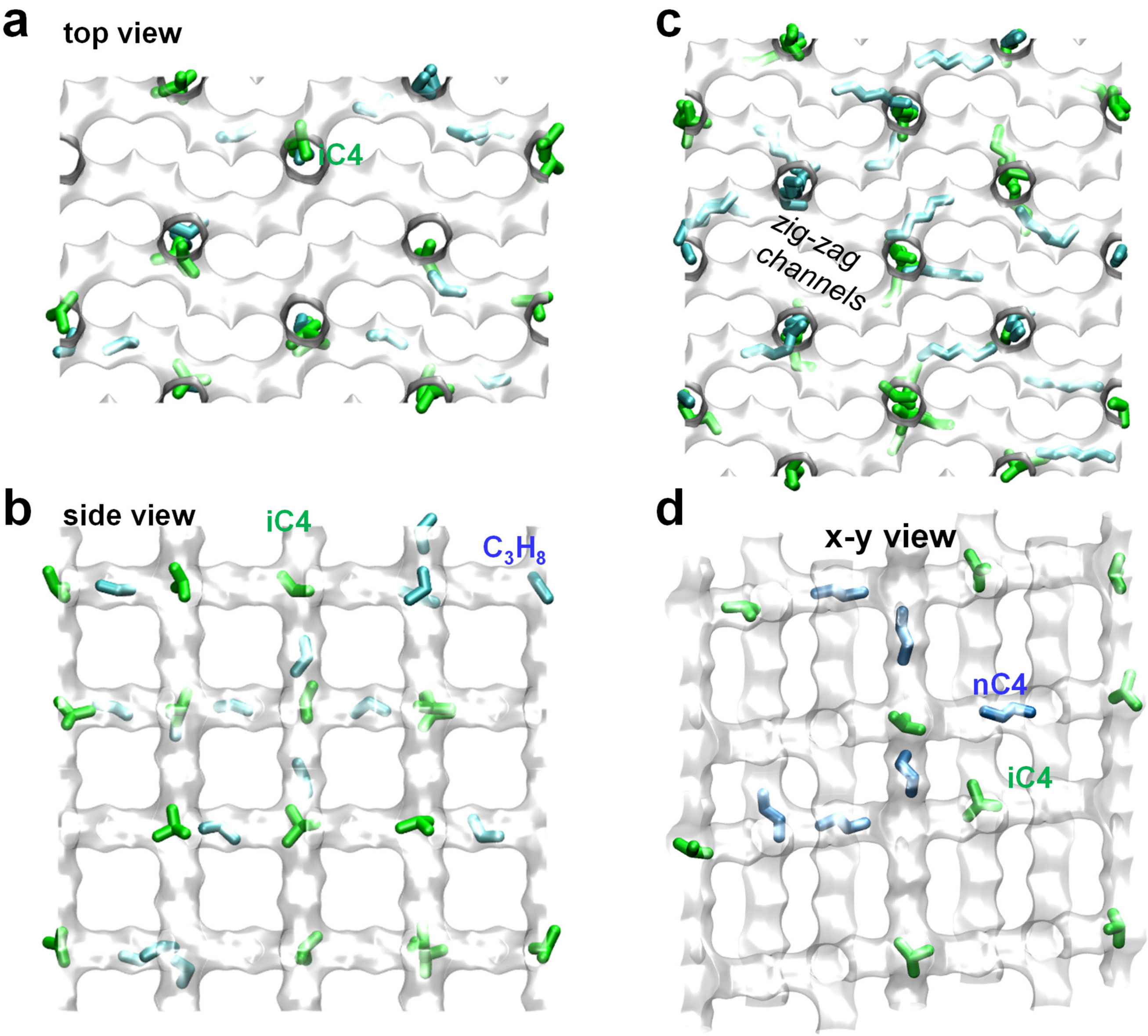

Figure S19. Computational snapshots showing the location of guest molecules for (a, b) C_3H_8(1)/iC4(2) and (c, d) nC4(1)/iC4(2) mixture adsorption in MFI zeolite at 300 K.

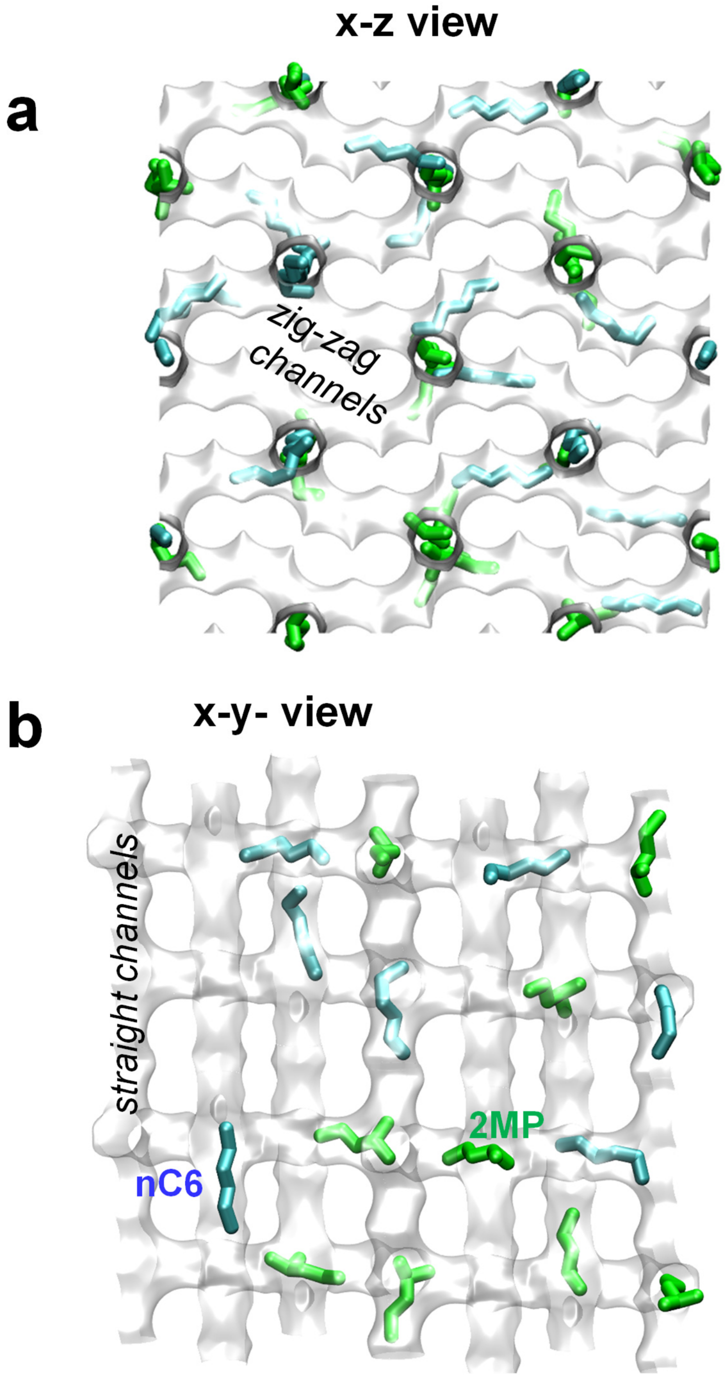

Figure S20. (a, b) Computational snapshots showing the location of guest molecules for nC6(1)/2MP(2) mixture adsorption in MFI zeolite at 300 K.

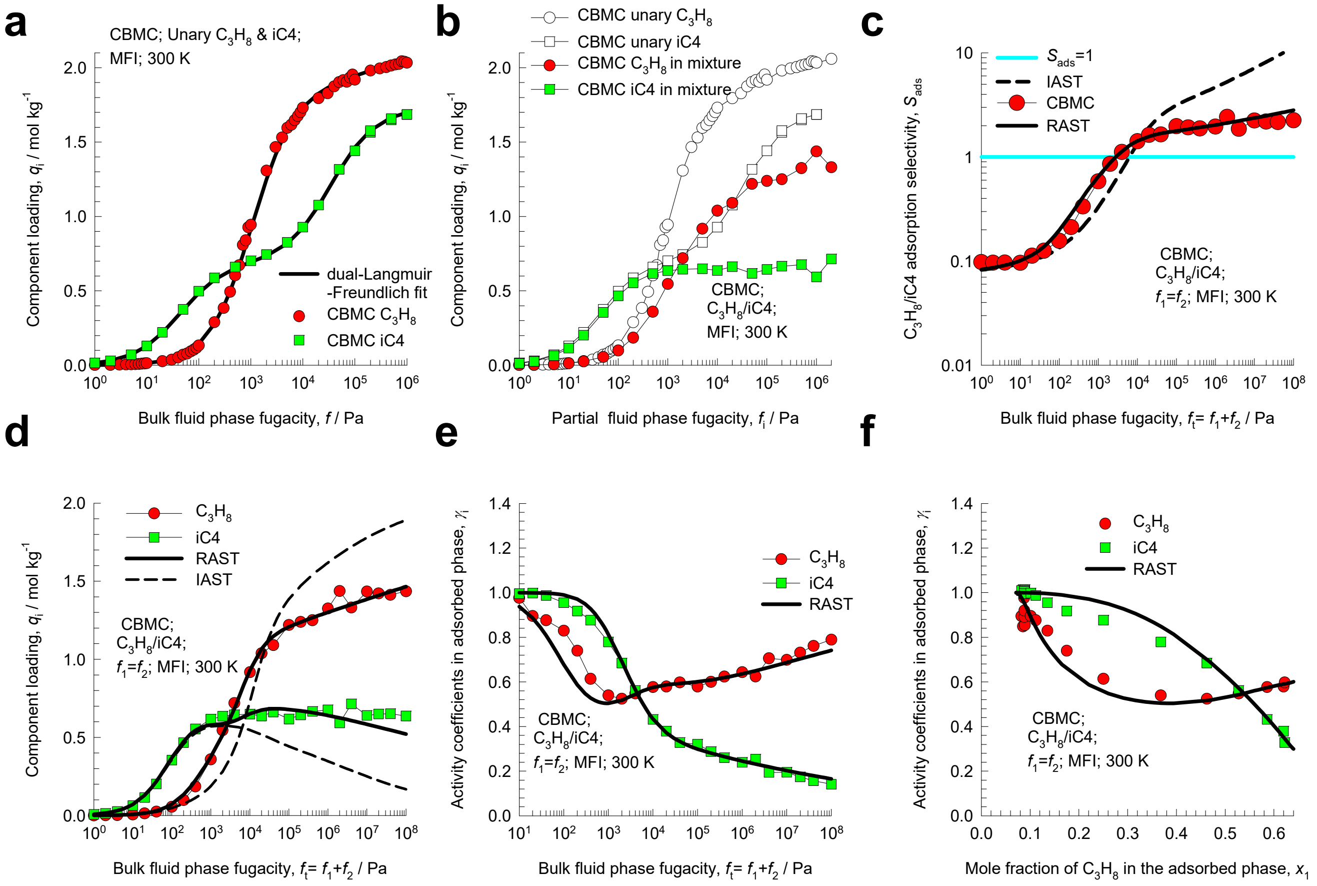

Figure S21. CBMC simulation data and analysis for Campaign A ($y_1 = 0.5$) for C_3H_8(1)/iC4(2) mixture adsorption in MFI zeolite at 300 K. (a) Unary isotherms and fits. (b) Component loadings in mixture compared with CBMC simulations of unary isotherms. (c) CBMC data for C_3H_8(1)/iC4(2) adsorption selectivity compared with IAST and RAST estimates. (d) CBMC data for component loadings in mixture compared with RAST estimates. (e, f) Activity coefficients from CBMC compared with RAST model calculations. The unary isotherm data fits and Margules parameters are provided in Table S5, and Table S6.

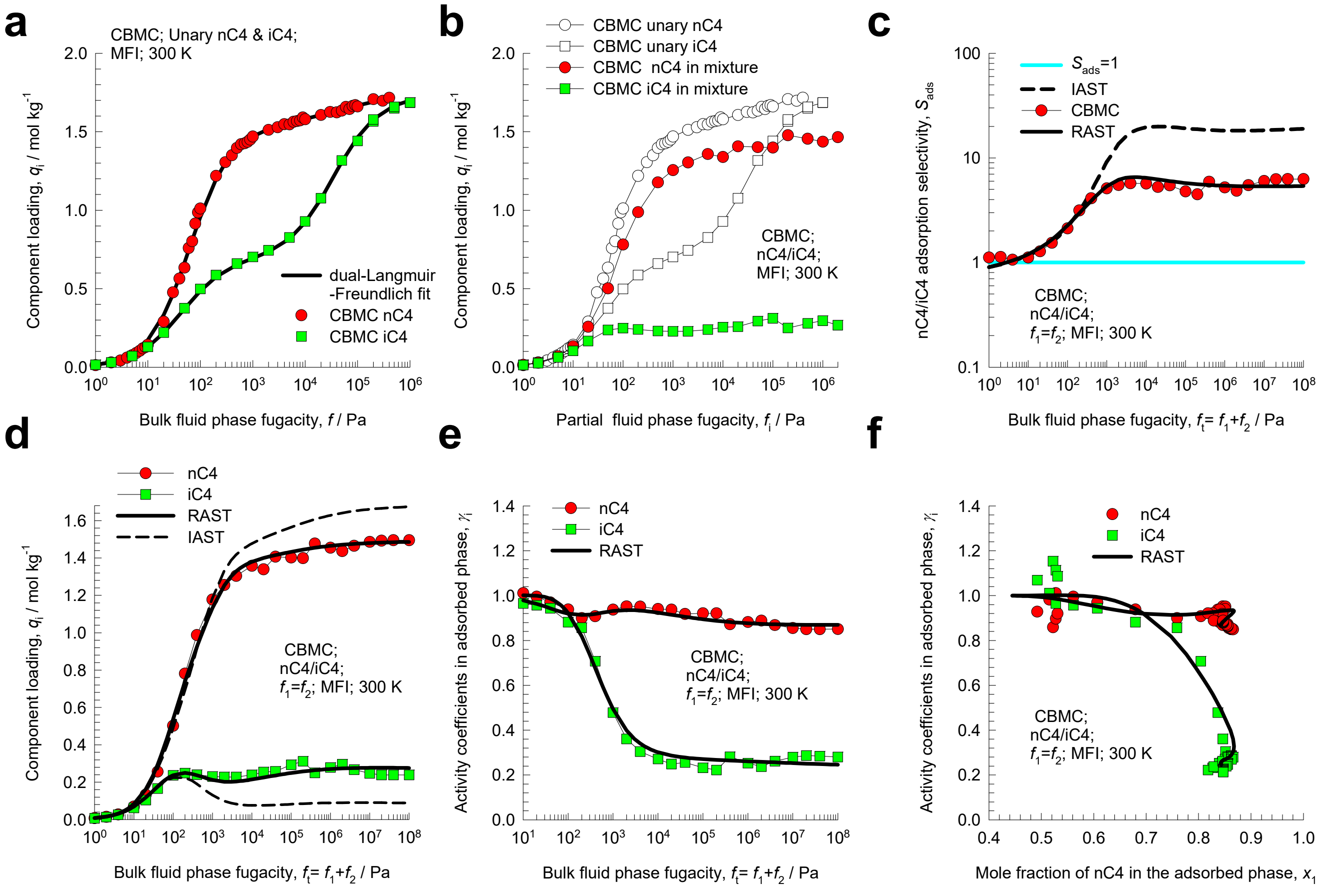

Figure S22. CBMC simulation data and analysis for Campaign A (y_1= 0.5) for nC4(1)/iC4(2) mixture adsorption in MFI zeolite at 300 K. (a) Unary isotherms and fits. (b) Component loadings in mixture compared with CBMC simulations of unary isotherms. (c) CBMC data for nC4(1)/iC4(2) adsorption selectivity compared with IAST and RAST estimates. (d) CBMC data for component loadings in mixture compared with RAST estimates. (e, f) Activity coefficients from CBMC compared with RAST model calculations. The unary isotherm data fits and Margules parameters are provided in Table S5, and Table S6.

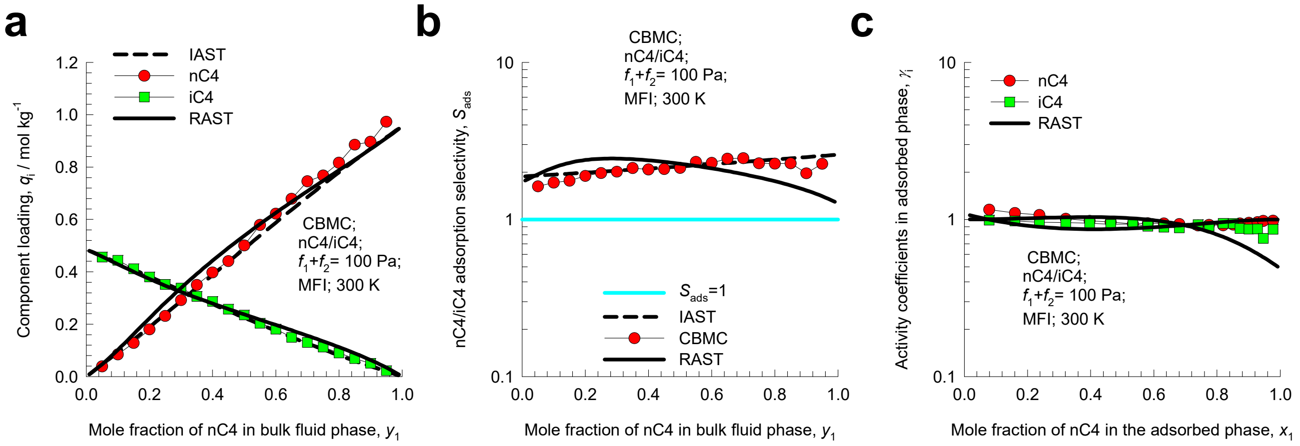

Figure S23. CBMC simulation data and analysis for Campaign B ($f_{\mathrm{t}} = 100$ Pa) for nC4(1)/iC4(2) mixture adsorption in MFI zeolite at 300 K. CBMC data for (a) component loadings and (b) nC4(1)/iC4(2) adsorption selectivity compared with IAST and RAST estimates. (c) Activity coefficients from CBMC compared with RAST model calculations. The unary isotherm data fits and Margules parameters are provided in Table S5, and Table S6.

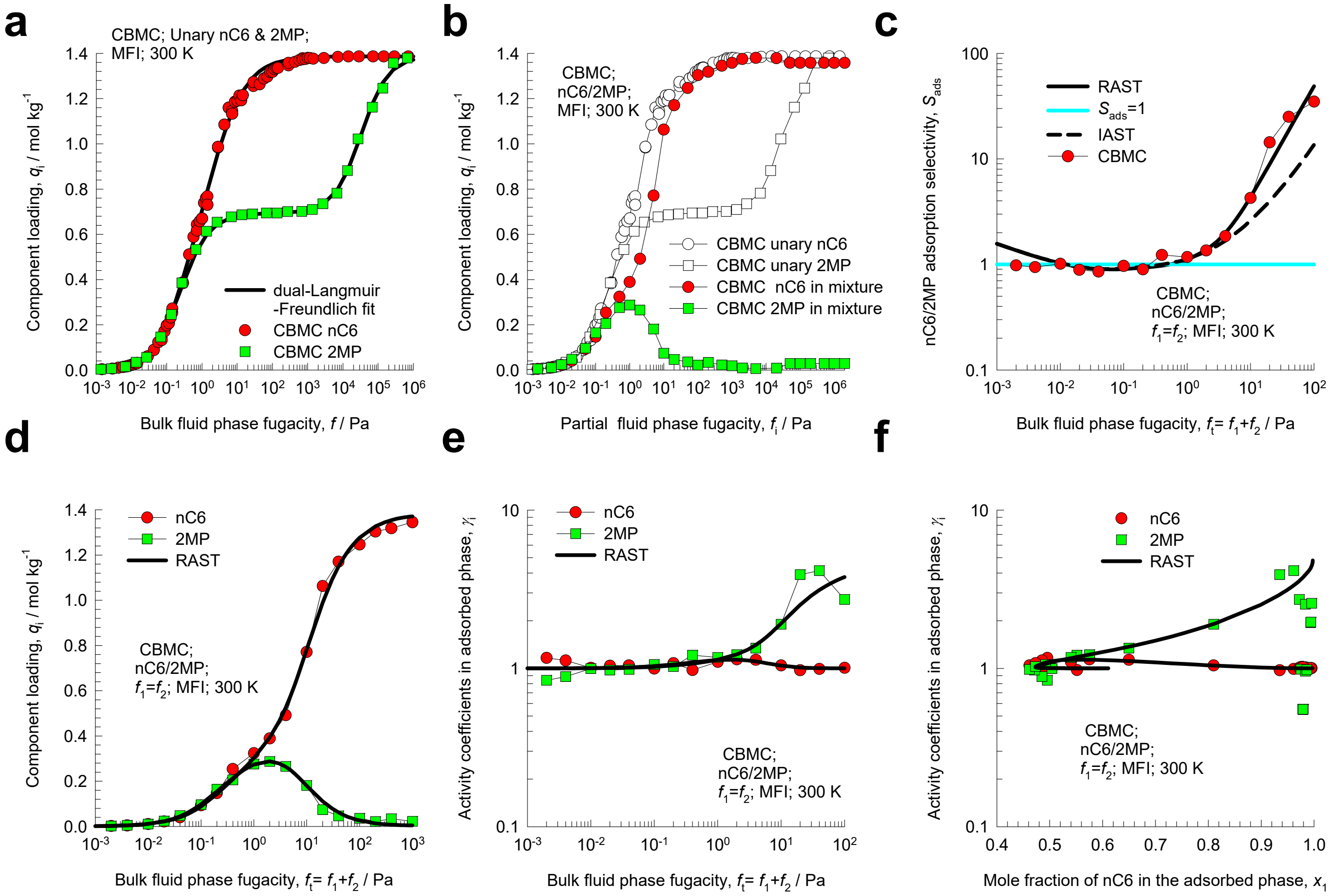

Figure S24. CBMC simulation data and analysis for Campaign A (y_1= 0.5) for nC6(1)/2MP(2) mixture adsorption in MFI zeolite at 300 K. (a) Unary isotherms and fits. (b) Component loadings in mixture compared with CBMC simulations of unary isotherms. (c) CBMC data for nC6(1)/2MP(2) adsorption selectivity compared with IAST and RAST estimates. (d) CBMC data for component loadings in mixture compared with RAST estimates. (e, f) Activity coefficients from CBMC compared with RAST model calculations. The unary isotherm data fits and Margules parameters are provided in Table S5, and Table S6.

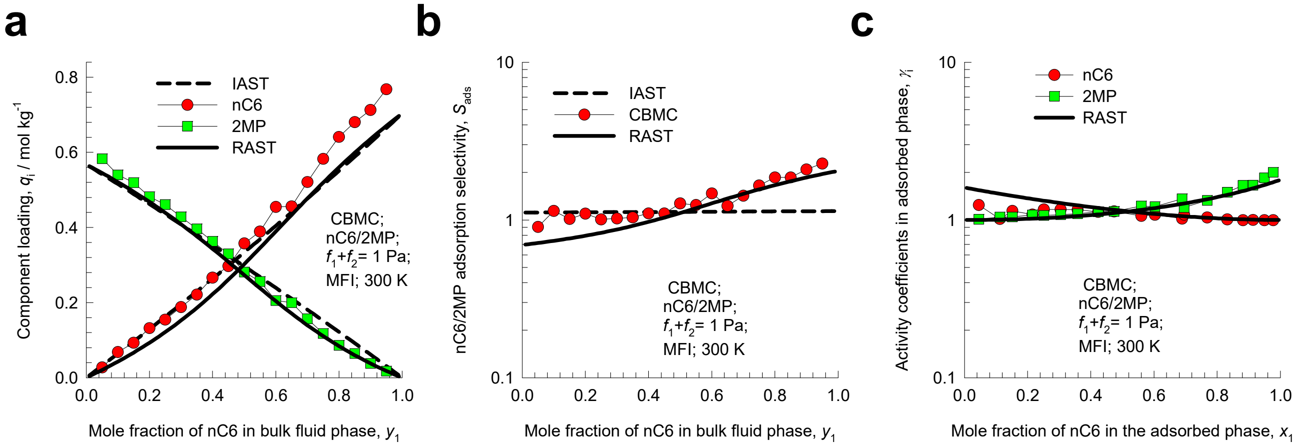

Figure S25. CBMC simulation data and analysis for Campaign B (f_t = 100 Pa) for nC6(1)/2MP(2) mixture adsorption in MFI zeolite at 300 K. CBMC data for (a) component loadings and (b) nC6(1)/2MP(2) adsorption selectivity compared with IAST and RAST estimates. (c) Activity coefficients from CBMC compared with RAST model calculations. The unary isotherm data fits and Margules parameters are provided in Table S5, and Table S6.

9 $CO_2/CH_4/N_2$ mixture adsorption in ISV

The pore landscapes and structural details of all-silica ISV zeolite are presented in Figure S26Figure S27. This zeolite has intersecting channels of two sizes: 12-ring of 6.1 Å -6.5 Å and 12-ring of 5.9 Å - 6.6 Å.

Figure S28 compares the CBMC simulations data (indicated by symbols) of the CO_2/CH_4 adsorption selectivity, S_{ads} , determined from two different CBMC campaigns: (i) 50/50 CO_2/CH_4 , (ii) equimolar ($f_1 = f_2 = f_3$) 1/1/1 $CO_2/CH_4/N_2$ mixtures in ISV zeolite at 300 K. In both cases the S_{ads} is plotted as function of the surface potential Φ, determined from IAST for binary or ternary mixture adsorption. The CBMC data all show a unique dependence on Φ, as prescribed by eq (S13). Put another way, the presence of component 3 in the ternary mixture has no influence of the adsorption selectivity for the 1-2 pair. The dashed lines are the IAST calculations (indicated by dashed lines); these show reasonably good agreement with the CBMC data.

9.1 List of Tables for CO2/CH4/N2 mixture adsorption in ISV

Table S7. Dual-site Langmuir parameters for guest molecules in ISV (all-silica) at 300 K.

	Site A			Site B		
	$q_{\mathrm{A,sat}}$ mol kg^{-1}	b_{A} $\mathrm{Pa}^{-\nu_A}$	$q_{\mathrm{A,sat}}$ mol kg^{-1}	b_{A} $\mathrm{Pa}^{-\nu_A}$	$q_{\mathrm{A,sat}}$ mol kg^{-1}	b_{A} $\mathrm{Pa}^{-\nu_A}$
CO_2	6.6	1.004E-06	1	2.2	1.544E-09	1
CH_4	3.6	1.224E-06	1	1.3	2.296E-08	1
N2	3.5	2.019E-07	1	2.5	1.469E-08	1

9.2 List of Figures for CO2/CH4/N2 mixture adsorption in ISV

ISV pore landscape

Intersecting 12-ring channels structure

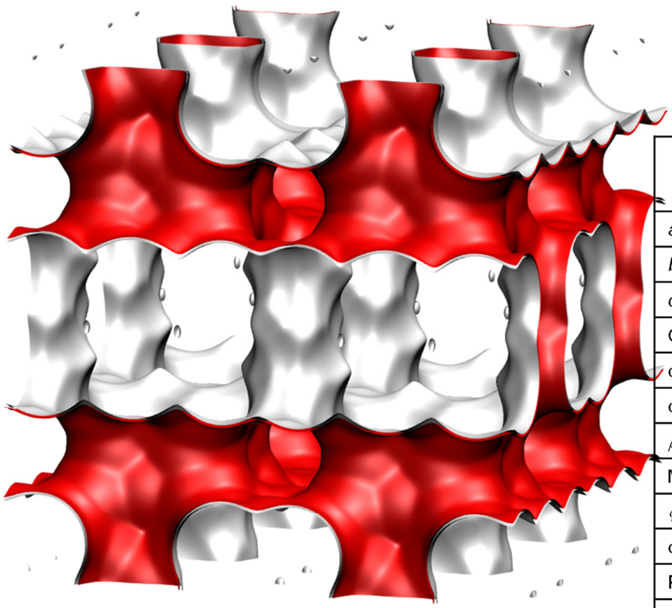

	ISV
a /Å	12.853
b /Å	12.853
c /Å	25.214
Cell volume / Å^3	4165.343
conversion factor for [molec/uc] to [mol per kg Framework]	0.2600
conversion factor for [molec/uc] to [kmol/m^3]	0.9361
ρ [kg/m3]	1533.027
MW unit cell [g/mol(framework)]	3845.427
ϕ, fractional pore volume	0.426
open space / Å^3/uc	1773.9
Pore volume / cm^3/g	0.278
Surface area /m^2/g	911.0
DeLaunay diameter /Å	5.96

Structural information from: C. Baerlocher, L.B. McCusker, Database of Zeolite Structures, International Zeolite Association, http://www.iza-structure.org/databases/

Figure S26. Pore landscape and structural details of ISV zeolite.

ISV pore dimensions

This plot of surface area versus pore dimension is determined using a combination of the DeLaunay triangulation method for pore dimension determination, and the procedure of Düren for determination of the surface area.

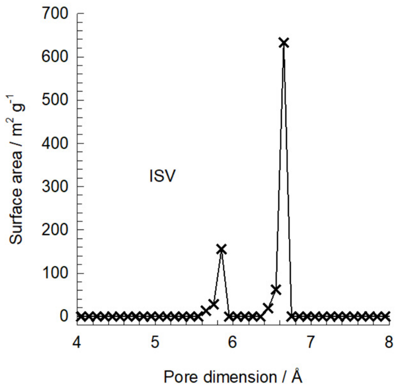

Intersecting 12-ring channels structure

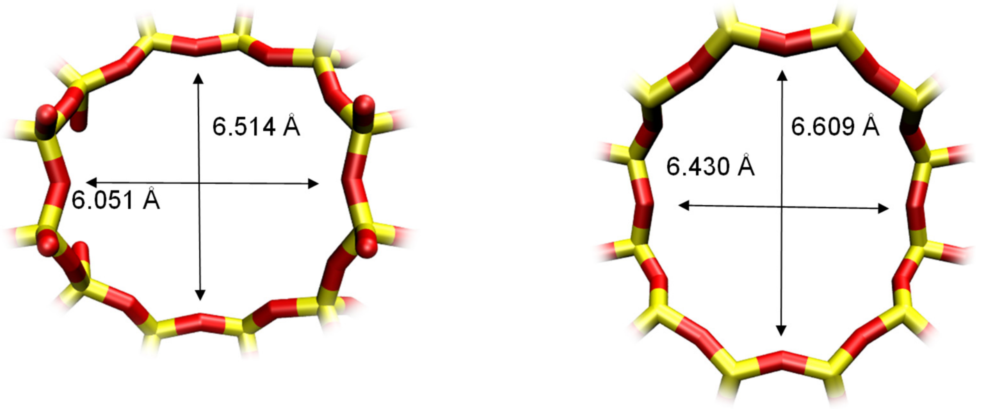

ISV [1 0 0]

ISV [0 0 1]

Figure S27. Channel dimensions of ISV zeolite.

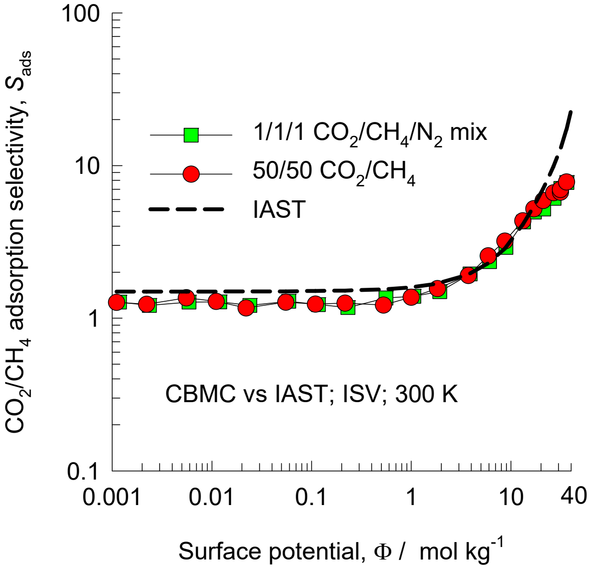

Figure S28. CBMC simulations (indicated by symbols) of the CO_2/CH_4 adsorption selectivity, S_{ads} , determined from two different CBMC campaigns: (i) 50/50 CO_2/CH_4 , (ii) equimolar ($f_1 = f_2 = f_3$) 1/1/1 $CO_2/CH_4/N_2$ mixtures in ISV zeolite at 300 K. The dashed lines are the IAST calculations (indicated by dashed lines), these calculations coincide for the two different CBMC campaigns. The unary isotherm fit parameters are provided in Table S7.

10 Binary mixture adsorption in all-silica CHA zeolite

CHA zeolite consists of cages of volume 316 Å^3, separated by 3.8 Å × 4.2 Å 8-ring windows; the pore landscape and structural details are provided in Figure S29, and Figure S30. SAPO-34 has the same structural topology of CHA zeolite.

10.1 CO_2/CH_4 mixture adsorption in all-silica CHA zeolite

A key assumption of the IAST is that the composition of the adsorbed phase is homogeneously and uniformly distributed within zeolite or metal-organic frameworks. Preferential location of molecules at certain locations within the crystalline, causes segregated adsorption and deviations from the assumption of homogeneous distribution. For separation of CO_2 from gaseous mixtures with CH_4, cage-type zeolites such as CHA, DDR, LTA, and ERI are of practical interest; these materials consist of cages separated by narrow windows, in the 3.3 – 4.5 Å range. For adsorption of CO_2/CH_4 mixtures, CBMC simulations[59] show that the window regions of cage-type zeolites has a significantly higher proportion of CO_2 than within the cages; see computational snapshots in Figure S31 for CHA zeolite.

To demonstrate non-ideality effects in mixture adsorption, three different sets of CBMC campaigns wre conducted.

Figure S32 presents the CBMC data and analysis for Campaign A the ratio of partial fugacities $f_1/f_2 = 1; \quad y_1 = 0.5$ and the bulk mixture fugacity, $f_t = f_1 + f_2$ is varied.

Figure S33 presents the CBMC data and analysis for Campaign A the ratio of partial fugacities $f_1/f_2 = 15/85; \quad y_1 = 0.15$ and the bulk mixture fugacity, $f_t = f_1 + f_2$ is varied.

Figure S34 presents the CBMC data and analysis for Campaign B in which total fugacity is held constant at the value f_t = 1 MPa and the bulk fluid phase mixture composition $y_1 = f_1/f_t$ is varied.

For all three sets of CBMC data, the IAST calculations overestimate the values of S_{ads} because the competitive adsorption is less severe due to the segregated nature of adsorption; the competition faced by CH_4 is less severe than anticipated because of the preferential location of CO_2 in the window regions. The departures from idealities are quantitatively captured by the RAST with fitted Wilson parameters.

In Figure S35, the CBMC simulated values of the adsorption selectivity S_{ads} determined from all three campaigns are plotted as function of the surface potential Φ. At values of $\Phi > 10$ mol kg^{-1}, corresponding to a pore occupancy $\theta > 0.7$, the IAST significantly overestimates S_{ads}.

10.2 Water/ethanol mixture adsorption in all-silica CHA zeolite

Two types of water/ethanol mixture adsorption campaigns were conducted.

Campaign A. The bulk fluid phase composition held constant at $y_1 = y_2 = 0.5$, and the bulk fluid phase fugacity $f_t = f_1 + f_2$ was varied over a wide range from the Henry regime of adsorption, $f_t \to 0; \quad \Phi \to 0$, to pore saturation conditions, typically $\Phi > 50$.

Campaign B. The bulk fluid phase fugacity was held at a constant value $f_t = f_1 + f_2 = 10$ kPa, and the bulk fluid phase mixture composition y_1 was varied $0 < y_1 < 1$.

The CBMC data and analysis for Campaign A are presented in Figure S36; the following major characteristics emerge. From Figure S36b we note that for a range of partial fugacities, f_1 in the bulk fluid phase, the component loading for water in the mixture (filled symbols) exceeds that of the pure component. The ethanol/water adsorption selectivity, S_{ads}, determined from CBMC mixture simulations (symbols) has a tendency to undergo selectivity reversal in favor of water at high values of the bulk fluid phase fugacity $f_t = f_1 + f_2$, as saturation conditions are approached; see Figure S36c. The selectivity reversal in favor of the smaller guest molecule, water, is the consequence of entropy effects that favor the guest species with the higher packing efficiency, as explained in earlier works.[45, 52, 53, 60-62] The selectivity reversal phenomena is also anticipated by the IAST model (shown by the dashed line). An important characteristic is that the IAST over-predicts the alcohol/water selectivity at values of $f_t = f_1 + f_2$ lower than that at which selectivity reversal occurs. For values of $f_t = f_1 + f_2$ higher than that at selectivity reversal, the IAST estimates lie below the values determined from CBMC. The conclusion to be drawn is that IAST exaggerates entropy effects. Put another way, hydrogen bonding effects tend to moderate the influence of entropy effects because of molecular clustering attendant with mixture adsorption. As is to be expected the RAST model captures the right trends in the dependence of S_{ads} on $f_t = f_1 + f_2$.

In Figure S36d, we note that the RAST estimates of the component loadings are in reasonably good agreement with CBMC simulated component loadings $q_{1,CBMC}; q_{2,CBMC}$ (filled symbols). This is to be expected because the model parameters are chosen to fit the CBMC simulated component loadings. The success of the RAST model is therefore to be regarded as testimony to the applicability of the Margules model to describe the activity coefficients for mixture adsorption.

The activity coefficients in the adsorbed phase are plotted in Figure S36e,f. Both activity coefficients tend to unity in the Henry regime, as $\gamma_i \to 1;\quad f_t \to 0$. The activity coefficient of water, γ_1, displays a minimum when plotted against the total bulk fluid phase fugacity $f_t = f_1 + f_2$. The activity coefficient of alcohol tends to decrease to low values as $f_t = f_1 + f_2$ increases. The activity coefficient of water, γ_1, tends to unity as the adsorbed phase mole fraction $x_1 \to 1$; it displays a minimum. The activity coefficient of alcohol, γ_2, tends to unity as the adsorbed phase mole fraction $x_2 = (1 - x_1) \to 1$, decreasing in magnitude as $x_1 \to 1$.

The CBMC data and analysis for Campaign B are presented in Figure S37. In Figure S37a, the RAST calculations using the fitted Margules parameters (continuous solid line) of the component loadings are, in agreement with CBMC simulated component loadings $q_{1,CBMC};q_{2,CBMC}$ (filled symbols) for binary mixture plotted as function of the mole fraction of component 1 in the bulk fluid phase, y_1. In Figure S37b, the adsorption selectivity, S_{ads}, determined from CBMC mixture simulations (symbols) are compared with calculations using the IAST (dashed line) and RAST (continuous solid line). The *x*-axis represents the mole fraction of component 1 in the bulk fluid phase, y_1.The ethanol/water adsorption selectivity experiences a selectivity reversal. The occurrence of selectivity reversal is caused by hydrogen bonding. This selectivity reversal is not anticipated by the IAST.

In Figure S38, the CBMC simulated values of the adsorption selectivity S_{ads} determined from both campaigns A and B are plotted as function of the surface potential Φ. The CBMC simulated selectivity S_{ads} do not uniquely depend on Φ, as prescribed by IAST. At values of $\Phi > 25$ mol kg^{-1}, the IAST significantly underestimates the ethanol/water selectivity due to moderation of entropy effects.

10.3 List of Tables for Binary mixture adsorption in all-silica CHA zeolite

Table S8. Dual-site Langmuir-Freundlich parameters for guest molecules in CHA (all-silica) at 300 K.

	Site A			Site B		
	$q_{A,sat}$ mol kg^{-1}	b_A $\mathrm{Pa}^{-\nu A}$	ν_A dimensionless	$q_{B,sat}$ mol kg^{-1}	b_B $\mathrm{Pa}^{-\nu B}$	ν_B dimensionless
CO_2	6.8	2.4464E-06	1.06	2.8	5.181E-06	0.7
CH_4	2.7	1.3131E-06	1.02	5.5	2.703E-07	0.84

Fitted Margules non-ideality parameters for binary CO_2/CH_4 mixture adsorption in CHA at 300 K.

	C / kg mol^{-1}	A_{12}	A_{21}
CO_2/CH_4	0.169	-0.496	-0.226

Table S9. Dual-site Langmuir-Freundlich parameters for water and unary 1-alcohols in CHA at 300 K. The fit parameters are based on the CBMC simulations of pure component isotherms presented in earlier work.[47, 61]

	Site A			Site B		
	$q_{A,sat}$ mol kg^{-1}	b_A $\mathrm{Pa}^{-\nu A}$	ν_A dimensionless	$q_{A,sat}$ mol kg^{-1}	b_A $\mathrm{Pa}^{-\nu A}$	ν_B
water	16.8	3.031E-54	15.6	4.6	2.218E-05	1
methanol	3.7	4.281E-11	3.37	3.7	4.545E-04	1
ethanol	2.5	8.578E-06	1.07	2.9	3.505E-03	1.1

Fitted Margules non-ideality parameters for binary mixture adsorption in CHA at 300 K. The fits are based on combining CBMC Campaigns A and B.

	C / kg mol^{-1}	A_{12}	A_{21}
water/ethanol	0.114	-7.334	-3.665

10.4 List of Figures for Binary mixture adsorption in all-silica CHA zeolite

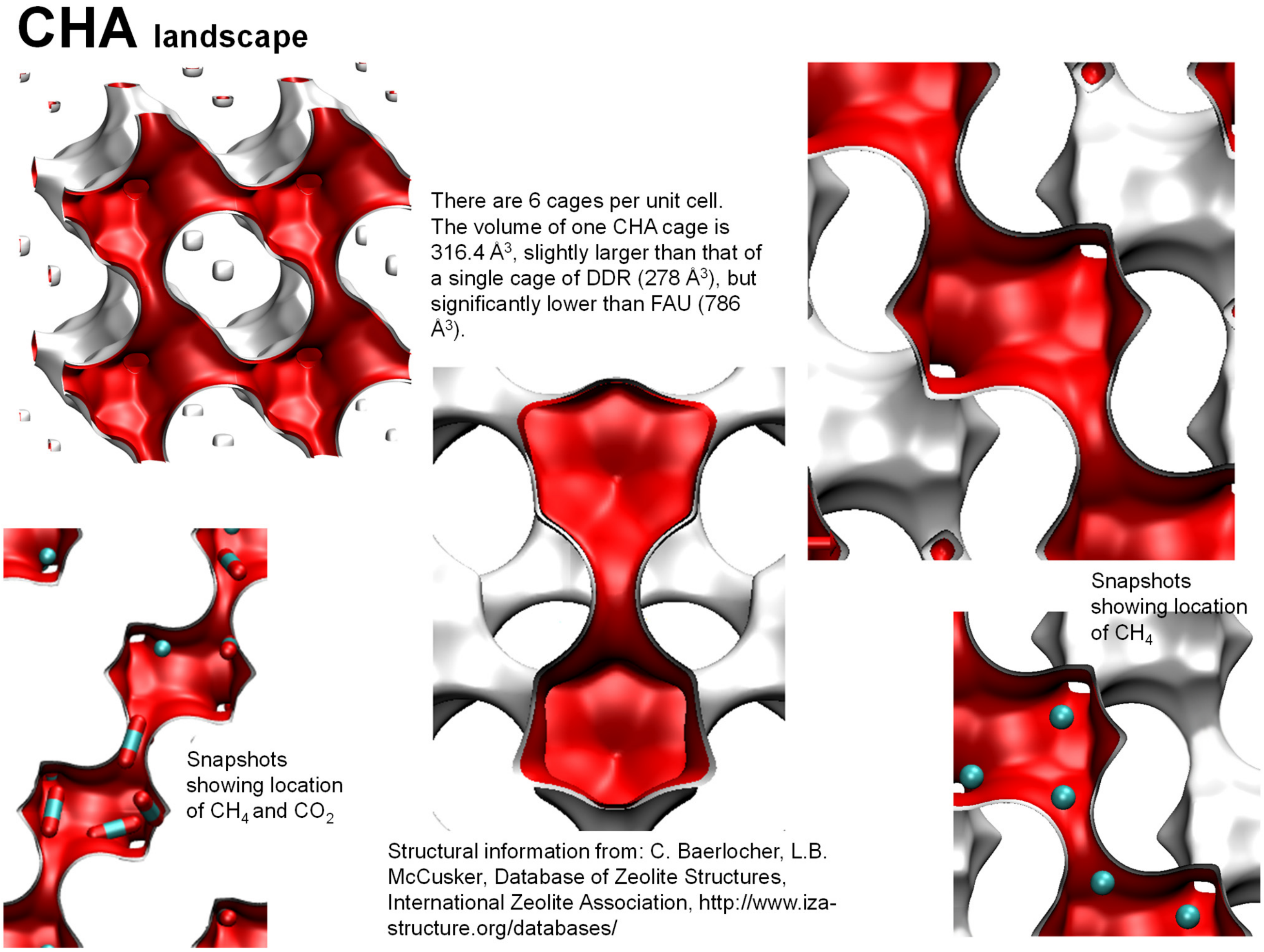

There are 6 cages per unit cell. The volume of one CHA cage is 316.4 Å^3, slightly larger than that of a single cage of DDR (278 Å^3), but significantly lower than FAU (786 Å^3).

Snapshots showing location of CH_4 and CO_2

Structural information from: C. Baerlocher, L.B. McCusker, Database of Zeolite Structures, International Zeolite Association, http://www.iza-structure.org/databases/

Snapshots showing location of CH_4

Figure S29. Pore landscape of all-silica CHA zeolite.

CHA window and pore dimensions

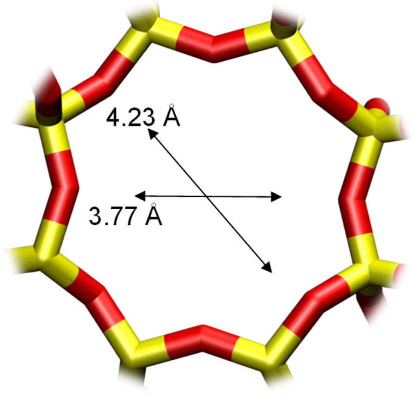

CHA

The window dimensions calculated using the van der Waals diameter of framework atoms = 2.7 Å are indicated above by the arrows.

	CHA
a /Å	15.075
b /Å	23.907
c /Å	13.803
Cell volume / Å^3	4974.574
conversion factor for [molec/uc] to [mol per kg Framework]	0.2312
conversion factor for [molec/uc] to [kmol/m^3]	0.8747
ρ [kg/m3]	1444.1
MW unit cell [g/mol(framework)]	4326.106
ϕ, fractional pore volume	0.382
open space / Å^3/uc	1898.4
Pore volume / cm^3/g	0.264
Surface area /m^2/g	758.0
DeLaunay diameter /Å	3.77

Figure S30. Structural details for CHA zeolite.

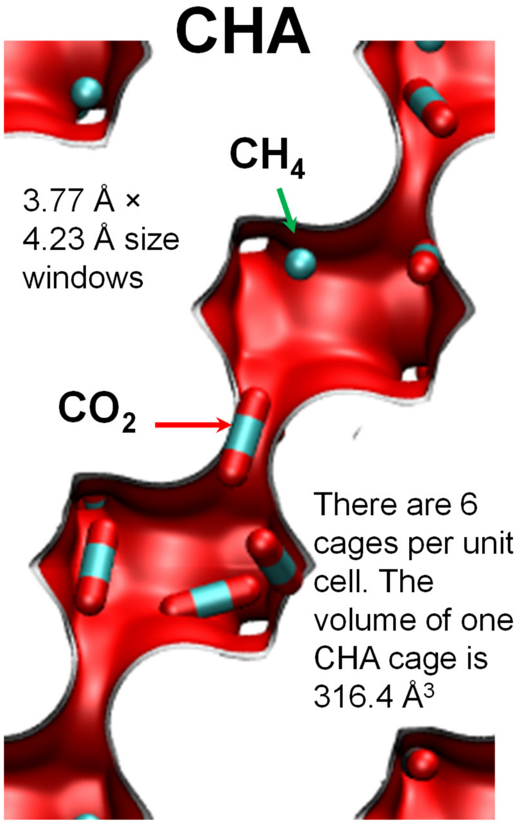

Figure S31. Computational snapshots for CO_2(1)/CH_4(2) mixture adsorption in CHA zeolite at 300 K.

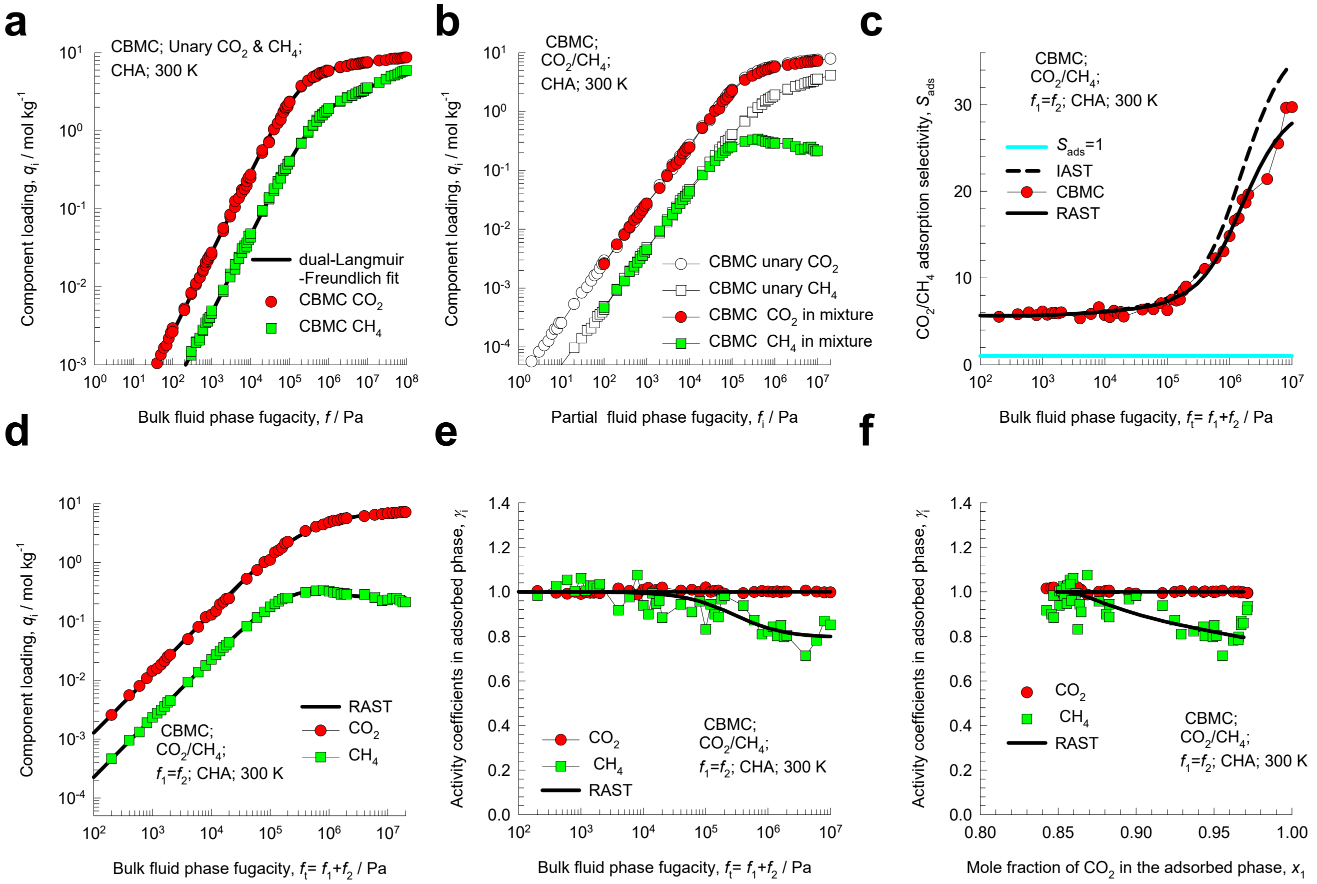

Figure S32. CBMC simulation data and analysis for Campaign A (y_1= 0.5) for CO_2(1)/CH_4(2) mixture adsorption in CHA zeolite at 300 K. (a) Unary isotherms and fits. (b) Component loadings in mixture compared with CBMC simulations of unary isotherms. (c) CBMC data for CO_2(1)/CH_4(2) adsorption selectivity compared with IAST and RAST estimates. (d) CBMC data for component loadings in mixture compared with RAST estimates. (e, f) Activity coefficients from CBMC compared with RAST model calculations. The unary isotherm data fits and Margules parameters are provided in Table S8.

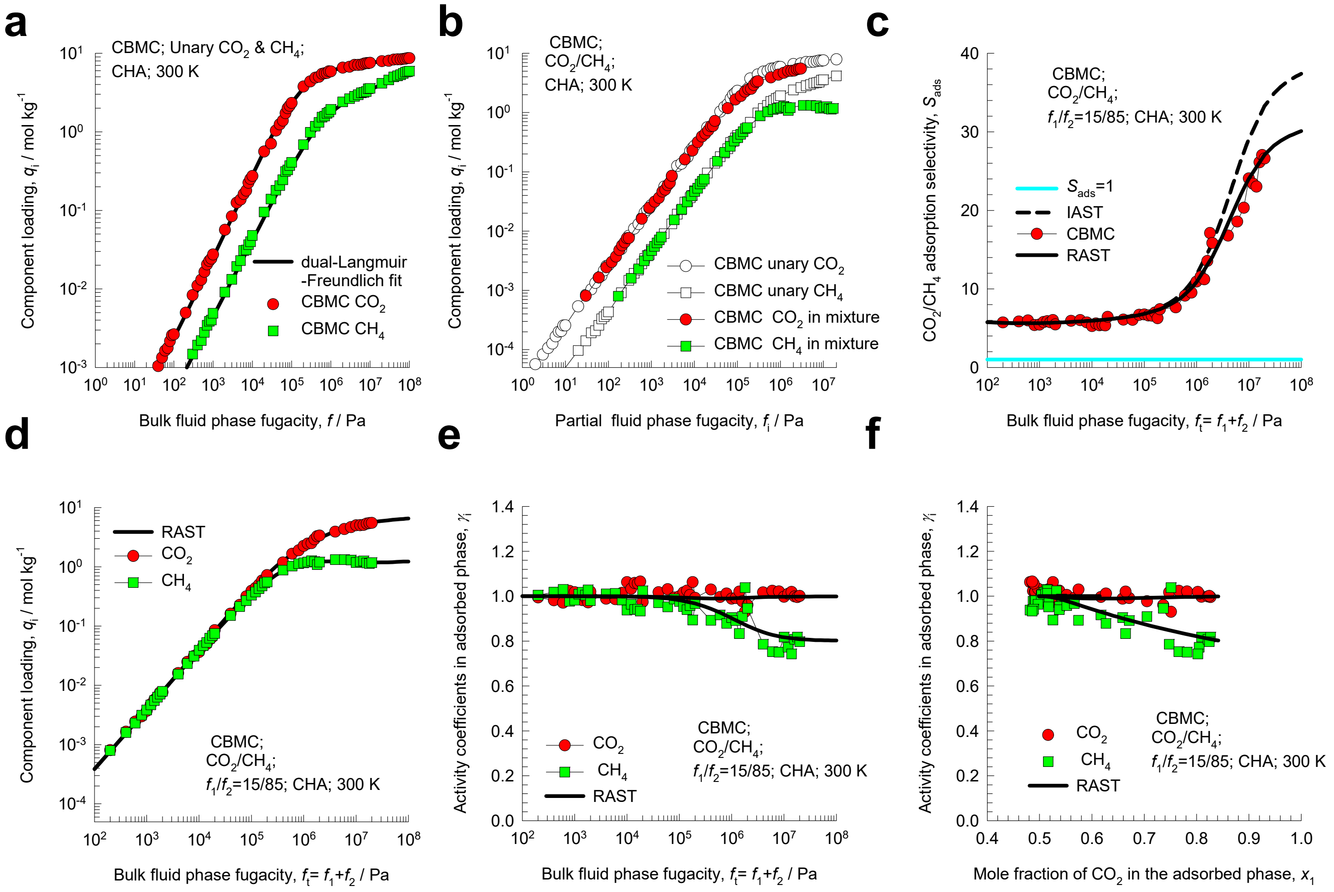

Figure S33. CBMC simulation data and analysis for Campaign A (y_1= 0.15) for CO_2(1)/CH_4(2) mixture adsorption in CHA zeolite at 300 K. (a) Unary isotherms and fits. (b) Component loadings in mixture compared with CBMC simulations of unary isotherms. (c) CBMC data for CO_2(1)/CH_4(2) adsorption selectivity compared with IAST and RAST estimates. (d) CBMC data for component loadings in mixture compared with RAST estimates. (e, f) Activity coefficients from CBMC compared with RAST model calculations. The unary isotherm data fits and Margules parameters are provided in Table S8.

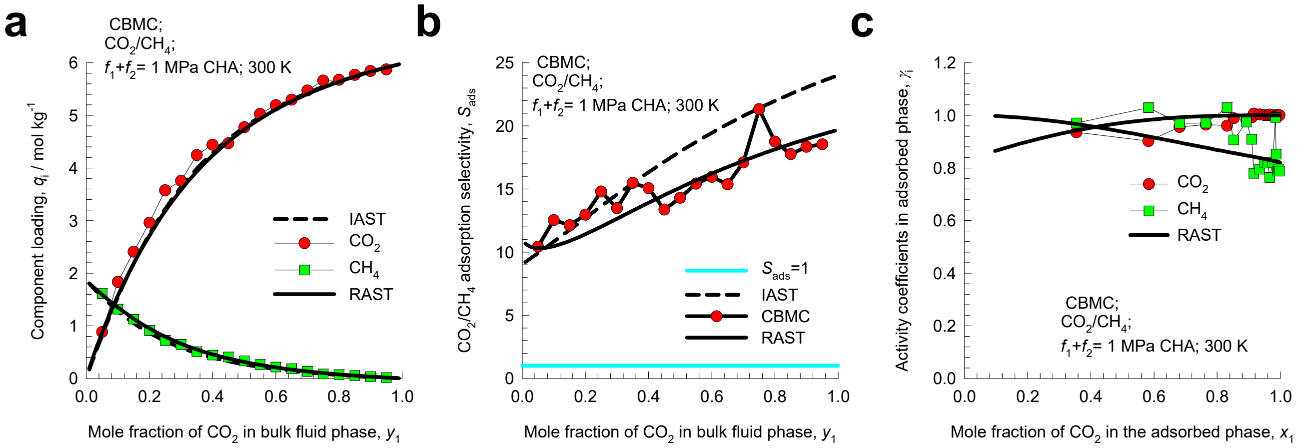

Figure S34. CBMC simulation data and analysis for Campaign B (f_t = 1 MPa) for $CO_2(1)/CH_4(2)$ mixture adsorption in CHA zeolite at 300 K. CBMC data for (a) component loadings and (b) $CO_2(1)/CH_4(2)$ adsorption selectivity compared with IAST and RAST estimates. (c) Activity coefficients from CBMC compared with RAST model calculations. The unary isotherm data fits and Margules parameters are provided in Table S8.

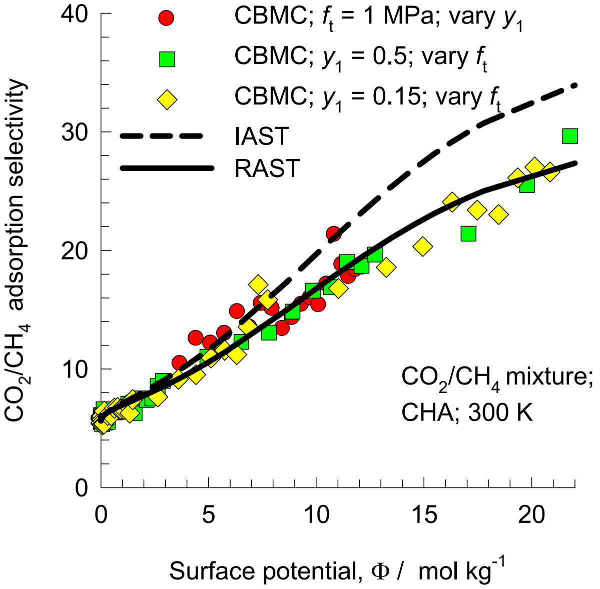

Figure S35. Adsorption selectivity S_{ads} for CO_2(1)/CH_4(2) mixture adsorption in CHA zeolite at 300 K, for three different campaigns (Campaign A (y_1= 0.5, and 0.15) and Campaign B (f_t = 1 MPa), plotted as function of the surface potential Φ. The CBMC simulated values (indicated by symbols) are compared with RAST (continuous solid lines), and IAST (dashed lines) estimates. The unary isotherm data fits and Margules parameters are provided in Table S8.

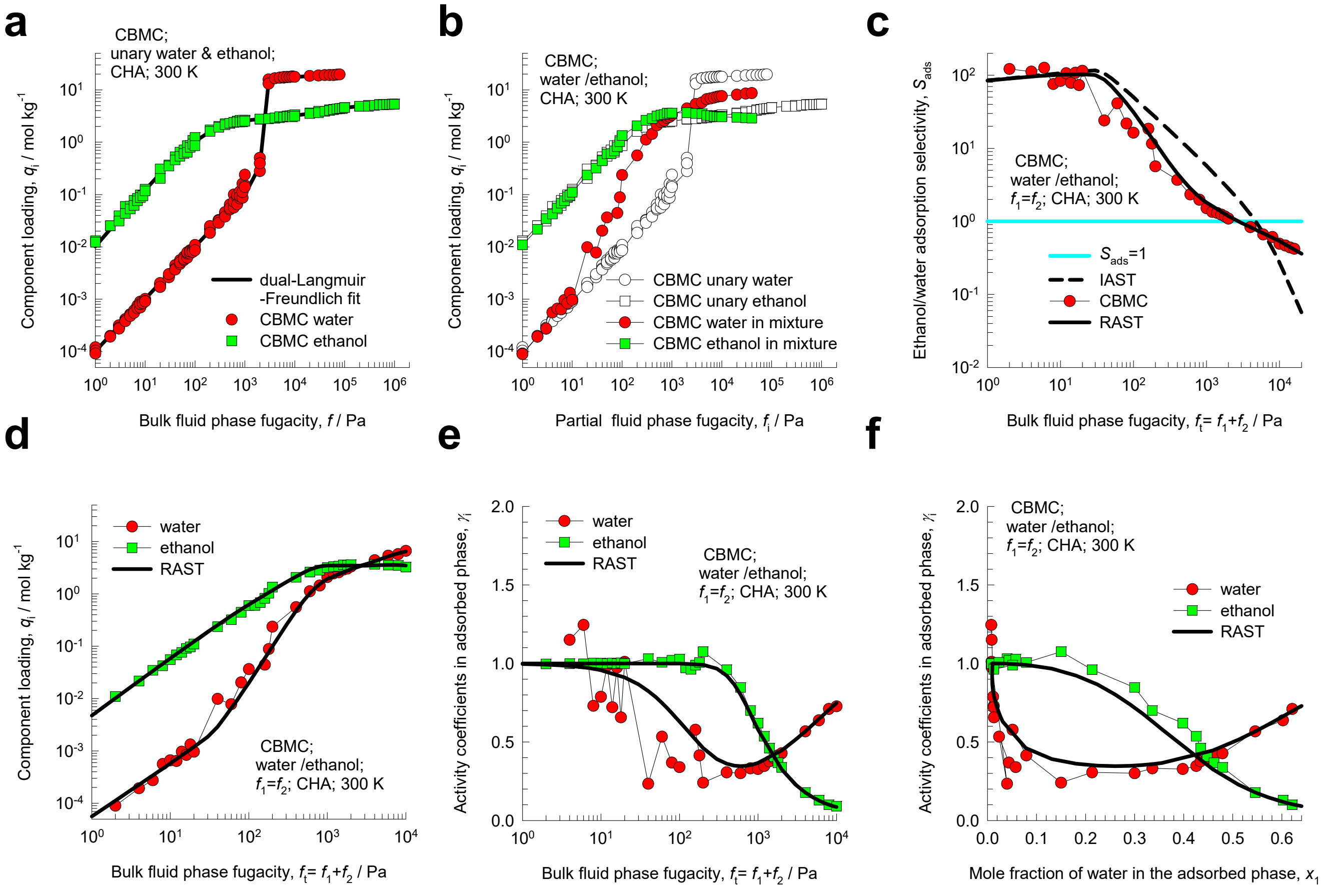

Figure S36. CBMC simulation data and analysis for Campaign A (y_1= 0.5) for water/ethanol mixture in CHA at 300 K. (a) Unary isotherms and fits. (b) Component loadings in mixture compared with CBMC simulations of unary isotherms. (c) CBMC data for alcohol/water selectivity compared with IAST and RAST estimates. (d) CBMC data for component loadings in mixture compared with RAST estimates. (e, f) Activity coefficients from CBMC compared with RAST model calculations. The unary isotherm data fits and Margules parameters are provided in Table S8.

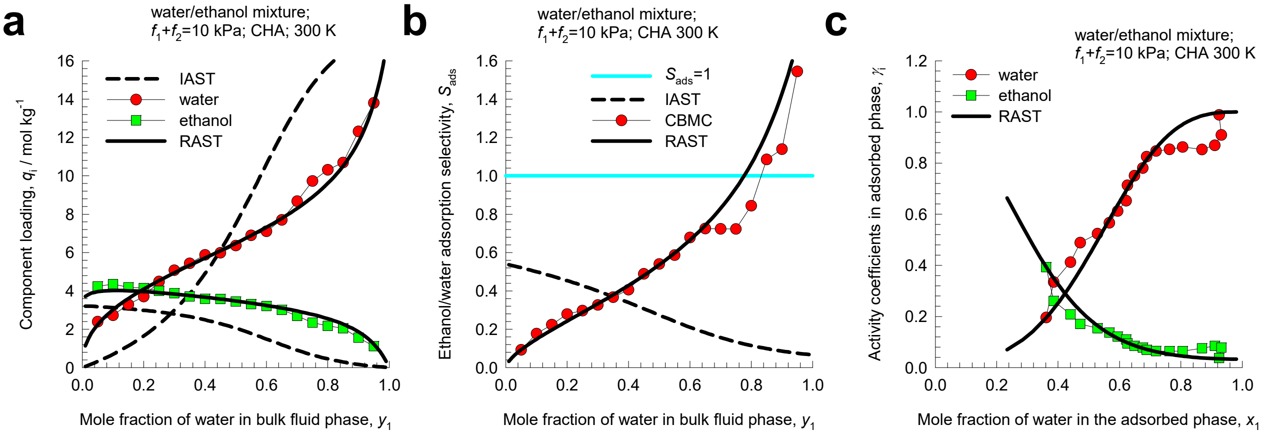

Figure S37. CBMC simulation data and analysis for Campaign B (f_t = 10 kPa) for water/ethanol mixture in CHA at 300 K. CBMC data on (a) component loadings, and (b) alcohol/water selectivity compared with IAST and RAST estimates. (c) Activity coefficients from CBMC compared with RAST model calculations.

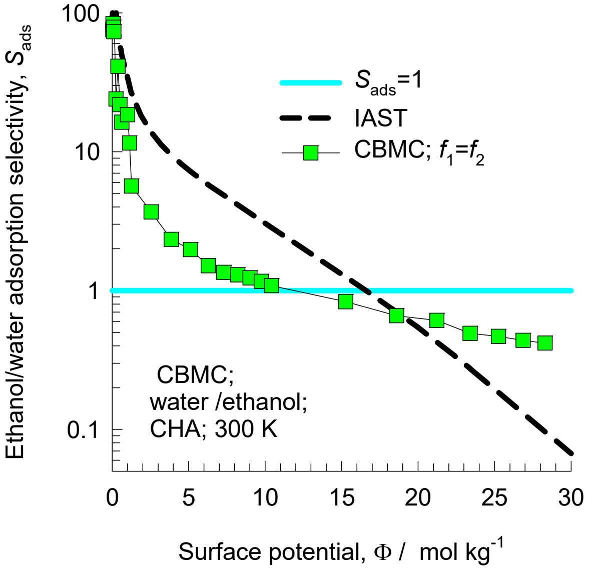

Figure S38. Adsorption selectivity S_{ads} for water/ethanol mixture in CHA at 300 K., for two different campaigns (Campaign A (y_1= 0.5) and Campaign B (f_t = 10 kPa), plotted as function of the surface potential Φ. The CBMC simulated values (indicated by symbols) are compared with IAST estimates (indicated by the dashed lines). The unary isotherm data fits and Margules parameters are provided in Table S9.

11 Binary mixture adsorption in all-silica DDR zeolite

DDR consists of cages of 277.8 Å^3 volume, separated by 3.65 Å × 4.37 Å 8-ring windows; the pore landscapes and structural details are provided in Figure S39, and Figure S40.

11.1 CO_2/CH_4 mixture adsorption in all-silica DDR zeolite

A key assumption of the IAST is that the composition of the adsorbed phase is homogeneously and uniformly distributed within zeolite or metal-organic frameworks. Preferential location of molecules at certain locations within the crystalline, causes segregated adsorption and deviations from the assumption of homogeneous distribution. For separation of CO_2 from gaseous mixtures with CH_4, cage-type zeolites such as CHA, DDR, LTA, and ERI are of practical interest; these materials consist of cages separated by narrow windows, in the 3.3 – 4.5 Å range. For adsorption of CO_2/CH_4 mixtures, CBMC simulations[59] show that the window regions of cage-type zeolites has a significantly higher proportion of CO_2 than within the cages; see computational snapshots in Figure S41 for DDR. Due to the segregated nature of mixture adsorption, the IAST is unable to predict the mixture loadings accurately. Due to preferential location of CO_2 in the window regions the CH_4 molecules experience a less severe competition from CO_2.

Figure S42, and Figure S43 present the CBMC data and analysis for two different campaigns. In Campaign A the ratio of partial fugacities $f_1/f_2=1; \quad y_1=0.5$ and the bulk mixture fugacity, $f_t=f_1+f_2$ is varied. In Campaign B in which total fugacity is held constant at the value f_t = 1 MPa and the bulk fluid phase mixture composition $y_1=f_1/f_t$ is varied. The IAST calculations overestimate the values of S_{ads} because the competitive adsorption is less severe due to the segregated nature of adsorption; the competition faced by CH_4 is less severe than anticipated because of the preferential location of CO_2 in the window regions,. The departures from idealities are quantitatively captured by the RAST with fitted Margules parameters.

In Figure S44, the CBMC simulated values of the adsorption selectivity S_{ads} determined from both campaigns A and B are plotted as function of the surface potential Φ. The CBMC simulated selectivity S_{ads} do not uniquely depend on Φ, as prescribed by IAST. At values of $\Phi > 5$ mol kg^{-1}, the IAST significantly overestimates S_{ads}.

11.2 Water/ethanol mixture adsorption in all-silica DDR zeolite

Two types of water/ethanol mixture adsorption campaigns were conducted.

Campaign A. The bulk fluid phase composition held constant at $y_1 = y_2 = 0.5$, and the bulk fluid phase fugacity $f_t = f_1 + f_2$ was varied over a wide range from the Henry regime of adsorption, $f_t \to 0; \quad \Phi \to 0$, to pore saturation conditions, typically $\Phi > 50$.

Campaign B. The bulk fluid phase fugacity was held at a constant value $f_t = f_1 + f_2 = 10$ kPa, and the bulk fluid phase mixture composition y_1 was varied $0 < y_1 < 1$.

The CBMC data and analysis for Campaign A are presented in Figure S45; the following major characteristics emerge. From Figure S45b we note that for a range of partial fugacities, f_1 in the bulk fluid phase, the component loading for water in the mixture (filled symbols) exceeds that of the pure component. The ethanol/water adsorption selectivity, S_{ads}, determined from CBMC mixture simulations (symbols) has a tendency to undergo selectivity reversal in favor of water at high values of the bulk fluid phase fugacity $f_t = f_1 + f_2$, as saturation conditions are approached; see Figure S45c. The selectivity reversal in favor of the smaller guest molecule, water, is the consequence of entropy effects that favor the guest species with the higher packing efficiency, as explained in earlier works.[45, 52, 53, 60-62] The selectivity reversal phenomena is also anticipated by the IAST model (shown by the dashed line). An important characteristic is that the IAST over-predicts the alcohol/water selectivity at values of $f_t = f_1 + f_2$ lower than that at which selectivity reversal occurs. For values of $f_t = f_1 + f_2$ higher than that at selectivity reversal, the IAST estimates lie below the values determined from CBMC. The conclusion to be drawn is that IAST exaggerates entropy effects. Put another way, hydrogen bonding effects tend to moderate the influence of entropy effects because of molecular clustering attendant with mixture adsorption. As is to be expected the RAST model captures the right trends in the dependence of S_{ads} on $f_t = f_1 + f_2$.

In Figure S45d, we note that the RAST estimates of the component loadings are in reasonably good agreement with CBMC simulated component loadings $q_{1,CBMC}; q_{2,CBMC}$ (filled symbols). This is to be expected because the model parameters are chosen to fit the CBMC simulated component loadings. The success of the RAST model is therefore to be regarded as testimony to the applicability of the Margules model to describe the activity coefficients for mixture adsorption.

The activity coefficients in the adsorbed phase are plotted in Figure S45e,f. Both activity coefficients tend to unity in the Henry regime, as $\gamma_i \rightarrow 1; \quad f_t \rightarrow 0$. The activity coefficient of water, γ_1, displays a minimum when plotted against the total bulk fluid phase fugacity $f_t = f_1 + f_2$. The activity coefficient of alcohol tends to decrease to low values as $f_t = f_1 + f_2$ increases. The activity coefficient of water, γ_1, tends to unity as the adsorbed phase mole fraction $x_1 \rightarrow 1$; it displays a minimum. The activity coefficient of alcohol, γ_2, tends to unity as the adsorbed phase mole fraction $x_2 = (1 - x_1) \rightarrow 1$, decreasing in magnitude as $x_1 \rightarrow 1$.

The CBMC data and analysis for Campaign B are presented in Figure S46; the following characteristics emerge. In Figure S46a, the RAST calculations using the fitted Margules parameters (continuous solid line) of the component loadings are, in agreement with CBMC simulated component loadings $q_{1,CBMC}; q_{2,CBMC}$ (filled symbols) for binary mixture plotted as function of the mole fraction of component 1 in the bulk fluid phase, y_1. In Figure S46b, the adsorption selectivity, S_{ads}, determined from CBMC mixture simulations (symbols) are compared with calculations using the IAST (dashed line) and RAST (continuous solid line). The *x*-axis represents the mole fraction of component 1 in the bulk fluid phase, y_1.The ethanol/water adsorption selectivity experiences a selectivity reversal. The occurrence of selectivity reversal is caused by hydrogen bonding. This selectivity reversal is not anticipated by the IAST.

In Figure S47, the CBMC simulated values of the adsorption selectivity S_{ads} determined from both campaigns A and B are plotted as function of the surface potential Φ. The CBMC simulated selectivity S_{ads} do not uniquely depend on Φ, as prescribed by IAST. At values of $\Phi > 10$ mol kg^{-1}, the IAST significantly underestimates the ethanol/water selectivity due to moderation of entropy effects.

11.3 List of Tables for Binary mixture adsorption in all-silica DDR zeolite

Table S10. Dual-site Langmuir-Freundlich parameters for guest molecules in DDR (all-silica) at 300 K.

	Site A			Site B		
	$q_{A,sat}$ mol kg^{-1}	b_A $Pa^{-\nu A}$	ν_A dimensionless	$q_{B,sat}$ mol kg^{-1}	b_B $Pa^{-\nu B}$	ν_B dimensionless
CO_2	1.5	1.010E-06	0.79	3	6.076E-06	1
CH_4	1.4	4.035E-06	1	1.95	1.814E-06	0.75

Fitted Margules non-ideality parameters for binary CO_2/CH_4 mixture adsorption in DDR at 300 K.

	C / kg mol^{-1}	A_{12}	A_{21}
CO_2/CH_4	0.310	-1.170	-1.235

Table S11. Dual-site Langmuir-Freundlich parameters for pure component water, methanol, and ethanol at 300 K in all-silica DDR zeolite. The fit parameters are based on the CBMC simulations of pure component isotherms presented in earlier work.[21, 47]

	Site A			Site B		
	$q_{A,sat}$ mol kg^{-1}	b_A $\mathrm{Pa}^{-\nu A}$	ν_A	$q_{A,sat}$ mol kg^{-1}	b_A $\mathrm{Pa}^{-\nu A}$	ν_B
water	6.45	2.776E-17	4.3	2.4	1.300E-05	1.06
methanol	1.7	1.186E-04	1.3	1.7	6.055E-04	0.78
ethanol	1.6	9.962E-03	0.88	1.2	9.160E-05	0.66

Fitted Margules non-ideality parameters for binary mixture adsorption in DDR at 300 K. The fits are based on combining CBMC Campaigns A and B

	C / kg mol^{-1}	A_{12}	A_{21}
water/ethanol	1.868	-5.325	-1.665

11.4 List of Figures for Binary mixture adsorption in all-silica DDR zeolite

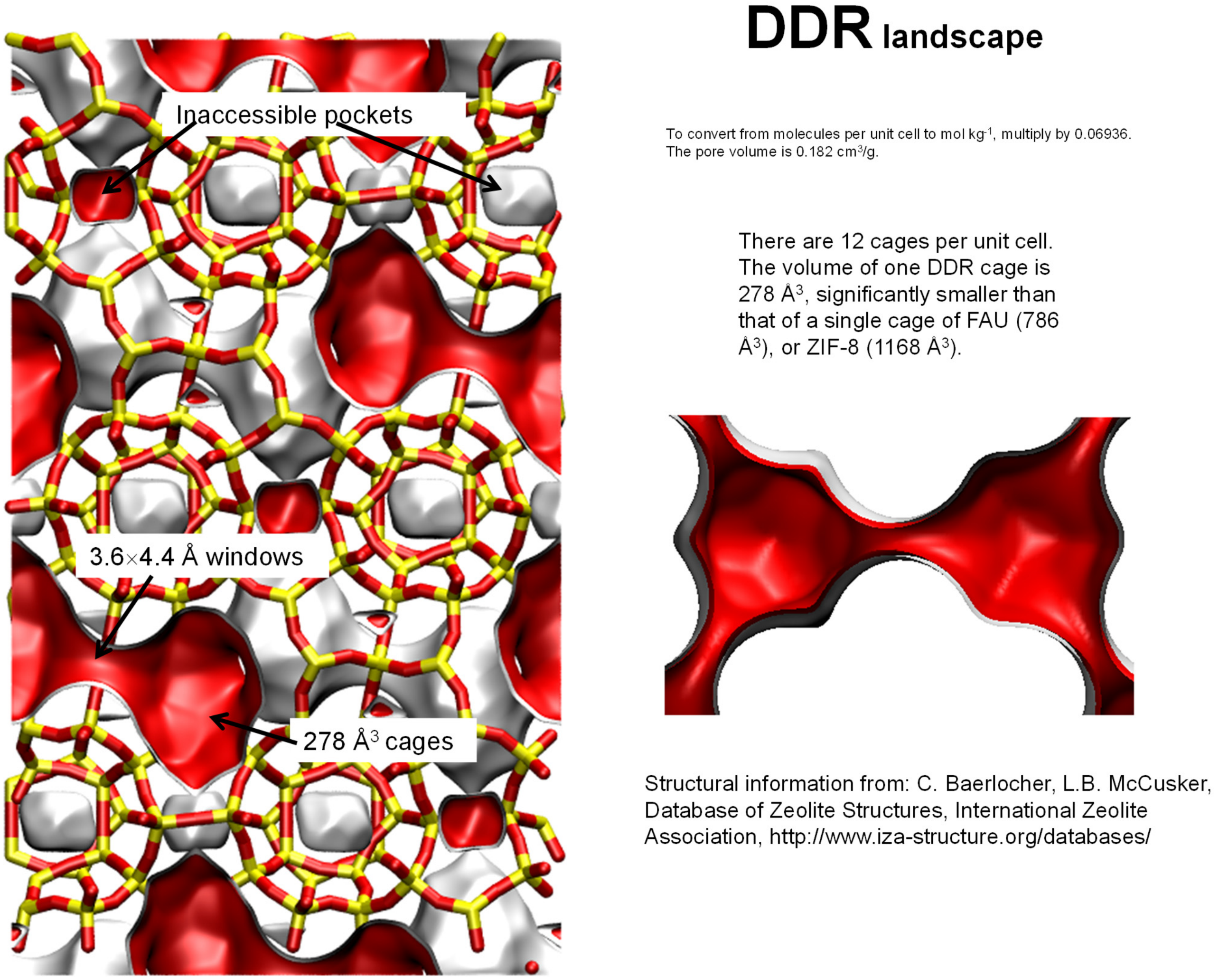

DDR landscape

To convert from molecules per unit cell to mol kg^{-1}, multiply by 0.06936.
The pore volume is 0.182 cm^3/g.

There are 12 cages per unit cell. The volume of one DDR cage is 278 Å^3, significantly smaller than that of a single cage of FAU (786 Å^3), or ZIF-8 (1168 Å^3).

Structural information from: C. Baerlocher, L.B. McCusker, Database of Zeolite Structures, International Zeolite Association, http://www.iza-structure.org/databases/

Figure S39. Pore landscape of all-silica DDR zeolite.

DDR window and pore dimensions

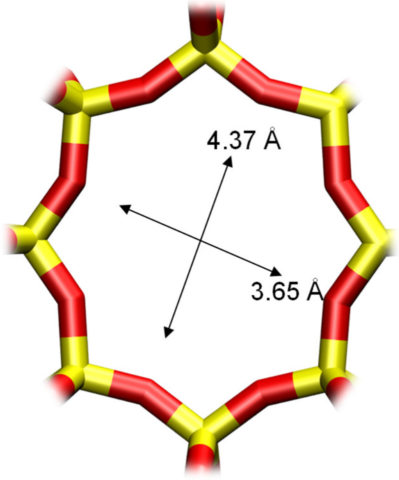

DDR

The window dimensions calculated using the van der Waals diameter of framework atoms = 2.7 Å are indicated above by the arrows.

	DDR
a /Å	24.006
b /Å	13.86
c /Å	40.892
Cell volume / Å^3	13605.72
conversion factor for [molec/uc] to [mol per kg Framework]	0.0693
conversion factor for [molec/uc] to [kmol/m^3]	0.4981
ρ [kg/m3]	1759.991
MW unit cell [g/mol(framework)]	14420.35
ϕ, fractional pore volume	0.245
open space / Å^3/uc	3333.5
Pore volume / cm^3/g	0.139
Surface area /m^2/g	350.0
DeLaunay diameter /Å	3.65

Figure S40. Structural details for DDR zeolite.

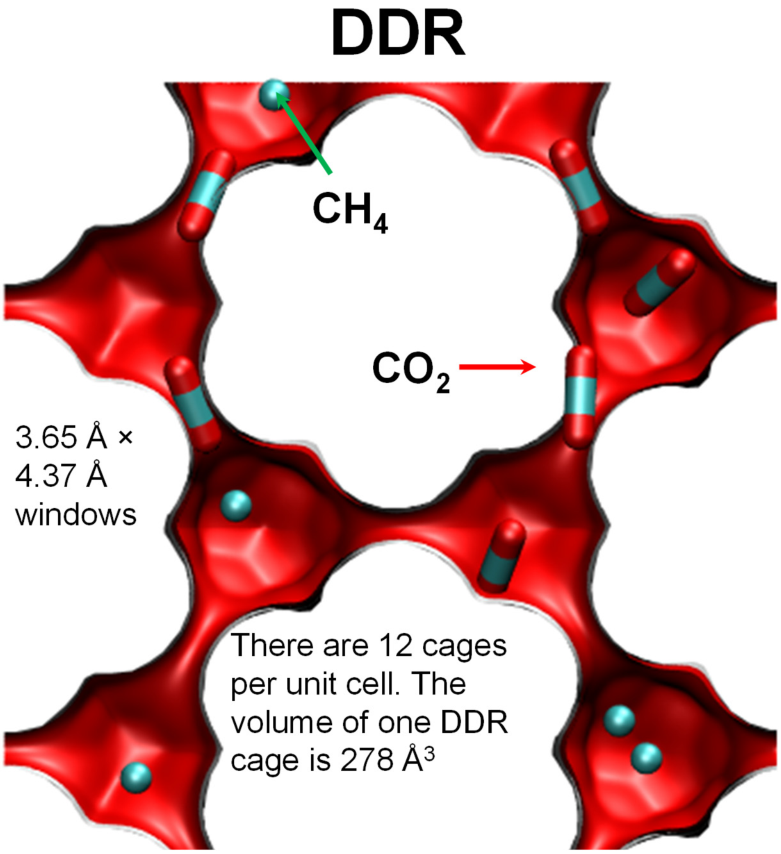

Figure S41. Computational snapshots for CO_2(1)/CH_4(2) mixture adsorption in DDR zeolite at 300 K.

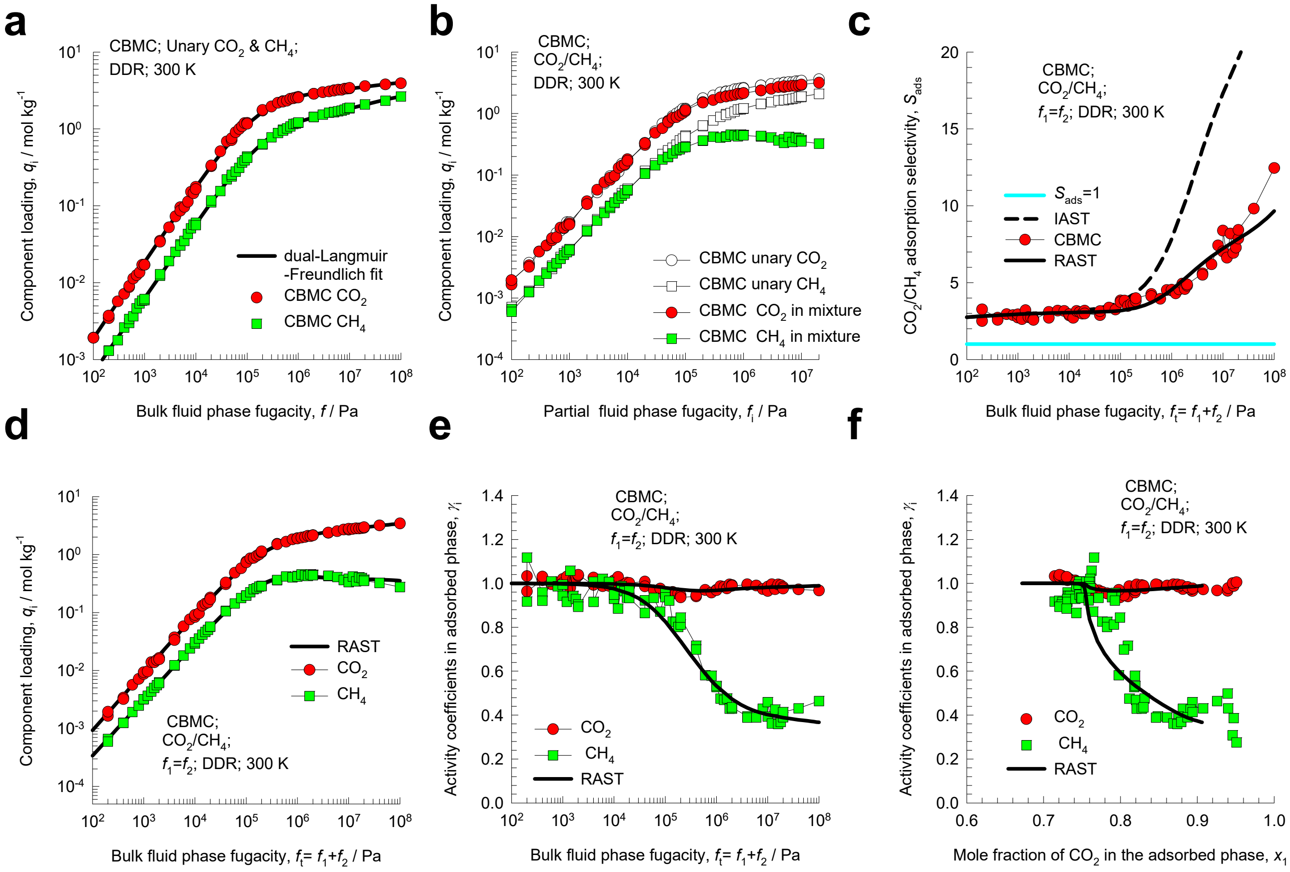

Figure S42. CBMC simulation data and analysis for Campaign A (y_1= 0.5) for CO_2(1)/CH_4(2) mixture adsorption in DDR zeolite at 300 K. (a) Unary isotherms and fits. (b) Component loadings in mixture compared with CBMC simulations of unary isotherms. (c) CBMC data for CO_2(1)/CH_4(2) adsorption selectivity compared with IAST and RAST estimates. (d) CBMC data for component loadings in mixture compared with RAST estimates. (e, f) Activity coefficients from CBMC compared with RAST model calculations. The unary isotherm data fits and Wilson parameters are provided in Table S10.

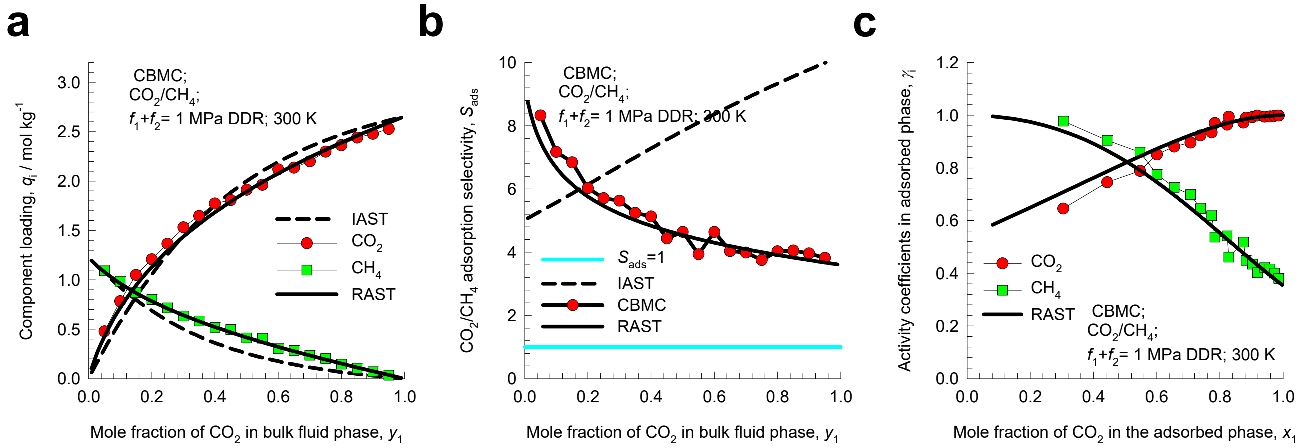

Figure S43. CBMC simulation data and analysis for Campaign B (f_t = 1 MPa) for CO$_2$(1)/CH$_4$(2) mixture adsorption in DDR zeolite at 300 K. CBMC data for (a) component loadings and (b) CO$_2$(1)/CH$_4$(2) adsorption selectivity compared with IAST and RAST estimates. (c) Activity coefficients from CBMC compared with RAST model calculations. The unary isotherm data fits and Wilson parameters are provided in Table S10.

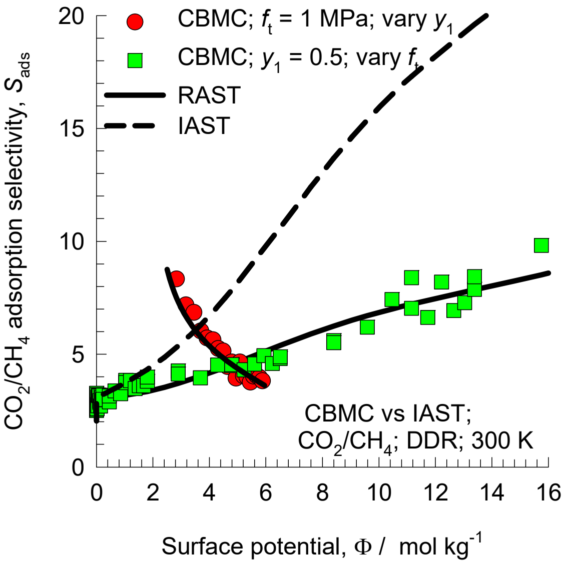

Figure S44. Adsorption selectivity S_{ads} for CO_2(1)/CH_4(2) mixture adsorption in DDR zeolite at 300 K, for two different campaigns (Campaign A (y_1= 0.5) and Campaign B (f_t = 1 MPa), plotted as function of the surface potential Φ. The CBMC simulated values (indicated by symbols) are compared with RAST (continuous solid lines), and IAST (dashed lines) estimates. The unary isotherm data fits and Wilson parameters are provided in Table S10.

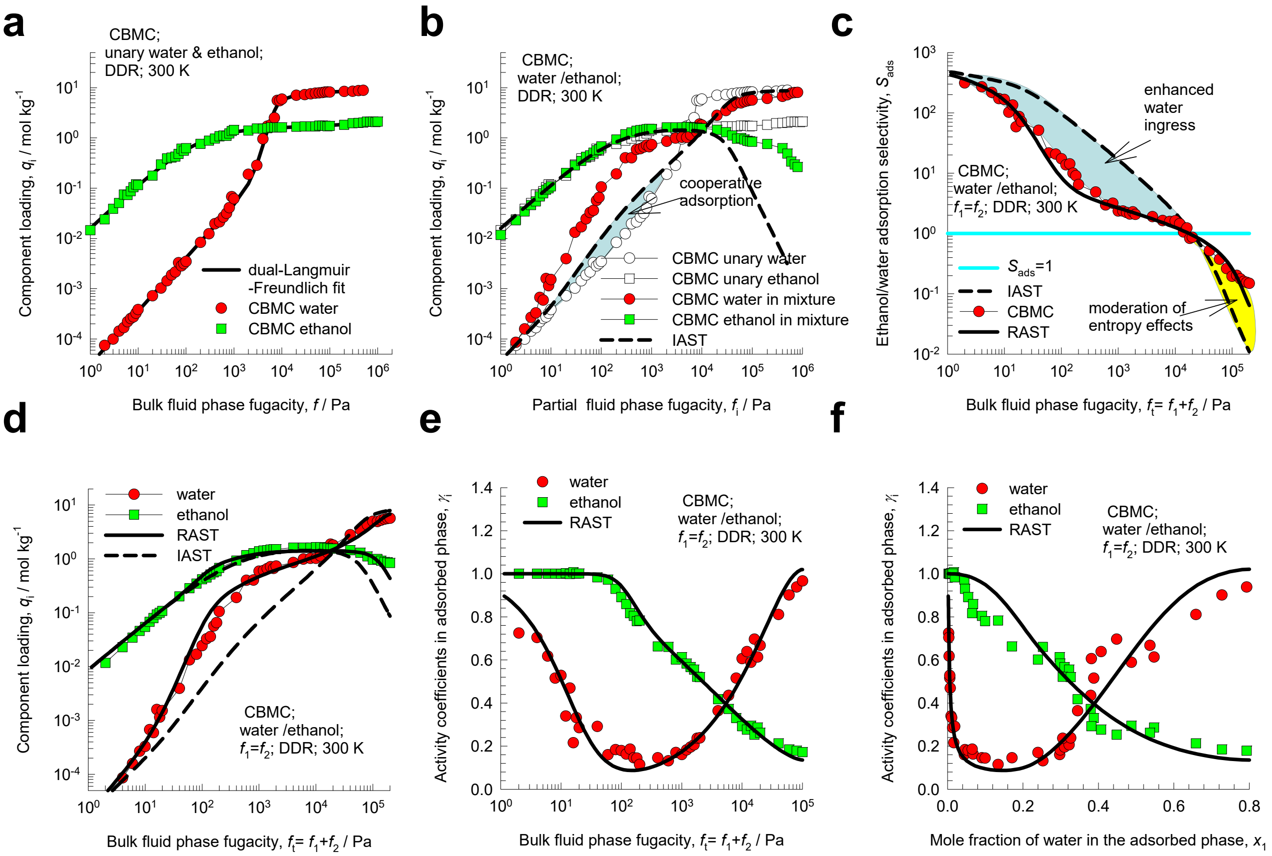

Figure S45. CBMC simulation data and analysis for Campaign A (y_1= 0.5) for water/ethanol mixture in DDR at 300 K. (a) Unary isotherms and fits. (b) Component loadings in mixture compared with CBMC simulations of unary isotherms. (c) CBMC data for alcohol/water selectivity compared with IAST and RAST estimates. (d) CBMC data for component loadings in mixture compared with RAST estimates. (e, f) Activity coefficients from CBMC compared with RAST model calculations. The unary isotherm data fits and Margules parameters are provided in Table S11.

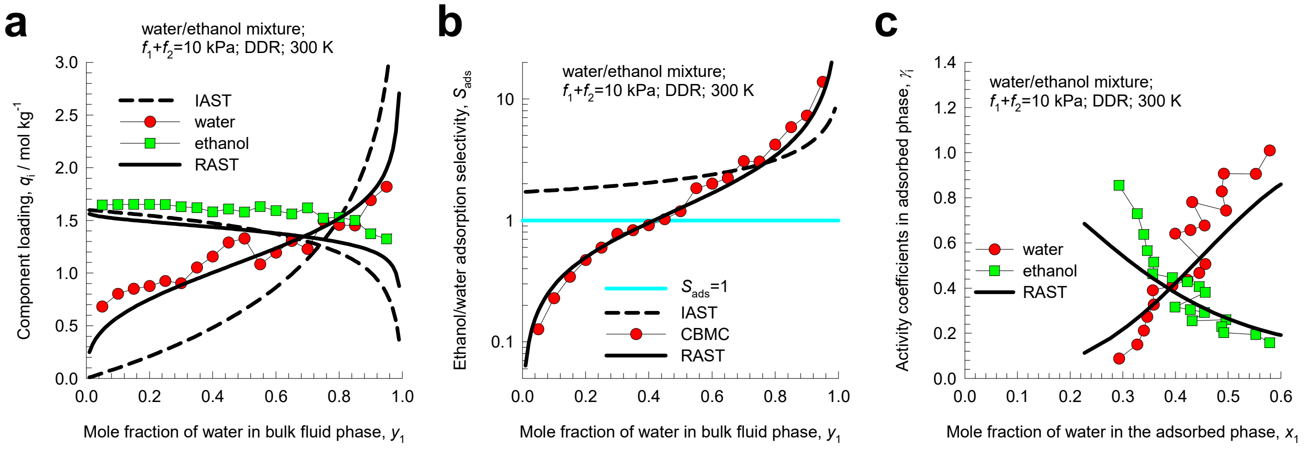

Figure S46. CBMC simulation data and analysis for Campaign B (f_t = 10 kPa) for water/ethanol mixture in DDR at 300 K. CBMC data on (a) component loadings, and (b) alcohol/water selectivity compared with IAST and RAST estimates. (c) Activity coefficients from CBMC compared with RAST model calculations. The unary isotherm data fits and Margules parameters are provided in Table S11.

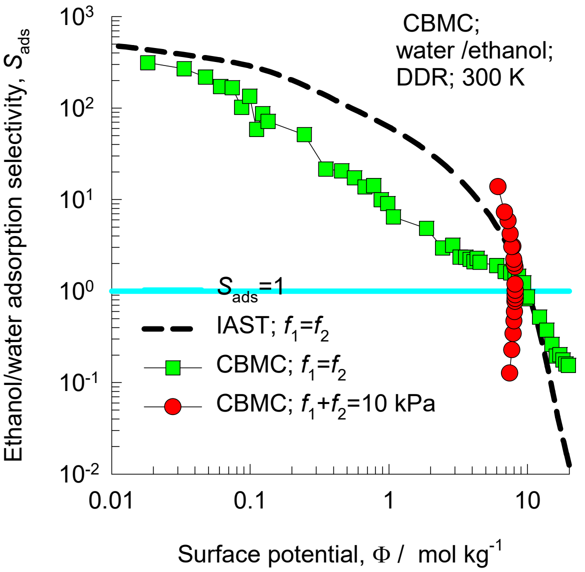

Figure S47. Adsorption selectivity S_{ads} for water/ethanol mixture in DDR at 300 K for two different campaigns (Campaign A (y_1= 0.5) and Campaign B (f_t = 10 kPa), plotted as function of the surface potential Φ. The CBMC simulated values (indicated by symbols) are compared with IAST estimates (indicated by the dashed lines). The unary isotherm data fits and Margules parameters are provided in Table S11.

12 Binary mixture adsorption in all-silica MOR zeolite

MOR zeolite (Mordenite) consists of 12-ring (7.0 Å × 6.5 Å) 1D channels, connected to 8-ring (5.7 Å × 2.6 Å) pockets; the pore landscapes and structural details are provided in Figure S48, and Figure S49.

12.1 CO_2/CH_4 mixture adsorption in all-silica MOR zeolite

Computational snapshots of the location of molecules for CO_2/CH_4 mixture adsorption show that CO_2 get preferentially ensconced in the side-pockets; see Figure S50a. The CH_4 molecules can also occupy the side pockets, but their preferred locations are the 12-ring channels. The RDF data in Figure S50b confirms the distances of CO_2-CH_4 pairs are significantly higher than for CH_4-CH_4 pairs.

Figure S51 presents CBMC simulation data for adsorption of equimolar (partial fugacities f_1=f_2) CO_2/CH_4 mixtures in MOR zeolite at 300 K. The conventional IAST calculation assumes that CH_4 molecules compete with *all* of the CO_2, making no allowance for segregation. We note that the IAST under-predicts the loading of the more weakly adsorbed CH_4 in the CO_2/CH_4 mixture. The conventional IAST calculation assumes that CH_4 molecules compete with *all* of the CO_2, making no allowance for segregation. Due to segregation effects the competition faced by CH_4 molecules within the 12-ring channels, where they almost exclusively reside, is *smaller* than that in the entire pore space. The IAST anticipates a stiffer competition between CO_2 and CH_4 as it assumes a uniform distribution of composition; consequently the separation selectivity is *over*estimated. Figure S51c compares CO_2/CH_4 adsorption selectivities obtained from CBMC with IAST and RAST estimations.

The estimations of the RAST with fitted Wilson parameters, are shown by the continuous solid lines. Figure S51d presents a comparison of the estimations using the RAST with CBMC simulations of component loadings of equimolar (partial fugacities f_1=f_2) CO_2/CH_4 mixtures in MOR zeolite at 300 K.

Figure S51e,f shows RAST calculations of the component activity coefficients γ_i, for CO_2 and CH_4.

12.2 CO_2/C_3H_8 mixture adsorption in all-silica MOR zeolite

For $CO_2(1)$/$C_3H_8(2)$ mixture adsorption in all-silica MOR zeolite at 300 K, the computational snapshots for partial fugacities $f_1 = f_2 = 20$ kPa are shown in Figure S52. CO_2 get preferentially ensconced in the side-pockets, but when the side pockets are fully occupied the CO_2 can also locate in the 12-ring 1D channels. The C_3H_8 molecules are unable to occupy the side pockets, but their preferred locations are the 12-ring channels.

Figure S53, and Figure S54 present the CBMC data and analysis for two different campaigns. In Campaign A the ratio of partial fugacities $f_1/f_2 = 15/85$ and the bulk mixture fugacity, $f_t = f_1 + f_2$ is varied. In Campaign B in which total fugacity is held constant at the value $f_t = 40$ kPa and the bulk fluid phase mixture composition $y_1 = f_1/f_t$ is varied.

The unary isotherm data are shown in Figure S53a. In the Henry regime, the adsorption strengths are nearly equal. CO_2 has a significantly higher saturation capacity, and therefore entropy effects favor the adsorption of CO_2 at high pore occupancies. The CBMC data for Campaign A shows that the $CO_2(1)$/$C_3H_8(2)$ adsorption selectivity S_{ads} increases significantly with increasing values of $f_t = f_1 + f_2$. Due to the segregated nature of adsorption, the IAST overestimates the S_{ads} for $f_t > 0.5$ MPa. Interesting, the IAST underestimates the S_{ads} for $f_t < 0.5$ MPa.

The results for Campaign B are even more interesting; see Figure S54. For $y_1 = f_1/f_t < 0.6$, $S_{ads} > 1$, and the selectivity is in favor of CO_2. The CBMC simulations show that the adsorption selectivity S_{ads} is increasingly lowered below unity, i.e. in favor of the alkane, with increasing proportion of $CO_2(1)$ in the bulk gas phase; see Figure S54b. The IAST anticipates S_{ads} to be virtually independent of y_1. The conventional IAST calculation assumes that C_3H_8 molecules compete with *all* of the CO_2, making no allowance for segregation. Due to segregation effects the competition faced by C_3H_8 molecules within the 12-ring channels, where C_3H_8 exclusively reside, is *smaller* than that in the entire pore space. The IAST anticipates a stiffer competition between CO_2 and C_3H_8 as it assumes a uniform distribution of composition; consequently, the separation selectivity is *over*estimated to a significant extent.

In Figure S55 the adsorption selectivity S_{ads} is plotted as a function of the surface potential Φ. The dashed lines are the IAST calculations. With increasing values of Φ, as pore saturation conditions are approached, the IAST severely overestimates the S_{ads}. Segregation effects have the influence of moderating the influence of entropy effects that favor CO_2 that has the higher saturation capacity.

12.3 List of Tables for Binary mixture adsorption in all-silica MOR zeolite

Table S12. Dual-site Langmuir parameters for CO_2, CH_4, and C_3H_8 at 300 K in all-silica MOR zeolite. The fit parameters are based on the CBMC simulations of pure component isotherms presented in earlier works.[11, 63]

	Site A			Site B		
	$q_{A,sat}$ mol kg^{-1}	b_A Pa $^{-\nu_A}$	ν_A dimensionless	$q_{B,sat}$ mol kg^{-1}	b_B Pa $^{-\nu_B}$	ν_B dimensionless
CO_2	1.4	4.865E-04	1	4.65	1.234E-06	1
CH_4	1.05	1.587E-08	1	2.8	2.391E-06	1
C_3H_8	0.18	2.112E-06	1	1	3.551E-04	1

Fitted Margules non-ideality parameters for binary mixture adsorption in MOR at 300 K.

	C / kg mol^{-1}	A_{12}	A_{21}
CO_2/CH_4 in MOR	0.37	-1.90	-1.31
CO_2/C_3H_8 in MOR	0.13	-15.91	-14.99

12.4 List of Figures for Binary mixture adsorption in all-silica MOR zeolite

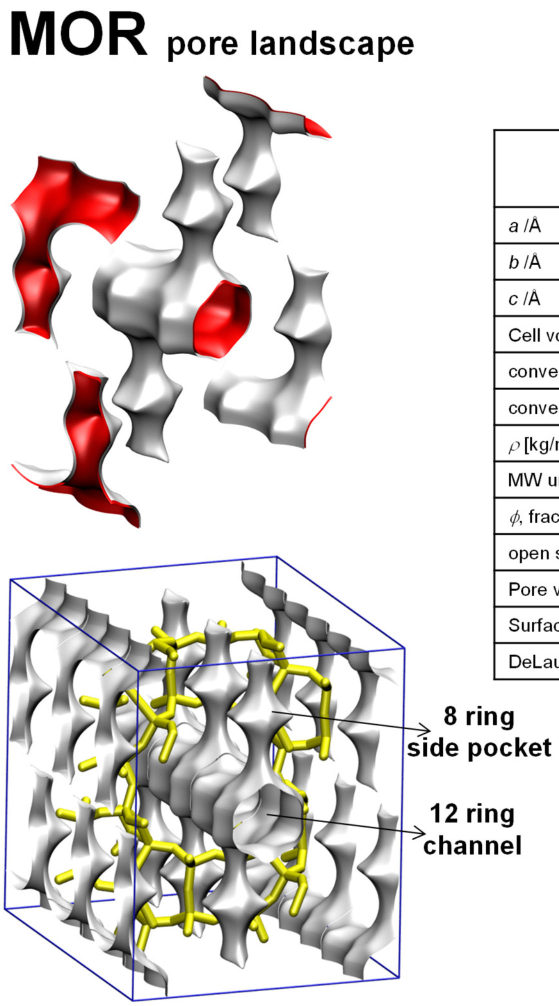

	MOR
a /Å	18.094
b /Å	20.516
c /Å	7.524
Cell volume / Å^3	2793.033
conversion factor for [molec/uc] to [mol per kg Framework]	0.3467
conversion factor for [molec/uc] to [kmol/m^3]	2.0877
ρ [kg/m3]	1714.691
MW unit cell [g/mol(framework)]	2884.07
ϕ, fractional pore volume	0.285
open space / Å^3/uc	795.4
Pore volume / cm^3/g	0.166
Surface area /m^2/g	417.0
DeLaunay diameter /Å	6.44

Figure S48. Pore landscape of all-silica MOR zeolite.

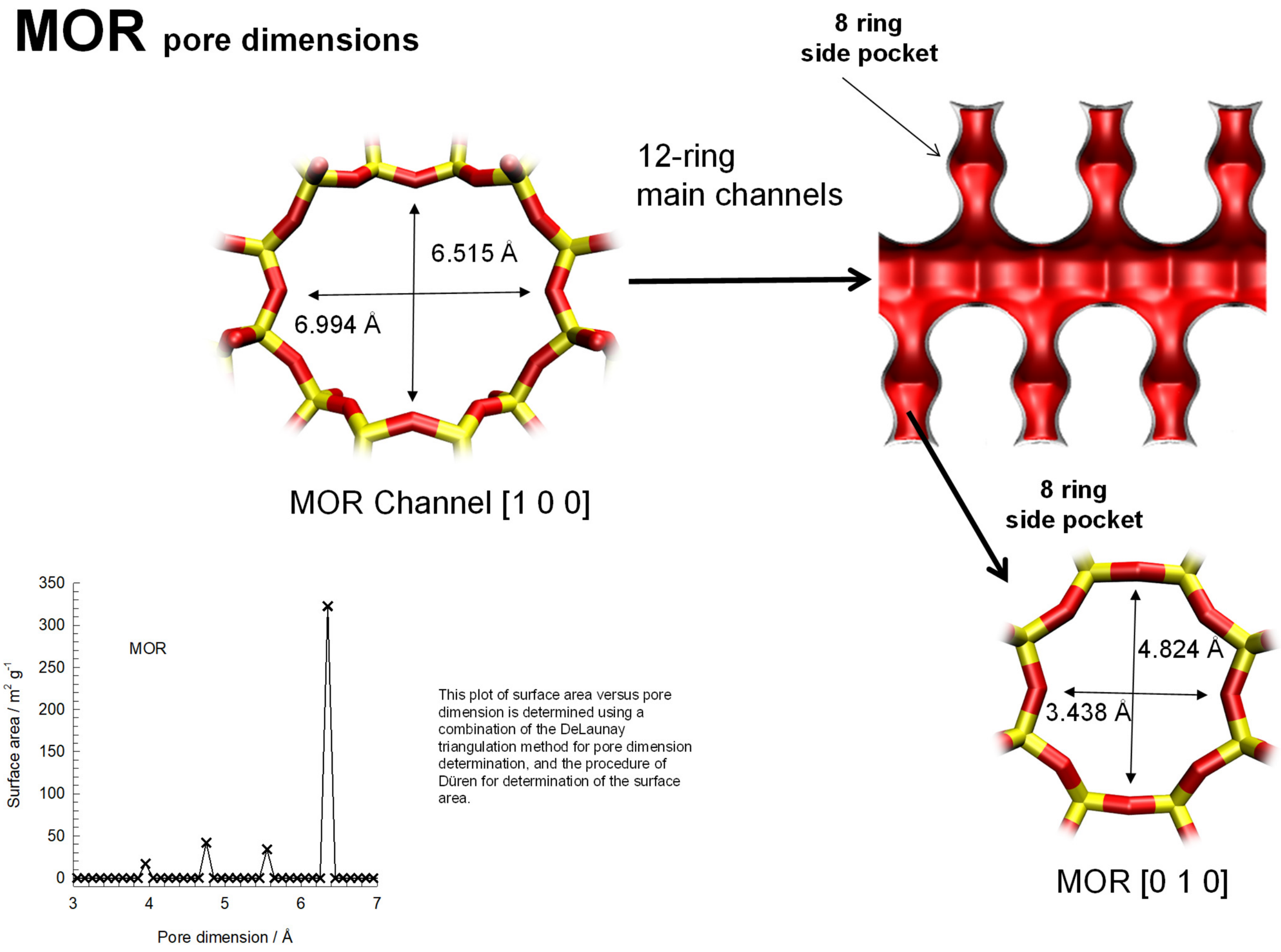

This plot of surface area versus pore dimension is determined using a combination of the DeLaunay triangulation method for pore dimension determination, and the procedure of Düren for determination of the surface area.

Figure S49. Structural details for MOR zeolite.

Binary mixture adsorption in all-silica MOR zeolite

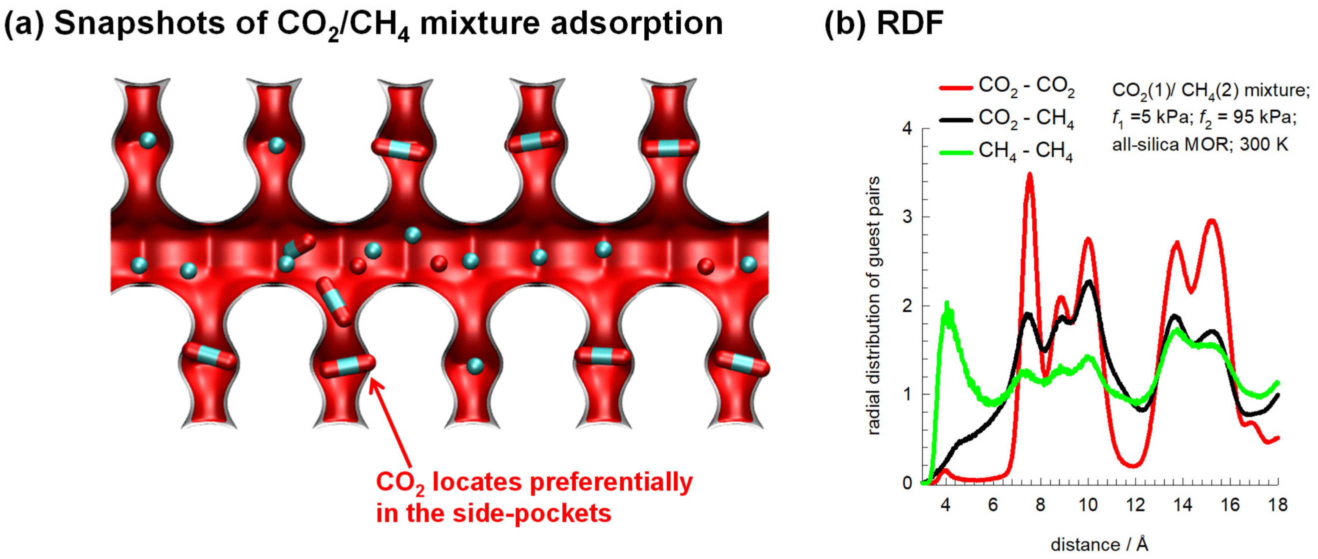

Figure S50. (a) Snapshots showing the location of guest molecules for $CO_2(1)/CH_4(2)$ mixture adsorption in MOR zeolite at 300 K. (b) RDF for $CO_2(1)/CH_4(2)$ mixture adsorption in MOR zeolite at 300 K

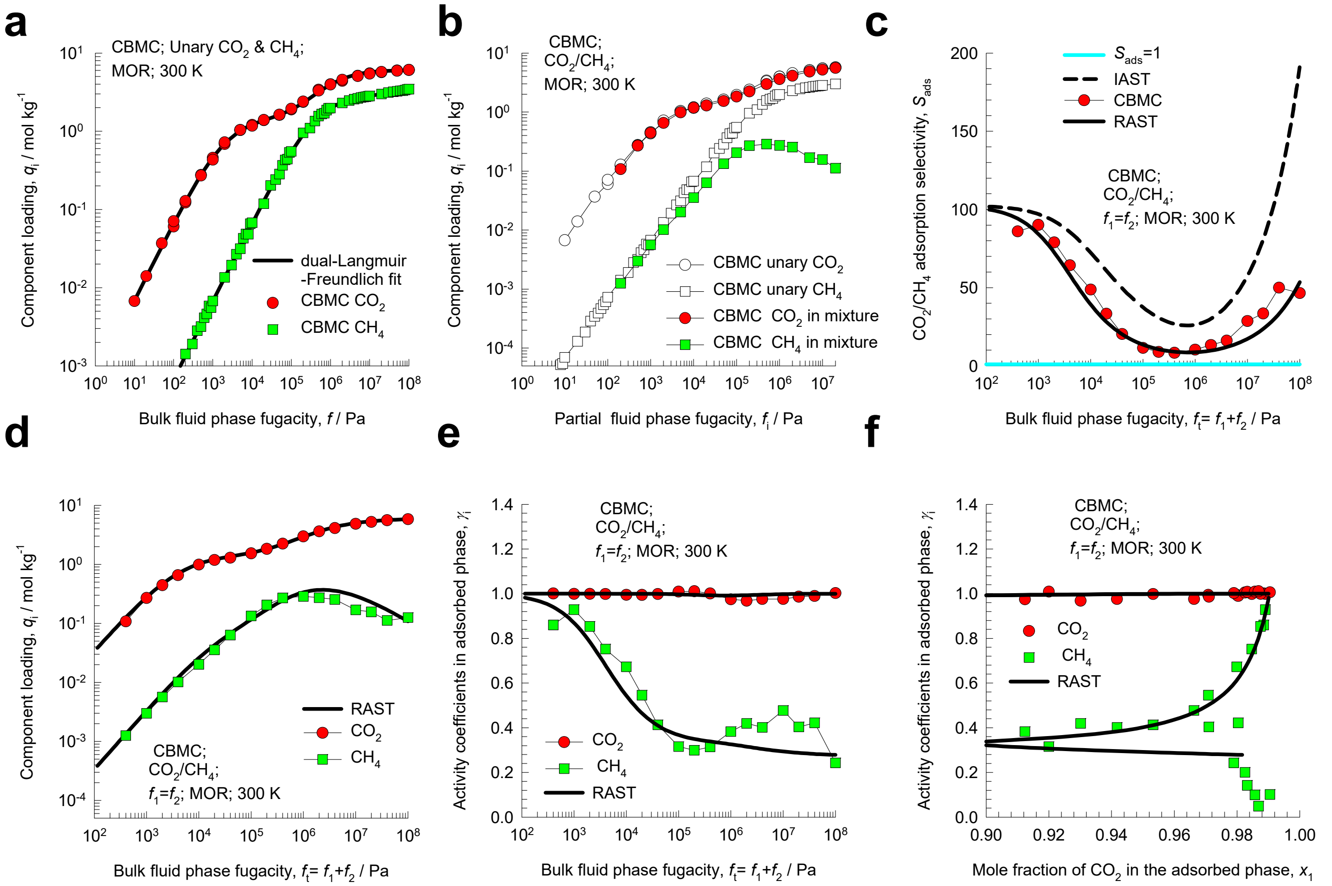

Figure S51. CBMC simulation data and analysis for Campaign A (y_1= 0.5) for CO$_2$(1)/CH$_4$(2) mixture adsorption in MOR zeolite at 300 K. (a) Unary isotherms and fits. (b) Component loadings in mixture compared with CBMC simulations of unary isotherms. (c) CBMC data for CO$_2$(1)/CH$_4$(2) adsorption selectivity compared with IAST and RAST estimates. (d) CBMC data for component loadings in mixture compared with RAST estimates. (e, f) Activity coefficients from CBMC compared with RAST model calculations. The unary isotherm fit parameters and Margules parameters are provided in Table S12.

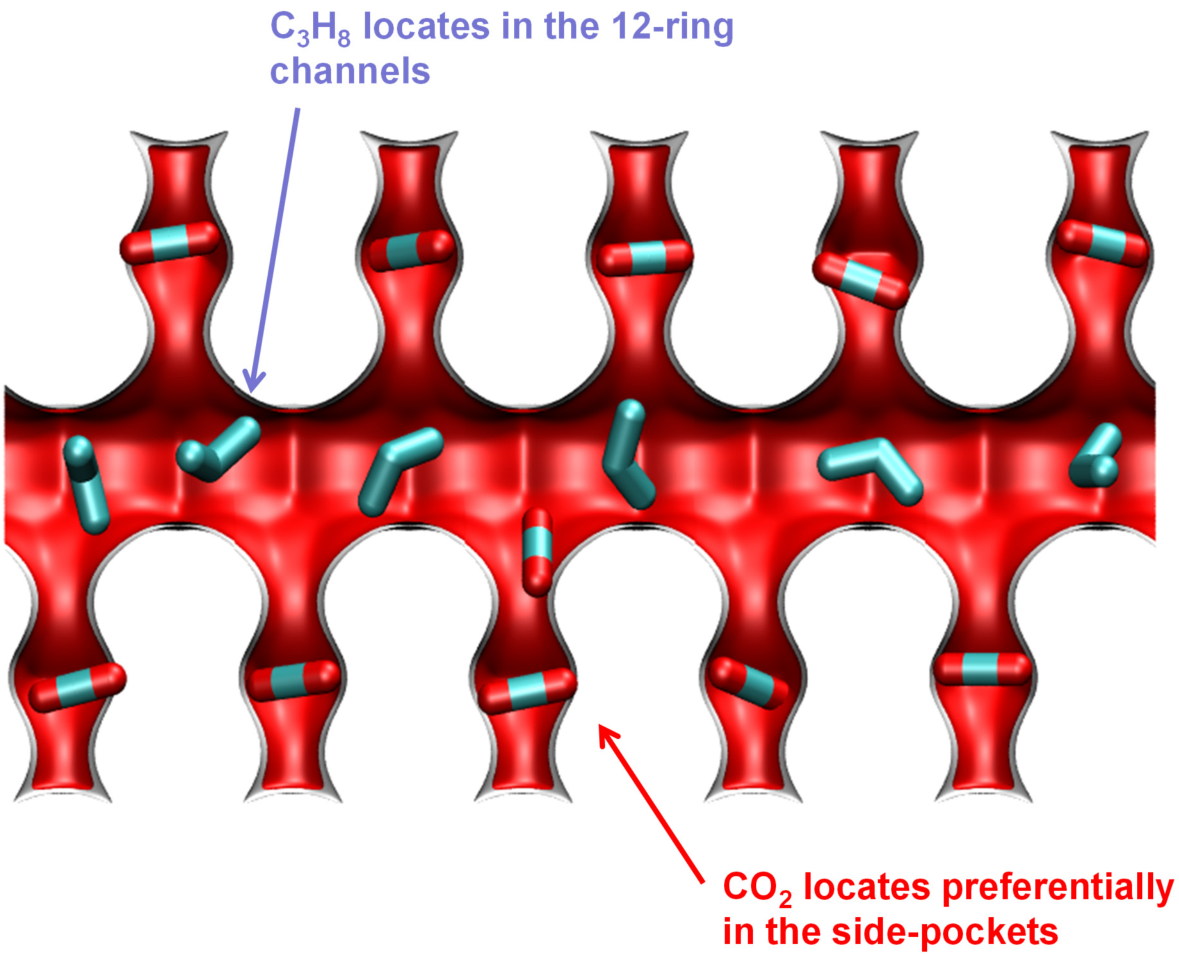

Figure S52. Snapshots showing the location of guest molecules for $CO_2(1)/C_3H_8(2)$ mixture adsorption in MOR zeolite at 300 K.

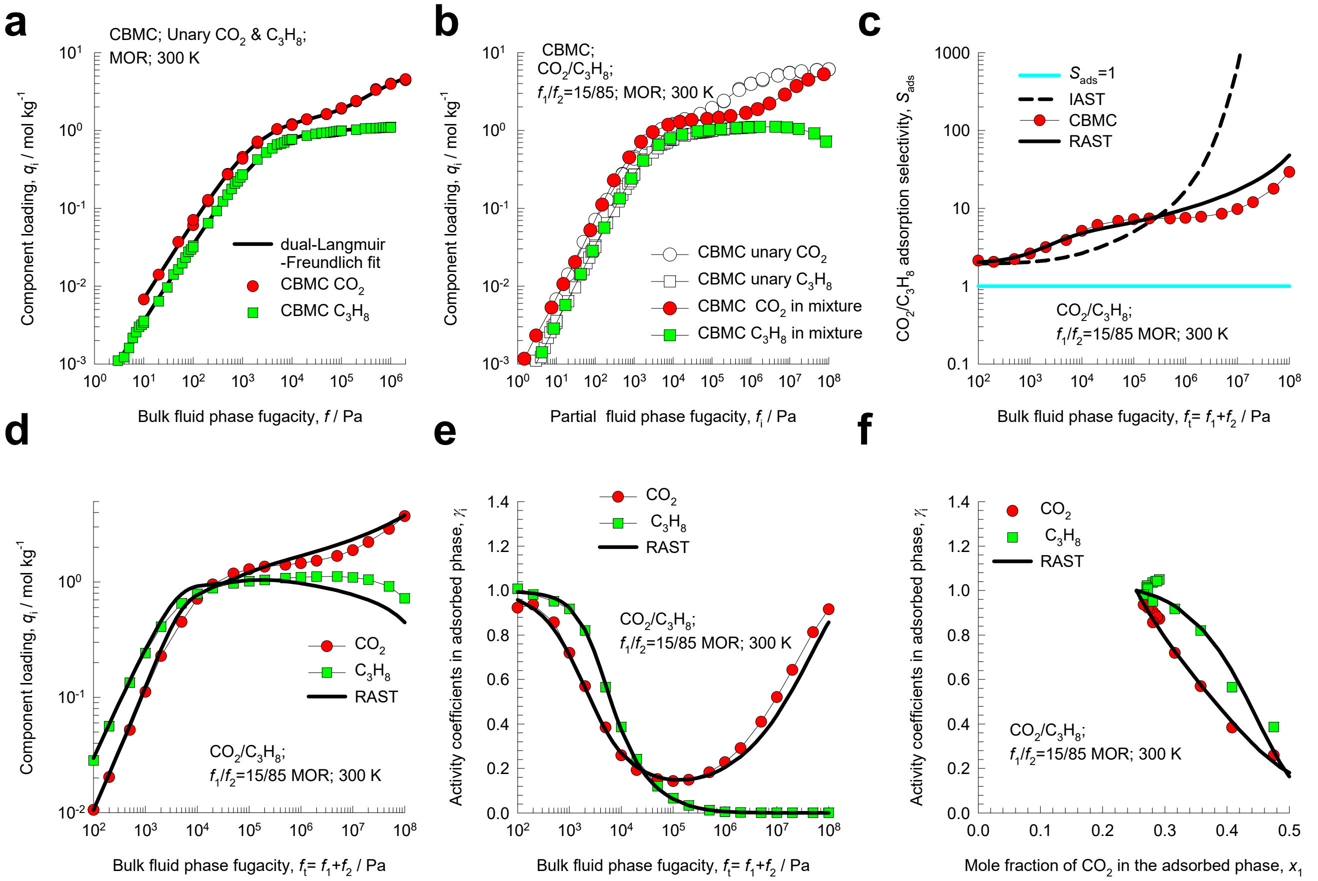

Figure S53. CBMC simulation data and analysis for Campaign A (y_1= 0.15) for CO$_2$(1)/C$_3$H$_8$(2) mixture adsorption in MOR zeolite at 300 K. (a) Unary isotherms and fits. (b) Component loadings in mixture compared with CBMC simulations of unary isotherms. (c) CBMC data for CO$_2$(1)/C$_3$H$_8$(2) adsorption selectivity compared with IAST and RAST estimates. (d) CBMC data for component loadings in mixture compared with RAST estimates. (e, f) Activity coefficients from CBMC compared with RAST model calculations. The unary isotherm fit parameters and Margules parameters are provided in Table S12.

Binary mixture adsorption in all-silica MOR zeolite

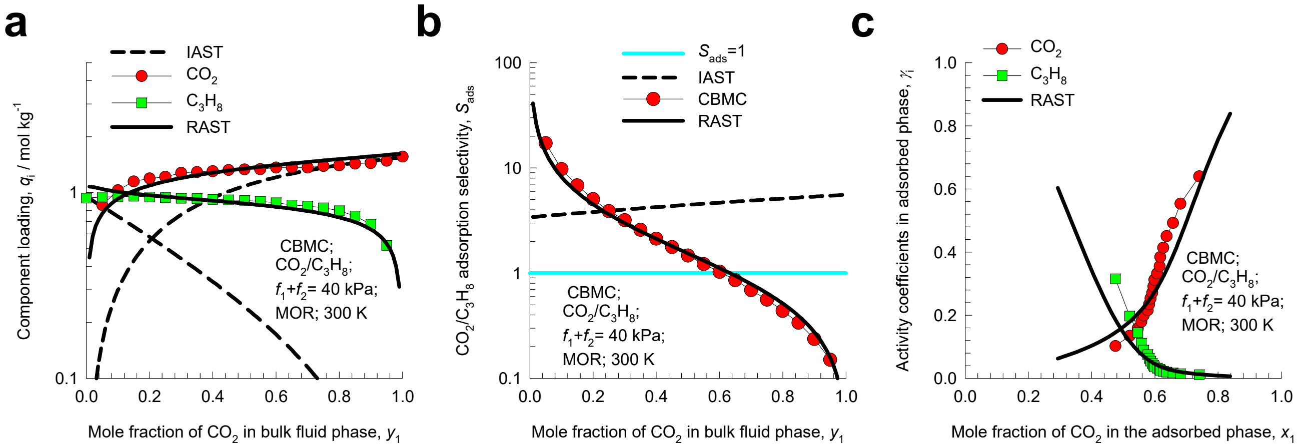

Figure S54. CBMC simulation data and analysis for Campaign B (f_t = 40 kPa) for CO_2(1)/C_3H_8(2) mixture adsorption in MOR zeolite at 300 K. CBMC data for (a) component loadings and (b) CO_2(1)/ C_3H_8(2) adsorption selectivity compared with IAST and RAST estimates. (c) Activity coefficients from CBMC compared with RAST model calculations. The unary isotherm fit parameters and Margules parameters are provided in Table S12.

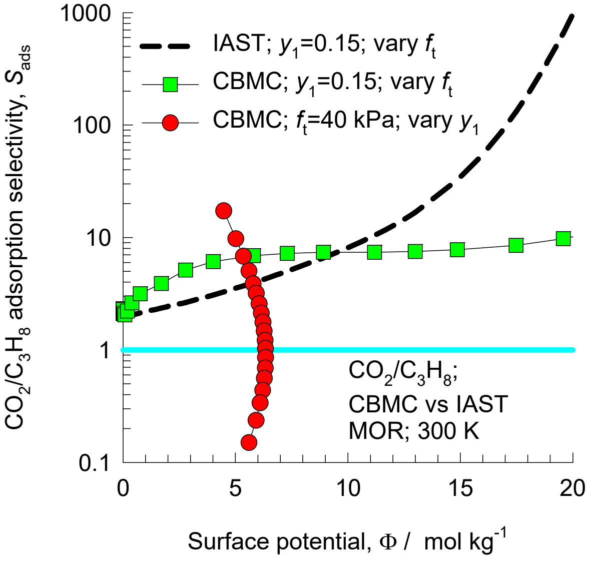

Figure S55. Adsorption selectivity S_{ads} for CO$_2$(1)/C$_3$H$_8$(2) mixture adsorption in MOR zeolite at 300 K for two different campaigns (Campaign A (y_1= 0.5) and Campaign B (f_t = 40 kPa), plotted as function of the surface potential Φ. The CBMC simulated values (indicated by symbols) are compared with IAST estimates (indicated by the dashed lines). The unary isotherm fit parameters and Margules parameters are provided in Table S12.

13 CO_2/CH_4 adsorption in AFX and JBW zeolites

The pore landscapes and structural details of AFX zeolite are presented in Figure S56, and Figure S57. In one unit cell of AFX there are four 490 Å^3 size cages, connected to four small pockets each of 98 Å^3. The 8-ring windows separating two cages are 3.44 Å × 3.88 Å in size. Guests such as CH_4, N_2, or H_2 do not prefer to locate at the window regions, and are preferentially located within the cages. The window regions and the small pockets are preferred locations for CO_2;[11, 59, 63, 64] the pockets can be viewed as providing an "egg-carton" structure. Figure S58a shows snapshots for adsorption of binary mixture of CO_2 and CH_4. Since there are 12 windows per unit cell of AFX, the adsorption selectivity for CO_2 is exceptionally high. Due to the slow diffusion of CO_2 it is likely that that the CO_2 ensconced in the pockets are practically stagnant, and the high selectivities predicted by CBMC simulations may not be realizable in practice. The RDF data in Figure S58b confirms that the distance between CO_2 and CH_4 pairs is larger than for the CH_4 and CH_4 pairs.

Figure S59 presents CBMC simulation data for adsorption of equimolar (partial fugacities f_1=f_2) CO_2/CH_4 mixtures in AFX zeolite at 300 K. The conventional IAST calculation assumes that CH_4 molecules compete with *all* of the CO_2, making no allowance for segregation. Due to segregation effects the competition faced by CH_4 molecules within the cages, where they almost exclusively reside, is *smaller* than that in the entire pore space. The IAST anticipates a stiffer competition between CO_2 and CH_4 as it assumes a uniform distribution of composition; consequently, the adsorption selectivity is *over*estimated. The estimations of the RAST with fitted Wilson parameters, are shown by the continuous solid lines.

JBW has one-dimensional 8-ring channel structures of about 3.7 Å size; see structural details and pore landscapes in Figure S60, and Figure S61. Interestingly, JBW has the low values of pore volume and surface area. The channel topologies are such that CO_2 can nestle nicely in each channel segment; see computational snapshots in Figure S62. The curvature and size of the channels are energetically optimum for location of CO_2 molecules. CH_4 molecules are too severely constrained in the channel segments and can only occupy the more spacious vertex regions. Due to the segregated nature of the adsorption of CO_2

and CH_4 molecules, the competition endured by CH_4 molecules is less severe than anticipated on the basis of the IAST prescription.

Figure S63 presents CBMC simulation data for adsorption of equimolar (partial fugacities $f_1=f_2$) CO_2/CH_4 mixtures in JBW zeolite at 300 K. The conventional IAST calculation assumes that CH_4 molecules compete with *all* of the CO_2, making no allowance for segregation. Due to segregation effects the competition faced by CH_4 molecules that locates preferentially at the vertices is *reduced.* The IAST anticipates a stiffer competition between CO_2 and CH_4 as it assumes a uniform distribution of composition; consequently, the adsorption selectivity is *over*estimated.

Figure S64 compares the CO_2/CH_4 mixture adsorption selectivity for MOR, JBW, and AFX zeolites. In all cases, the IAST tends to overestimate the selectivities due to segregated nature of adsorption.

13.1 List of Tables for CO2/CH4 adsorption in AFX and JBW zeolites

Table S13. Dual-site Langmuir-Freundlich parameters for guest molecules in AFX (all-silica) at 300 K.

	Site A			Site B		
	$q_{A,sat}$ mol kg^{-1}	b_A $\mathrm{Pa}^{-\nu A}$	ν_A dimensionless	$q_{B,sat}$ mol kg^{-1}	b_B $\mathrm{Pa}^{-\nu B}$	ν_B dimensionless
CO_2	3	1.070E-05	0.78	6.4	7.954E-05	0.92
CH_4	2.9	1.761E-08	1	3.1	1.235E-06	1

Fitted Wilson non-ideality parameters for binary CO_2/CH_4 mixture adsorption in AFX at 300 K.

	C / kg mol^{-1}	Λ_{12}	Λ_{21}
CO_2/CH_4	0.18	3.05	0.33

Table S14. Langmuir parameters for guest molecules in JBW (all-silica) at 300 K.

	Site A		
	$q_{A,sat}$ mol kg^{-1}	b_A $\mathrm{Pa}^{-\nu A}$	ν_A dimensionless
CO_2	2.8	6.937E-05	1
CH_4	2.6	1.2E-07	1

13.2 List of Figures for CO2/CH4 adsorption in AFX and JBW zeolites

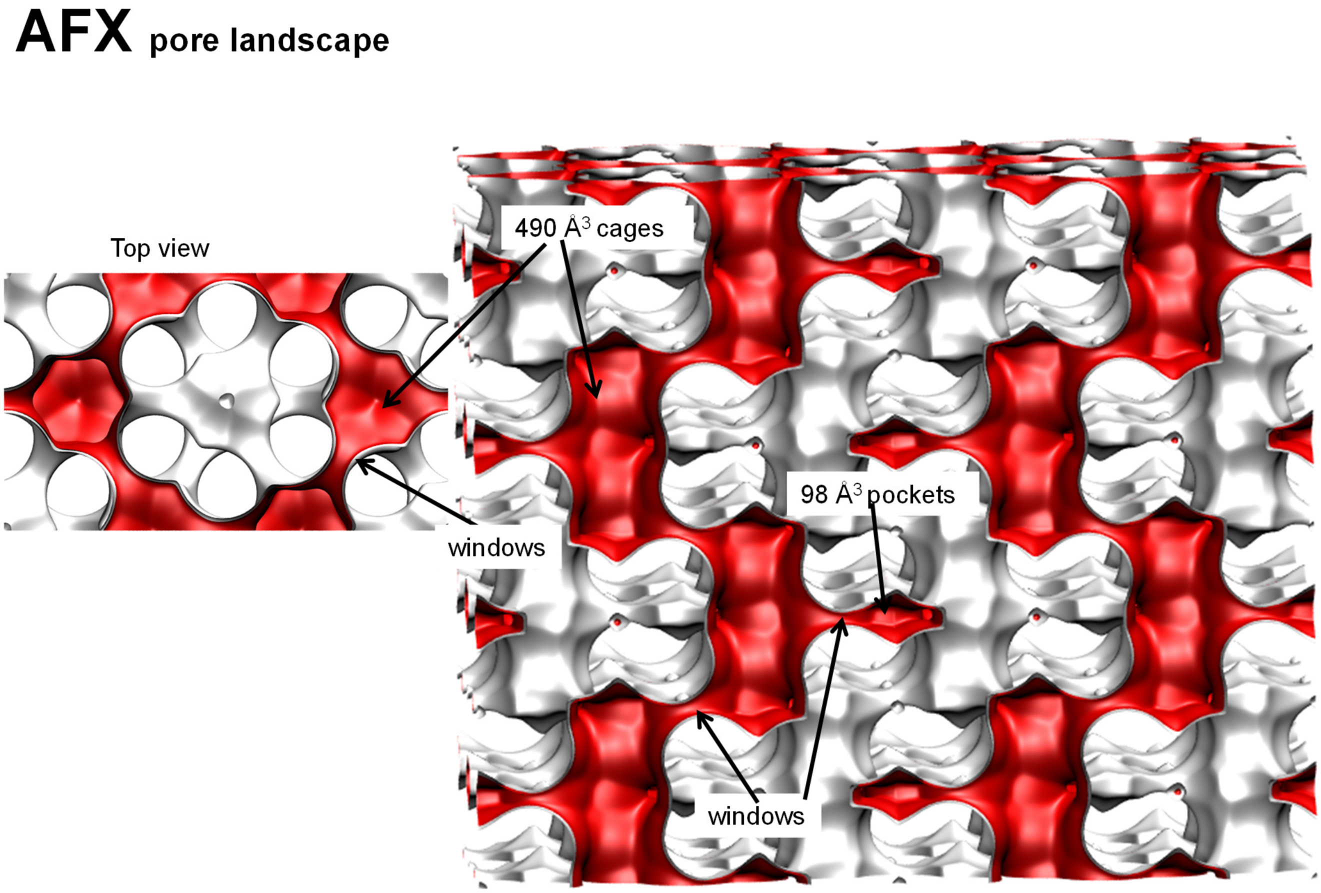

Structural information from: C. Baerlocher, L.B. McCusker, Database of Zeolite Structures, International Zeolite Association, http://www.iza-structure.org/databases/

Figure S56. Pore landscape of all-silica AFX zeolite.

AFX window sizes and pore dimensions

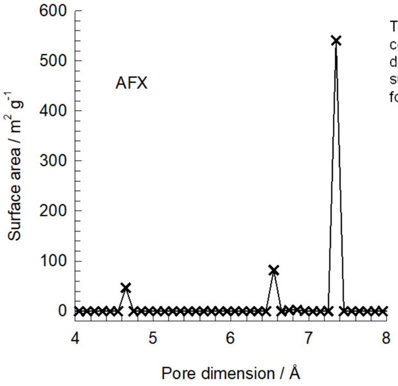

This plot of surface area versus pore dimension is determined using a combination of the DeLaunay triangulation method for pore dimension determination, and the procedure of Düren for determination of the surface area. The computational details will be described in detail in a forthcoming publication.

	AFX
a /Å	23.836
b /Å	13.762
c /Å	19.949
Cell volume / Å^3	6543.891
conversion factor for [molec/uc] to [mol per kg Framework]	0.1734
conversion factor for [molec/uc] to [kmol/m^3]	0.7059
ρ [kg/m3]	1463.713
MW unit cell [g/mol(framework)]	5768.141
ϕ, fractional pore volume	0.359
open space / Å^3/uc	2352.5
Pore volume / cm^3/g	0.246
Surface area /m^2/g	674.0
DeLaunay diameter /Å	3.44

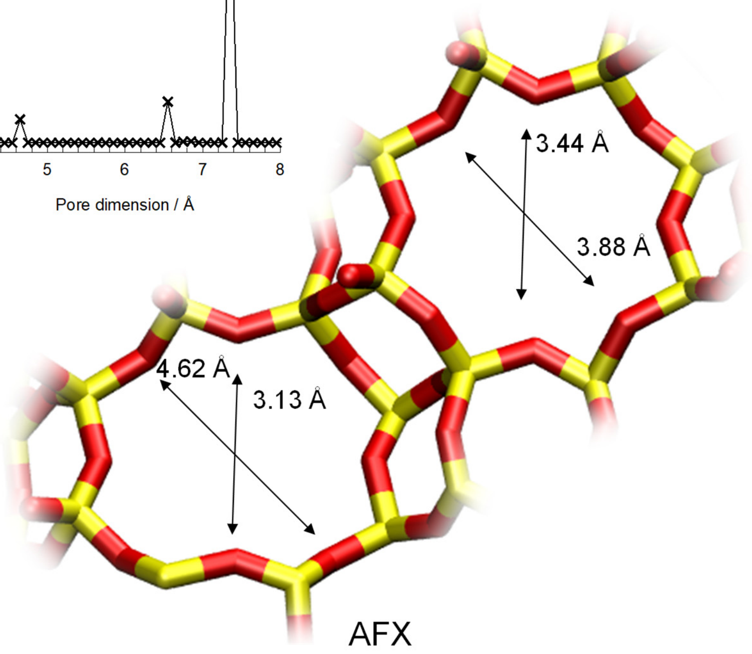

The window dimension calculated using the van der Waals diameter of framework atoms = 2.7 Å are indicated above by the arrows.

Figure S57. Structural details for AFX zeolite.

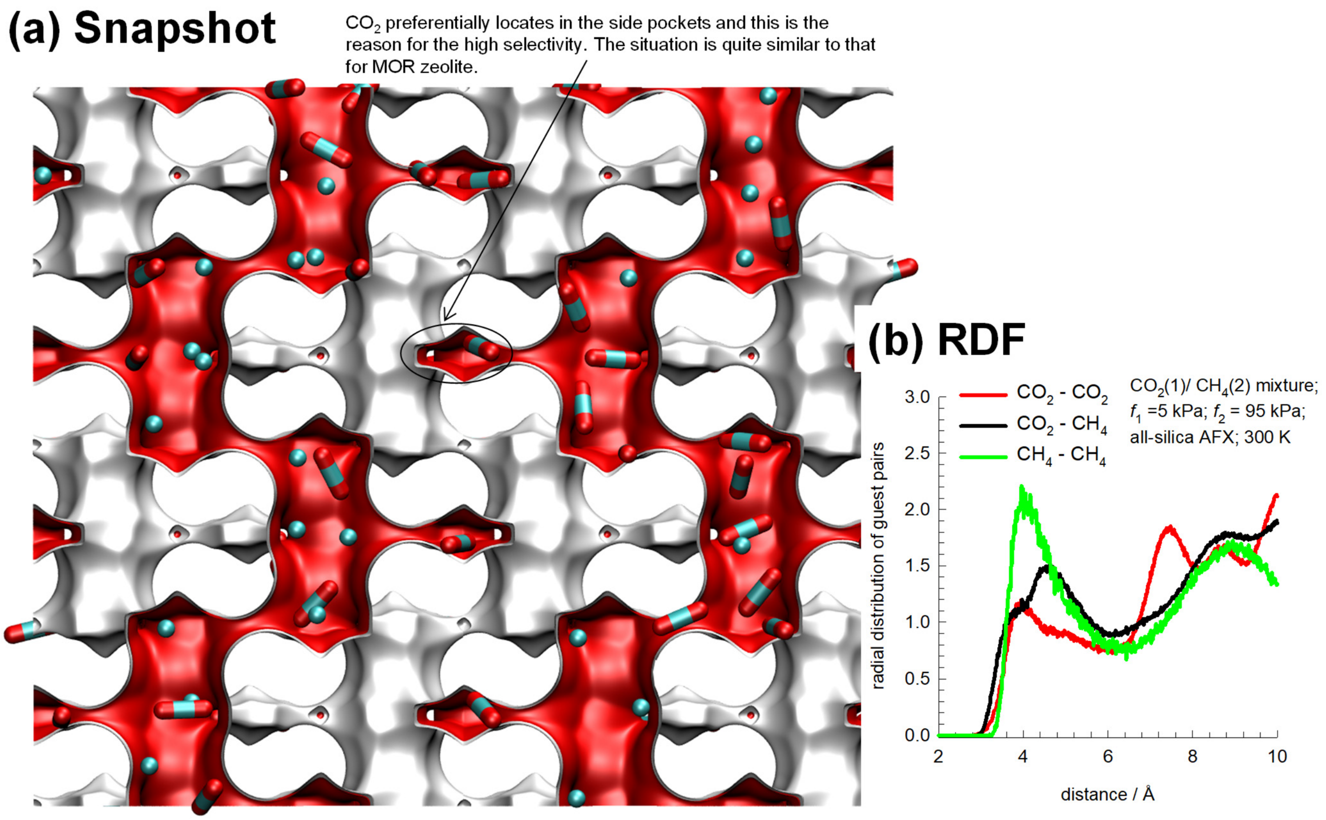

CO$_2$ preferentially locates in the side pockets and this is the reason for the high selectivity. The situation is quite similar to that for MOR zeolite.

CO$_2$(1)/ CH$_4$(2) mixture; f_1 =5 kPa; f_2 = 95 kPa; all-silica AFX; 300 K

Figure S58. (a) Snapshots showing the location of guest molecules for CO2(1)/CH4(2) mixture adsorption in AFX zeolite at 300 K. (b) RDFs for CO2(1)/CH4(2) mixture adsorption in AFX zeolite at 300 K

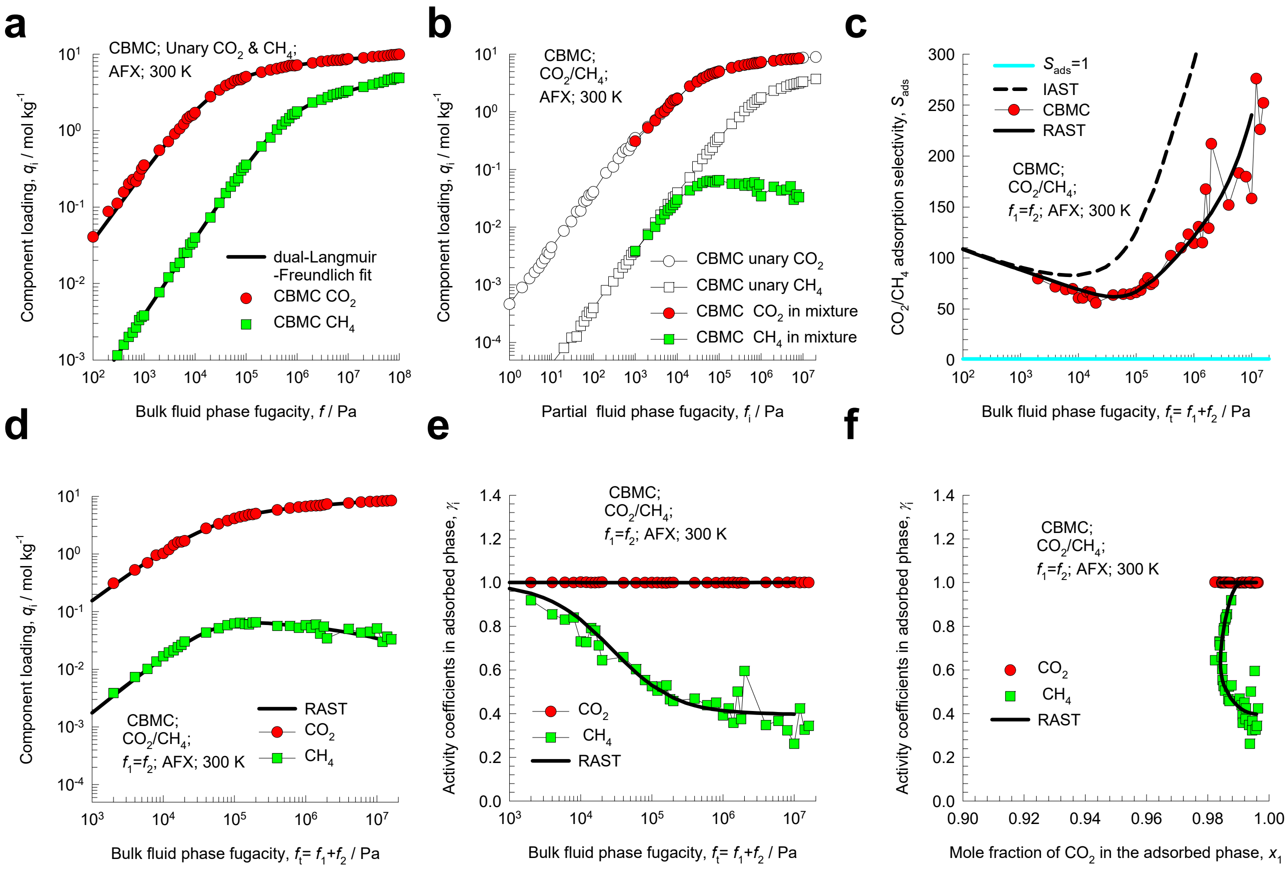

Figure S59. CBMC simulation data and analysis for Campaign A (y_1= 0.5) for CO$_2$(1)/CH$_4$(2) mixture adsorption in AFX zeolite at 300 K. (a) Unary isotherms and fits. (b) Component loadings in mixture compared with CBMC simulations of unary isotherms. (c) CBMC data for CO$_2$(1)/CH$_4$(2) adsorption selectivity compared with IAST and RAST estimates. (d) CBMC data for component loadings in mixture compared with RAST estimates. (e, f) Activity coefficients from CBMC compared with RAST model calculations. The unary isotherm fit parameters and Wilson parameters are provided in Table S13.

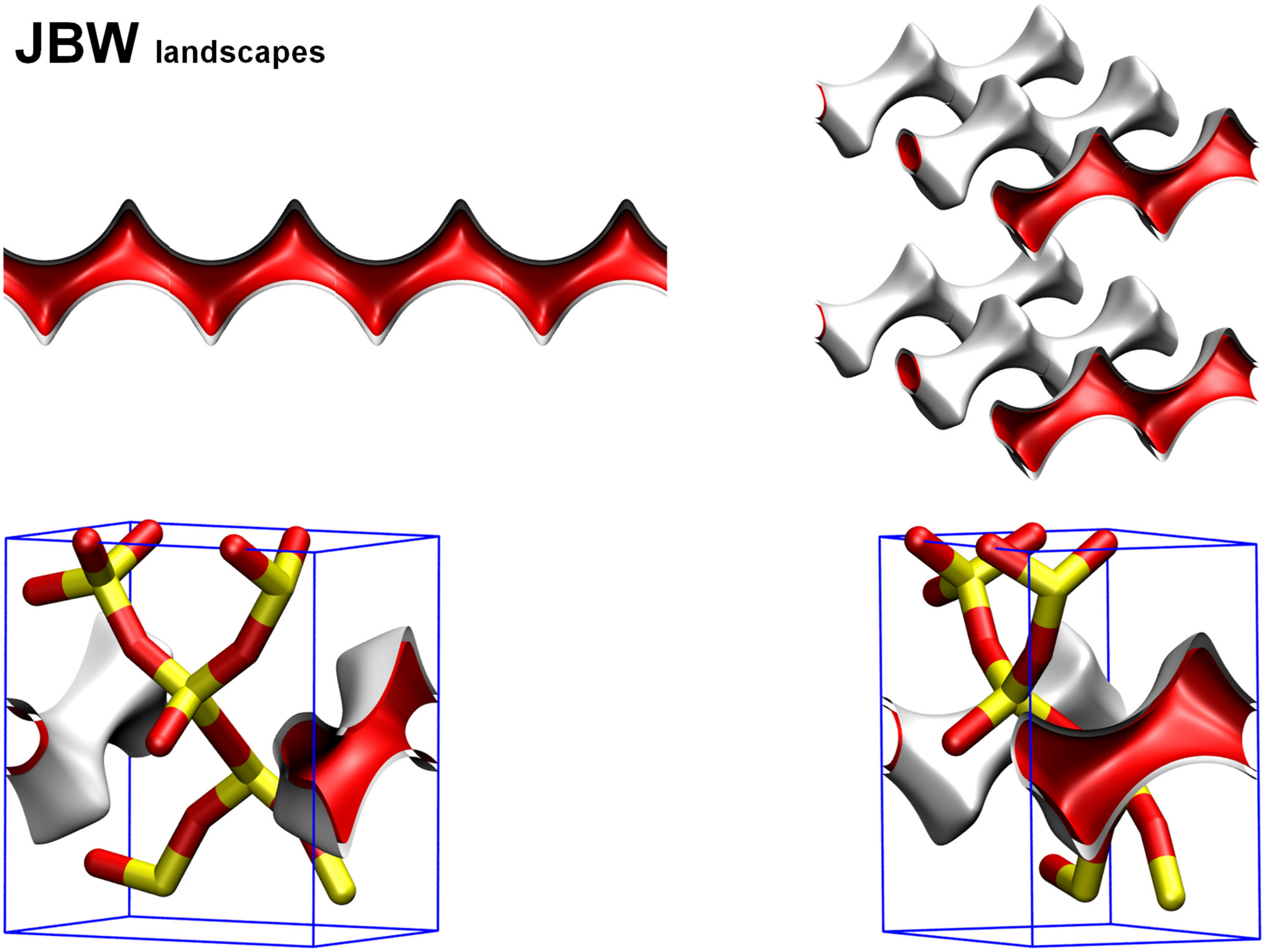

Figure S60. Pore landscape of all-silica JBW zeolite.

JBW pore dimensions

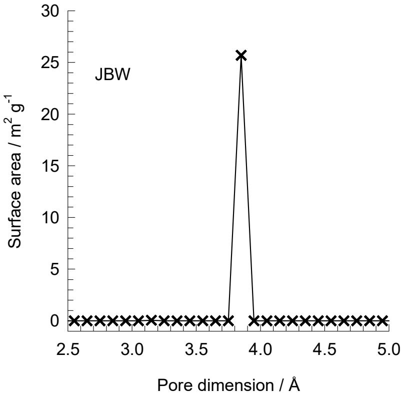

This plot of surface area versus pore dimension is determined using a combination of the DeLaunay triangulation method for pore dimension determination, and the procedure of Düren for determination of the surface area. The computational details will be described in detail in a forthcoming publication.

	JBW
a /Å	5.256
b /Å	7.45
c /Å	8.159
Cell volume / Å^3	319.4836
conversion factor for [molec/uc] to [mol per kg Framework]	2.7739
conversion factor for [molec/uc] to [kmol/m^3]	32.2019
ρ [kg/m3]	1873.8
MW unit cell [g/mol (framework)]	360.5088
ϕ, fractional pore volume	0.161
open space / Å^3/uc	51.6
Pore volume / cm^3/g	0.086
Surface area /m^2/g	25.1
DeLaunay diameter /Å	3.66

Figure S61. Structural details for JBW zeolite.

JBW snapshots

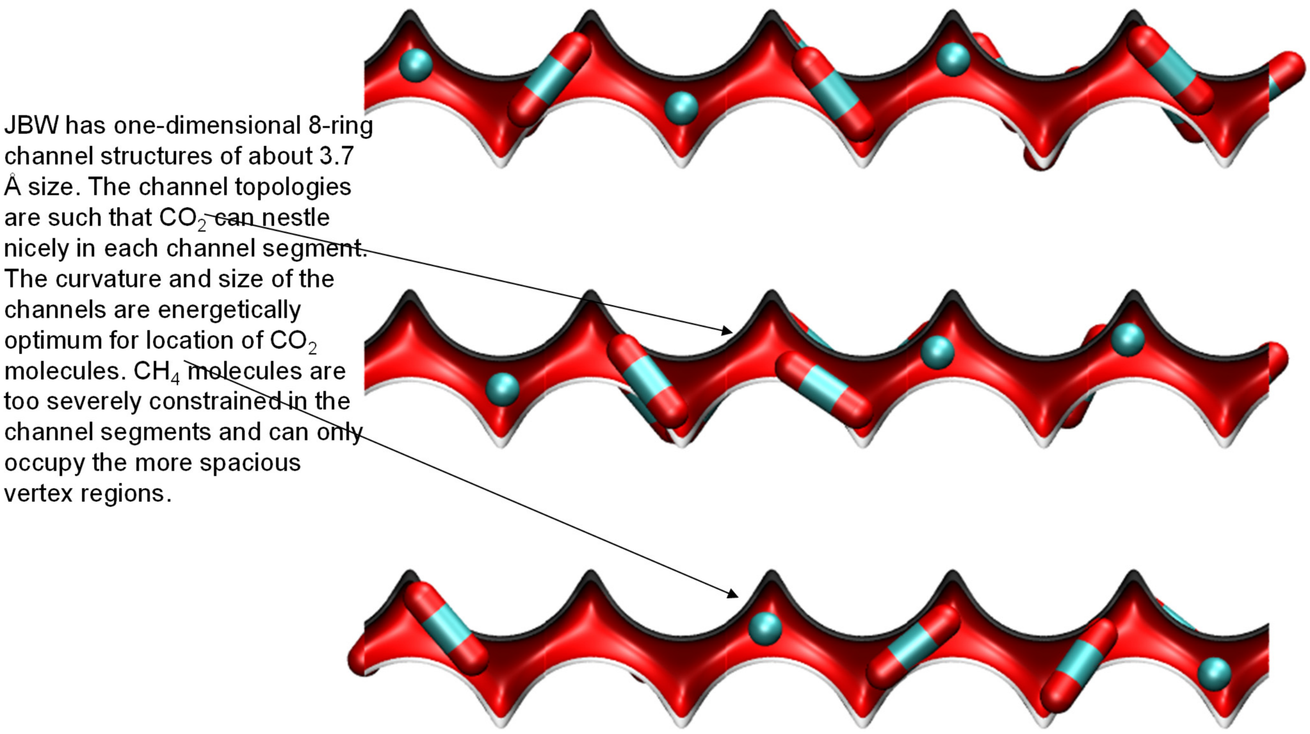

JBW has one-dimensional 8-ring channel structures of about 3.7 Å size. The channel topologies are such that CO_2 can nestle nicely in each channel segment. The curvature and size of the channels are energetically optimum for location of CO_2 molecules. CH_4 molecules are too severely constrained in the channel segments and can only occupy the more spacious vertex regions.

Figure S62. Snapshots showing the location of guest molecules for CO_2(1)/CH_4(2) mixture adsorption in JBW zeolite at 300 K.

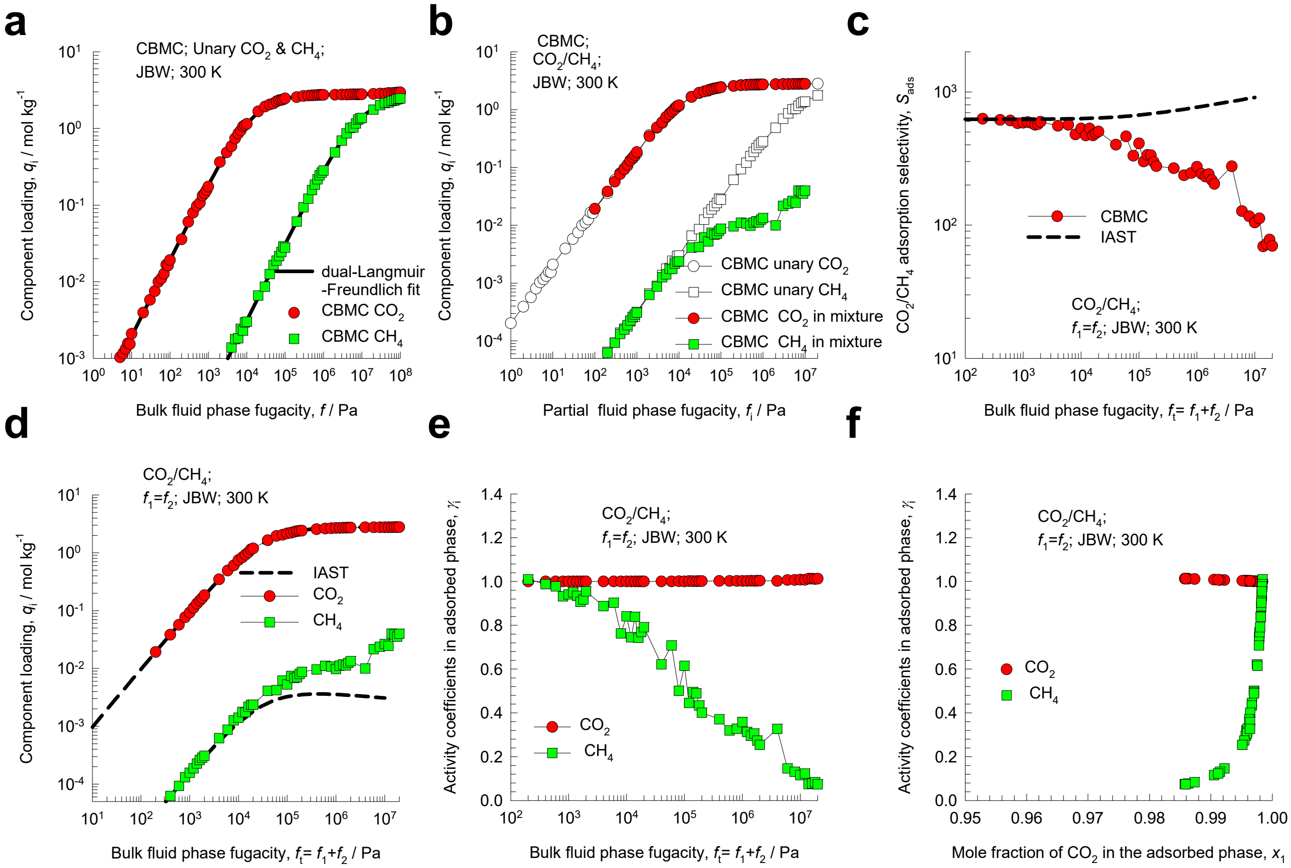

Figure S63. CBMC simulation data and analysis for Campaign A (y_1= 0.5) for CO_2(1)/CH_4(2) mixture adsorption in JBW zeolite at 300 K. (a) Unary isotherms and fits. (b) Component loadings in mixture compared with CBMC simulations of unary isotherms. (c) CBMC data for CO_2(1)/CH_4(2) adsorption selectivity compared with IAST estimates. (d) CBMC data for component loadings in mixture compared with IAST estimates. (e, f) Activity coefficients from CBMC simulation data. The unary isotherm fit parameters in Table S14.

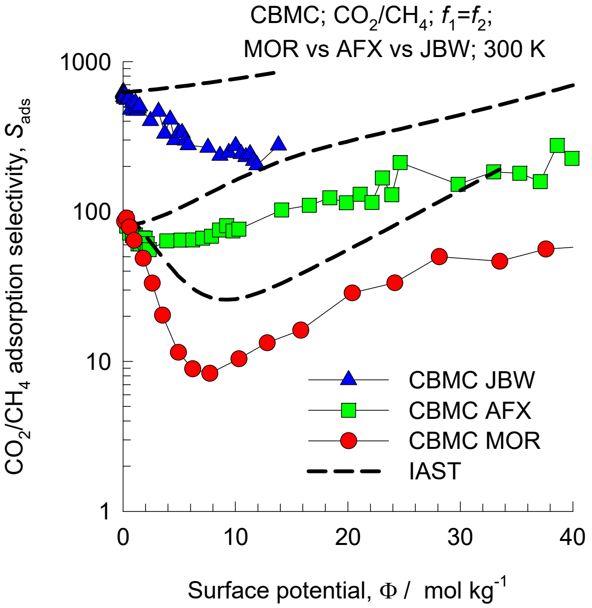

Figure S64. Adsorption selectivity S_{ads} for $CO_2(1)/CH_4(2)$ mixture adsorption in AFX, MOR, and JBW zeolites at 300 K for Campaign A (y_1= 0.5), plotted as function of the surface potential Φ. The CBMC simulated values (indicated by symbols) are compared with IAST estimates (indicated by the dashed lines).

14 Mixture adsorption in LTA zeolite

LTA (Linde Type A) all-silica zeolite consist of cages of 743 Å^3 volume, separated by 4.11 Å × 4.47 Å 8-ring windows; the pore landscapes and structural details are provided in Figure S65, and Figure S66. Figure S67 presents the structural details of cation-exchanged LTA-4A; per unit cell LTA-4A has 96 Si, 96 Al, 96 Na$^+$, Si/Al=1.

14.1 CO_2/C_3H_8 mixture adsorption in LTA-4A zeolite

Two different campaigns were carried out for CBMC simulations of $CO_2(1)/C_3H_8(2)$ mixture adsorption in LTA-4A zeolite at 300 K. In Campaign A, the mole fraction of $CO_2(1)$ in the bulk gas phase is held constant, $y_1 = 0.1$, and the bulk gas phase fugacity $f_t = f_1 + f_2$ was varied, and in Campaign B, the mole fraction of $CO_2(1)$ in the bulk gas phase, y_1 was varied from 0 to 1, keeping the bulk gas phase mixture fugacity $f_t = f_1 + f_2$ constant at a value of 1 MPa. The results of these two separate campaigns are presented, respectively, in Figure S68, and Figure S69.

The CBMC data in Figure S68 for Campaign A show that for $f_t = f_1 + f_2 < 10^6$ Pa, the selectivity S_{ads} is in favor of C_3H_8; with increasing values of the bulk gas phase fugacity $f_t = f_1 + f_2 > 10^6$, the adsorption selectivity S_{ads} becomes increasingly in favor of CO_2, due to strong Coulombic interactions with the extra-framework cations Na$^+$; see Figure S68c. The IAST does not anticipate this selectivity reversal in favor of CO_2.

The CBMC simulations can be matched by quantification of thermodynamic non-idealities using the Margules parameters as specified in Table S15. Figure S68e,f show the RAST calculations of the activity coefficients.

The CBMC simulations for $CO_2(1)/C_3H_8(2)$ mixture adsorption at $f_t = 1$ MPa, and varying mole fractions of $CO_2(1)$ in the bulk gas phase, y_1, are shown in Figure S69. For $y_1 < 0.1$, $S_{ads} > 1$, and the selectivity is in favor of CO_2. The CBMC simulations show that the adsorption selectivity S_{ads} is increasingly lowered below unity, i.e. in favor of the alkane, with increasing proportion of $CO_2(1)$ in the bulk gas phase; see Figure S69b. The IAST anticipates S_{ads} to be virtually independent of composition in the bulk fluid phase. Figure S69c shows the RAST calculations of the activity coefficients as function of the mole fraction of $CO_2(1)$ in the adsorbed phase, x_1.

In Figure S70, the two sets of CBMC data on the adsorption selectivity S_{ads} are plotted against the surface potential Φ. Due to thermodynamic non-idealities, the adsorption selectivity is not uniquely determined by Φ. CBMC simulations show that two types of selectivity reversals can be realized: (i) maintaining the bulk gas composition constant at $y_1 = 0.1$, and increasing the total mixture fugacity to values $f_t = f_1 + f_2 > 10^6$ Pa, ensuring that $\Phi > 27 \text{ mol kg}^{-1}$, and (ii) maintain the total mixture fugacity $f_t = f_1 + f_2 = 10^6$ Pa, and increasing the mole fraction of CO_2 in the bulk gas mixture to values in excess of 0.1, again ensuring that $\Phi > 27 \text{ mol kg}^{-1}$.

The rationale for the quantitative failures IAST estimates can be traced to congregation of CO_2 near the Na^+ cations, as witnessed in the RDFs for various guest pairs CO_2-CO_2, CO_2-Na^+, CO_2-C_3H_8, and C_3H_8-C_3H_8 shown in Figure S71. It is noteworthy that the first peaks of CO_2-CO_2 and Na^+-Na^+ are close together. Also noteworthy is that the first peaks of CO_2-CO_2 and CO_2-C_3H_8 are farther apart, indicating segregation effects. Also noteworthy, is that a number of peaks occur for CO_2-CO_2 pairs; two of these peaks correspond to the window-to-window distances of 8.68, and 12.27 Å.

Figure S72 shows snapshots of the location of $CO_2(1)$, and $C_3H_8(2)$ molecules within the pore topology of LTA-4A zeolite. We note that the CO_2 is almost exclusively located at the windows, or near the window entrance regions. Due to configurational restraints C_3H_8 can only located at the cage interiors.

Consequently, the competition between the adsorption of CO_2 and C_3H_8 is less severe than assumed in the homogenous distribution that is inherent in the IAST prescription.

14.2 CO_2/nC_4H_{10} mixture adsorption in LTA-4A zeolite

Thermodynamic non-ideality effects were also investigated for $CO_2(1)/nC_4H_{10}(2)$ mixture adsorption in LTA-4A zeolite at 300 K. Four different CBMC simulation campaigns were conducted.

(i) Campaign A ($y_1 = 0.5$) for $CO_2(1)/nC_4H_{10}(2)$ mixture adsorption

(ii) Campaign A ($y_1 = 0.9$) for $CO_2(1)/nC_4H_{10}(2)$ mixture adsorption

(iii) Campaign B ($f_t = 100$ kPa) for $CO_2(1)/nC_4H_{10}(2)$ mixture adsorption

(iv) Campaign B ($f_t = 500$ kPa) for $CO_2(1)/nC_4H_{10}(2)$ mixture adsorption

The CBMC data and analysis are presented in Figure S73, Figure S74, Figure S75, and Figure S76.

The IAST fails to anticipate the selectivity reversals in the two campaigns B; see Figure S75, and Figure S76.

14.3 $CO_2/CH_4/N_2$ mixture adsorption in all-silica LTA zeolite

CBMC simulations were carried out for five different mixtures in LTA (all-silica) zeolite at 300 K: (i) 50/50 CO_2/CH_4, (ii) 50/50 CO_2/N_2, (iii) 15/85 CO_2/N_2, (iv) 50/50 CH_4/N_2, and (v) equimolar ($f_1 = f_2 = f_3$) 1/1/1 $CO_2/CH_4/N_2$. The adsorption selectivities, S_{ads} of the three different pairs CO_2/CH_4, CO_2/N_2, and CH_4/N_2 were determined both from binary and ternary mixtures. The CBMC data on the pair selectivities are plotted in Figure S77a,b,c as function of the surface potential, Φ, determined from IAST calculations using the isotherm fits reported in Table S16. When compared at the same value of Φ, the selectivities are the same in the binary mixture as in the ternary mixture, in agreement with the IAST prescription. Put another way, the presence of component 3 in the ternary mixture has no influence of the adsorption selectivity for the 1-2 pair.

Mixture adsorption in LTA zeolite

14.4 List of Tables for Mixture adsorption in LTA zeolite

Table S15. Dual-site Langmuir-Freundlich parameters for pure components CO_2, C_3H_8, and nC_4H_{10}, at 300 K in LTA-4A zeolite (96 Si, 96 Al, 96 Na^+, Si/Al=1). The fit parameters are based on the CBMC simulations of pure component isotherms.

	Site A			Site B		
	$q_{A,sat}$ mol kg^{-1}	b_A $Pa^{-\nu_A}$	ν_A dimensionless	$q_{B,sat}$ mol kg^{-1}	b_B $Pa^{-\nu_B}$	ν_B dimensionless
CO_2	3.1	4.13×10^{-4}	1	1.7	2.095×10^{-7}	1
C_3H_8	2.5	2.21×10^{-2}	1	0.9	6.18×10^{-6}	1
nC_4H_{10}	1.8	1.14	1	0.55	5.06×10^{-3}	1

Fitted Margules non-ideality parameters for binary mixture adsorption in LTA-4A at 300 K.

	C / kg mol^{-1}	A_{12}	A_{21}
CO_2/C_3H_8 in LTA-4A	0.142	-3.736	-0.511

Table S16. Dual-site Langmuir-Freundlich parameters for guest molecules in LTA (all-silica) at 300 K. To convert from molecules uc^{-1} to mol kg^{-1}, multiply by 0.086683044.

	Site A			Site B		
	$\Theta_{A,sat}$ molecules uc^{-1}	b_A $Pa^{-\nu}$	ν_A dimensionless	$\Theta_{B,sat}$ molecules uc^{-1}	b_B $Pa^{-\nu}$	ν_B dimensionless
N_2	70	1.36E-07	1	60	5.03E-10	1
CO_2	36	1.51E-05	0.54	85	2.06E-07	1.15
CH_4	52	6.63E-08	0.82	65	3.77E-07	1

14.5 List of Figures for Mixture adsorption in LTA zeolite

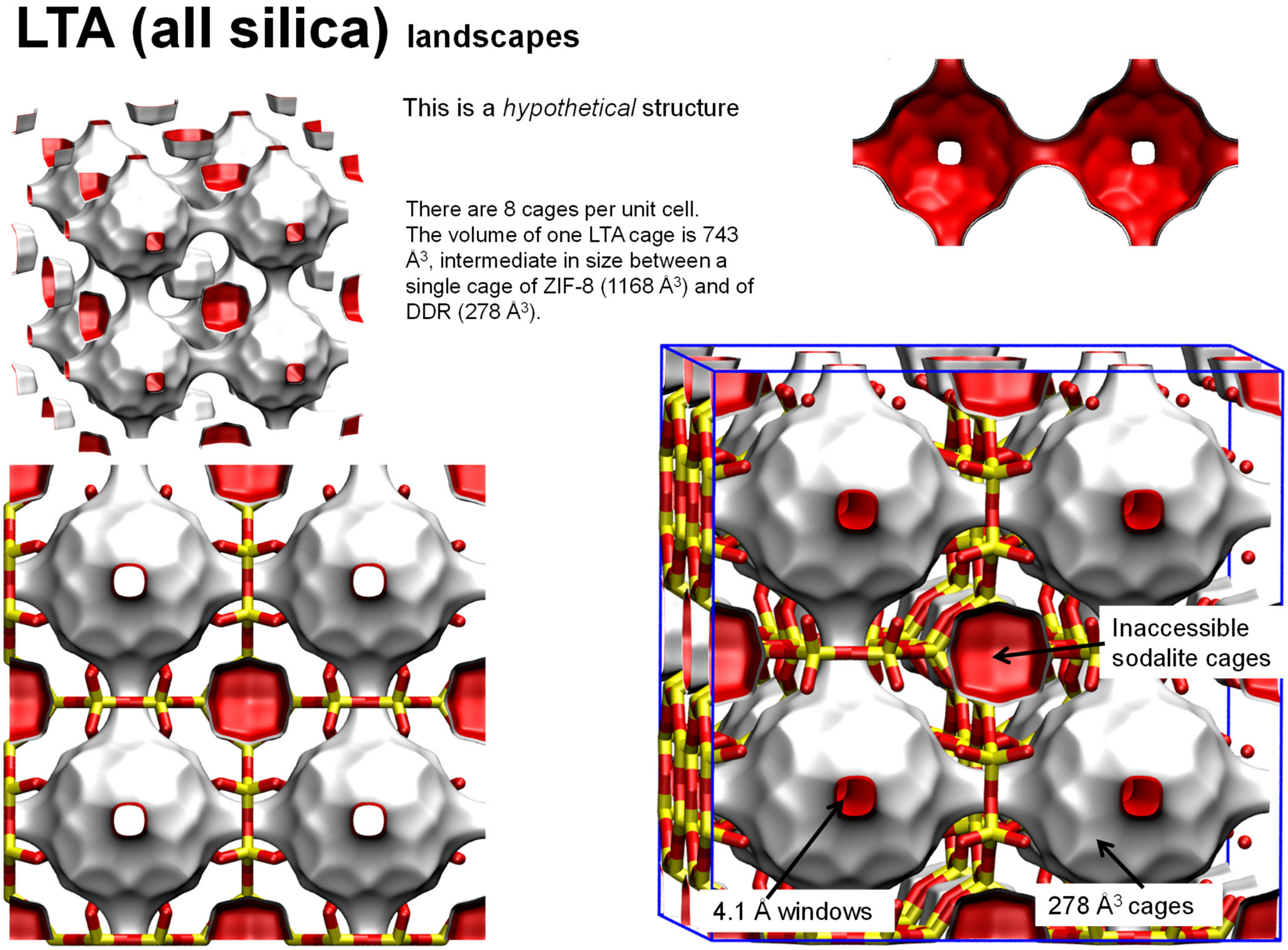

LTA (all silica) landscapes

This is a *hypothetical* structure

There are 8 cages per unit cell. The volume of one LTA cage is 743 Å^3, intermediate in size between a single cage of ZIF-8 (1168 Å^3) and of DDR (278 Å^3).

Figure S65. Pore landscape of all-silica LTA zeolite.

LTA (all-silica) window and pore dimensions

8-ring window of LTA

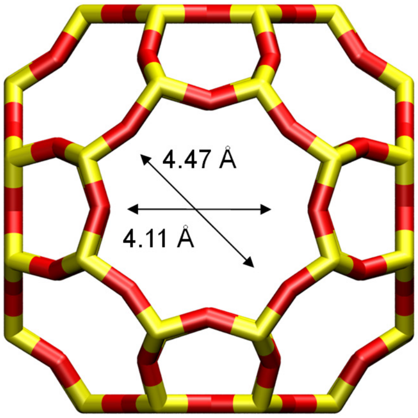

This plot of surface area versus pore dimension is determined using a combination of the DeLaunay triangulation method for pore dimension determination, and the procedure of Düren for determination of the surface area.

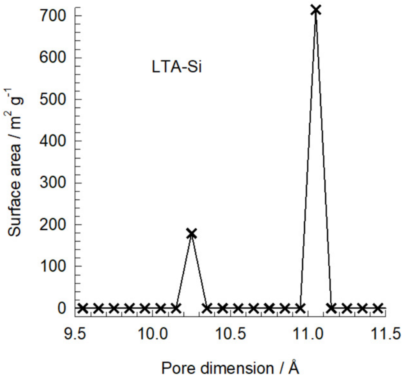

The window dimension calculated using the van der Waals diameter of framework atoms = 2.7 Å is indicated above by the arrows.

	LTA-Si
a /Å	24.61
b /Å	24.61
c /Å	24.61
Cell volume / Å^3	14905.1
conversion factor for [molec/uc] to [mol per kg Framework]	0.0867
conversion factor for [molec/uc] to [kmol/m^3]	0.2794
ρ [kg/m3]	1285.248
MW unit cell [g/mol(framework)]	11536.28
ϕ, fractional pore volume	0.399
open space / Å^3/uc	5944.4
Pore volume / cm^3/g	0.310
Surface area /m^2/g	896.0
DeLaunay diameter /Å	4.10

Figure S66. Structural details for all-silica LTA zeolite.

LTA-4A

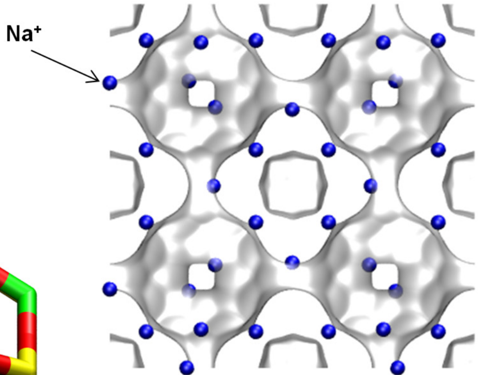

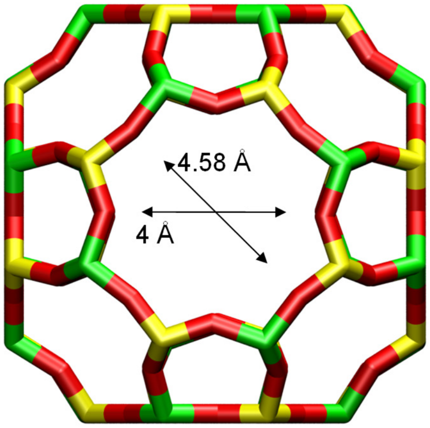

LTA-4A

The window dimension calculated using the van der Waals diameter of framework atoms = 2.7 Å is indicated above by the arrow.

LTA-4A (96 Na+)

	LTA-4A
a /Å	24.555
b /Å	24.555
c /Å	24.555
Cell volume / Å^3	14805.39
conversion factor for [molec/uc] to [mol per kg Framework]	0.0733
conversion factor for [molec/uc] to [kmol/m^3]	0.2991
ρ [kg/m3] (with cations)	1529.55
MW unit cell [g/mol(framework+cations)]	13637.27
ϕ, fractional pore volume	0.375
open space / Å^3/uc	5552.0
Pore volume / cm^3/g	0.245
Surface area /m^2/g	
DeLaunay diameter /Å	4.00

Figure S67. Structural details for LTA-4A zeolite.

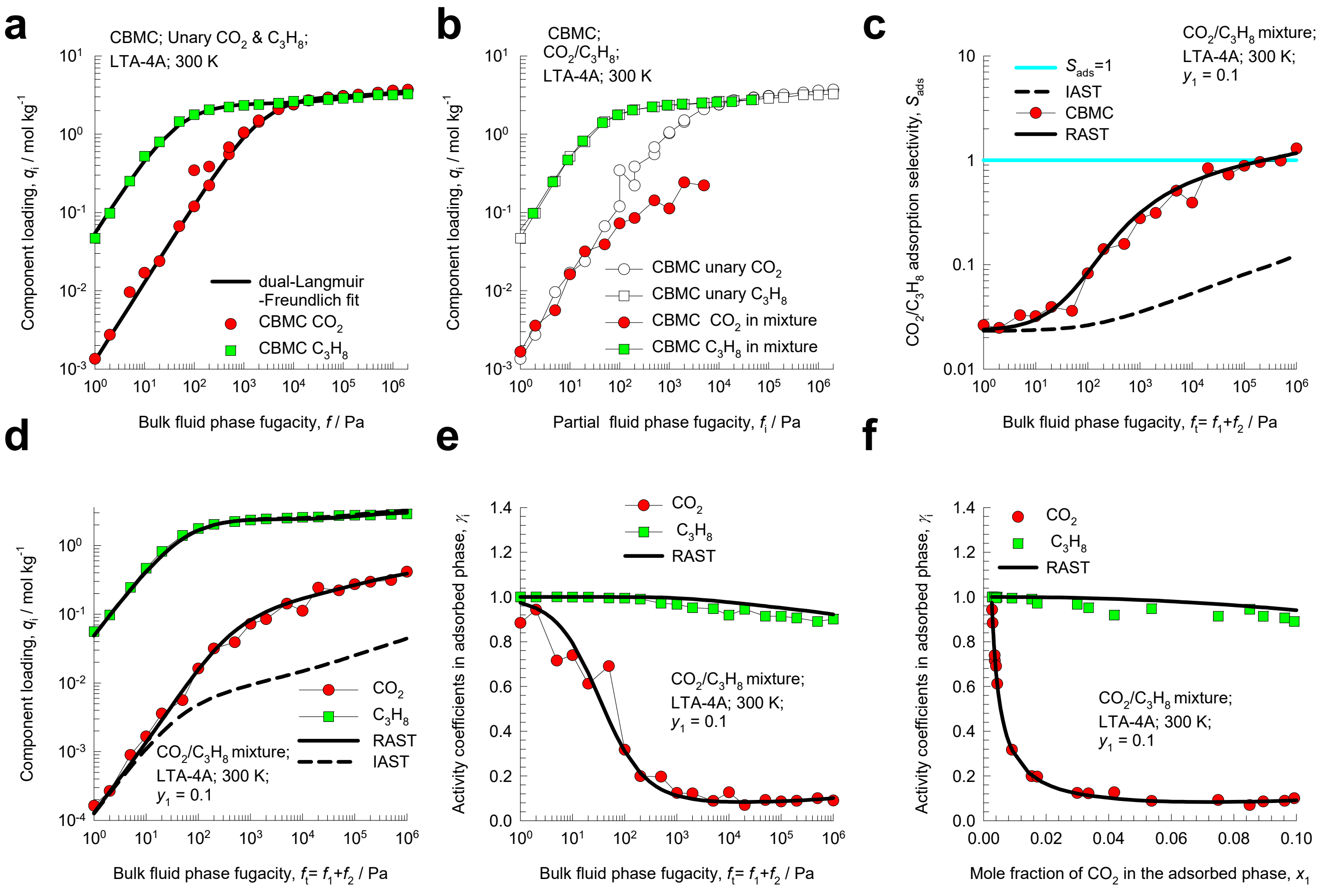

Figure S68. CBMC simulation data and analysis for Campaign A ($y_1 = 0.1$) for $CO_2(1)/C_3H_8(2)$ mixture adsorption in LTA-4A zeolite at 300 K. (a) Unary isotherms and fits. (b) Component loadings in mixture compared with CBMC simulations of unary isotherms. (c) CBMC data for $CO_2(1)/C_3H_8(2)$ adsorption selectivity compared with IAST and RAST estimates. (d) CBMC data for component loadings in mixture compared with RAST estimates. (e, f) Activity coefficients from CBMC compared with RAST model calculations. The unary isotherm fit parameters and Margules parameters are provided in Table S15.

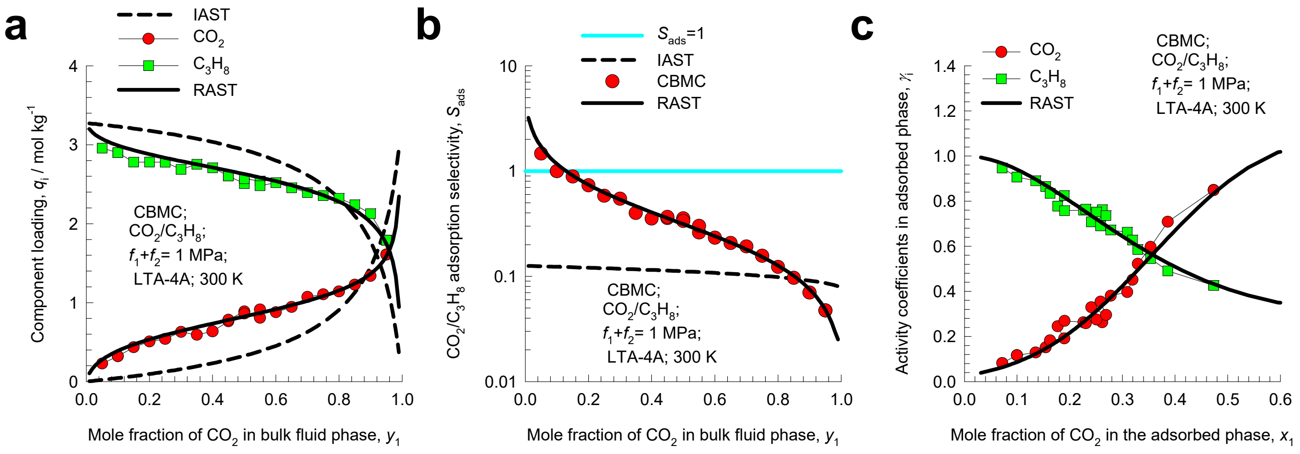

Figure S69. CBMC simulation data and analysis for Campaign B (f_t = 1 MPa) for $CO_2(1)/C_3H_8(2)$ mixture adsorption in LTA-4A zeolite at 300 K. CBMC data for (a) component loadings and (b) $CO_2(1)/C_3H_8(2)$ adsorption selectivity compared with IAST and RAST estimates. (c) Activity coefficients from CBMC compared with RAST model calculations. The unary isotherm fit parameters and Margules parameters are provided in Table S15.

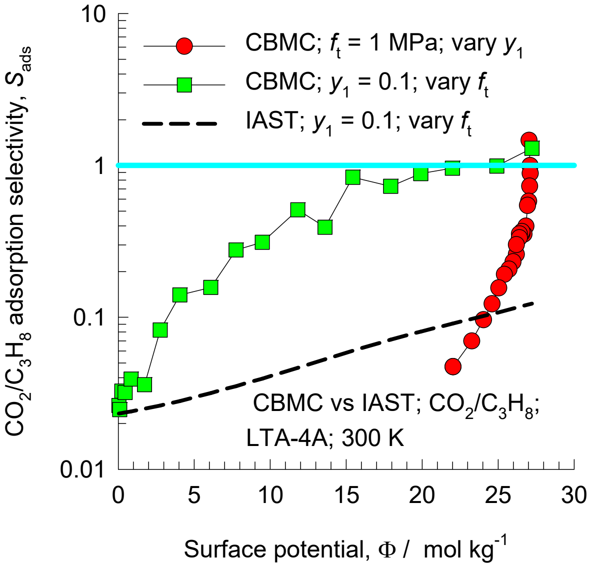

Figure S70. Adsorption selectivity S_{ads} for $CO_2(1)/C_3H_8(2)$ mixture adsorption in LTA-4A zeolite at 300 K for two different campaigns (Campaign A (y_1= 0.1) and Campaign B (f_t = 1 MPa), plotted as function of the surface potential Φ. The CBMC simulated values (indicated by symbols) are compared with IAST estimates (indicated by the dashed lines). The unary isotherm fit parameters and Margules parameters are provided in Table S15.

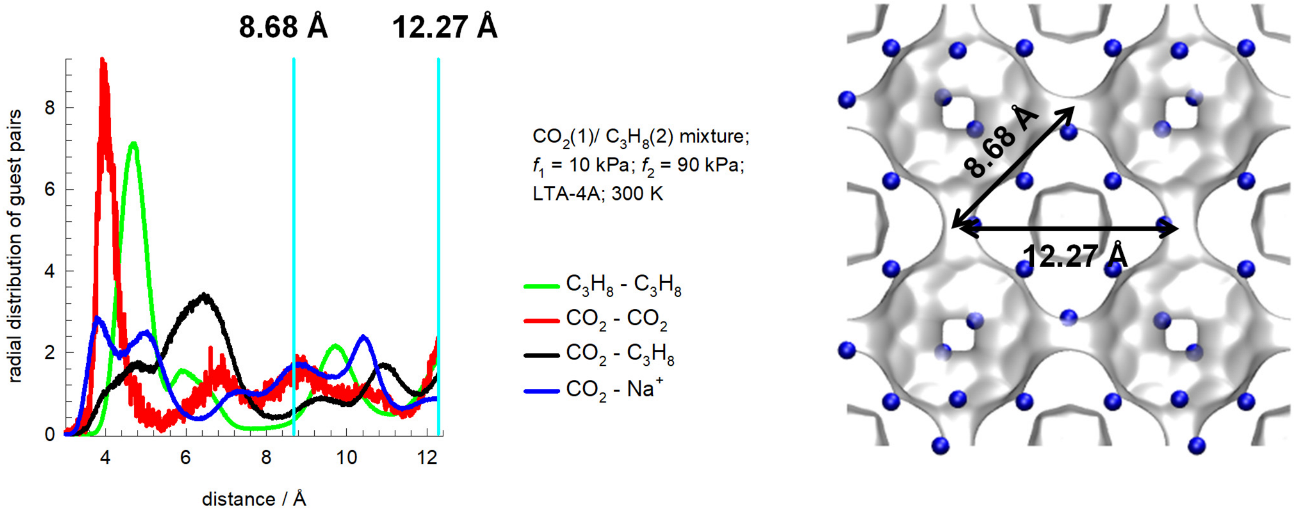

Figure S71. Radial distribution of guest pairs determined from CBMC simulations for adsorption of CO_2/C_3H_8 mixtures in LTA-4A zeolite at 300 K and total fugacity f_t = 100 kPa, and y_1=0.1.

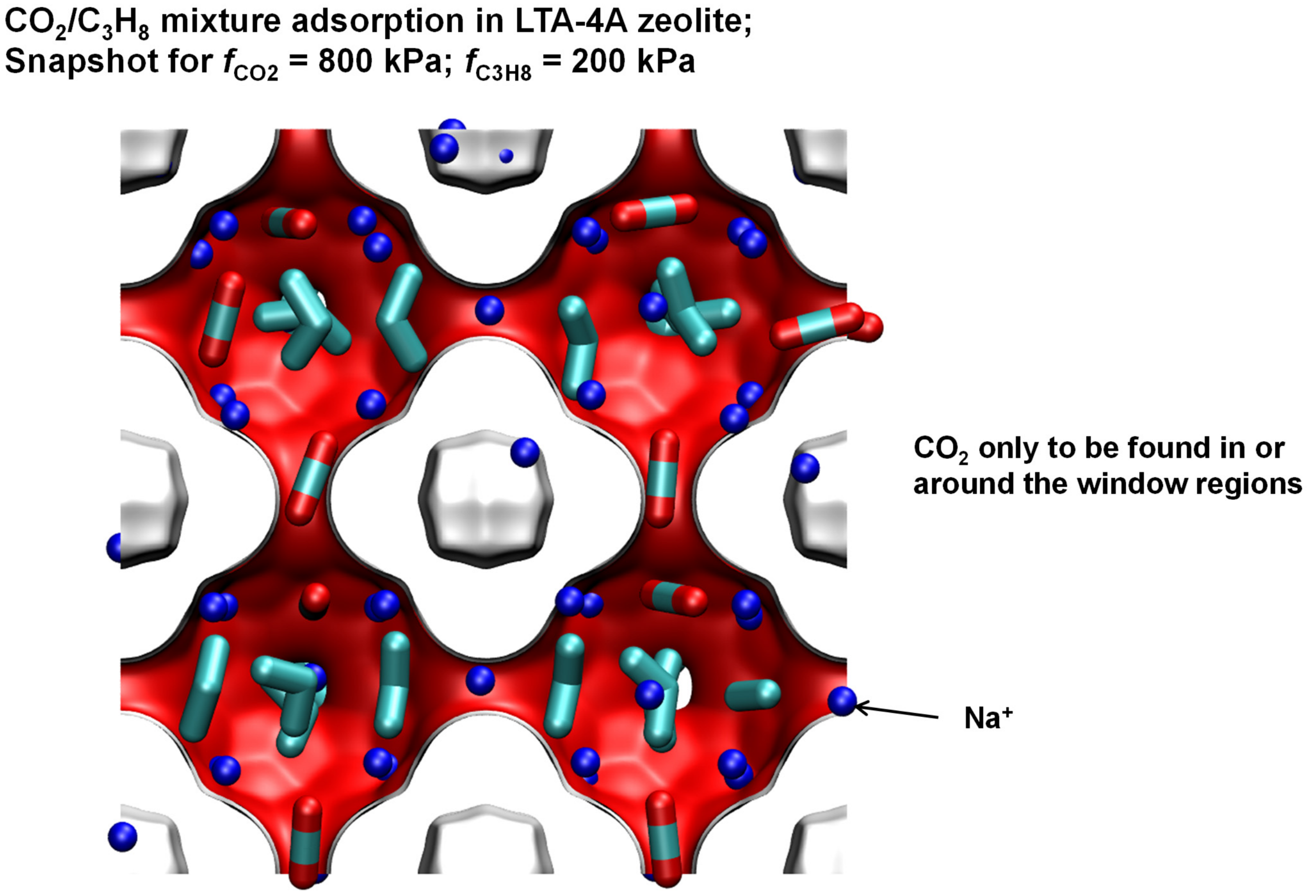

Figure S72. Computational snapshot showing the location of CO_2, and C_3H_8 within the cages of LTA-4A zeolite at 300 K and total fugacity f_t = 1 MPa. The component partial fugacities are f_1 = 0.8 MPa, and f_2 = 0.2 MPa.

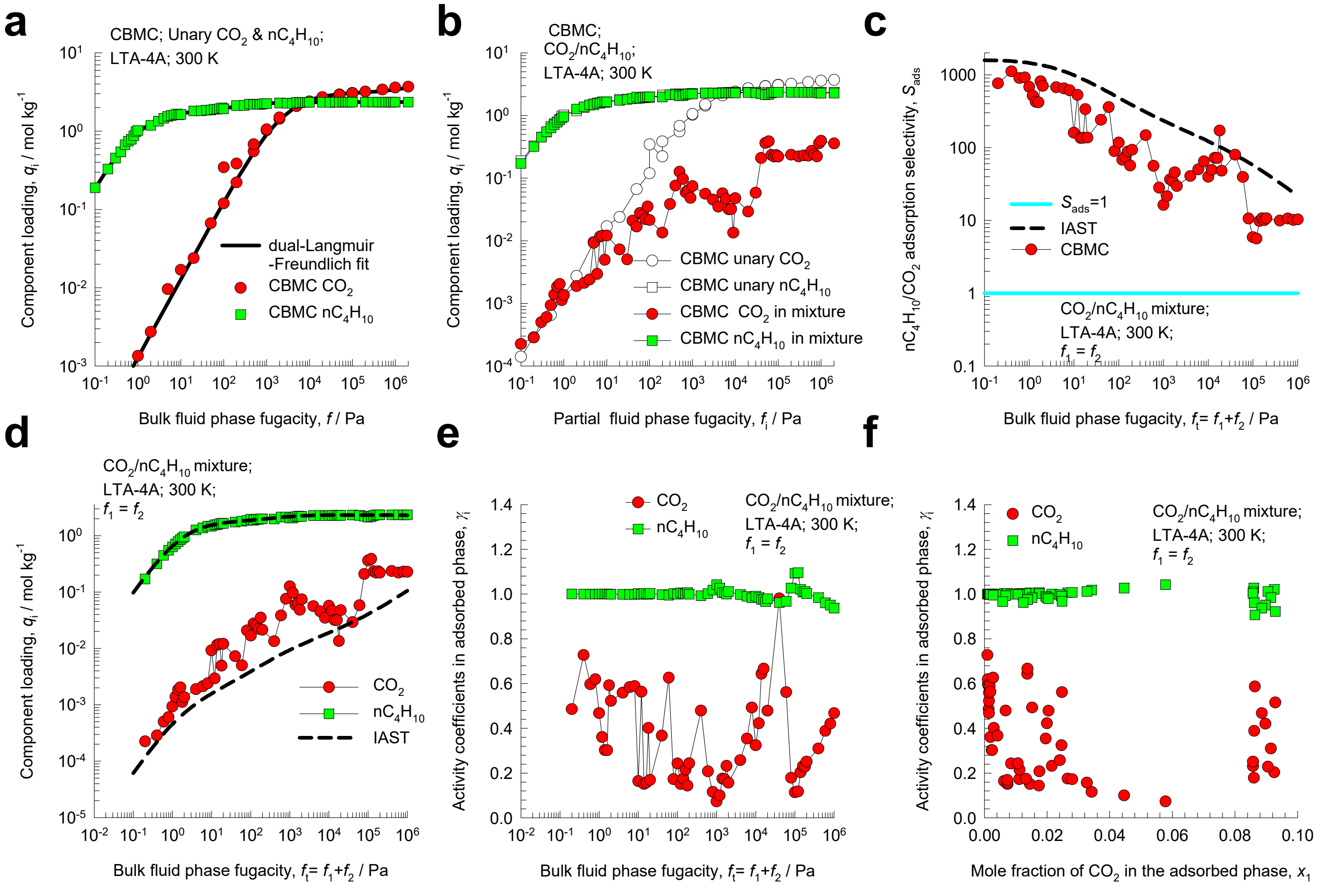

Figure S73. CBMC simulation data and analysis for Campaign A (y_1= 0.5) for $CO_2(1)/nC_4H_{10}(2)$ mixture adsorption in LTA-4A zeolite at 300 K. (a) Unary isotherms and fits. (b) Component loadings in mixture compared with CBMC simulations of unary isotherms. (c) CBMC data for $nC_4H_{10}(2)/CO_2(1)$ adsorption selectivity compared with IAST estimates. (d) CBMC data for component loadings in mixture compared with IAST estimates. (e, f) Activity coefficients from CBMC. The unary isotherm fit parameters are provided in Table S15.

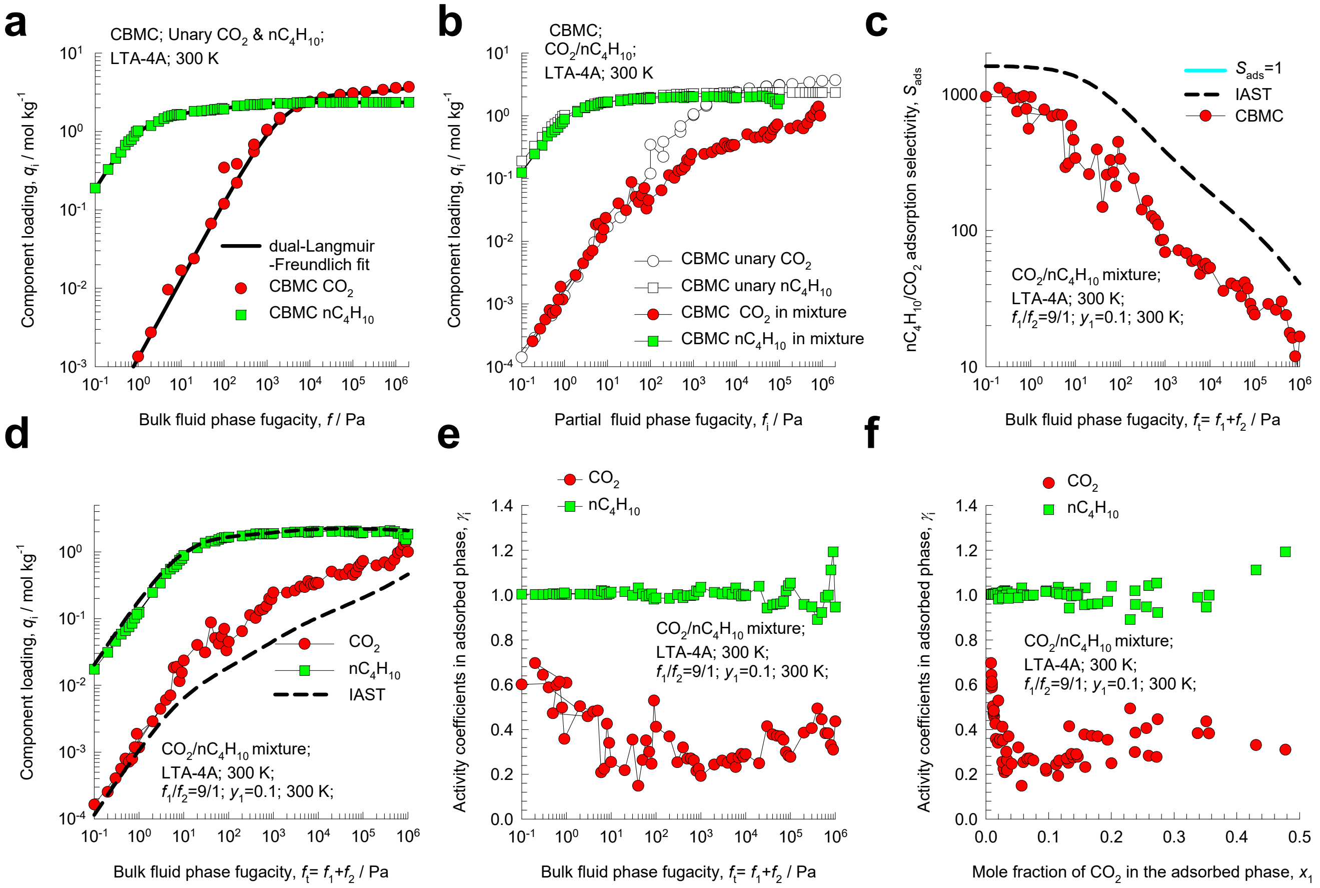

Figure S74. CBMC simulation data and analysis for Campaign A (y_1= 0.9) for CO_2(1)/nC_4H_{10}(2) mixture adsorption in LTA-4A zeolite at 300 K. (a) Unary isotherms and fits. (b) Component loadings in mixture compared with CBMC simulations of unary isotherms. (c) CBMC data for nC_4H_{10}(2)/CO_2(1) adsorption selectivity compared with IAST estimates. (d) CBMC data for component loadings in mixture compared with IAST estimates. (e, f) Activity coefficients from CBMC. The unary isotherm fit parameters are provided in Table S15.

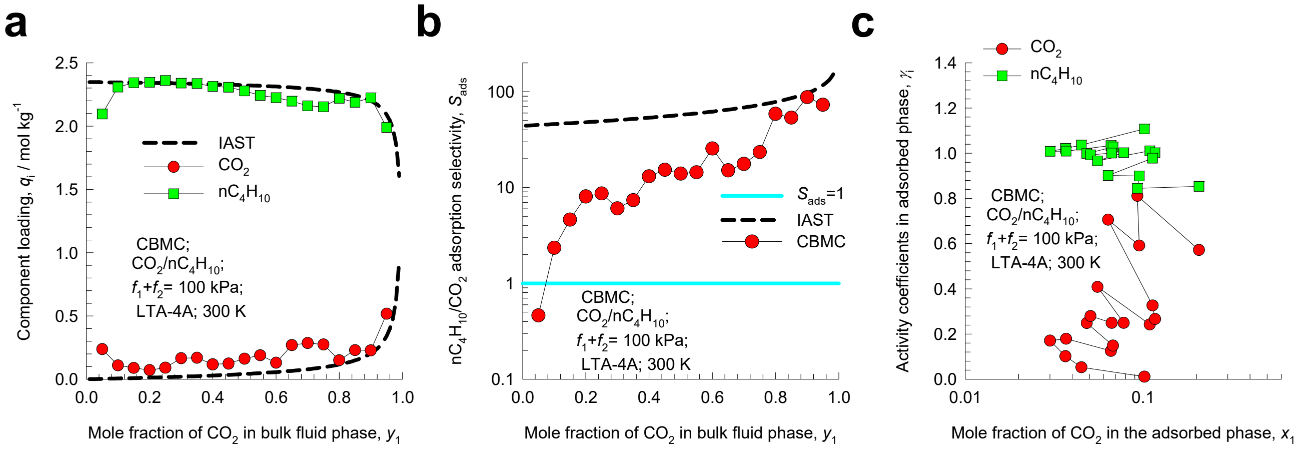

Figure S75. CBMC simulation data and analysis for Campaign B (f_t = 100 kPa) for $CO_2(1)/nC_4H_{10}(2)$ mixture adsorption in LTA-4A zeolite at 300 K. CBMC data for (a) component loadings and (b) $nC_4H_{10}(2)/CO_2(1)$ adsorption selectivity compared with IAST estimates. (c) Activity coefficients from CBMC. The unary isotherm fit parameters are provided in Table S15.

Mixture adsorption in LTA zeolite

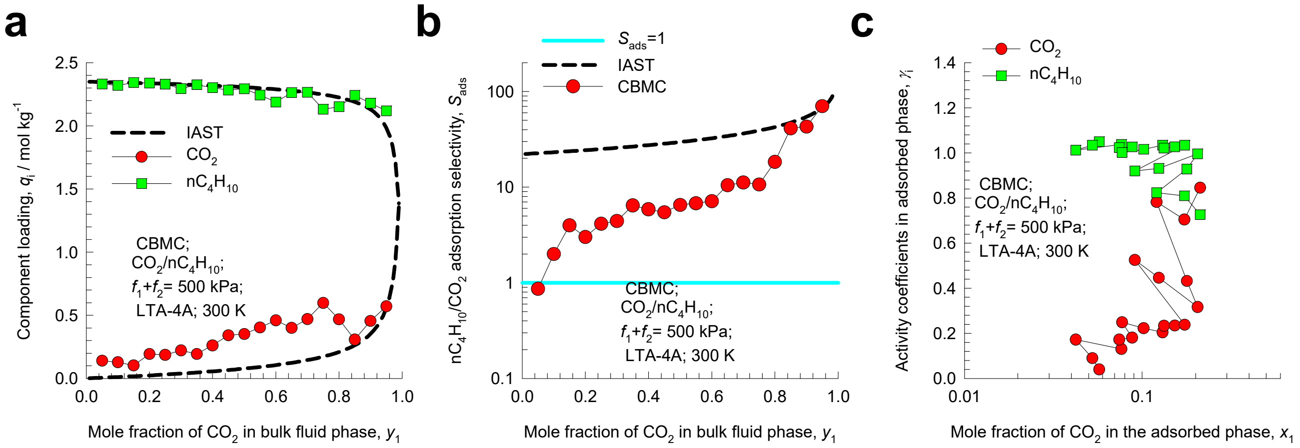

Figure S76. CBMC simulation data and analysis for Campaign B (f_t = 500 kPa) for CO_2(1)/nC_4H_{10}(2) mixture adsorption in LTA-4A zeolite at 300 K. CBMC data for (a) component loadings and (b) nC_4H_{10}(2)/CO_2(1) adsorption selectivity compared with IAST estimates. (c) Activity coefficients from CBMC. The unary isotherm fit parameters are provided in Table S15.

Mixture adsorption in LTA zeolite

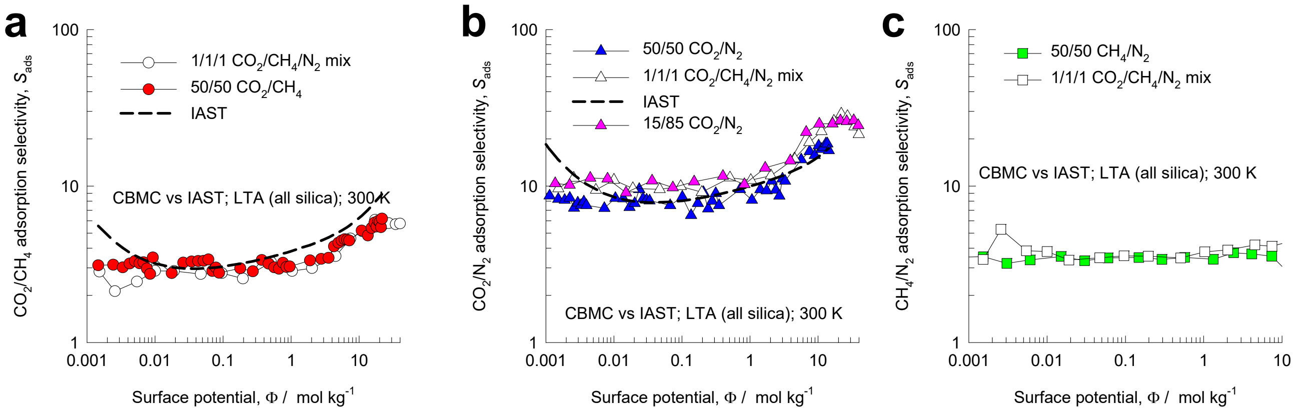

Figure S77. CBMC simulations (indicated by symbols) of the (a) CO_2/CH_4, (b) CO_2/N_2, and (c) CH_4/N_2, adsorption selectivities, S_{ads}, determined from different CBMC campaigns: (i) 50/50 CO_2/CH_4, (ii) 50/50 CO_2/N_2, (iii) 15/85 CO_2/N_2, (iv) 50/50 CH_4/N_2, and (v) equimolar ($f_1 = f_2 = f_3$) 1/1/1 $CO_2/CH_4/N_2$, mixtures in LTA (all-silica) zeolite at 300 K. The dashed lines are the IAST calculations (indicated by dashed lines). The *x*-axes represent the surface potential, Φ, determined from IAST model calculations.

15 Mixture adsorption in FAU (all-silica) and NaX zeolites

Figure S78 presents the structural details of FAU (all-silica) zeolite. It has cages of 786 Å^3 volume, separated by 7.4 Å 12-ring windows. Figure S79 show the structural details of NaX (= 86 Na$^+$/uc = 13X) zeolite. Per unit cell of NaX zeolite we have 106 Si, 86 Al, 86 Na$^+$ with Si/Al=1.23. This material is also commonly referred to by its trade name: 13X zeolite.

15.1 CO_2/CH_4 mixture adsorption in NaX zeolite

Figure S80 presents the CBMC data for simulation of Campaign A (y_1= 0.5, varying f_t) CO_2/CH_4 mixtures in NaX zeolite at 300 K. Figure S81 presents the CBMC data for simulation of Campaign B (f_t= 1 MPa, varying y_1) CO_2/CH_4 mixtures in NaX zeolite at 300 K. The IAST severely overestimated the adsorption selectivity S_{ads} because it assumes a homogeneous distribution of both guest adsorbates over the entire pore space. Due to congregation of CO_2 around the cations Na+, there is segregation of adsorbates. The competition faced by CH_4 is less severe than anticipated by the IAST. To match the CBMC mixture simulation data on the component loadings, we need to introduce activity coefficients. Use of the RAST with fitted Margules parameters results in a good match with the CBMC mixture data; see Figure S80d, and Figure S81a. Figure S80e,f and Figure S81c show RAST calculations of the activity coefficients in the adsorbed phase. It is noteworthy that the activity coefficient of CO_2 is virtually unity over the entire composition range. On the other hand, the activity coefficient of CH_4 shows increasing departure from unity with increasing bulk fluid phase fugacity f_t. The activity coefficient of CH_4 shows increasing departure from unity with increasing mole fraction of CO_2 in the adsorbed phase, x_1.

The failure of the IAST is traceable to the non-uniform distribution of the guest molecules CO_2, and CH_4 within the cages of NaX zeolite. To demonstrate this, the CBMC simulation data on the spatial locations of the guest molecules were sampled to determine the inter-molecular distances. By sampling a total of 10^5 simulation steps, the radial distribution of the separation distances between the molecular pairs CO_2-CO_2, CO_2-Na^+, CO_2-CH_4, and CH_4-CH_4 were determined. The samples were taken up to a radial distance of 12 Å, but the *x*-axis has been truncated at 8 Å because only the first peaks are of interest in the discussions to follow. The plotted RDF data has been normalized such that the area under each of the curves is identical to one another (and equals 1000). Figure S82a presents the RDF data for a total fugacity f_t = 1 MPa and y_1=0.01. If we compare the first peaks, it is noteworthy that the CO_2-CO_2, and CO_2-Na^+ pairs are close together, indicating that the major proportion of CO_2 congregates around the cations. A further point to note is that the CO_2-CH_4 separation distance is significantly higher than the CO_2-CO_2 and CH_4-CH_4 separation distances. This implies that the CH_4 molecules face a less severe competitive adsorption with CO_2 than is anticipated by the IAST.

A visual appreciation of the congregation effects can be gained from the snapshot presented in Figure S83.

The primary reason for the congregation of CO_2 molecules is the presence of cations. In order to demonstrate this, we also carried out CBMC simulations for adsorption of CO_2/CH_4 mixtures in all-silica zeolite at a total fugacity f_t = 500 kPa and y_1=0.2 at 300 K. The RDF data on the distances between the molecular pairs CO_2-CO_2, CO_2-CH_4, and CH_4-CH_4 are shown in Figure S82b. We note that the peaks occur at practically the same intermolecular distances. This indicates that there are no congregation effects and that the guest molecules are homogeneously distributed within the pore landscape. Such a homogeneous distribution of guest molecules fulfils the requirement of the IAST theory. Consequently, we should expect the IAST to provide a good quantitative description of CO_2/CH_4 mixture adsorption in all-silica zeolite.

To confirm this expectation, Figure S84a compares the CBMC simulated values of the adsorption selectivity for 50/50 CO_2/CH_4, 20/80 CO_2/CH_4, 15/85 CO_2/N_2, 20/80 CO_2/N_2, and 20/40/40 CO_2/CH_4/N_2 mixtures in all-silica FAU with the corresponding IAST calculations. The CO_2/CH_4, and CO_2/N_2 selectivities are uniquely determined by the surface potential Φ, irrespective of the composition of the bulk fluid phase mixture and the presence of the third component. The IAST estimations are in good agreement with the CBMC simulated values of S_{ads}.

In sharp contrast, the IAST calculations severely over-predict the adsorption selectivity for equimolar CO_2/CH_4 mixtures in NaX zeolite because the actual competition faced by CH_4 is less severe due to congregation effects; Figure S84b. Also shown in Figure S84b are the CBMC data for CO_2/CH_4 mixture adsorption in NaY zeolite (138 Si, 54 Al, 54 Na^+, Si/Al=2.56); the IAST estimates are also in excess of the CBMC data, but the departures are less than that experienced with NaX.

15.2 CO_2/C_3H_8 mixture adsorption in NaX zeolite

Three different CBMC simulation campaigns were conducted for CO_2/C_3H_8 mixture adsorption in NaX zeolite at 300 K. In Campaign A the composition of the bulk fluid mixture was maintained at y_1=0.5, and the total fluid phase mixture fugacity f_t was varied; the data analysis is shown in Figure S85. Figure S86, and Figure S87 show the results of two CBMC campaigns in which in which the total bulk fluid phase fugacity was maintained, respectively, at f_t = 50 kPa, and f_t = 1 MPa. The CBMC data for all three data sets were combined to determine the Margules parameters for use in the RAST.

With increasing f_t the IAST estimates become progressively worse; see Figure S85c. The RAST estimates of the component loadings are in good agreement with the CBMC data, as is to be expected. The RAST calculations of the activity coefficients of CO_2, and C_3H_8 are shown in Figure S85e,f. Figure S86c, and Figure S87c. It is noteworthy that the activity coefficient of CO_2 is virtually unity over the entire composition range. On the other hand, the activity coefficient of C_3H_8 shows increasing departure from unity with increasing bulk fluid phase fugacity f_t. The activity coefficient of C_3H_8 shows increasing departure from unity with increasing mole fraction of CO_2 in the adsorbed phase, x_1.

Figure S88 plots the adsorption selectivity S_{ads} for $CO_2(1)/C_3H_8(2)$ mixture adsorption in NaX zeolite at 300 K for three different campaigns (Campaign A (y_1= 0.5) and Campaign B (f_t = 1 MPa, and f_t = 50 kPa), plotted as function of the surface potential Φ. The IAST anticipates an unique dependence of S_{ads}

on Φ. The CBMC data however show that S_{ads} is not uniquely determined by surface potential Φ due to non-idealities that vary with composition of the adsorbed mixture.

Particularly remarkable are the results of Campaign B in which the total bulk fluid phase fugacity is maintained at f_t = 50 kPa; see Figure S86. We note that as the mole fraction of CO_2 in the bulk gas phase, y_1, is increased, the CBMC data shows selectivity reversal at $y_1 > 0.8$, in agreement with the experimental findings of Costa et al.[65] This selectivity reversal in disfavor of CO_2 is not anticipated by the IAST.

The failure of the IAST to provide quantitatively accurate estimates of component loadings, and adsorption selectivities is attributable to the inhomogeneous distribution of adsorbates in the pore space of NaX zeolite, caused by strong binding of CO_2 with the extra-framework cations. The inhomogeneous distribution is clearly visualized by the computational snapshot in Figure S89 for f_1 = 0.5 MPa, and f_2 = 0.5 MPa. We note that the bottom cage contains only CO_2, and there is no C_3H_8 present in that cage. One of the key assumptions of the IAST is that the distribution of adsorbates within the pore space is homogenous.

To quantify the inhomogeneous distribution of adsorbates, the CBMC simulation data on the spatial locations of the guest molecules were sampled to determine the inter-molecular distances. By sampling a total of 10^7 simulation steps, the radial distribution of the separation distances between the molecular pairs CO_2-CO_2, CO_2-Na^+, CO_2-C_3H_8, and C_3H_8-C_3H_8 were determined. Figure S90 presents the RDF data for a total fugacity f_t = 1 MPa and y_1=0.5. The samples were taken up to a radial distance of 12 Å, but the *x*-axis has been truncated at 8 Å because only the first peaks are of interest in the discussions to follow. The plotted RDF data has been normalized such that the area under each of the curves is identical to one another (and equals 1000). If we compare the first peaks, it is noteworthy that the CO_2-CO_2, and CO_2-Na^+ pairs are close together, indicating that the major proportion of CO_2 congregates around the cations. A further point to note is that the CO_2-C_3H_8 separation distance is significantly higher than the CO_2-CO_2 and CO_2-Na^+ separation distances. This implies that the C_3H_8 molecules face a less severe competitive adsorption with CO_2 than is anticipated by the IAST.

Mixture adsorption in FAU (all-silica) and NaX zeolites

A different way to establish the reasons for the failure of the IAST is to compare the adsorption selectivities of CO_2(1)/C_3H_8(2) and CH_4(1)/C_3H_8(2) mixtures. For the mixture of alkanes, there are no segregation effects to be expected, and the IAST estimates are in good agreement with CBMC simulation data; see Figure S91. The IAST estimates become poor when we replace CH_4 by CO_2.

15.3 List of Tables for Mixture adsorption in FAU (all-silica) and NaX zeolites

Table S17. Dual-site Langmuir parameters for pure components CO_2, CH_4, and C_3H_8 at 300 K in NaX zeolite containing 86 Na^+/uc with Si/Al=1.23. The fit parameters are based on the CBMC simulations of pure component isotherms.

	Site A		Site B	
	$q_{A,sat}$ mol kg^{-1}	b_A Pa^{-1}	$q_{B,sat}$ mol kg^{-1}	b_B Pa^{-1}
CO_2	1.7	1.39×10^{-5}	4.2	4.78×10^{-4}
CH_4	5.8	2.07×10^{-6}		
C_3H_8	3.1	8.91×10^{-4}	0.65	4.09×10^{-6}

Fitted Margules non-ideality parameters for binary mixture adsorption in NaX at 300 K.

	C / kg mol^{-1}	A_{12}	A_{21}
CO_2/CH_4 in NaX	1.021	-0.632	-0.693
CO_2/C_3H_8 in NaX	0.038	-3.082	-2.170

Table S18. Dual-site Langmuir-Freundlich parameters for pure components CO_2, CH_4, H_2,and N_2 at 300K in all-silica FAU. The fit parameters are based on the CBMC simulations of pure component isotherms presented in earlier works.[11, 64, 66]

	Site A			Site B		
	$q_{A,sat}$ mol kg^{-1}	b_A Pa $^{-\nu_A}$	ν_A dimensionless	$q_{B,sat}$ mol kg^{-1}	b_B Pa $^{-\nu_B}$	ν_B dimensionless
CO_2	2.4	2.52×10^{-14}	2.4	6.7	6.74×10^{-7}	1
CH_4	4	7×10^{-9}	0.86	6.5	2.75×10^{-7}	1
H_2	6.9	3.506E-08	1	16.7	3.848E-09	1
N_2	5.2	1.55×10^{-9}	1	5.8	1.32×10^{-7}	1

15.4 List of Figures for Mixture adsorption in FAU (all-silica) and NaX zeolites

FAU all-silica structural details

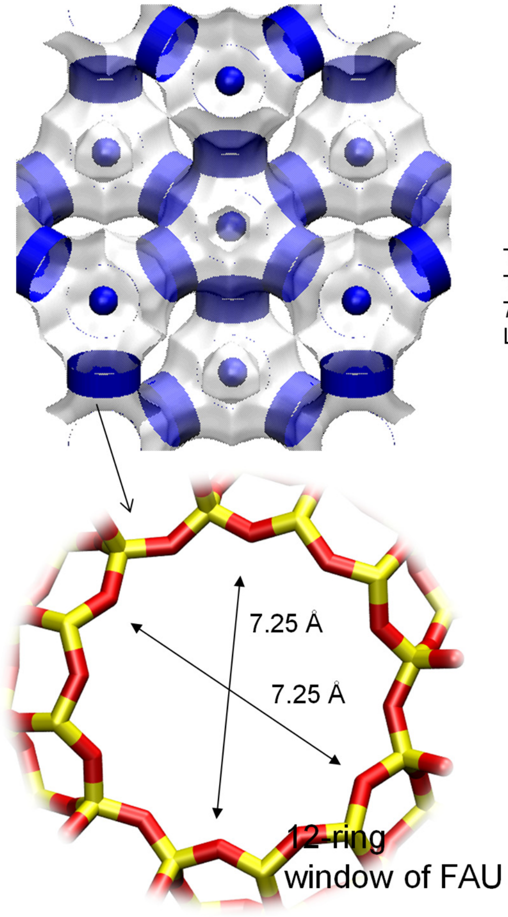

There are 8 cages per unit cell.
The volume of one FAU cage is
786 Å^3, larger in size than that of
LTA (743 Å^3) and DDR (278 Å^3).

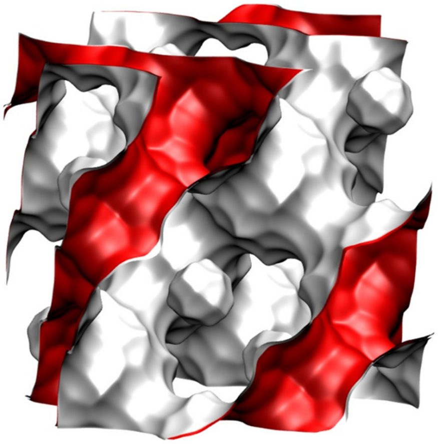

	FAU-Si
a /Å	24.28
b /Å	24.28
c /Å	24.28
Cell volume / Å^3	14313.51
conversion factor for [molec/uc] to [mol per kg Framework]	0.0867
conversion factor for [molec/uc] to [kmol/m^3]	0.2642
ρ [kg/m3]	1338.369
MW unit cell [g/mol (framework)]	11536.28
ϕ, fractional pore volume	0.439
open space / Å^3/uc	6285.6
Pore volume / cm^3/g	0.328
Surface area /m^2/g	1086.0
DeLaunay diameter /Å	7.37

Figure S78. Pore landscape for all-silica FAU zeolite.

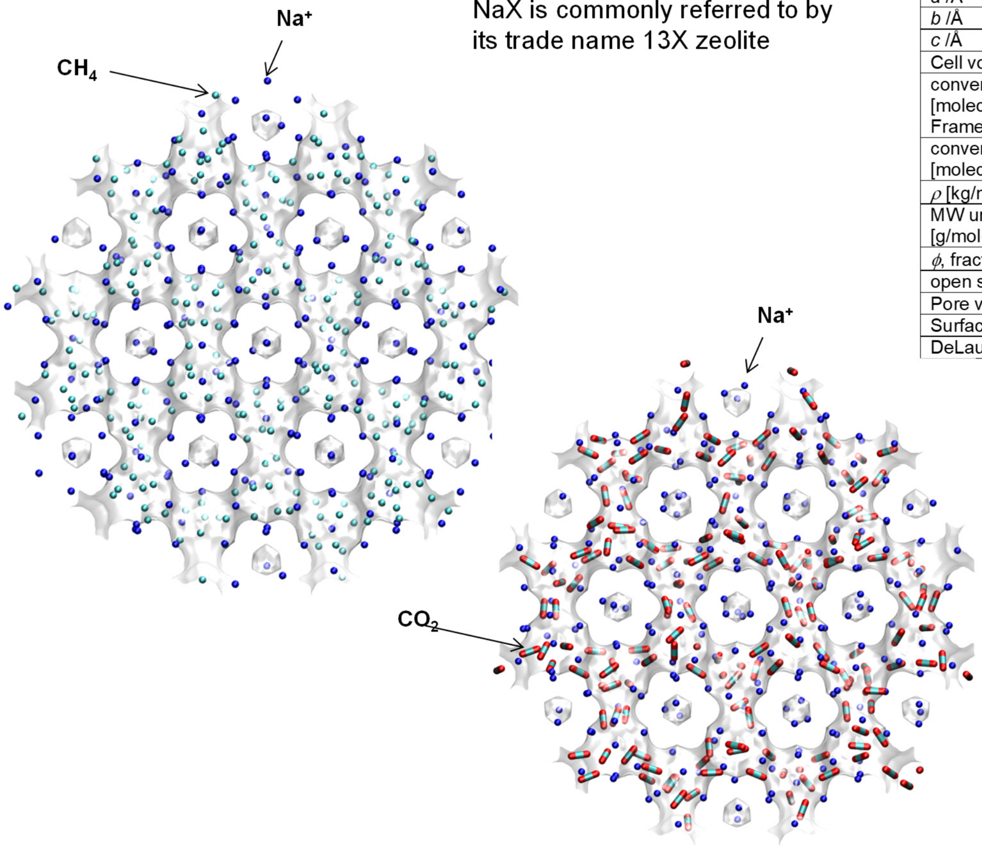

NaX is commonly referred to by its trade name 13X zeolite

	NaX 86 Na/uc
a /Å	25.028
b /Å	25.028
c /Å	25.028
Cell volume / Å^3	15677.56
conversion factor for [molec/uc] to [mol per kg Framework]	0.0745
conversion factor for [molec/uc] to [kmol/m^3]	0.2658
ρ [kg/m3] (with cations)	1421.277
MW unit cell [g/mol(framework+cations)]	13418.42
ϕ, fractional pore volume	0.399
open space / Å^3/uc	6248.0
Pore volume / cm^3/g	0.280
Surface area /m^2/g	
DeLaunay diameter /Å	7.37

Figure S79. Structural details for NaX zeolite (106 Si, 86 Al, 86 Na$^+$, Si/Al=1.23)

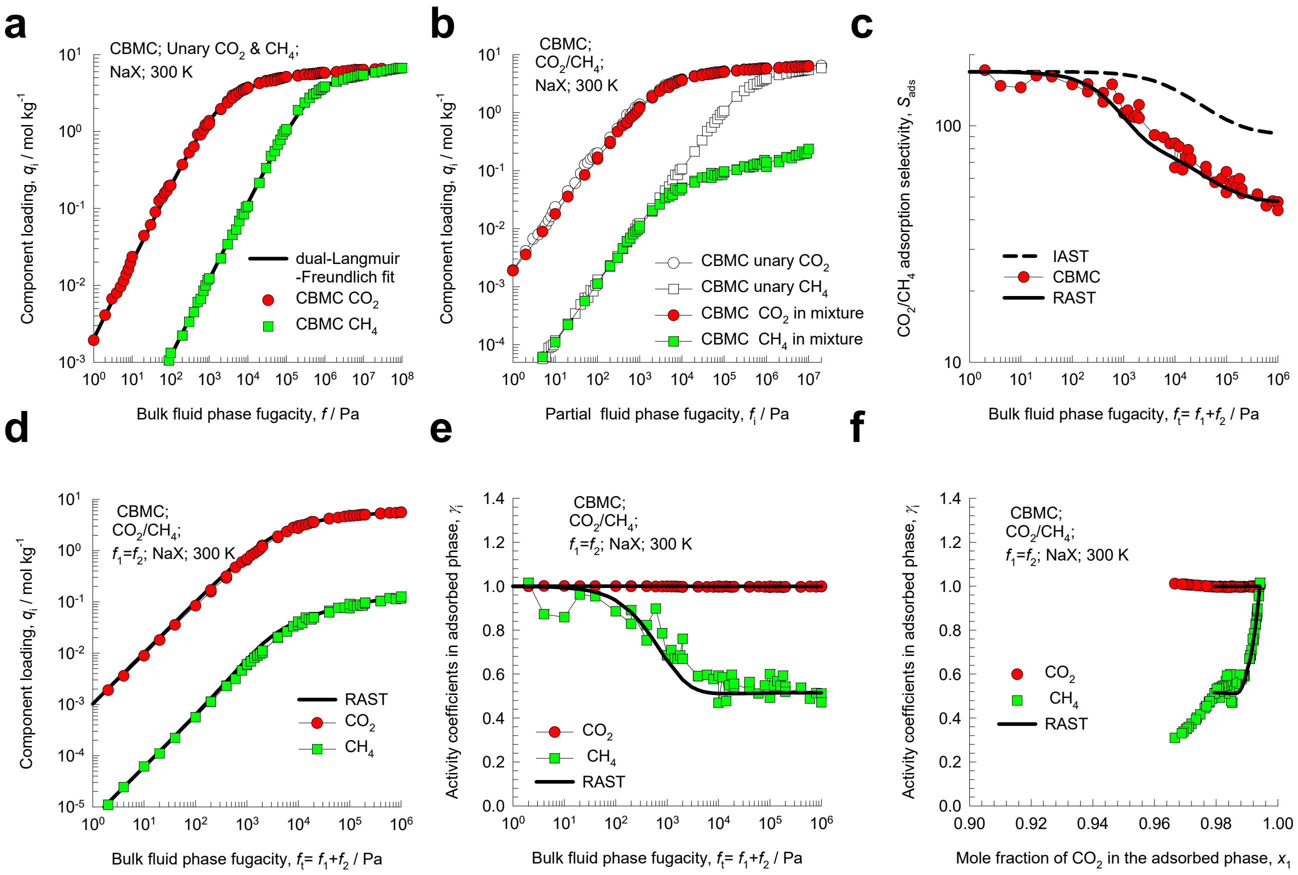

Figure S80. CBMC simulation data and analysis for Campaign A (y_1= 0.5) for CO_2(1)/CH_4(2) mixture adsorption in NaX zeolite at 300 K. (a) Unary isotherms and fits. (b) Component loadings in mixture compared with CBMC simulations of unary isotherms. (c) CBMC data for CO_2(1)/CH_4(2) adsorption selectivity compared with IAST and RAST estimates. (d) CBMC data for component loadings in mixture compared with RAST estimates. (e, f) Activity coefficients from CBMC compared with RAST model calculations. The unary isotherm fit parameters and Margules parameters are provided in Table S17.

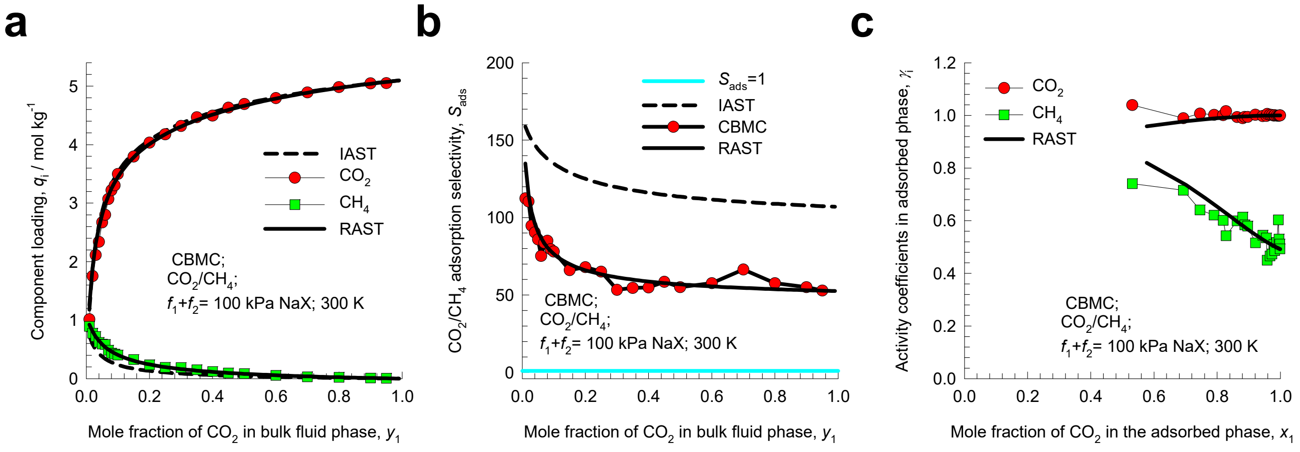

Figure S81. CBMC simulation data and analysis for Campaign B (f_t = 100 kPa) for CO_2(1)/CH_4(2) mixture adsorption in NaX zeolite at 300 K. CBMC data for (a) component loadings and (b) CO_2(1)/ CH_4(2) adsorption selectivity compared with IAST and RAST estimates. (c) Activity coefficients from CBMC compared with RAST model calculations. The unary isotherm fit parameters and Margules parameters are provided in Table S17.

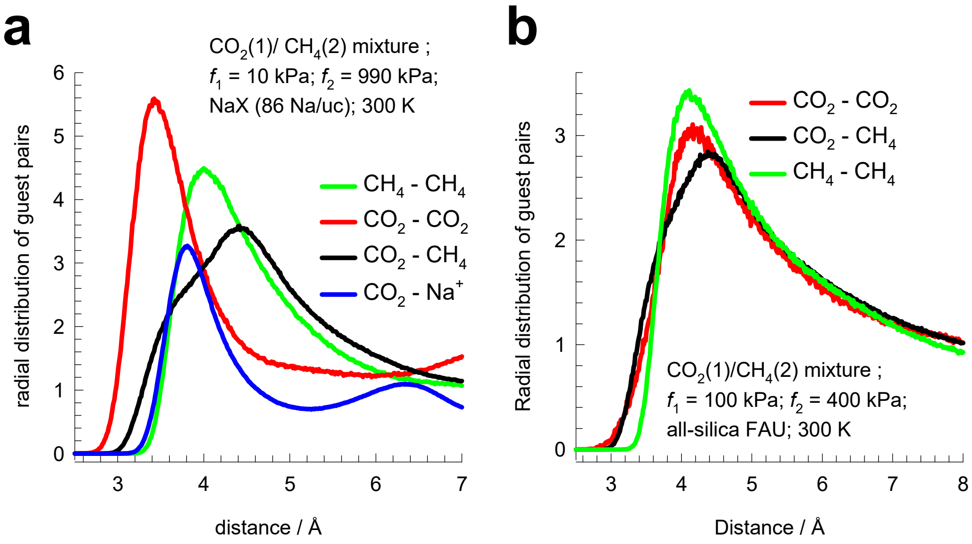

Figure S82. (a) Radial distribution of guest pairs determined from CBMC simulations for adsorption of CO_2/CH_4 mixtures in NaX zeolite at 300 K and total fugacity f_t = 1 MPa, and y_1=0.01. (b) Radial distribution of guest pairs determined from CBMC simulations for adsorption of CO_2/CH_4 mixtures in all-silica FAU zeolite at 300 K and total fugacity f_t = 500 kPa, and y_1=0.2.

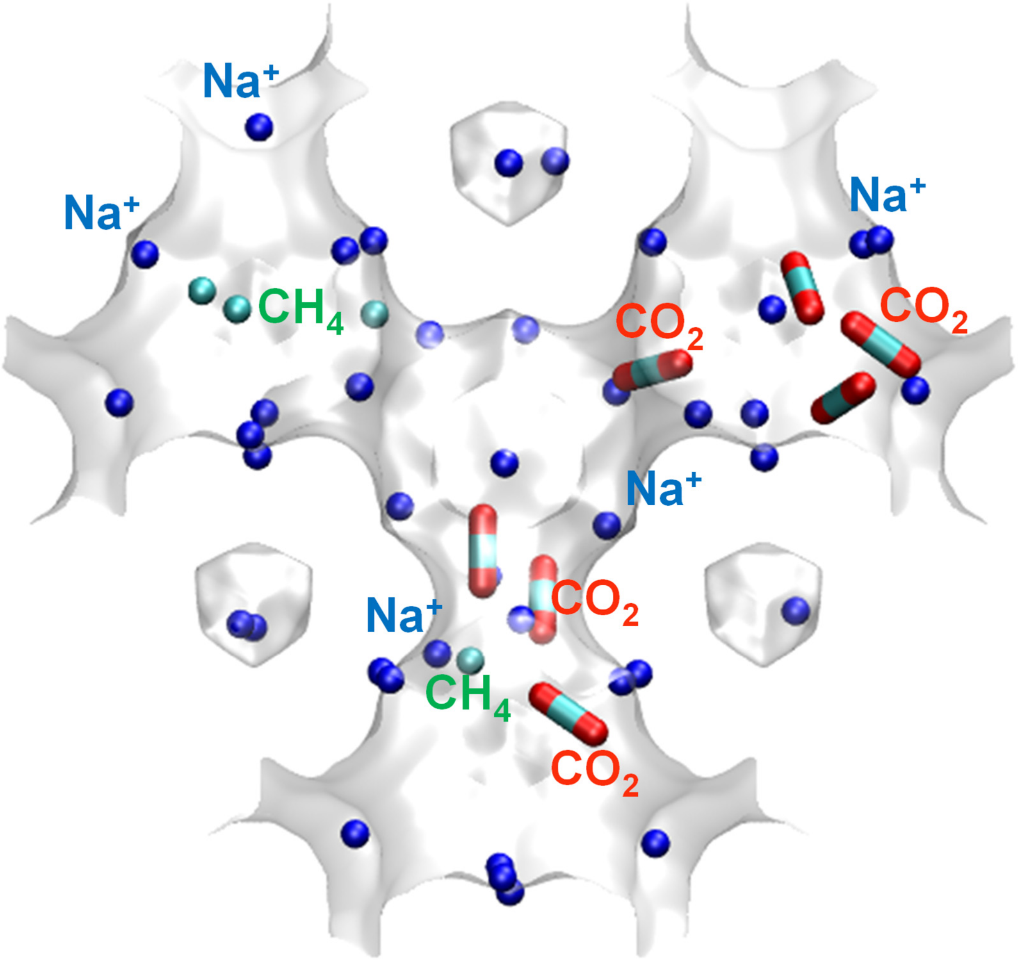

Figure S83. Snapshot showing the location of CO_2, CH_4, and Na+ cations within the pore landscape of NaX (106 Si, 86 Al, 86 Na^+, Si/Al=1.23) zeolite at 300 K and total fugacity f_t = 100 kPa, and y_1=0.02.

Mixture adsorption in FAU (all-silica) and NaX zeolites

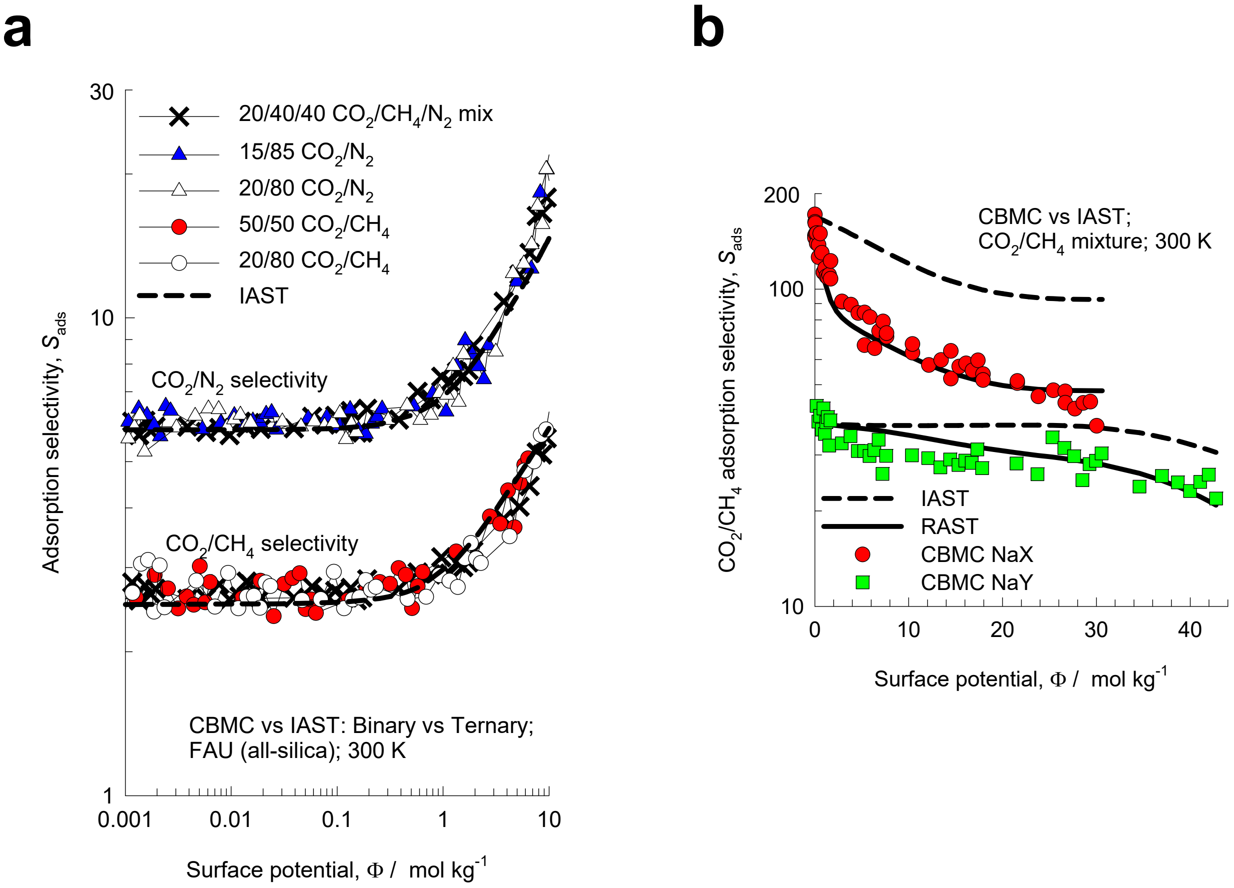

Figure S84. (a) CBMC data for adsorption selectivity of 50/50 CO_2/CH_4, 20/80 CO_2/CH_4, 15/85 CO_2/N_2, 20/80 CO_2/N_2, and 20/40/40 $CO_2/CH_4/N_2$ mixtures in all-silica FAU. (b) Comparison CO_2/CH_4 adsorption selectivities determined from CBMC simulations for NaY (138 Si, 54 Al, 54 Na^+, Si/Al=2.56), and NaX (106 Si, 86 Al, 86 Na^+, Si/Al=1.23) zeolites for at 300 K. The *x*-axes represent the surface potential Φ. The continuous solid and dashed lines are the RAST, and IAST estimations, respectively.

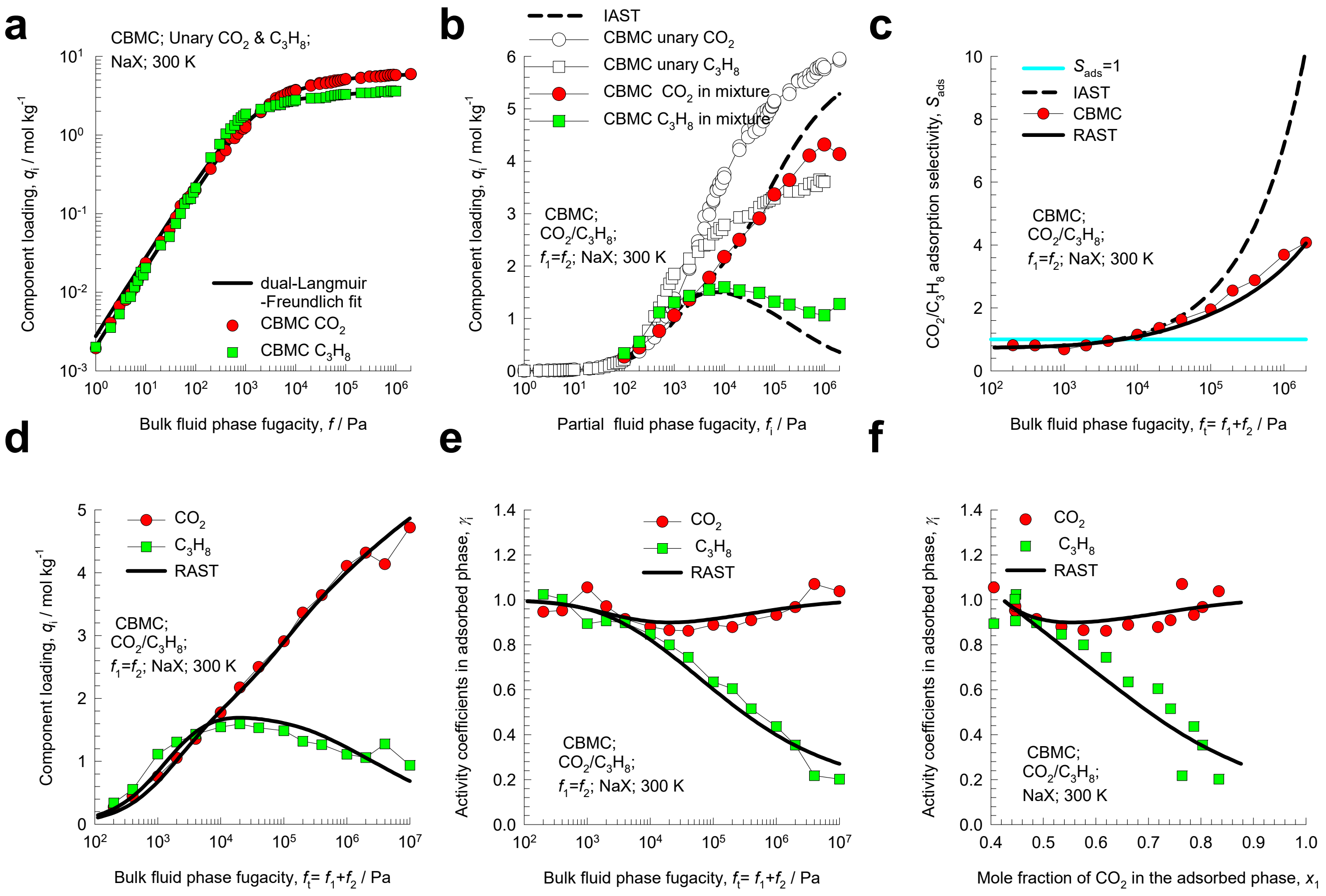

Figure S85. CBMC simulation data and analysis for Campaign A (y_1= 0.5) for CO_2(1)/C_3H_8(2) mixture adsorption in NaX zeolite at 300 K. (a) Unary isotherms and fits. (b) Component loadings in mixture compared with CBMC simulations of unary isotherms. (c) CBMC data for CO_2(1)/C_3H_8(2) adsorption selectivity compared with IAST and RAST estimates. (d) CBMC data for component loadings in mixture compared with RAST estimates. (e, f) Activity coefficients from CBMC compared with RAST model calculations. The unary isotherm fit parameters and Margules parameters are provided in Table S17.

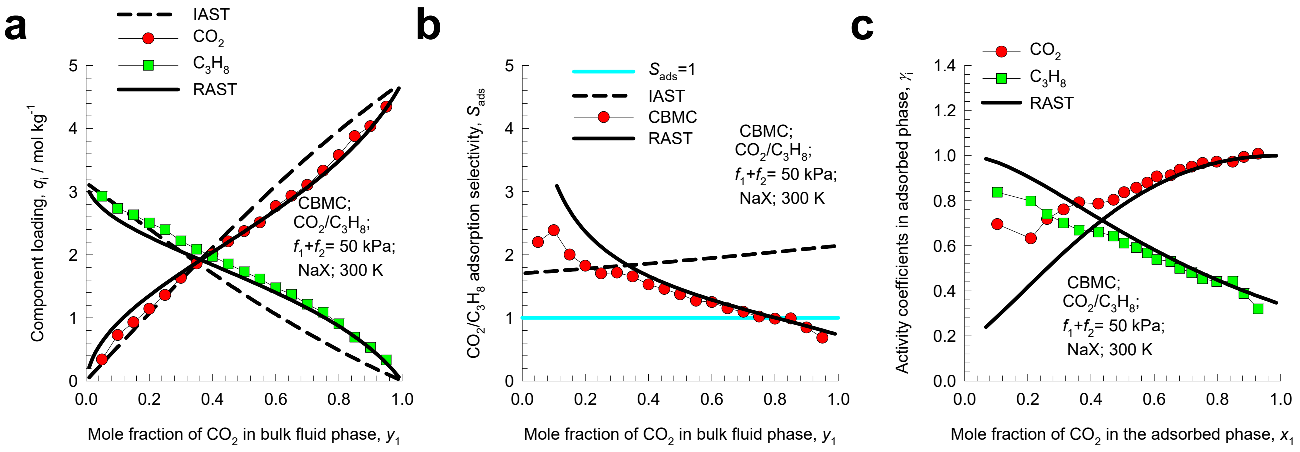

Figure S86. CBMC simulation data and analysis for Campaign B (f_t = 50 kPa) for CO_2(1)/C_3H_8(2) mixture adsorption in NaX zeolite at 300 K. CBMC data for (a) component loadings and (b) CO_2(1)/ C_3H_8(2) adsorption selectivity compared with IAST and RAST estimates. (c) Activity coefficients from CBMC compared with RAST model calculations. The unary isotherm fit parameters and Margules parameters are provided in Table S17.

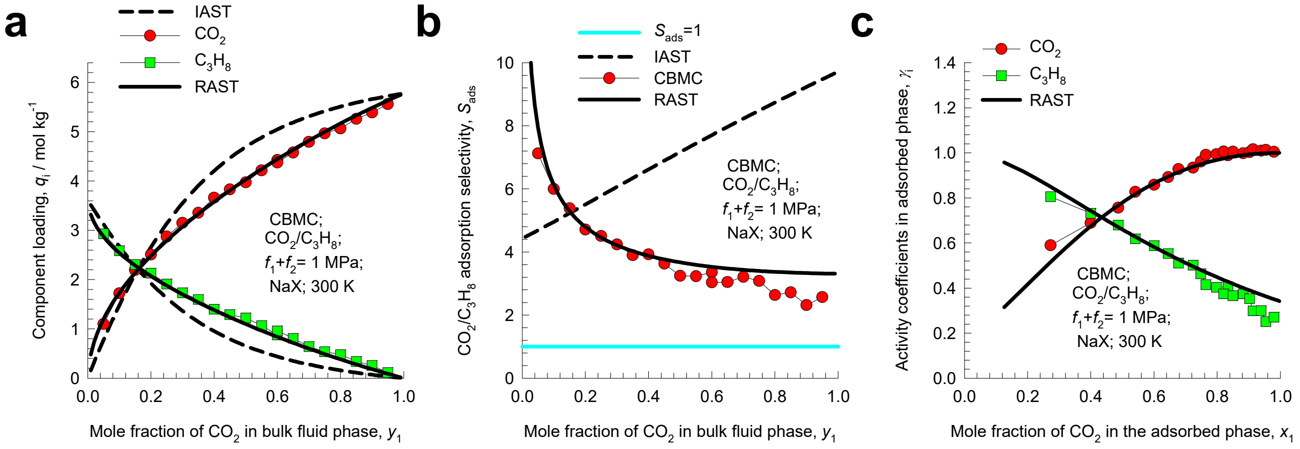

Figure S87. CBMC simulation data and analysis for Campaign B (f_t = 1 MPa) for CO_2(1)/C_3H_8(2) mixture adsorption in NaX zeolite at 300 K. CBMC data for (a) component loadings and (b) CO_2(1)/ C_3H_8(2) adsorption selectivity compared with IAST and RAST estimates. (c) Activity coefficients from CBMC compared with RAST model calculations. The unary isotherm fit parameters and Margules parameters are provided in Table S17.

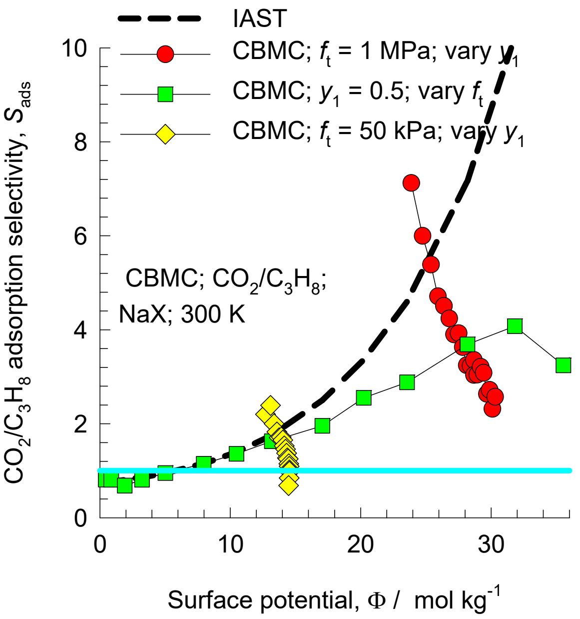

Figure S88. Adsorption selectivity S_{ads} for CO_2(1)/C_3H_8(2) mixture adsorption in NaX zeolite at 300 K for three different campaigns (Campaign A (y_1= 0.5) and Campaign B (f_t = 1 MPa, and f_t = 50 kPa), plotted as function of the surface potential Φ. The CBMC simulated values (indicated by symbols) are compared with IAST estimates (indicated by the dashed lines). The unary isotherm fit parameters and Margules parameters are provided in Table S17.

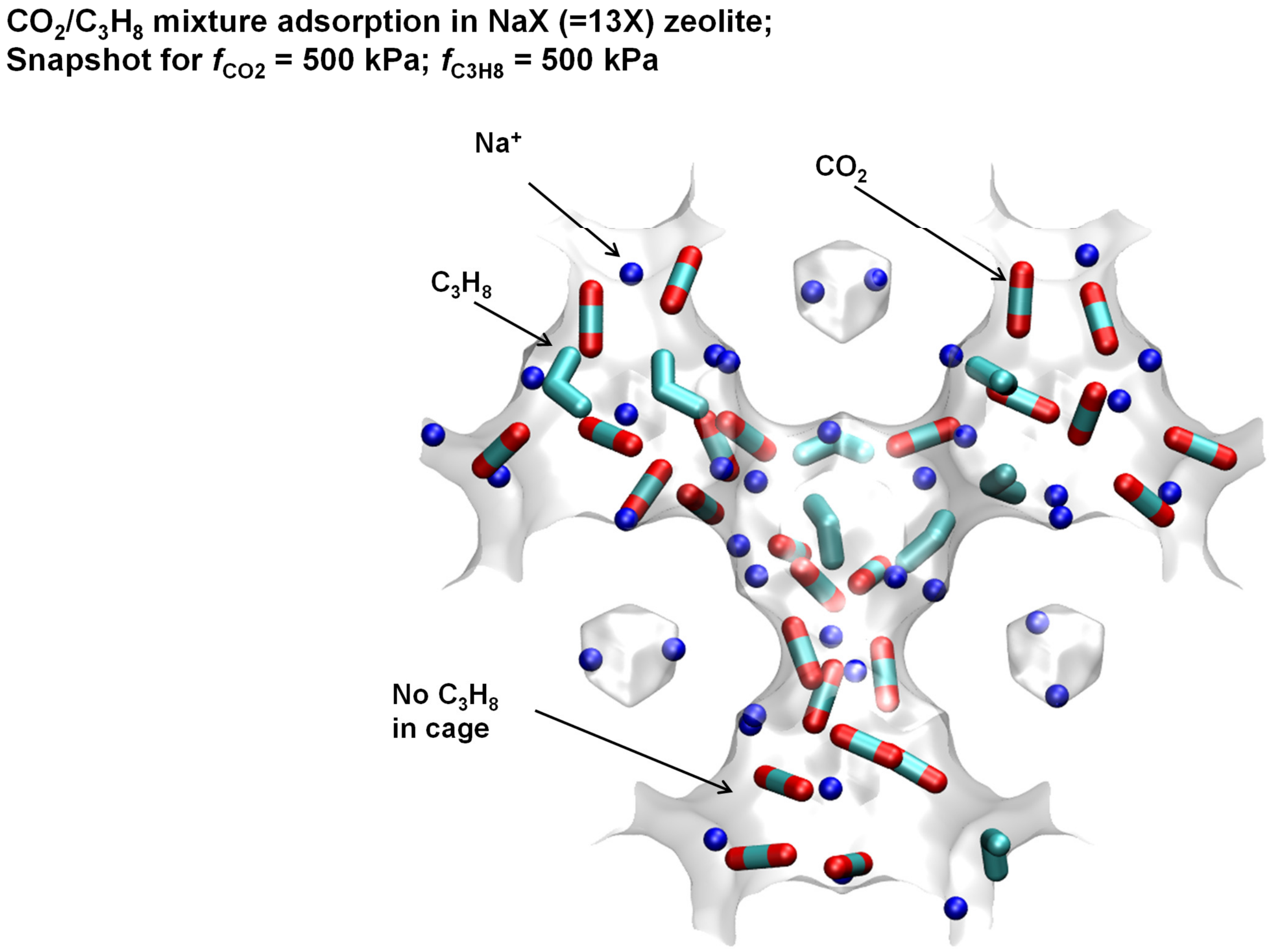

Figure S89. Computational snapshots showing the location of CO_2, and C_3H_8 within the cages of NaX zeolite at 300 K and total fugacity f_t = 1 MPa. The component partial fugacities are f_1 = 0.5 MPa, and f_2 = 0.5 MPa.

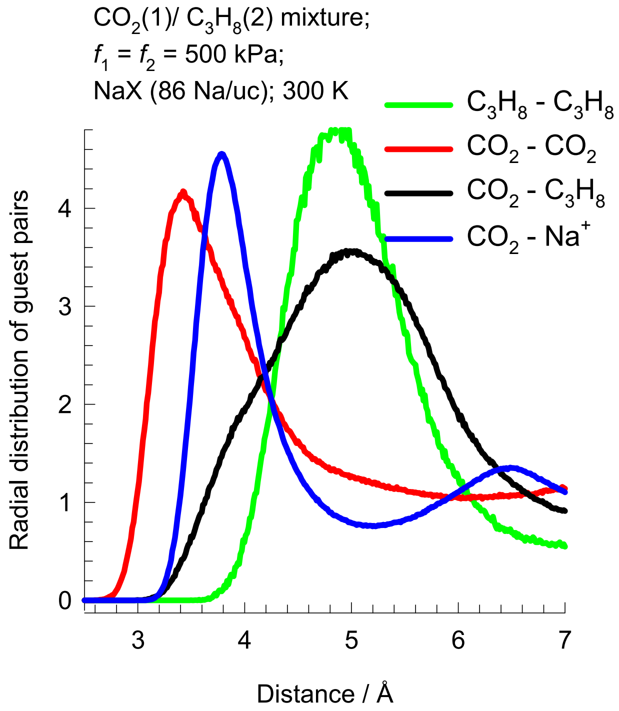

Figure S90. Radial distribution of guest pairs determined from CBMC simulations for adsorption of CO_2/C_3H_8 mixtures in NaX zeolite at 300 K and total fugacity f_t = 1 MPa, and y_1=0.5.

.

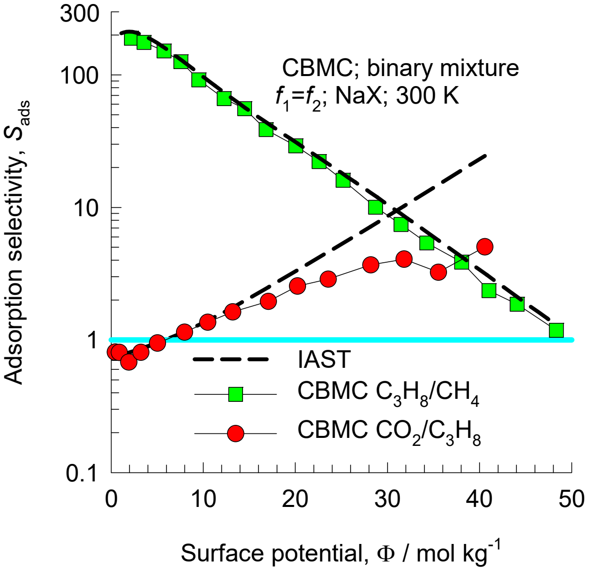

Figure S91. Adsorption selectivity S_{ads} for equimolar $\left(f_1 = f_2;\quad y_1 = 0.5\right)$ CO_2(1)/C_3H_8(2) and C_3H_8(1)/ CH_4(2) mixture adsorption in NaX zeolite at 300 K, plotted as function of the surface potential Φ. The CBMC simulated values (indicated by symbols) are compared with IAST estimates (indicated by the dashed lines).

16 CO_2/CH_4 mixture adsorption in Mg_2(dobdc)

The pore landscapes and structural details of Mg_2(dobdc) are presented in Figure S92, and Figure S93. This MOF consists of 1D hexagonal-shaped channels of 11 Å.

Computational snapshots in Figure S94 demonstrate that CO_2 molecules are in close proximity to the open metal Mg^{2+} sites, whereas non-polar guests such as CH_4 are farther removed and are predominantly located at the channel interiors. Put another way, the guest molecules for CO_2/CH_4 mixture adsorption are distributed non-homogeneously within the channels.

Figure S95 presents CBMC simulation data for adsorption of equimolar (partial fugacities $f_1=f_2$) CO_2/CH_4 mixtures in Mg_2(dobdc) at 300 K. The conventional IAST calculation assumes that CH_4 molecules compete with *all* of the CO_2, making no allowance for segregation. Due to segregation effects the competition faced by CH_4 molecules within the channel interiors, where they almost exclusively reside, is *smaller* than that in the entire pore space. The IAST anticipates a stiffer competition between CO_2 and CH_4 as it assumes a uniform distribution of composition; consequently, the adsorption selectivity is *over*estimated. The estimations of the RAST with fitted Wilson parameters, are shown by the continuous solid lines.

Figure S96 plots the adsorption selectivity S_{ads} for equimolar $\left(f_1=f_2;\quad y_1=0.5\right)$ $CO_2(1)/CH_4(2)$ and $CO_2(1)/N_2(2)$ mixture adsorption in Mg_2(dobdc) at 300 K, as function of the surface potential Φ. The CBMC simulated values (indicated by symbols) are compared with IAST estimates (indicated by the dashed lines). For both mixtures, the IAST tends to overestimate the selectivities due to segregated nature of adsorption.

16.1 List of Tables for CO2/CH4 mixture adsorption in Mg2(dobdc)

Table S19. Dual-site Langmuir-Freundlich parameters for guest molecules in Mg_2(dobdc) at 300 K.

	Site A			Site B		
	$q_{A,sat}$ mol kg^{-1}	b_A $Pa^{-\nu A}$	ν_A dimensionless	$q_{B,sat}$ mol kg^{-1}	b_B $Pa^{-\nu B}$	ν_B dimensionless
CO_2	13	2.459E-05	0.97	5.5	7.650E-06	0.78
CH_4	14.4	6.709E-07	1			
N_2	13.2	2.474E-07	1			

Fitted Wilson non-ideality parameters for binary CO_2/CH_4 mixture adsorption in Mg_2(dobdc) at 300 K.

	C / kg mol^{-1}	Λ_{12}	Λ_{21}
CO_2/CH_4	0.056	3.622	0.167

16.2 List of Figures for CO2/CH4 mixture adsorption in Mg2(dobdc)

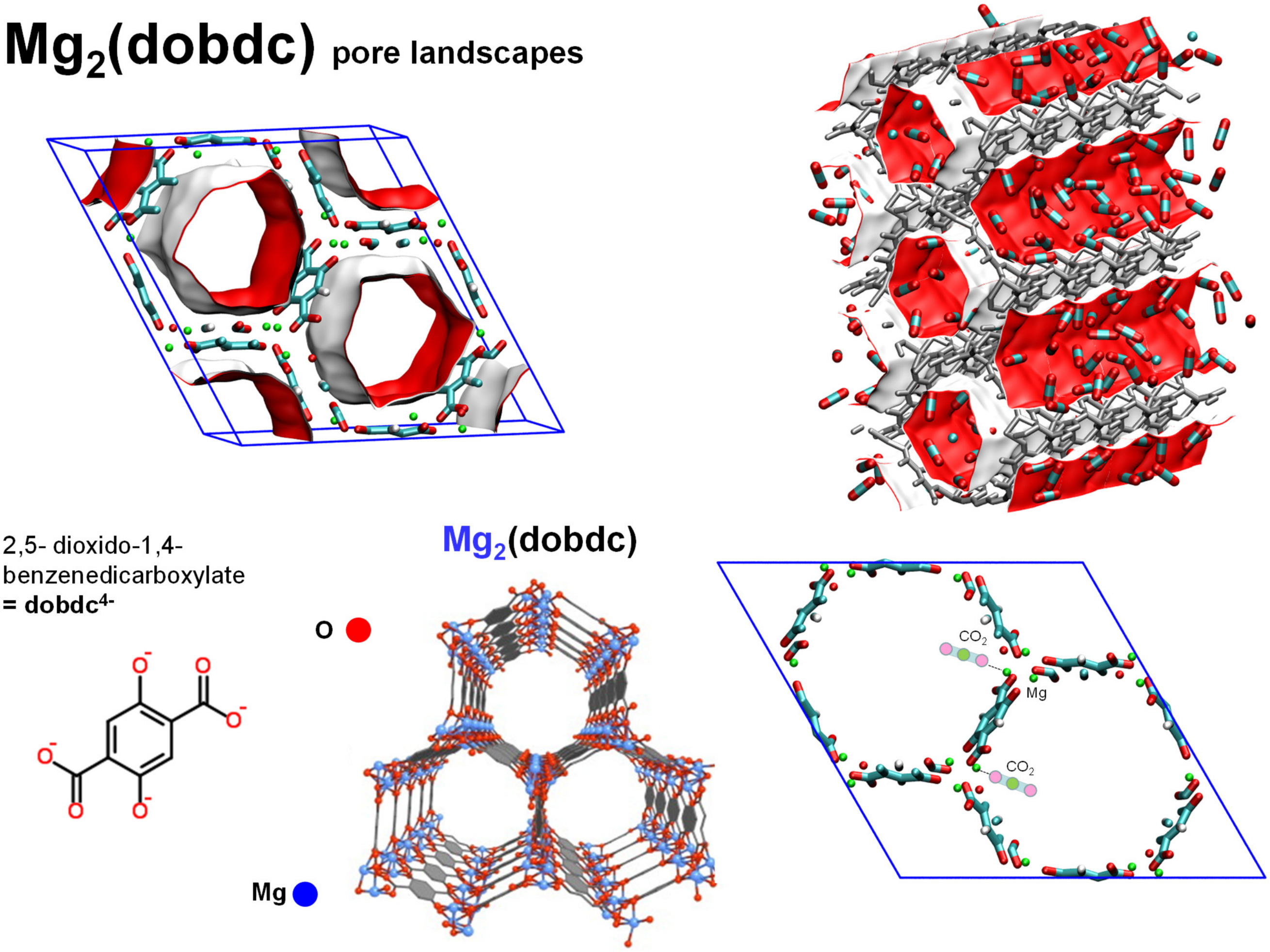

Figure S92. Pore landscape of Mg_2(dobdc).

Mg_2(dobdc) pore dimensions

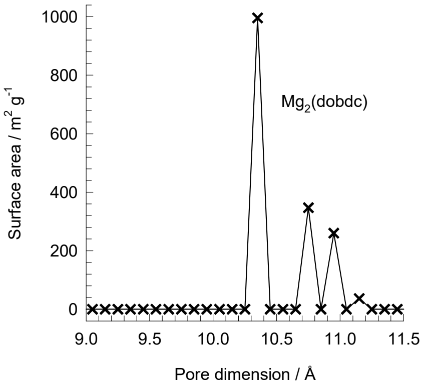

This plot of surface area versus pore dimension is determined using a combination of the DeLaunay triangulation method for pore dimension determination, and the procedure of Düren for determination of the surface area.

	MgMOF-74
a /Å	25.8621
b /Å	25.8621
c /Å	6.91427
Cell volume / Å^3	4005.019
conversion factor for [molec/uc] to [mol per kg Framework]	0.4580
conversion factor for [molec/uc] to [kmol/m^3]	0.5856
ρ [kg/m3]	905.367
MW unit cell [g/mol(framework)]	2183.601
ϕ, fractional pore volume	0.708
open space / Å^3/uc	2835.6
Pore volume / cm^3/g	0.782
Surface area /m^2/g	1640.0
DeLaunay diameter /Å	10.66

Figure S93. Structural details for Mg_2(dobdc).

$CO2/CH4$ mixture adsorption in Mg2(dobdc)

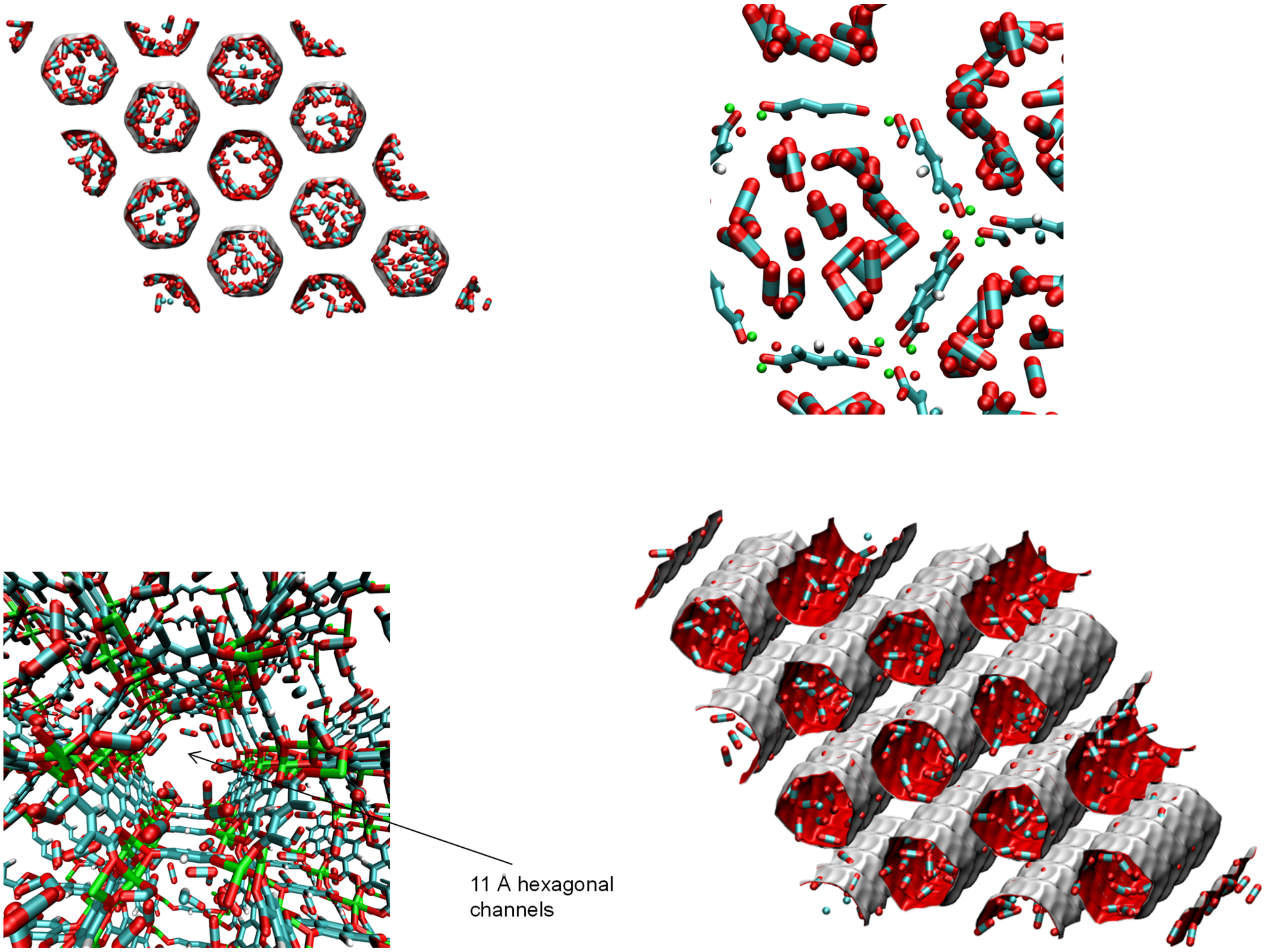

Figure S94. Snapshots showing the location of guest molecules CO_2(1), and CH_4(2) in Mg_2(dobdc) at 300 K.

CO2/CH4 mixture adsorption in Mg2(dobdc)

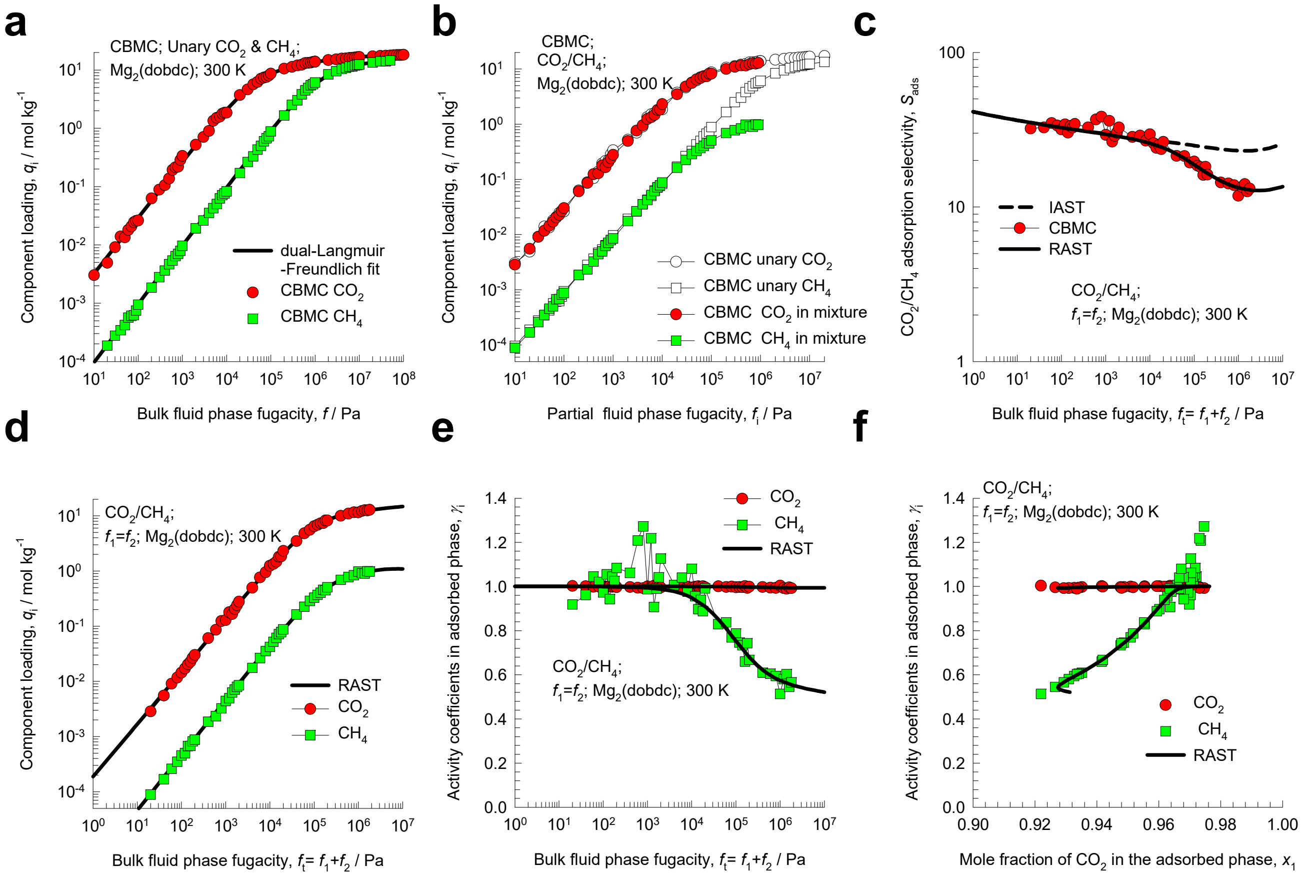

Figure S95. CBMC simulation data and analysis for equimolar $\left(f_1 = f_2; \quad y_1 = 0.5\right)$ $CO_2(1)/CH_4(2)$ mixture adsorption in Mg_2(dobdc) at 300 K. (a) Unary isotherms and fits. (b) Component loadings in mixture compared with CBMC simulations of unary isotherms. (c) CBMC data for $CO_2(1)/CH_4(2)$ adsorption selectivity compared with IAST and RAST estimates. (d) CBMC data for component loadings in mixture compared with RAST estimates. (e, f) Activity coefficients from CBMC compared with RAST model calculations. The unary isotherm fit parameters and Wilson parameters are provided in Table S19.

CO2/CH4 mixture adsorption in Mg2(dobdc)

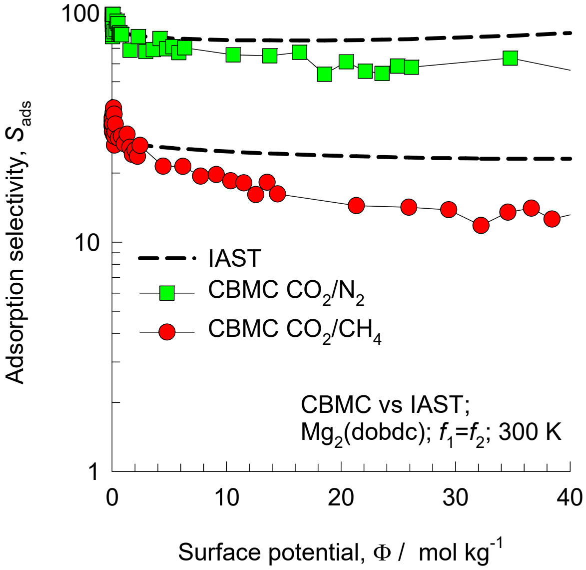

Figure S96. Adsorption selectivity S_{ads} for equimolar $(f_1 = f_2; \quad y_1 = 0.5)$ CO_2(1)/CH_4(2) and CO_2(1)/N_2(2) mixture adsorption in Mg_2(dobdc) at 300 K, plotted as function of the surface potential Φ. The CBMC simulated values (indicated by symbols) are compared with IAST estimates (indicated by the dashed lines).

17 Adsorption of hexane isomers in Mg_2(dobdc) and Co(BDP)

The separation of hexane isomers, n-hexane (nC6), 2-methylpentane (2MP), 3-methylpentane (3MP), 2,2 dimethylbutane (22DMB), and 2,3 dimethylbutane (23DMB) is required for production of high-octane gasoline. The values of the Research Octane Number (RON) increases with the degree of branching.[67] The di-branched isomers (22DMB, 23DMB) have significantly higher RON values than that of the linear isomer (nC6), and mono-branched isomers (2MP, 3MP). The RON values are: nC6 = 30, 2MP = 74.5, 3MP = 75.5, 22DMB = 94, 23DMB = 105. Therefore, di-branched isomers are preferred products for incorporation into the high-octane gasoline pool.[4, 68, 69]

Our earlier works,[4, 11, 67, 70, 71] had presented CBMC data for the adsorption of unary, ternary and 5-component mixtures of hexane isomers in a wide variety of zeolites, and MOFs. Here we analyze the adsorption of equimolar ternary $\left(f_1=f_2=f_3\right)$ nC6/3MP/22DMB and equimolar 5-component $\left(f_1=f_2=f_3=f_4=f_5\right)$ nC6/2MP.3MP/22DMB/23DMB mixtures at 433 K in two 1D MOFS: Mg_2(dobdc) (with hexagonal 11 Å channels) and Co(BDP) (with square channels of 10 Å). The The pore landscapes and structural details of Co(BDP) are presented in Figure S97, and Figure S98.

Computational snapshots of the conformation of hexane isomers within the channels of Mg_2(dobdc) Co(BDP) are shown in Figure S99, and Figure S100, respectively.

Figure S101a,b,c,d present CBMC simulation data on the component loadings for adsorption of (a, c) equimolar ternary $\left(f_1=f_2=f_3\right)$ nC6/3MP/22DMB and (b, d) equimolar 5-component $\left(f_1=f_2=f_3=f_4=f_5\right)$ C6/2MP.3MP/22DMB/23DMB mixtures at 433 K in two (a, b) Mg_2(dobdc) and (c, d) Co(BDP). These data were used to determine the nC6/3MP and 3MP/22DMB adsorption selectivities in Mg_2(dobdc) and Co(BDP), both from nC6/3MP/22DMB and nC6/2MP.3MP/22DMB/23DMB mixture simulations. The two data sets of the adsorption selectivities follow a unique dependence on the surface potential, Φ, determined using the IAST for either 3-component or 5-component mixtures as appropriate; see Figure S102 . This equivalence follows the IAST prescription of eq (S13).

Put another way, the adsorption selectivity for the 1-2 pair is independent of the presence of component 3 in the ternary mixture and of the presence of the 3,4, and 5 in the quinary mixture.

17.1 List of Tables for Adsorption of hexane isomers in Mg2(dobdc) and Co(BDP)

Table S20. Dual-site Langmuir-Freundlich parameters for pure component hexane isomers at 433 K in Mg_2(dobdc). The fits are based on CBMC simulation data of Krishna and van Baten.[11]

	Site A			Site B		
	$q_{i,A,sat}$ mol kg^{-1}	$b_{i,A}$ $Pa^{-\nu_i}$	$\nu_{i,A}$ dimensionless	$q_{i,B,sat}$ mol kg^{-1}	$b_{i,B}$ $Pa^{-\nu_i}$	$\nu_{i,B}$ dimensionless
nC6	3.3	4.396E-07	2.2	1.25	1.081E-03	0.7
2MP	3.25	2.350E-07	2.27	1.35	6.855E-04	0.76
3MP	2.25	5.478E-11	3.55	2.1	4.813E-04	1
22DMB	2.9	6.410E-06	1.5	1.45	2.514E-04	0.76
23DMB	2.8	1.401E-08	2.65	1.55	5.595E-04	0.9

Table S21. Dual-site Langmuir-Freundlich parameters for pure component hexane isomers at 433 K in Co(BDP). The fits are based on CBMC simulation data of Krishna and van Baten.[11]

	Site A			Site B		
	$q_{i,A,sat}$ mol kg^{-1}	$b_{i,A}$ Pa $^{-\nu_i}$	$\nu_{i,A}$ dimensionless	$q_{i,B,sat}$ mol kg^{-1}	$b_{i,B}$ Pa $^{-\nu_i}$	$\nu_{i,B}$ dimensionless
nC6	1.47	2.813E-04	0.77	4	2.286E-07	2
2MP	1.66	2.508E-04	0.75	3.95	6.834E-07	1.8
3MP	1.8	2.002E-04	0.76	3.9	1.151E-06	1.7
22DMB	2.06	5.431E-05	0.8	3.45	1.800E-05	1.2
23DMB	4.08	1.016E-04	1	1.1	1.055E-09	2.65

17.2 List of Figures for Adsorption of hexane isomers in Mg2(dobdc) and Co(BDP)

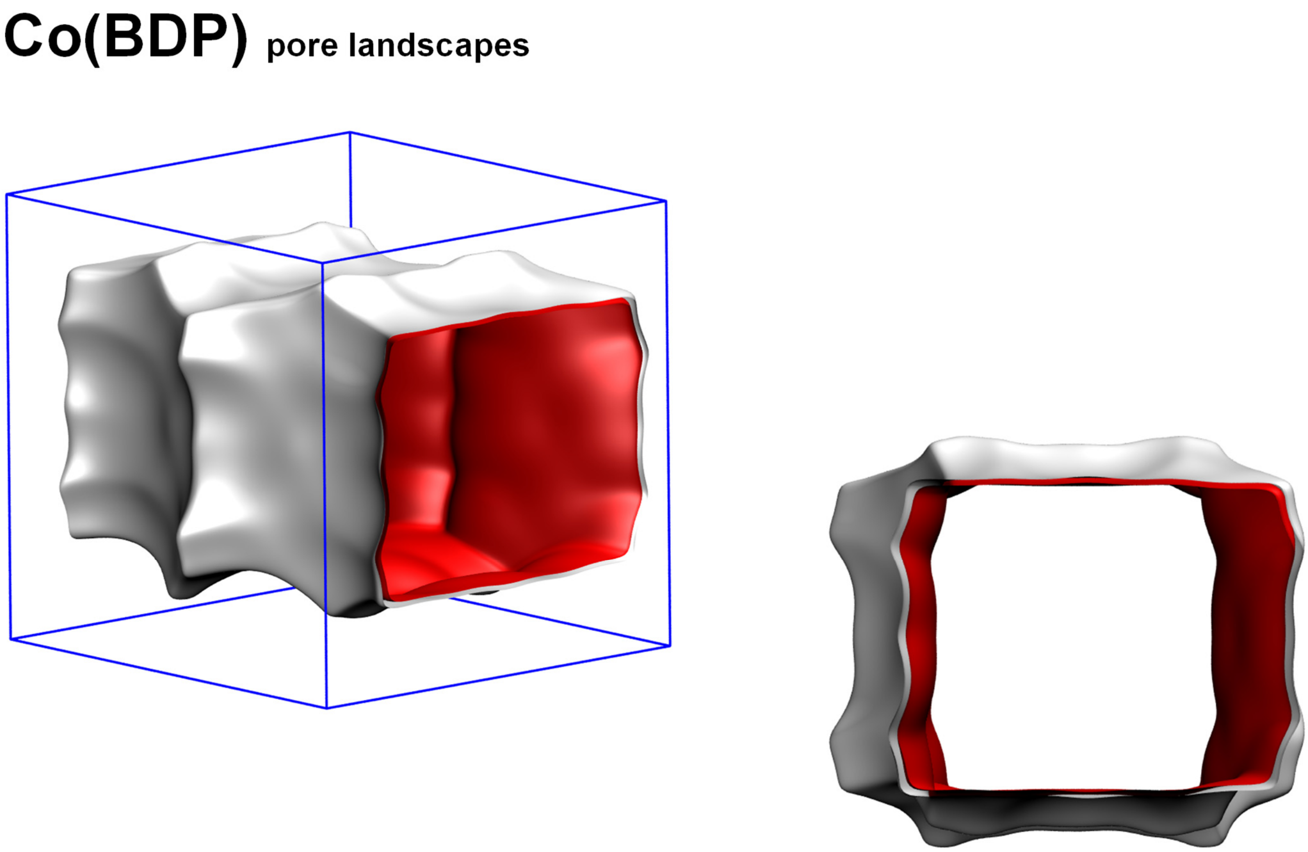

Figure S97. Pore landscape of Co(BDP)

Co(BDP) pore landscapes

	CoBDP
a /Å	13.2529
b /Å	13.253
c /Å	13.995
Cell volume / Å^3	2458.091
conversion factor for [molec/uc] to [mol per kg Framework]	0.9362
conversion factor for [molec/uc] to [kmol/m^3]	1.0102
ρ [kg/m3] (with cations)	721.5517
MW unit cell [g/mol(framework+cations)]	1068.094
ϕ, fractional pore volume	0.669
open space / Å^3/uc	1643.9
Pore volume / cm^3/g	0.927
Surface area /m^2/g	2148.8
DeLaunay diameter /Å	9.97

To convert from molecules per unit cell to mol kg^{-1}, multiply by 0.9362.
The pore volume is 0.927 cm^3/g.

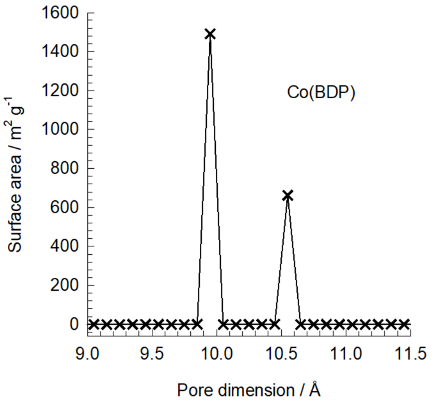

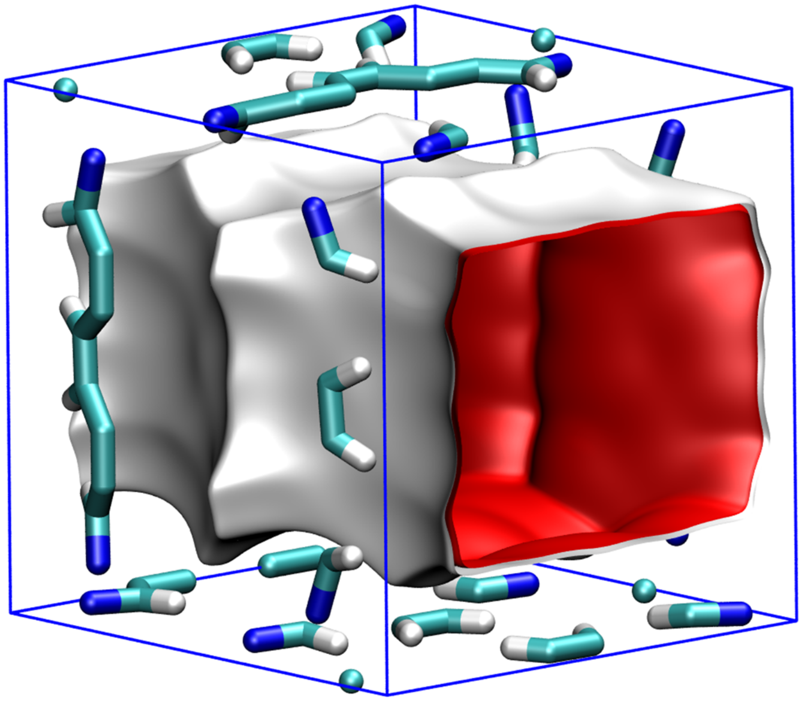

Figure S98. Structural details for Co(BDP).

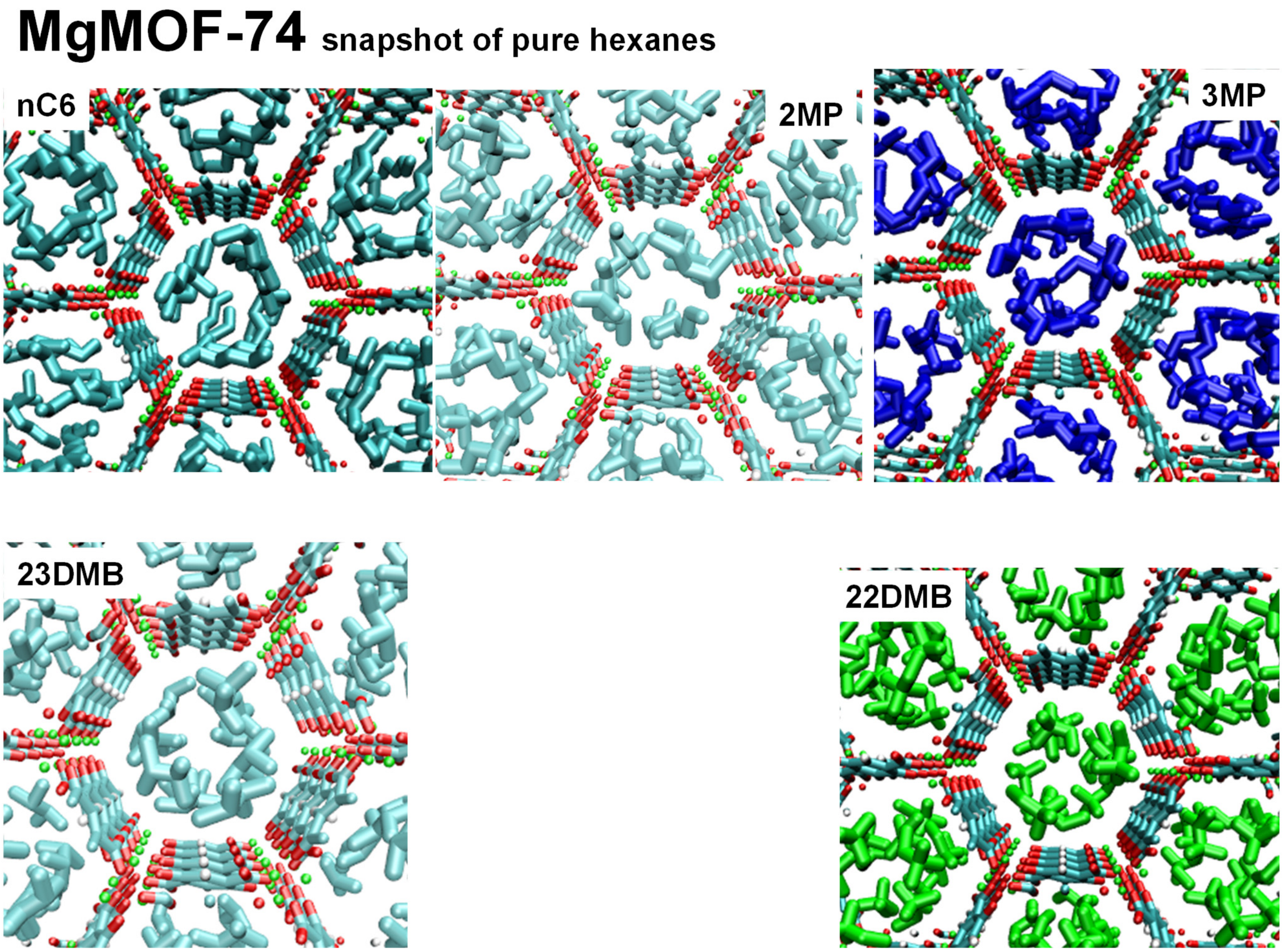

Figure S99. Computational snapshots of the conformation of hexane isomers within the 1D channels of Mg_2(dobdc).

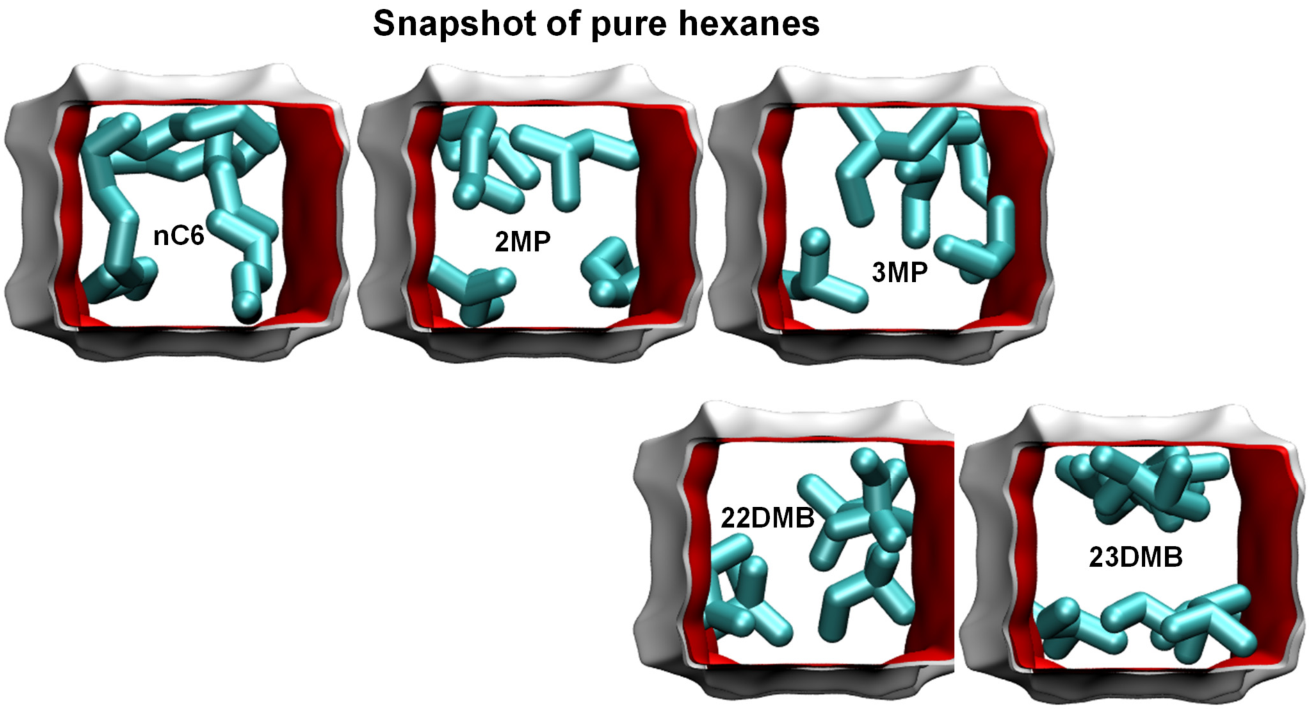

Figure S100. Computational snapshots of the conformation of hexane isomers within the 1D channels of Co(BDP).

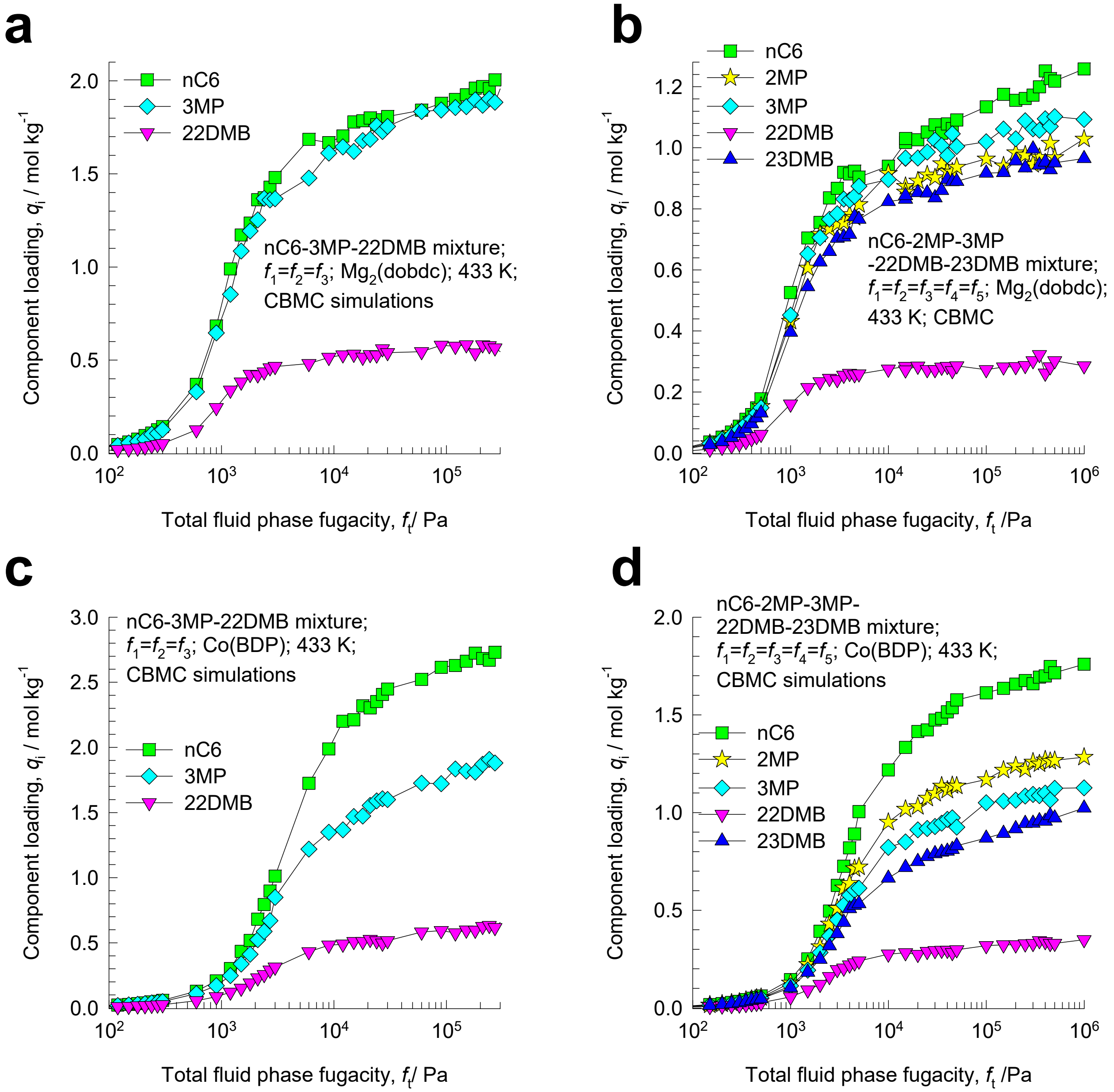

Figure S101. CBMC simulations for adsorption of (a, c) equimolar ternary $\left(f_1=f_2=f_3\right)$ nC6/3MP/22DMB and (b, d) equimolar 5-component $\left(f_1=f_2=f_3=f_4=f_5\right)$ nC6/2MP.3MP/22DMB/23DMB mixtures at 433 K in two 1D MOFs (a, b) Mg$_2$(dobdc) (with hexagonal 11 Å channels) and (c, d) Co(BDP) (with square channels of 10 Å).

Adsorption of hexane isomers in Mg2(dobdc) and Co(BDP)

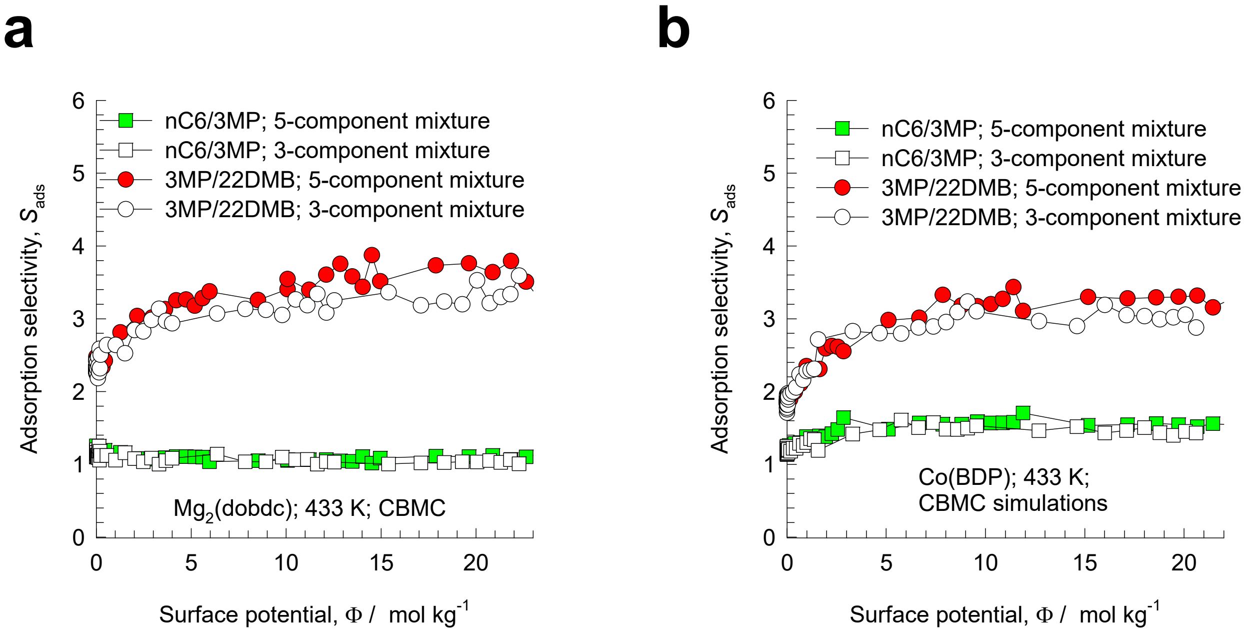

Figure S102. Comparing the nC6/3MP and 3MP/22DMB adsorption selectivities in (a) Mg$_2$(dobdc) and (b) Co(BDP). In the plots the adsorption selecitivities were determined from both CBMC simulations for adsorption of equimolar $\left(f_1=f_2=f_3\right)$ nC6/3MP/22DMB and equimolar $\left(f_1=f_2=f_3=f_4=f_5\right)$ nC6/2MP.3MP/22DMB/23DMB mixtures at 433 K. The *x*-axis represents the surface potential, Φ, determined using the IAST for either 3-component or 5-component mixtures as appropriate.

18 C_2H_2/C_2H_4 mixture adsorption in ZUL-100 and ZUL-200

Configurational-Bias Monte Carlo (CBMC) simulations, using the methodologies as detailed in earlier publications,[3, 5, 9, 11-14] were carried out to determine the adsorption isotherms for unary C_2H_2, unary C_2H_4, and 1/99 C_2H_2/C_2H_4 mixtures in ZUL-100 and ZUL-200 at 298 K. The structural details are provided in earlier work.[72] These MOFs have no open metal sites. The ZUL-100 and ZUL-200 structures were considered to be rigid in the simulations. simulation box for conducting CBMC simulations consisted of $3\times 2\times 3=18$ unit cells. The CBMC simulation data are the same as reported in our recent work.[72]

The interactions between adsorbed molecules are described with Lennard-Jones terms. For the atoms in the host metal organic framework, the generic UFF[29] and DREIDING[30] force fields were used; the Lennard-Jones parameters $\sigma_{host},\frac{\varepsilon_{host}}{k_B}$ values are specified in Table S22. The united atom model was used to describe -CH groups in C_2H_2, and $-CH_2$ groups in C_2H_4. The Lennard-Jones parameters for the $-CH_2$ groups in C_2H_4 were taken from Ban et al.[73] The Lennard-Jones parameters for the -CH groups in C_2H_2 were taken from Jorgenson et al..[74] The Lennard-Jones parameters $\sigma_{guest},\frac{\varepsilon_{guest}}{k_B}$ are tabulated in Table S23.

The Lorentz-Berthelot mixing rules were applied for calculating the Lennard-Jones parameters describing guest-host interactions

$$\begin{aligned}\sigma_{guest-host}&=\frac{\left(\sigma_{guest}+\sigma_{host}\right)}{2}\\ \frac{\varepsilon_{guest-host}}{k_B}&=\sqrt{\frac{\varepsilon_{guest}}{k_B}\times\frac{\varepsilon_{host}}{k_B}}\end{aligned}\qquad\text{(S44)}$$

C2H2/C2H4 mixture adsorption in ZUL-100 and ZUL-200

The interactions of the guest pseudo-atoms with the F atoms of the framework are dominant. Table S24 summarizes the values of the Lennard-Jones parameters for guest – F interactions that are used in the simulations.

The Lennard-Jones potentials are shifted and cut at 12 Å. Since both ZUL-100 and ZUL-200 do not contain open metal sites, the electrostatic charge interactions are not considered.

Figure S103 presents CBMC simulation data (indicated by the red and green symbols) for the component loadings for adsorption of 1/99 C_2H_2/C_2H_4 mixtures in ZUL-100 at 298 K. The dashed lines are IAST calculations of mixture adsorption equilibrium using the dual-Langmuir fits of unary isotherms determined from CBMC. There is good agreement between CBMC mixture simulations and IAST calculations.

Figure S104a presents CBMC simulation data (indicated by the red and green symbols) for the component loadings for adsorption of 1/99 C_2H_2/C_2H_4 mixtures in ZUL-200 at 298 K. The dashed lines are IAST calculations of adsorption equilibrium using the dual-Langmuir fits of unary isotherms determined from CBMC. There is good agreement between CBMC mixture simulations and IAST calculations.

Figure S105 plots the C_2H_2/C_2H_4 adsorption selectivity S_{ads} for 1/99 C_2H_2/C_2H_4 mixture adsorption in ZUL-100 and ZUL-200 zeolites at 298 K, as function of the surface potential Φ. The IAST estimates, shown by the dashed lines are in good agreement with the CBMC data for both hosts.

18.1 List of Tables for C2H2/C2H4 mixture adsorption in ZUL-100 and ZUL-200

Table S22. Lennard-Jones parameters for host atoms in ZUL-100, and ZUL-200.

atom	σ_{host} Å	$\frac{\varepsilon_{host}}{k_B}$ K	Literature source
Cu	3.1137	2.5164	UFF[29]
F	3.0932	36.4872	DREIDING[30]
N	3.2626	38.9532	DREIDING[30]
S	3.5903	173.1253	DREIDING[30]
Nb	2.8197	29.6930	UFF[29]
Ti	2.8286	8.5556	UFF[29]
C	3.4730	47.8611	DREIDING[30]
O	3.0332	48.1631	DREIDING[30]
H	2.8464	7.6497	DREIDING[30]

Table S23. Lennard-Jones parameters for guest pseudo-atoms.

(pseudo-) atom	σ_{guest} Å	$\frac{\varepsilon_{guest}}{k_B}$ K	Literature source
-CH	3.8	57.8782776	Gautam et al.[75]
$-CH_2$	3.68	92.5	Ban et al.[73]

Table S24. Lennard-Jones parameters for the guest – host (F atoms) interactions.

(pseudo-) atom	host atom	$\sigma_{guest-host}$ Å	$\frac{\varepsilon_{guest-host}}{k_B}$ K
-CH	F	$\frac{(3.8+3.0932)}{2}=3.446$	275.727
-CH$_2$	F	$\frac{(3.68+3.0932)}{2}=3.38$	58.09529

Table S25. Dual-site Langmuir-Freundlich parameters for guest molecules in ZUL-100 at 298 K.

	Site A			Site B		
	$q_{A,sat}$ mol kg^{-1}	b_A Pa $^{-\nu_A}$	$q_{A,sat}$ mol kg^{-1}	b_A Pa $^{-\nu_A}$	$q_{A,sat}$ mol kg^{-1}	ν_B dimensionless
C_2H_2	1.32	3.296E-02	1			
C_2H_4	1.75	5.301E-07	1	1.3	1.638E-04	1

Table S26. Dual-site Langmuir-Freundlich parameters for guest molecules in ZUL-200 at 298 K.

	Site A			Site B		
	$q_{A,sat}$ mol kg^{-1}	b_A Pa $^{-\nu_A}$	$q_{A,sat}$ mol kg^{-1}	b_A Pa $^{-\nu_A}$	$q_{A,sat}$ mol kg^{-1}	ν_B dimensionless
C_2H_2	1.24	1.146E-02	1			
C_2H_4	3	6.923E-08	1	1.25	1.687E-04	1

18.2 List of Figures for C2H2/C2H4 mixture adsorption in ZUL-100 and ZUL-200

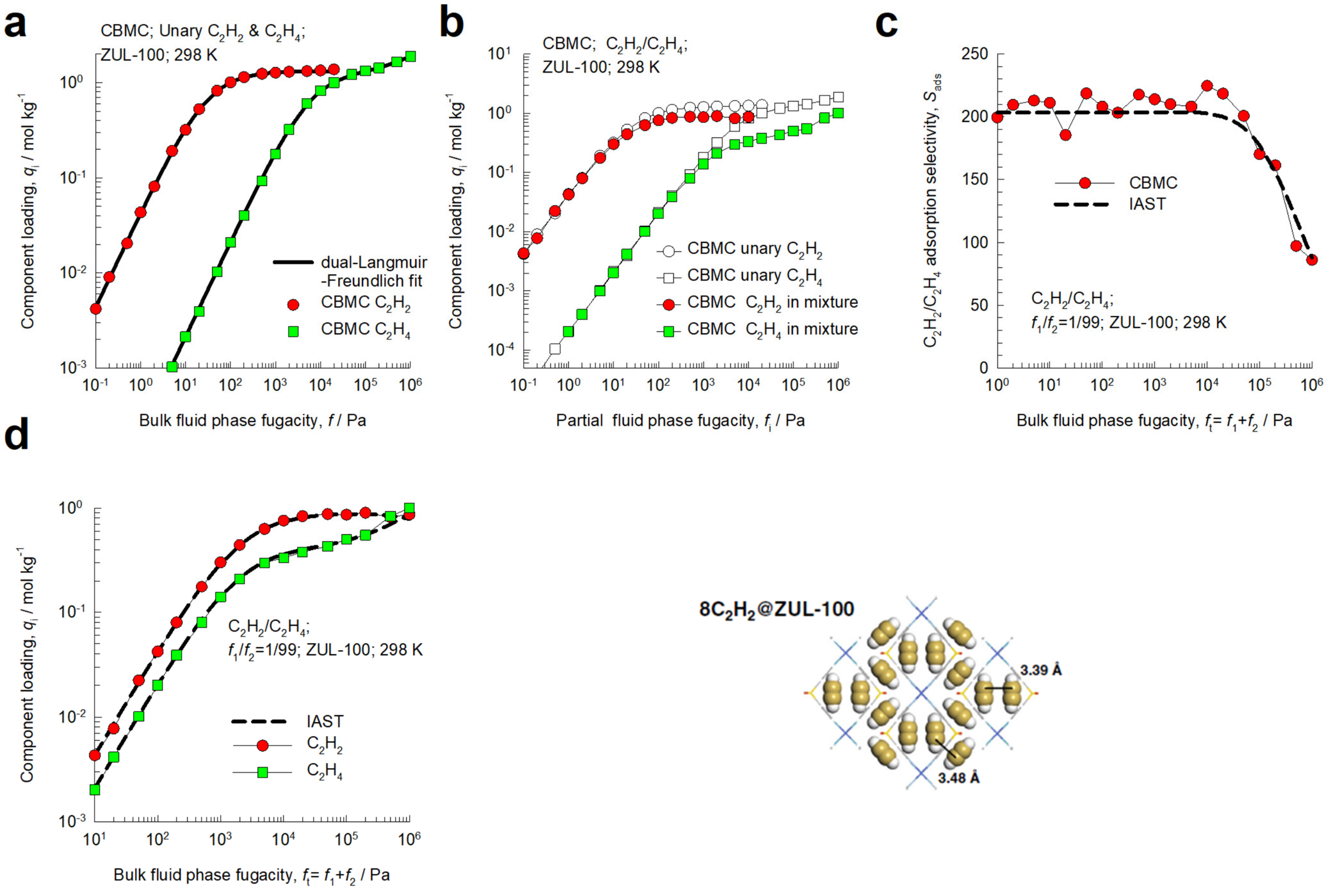

Figure S103. CBMC simulation data and analysis for 1/99 C_2H_2/C_2H_4 mixtures in ZUL-100 at 298 K. (a) Unary isotherms and fits. (b) Component loadings in mixture compared with CBMC simulations of unary isotherms. (c) CBMC data for C_2H_2/C_2H_4 adsorption selectivity compared with IAST estimates. (d) CBMC data for component loadings in mixture compared with IAST estimates. The unary isotherm fit parameters are provided in Table S25.

C2H2/C2H4 mixture adsorption in ZUL-100 and ZUL-200

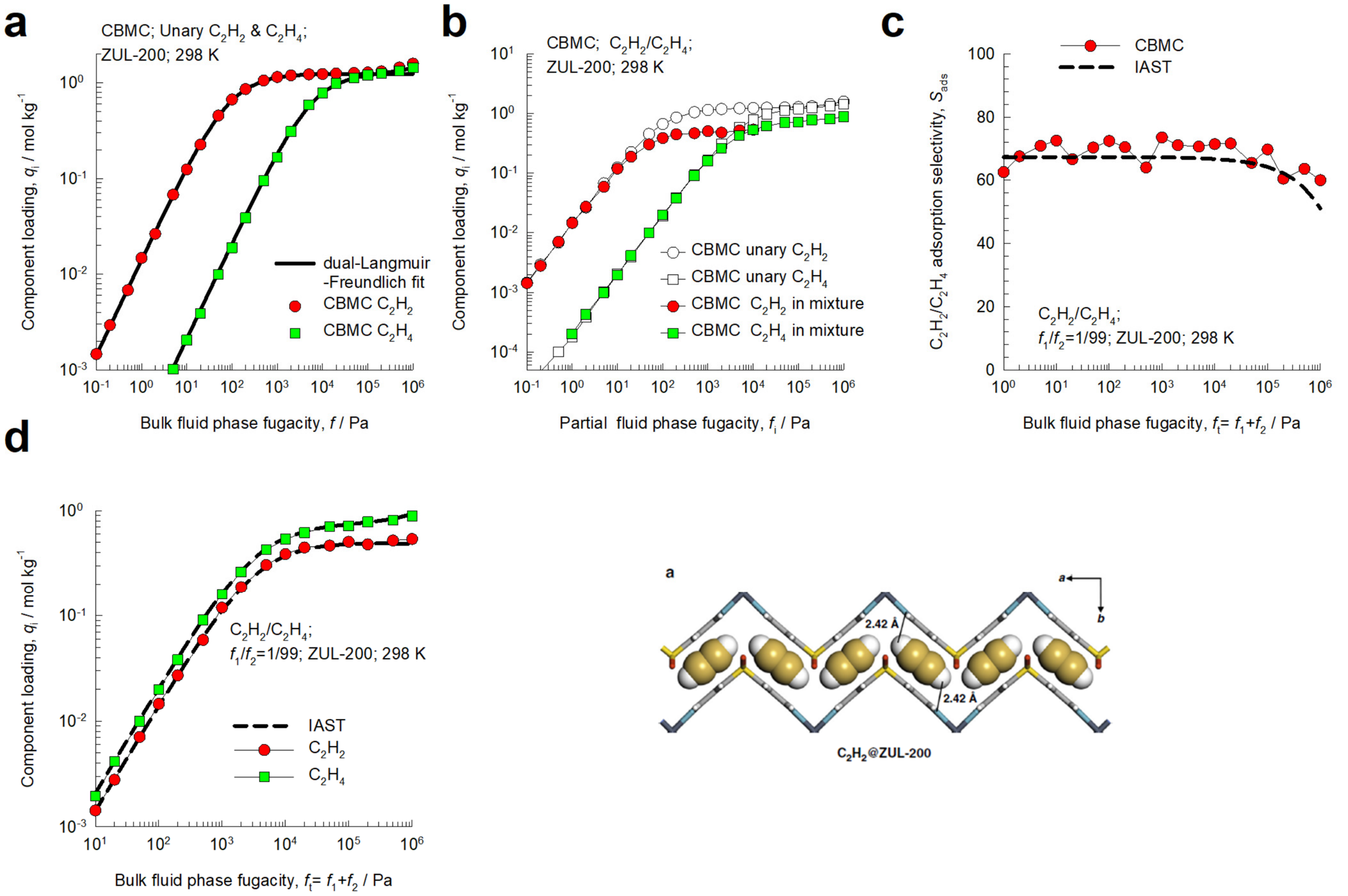

Figure S104. CBMC simulation data and analysis for 1/99 C_2H_2/C_2H_4 mixtures in ZUL-200 at 298 K. (a) Unary isotherms and fits. (b) Component loadings in mixture compared with CBMC simulations of unary isotherms. (c) CBMC data for C_2H_2/C_2H_4 adsorption selectivity compared with IAST estimates. (d) CBMC data for component loadings in mixture compared with IAST estimates. The unary isotherm fit parameters are provided in Table S26.

C2H2/C2H4 mixture adsorption in ZUL-100 and ZUL-200

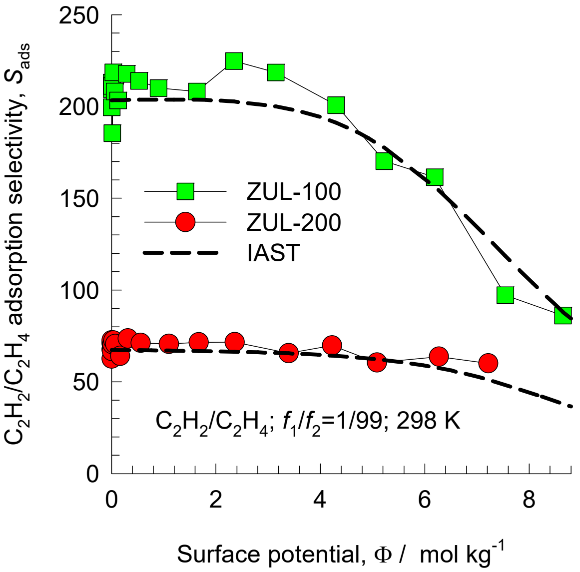

Figure S105. Adsorption selectivity S_{ads} for 1/99 C_2H_2/C_2H_4 mixture adsorption in ZUL-100 and ZUL-200 zeolites at 298 K, plotted as function of the surface potential Φ. The CBMC simulated values (indicated by symbols) are compared with IAST estimates (indicated by the dashed lines).

19 Nomenclature

Latin alphabet

A	surface area per kg of framework, $\mathrm{m}^2\ \mathrm{kg}^{-1}$
A_{12}, A_{21}	Margules parameters, dimensionless
b_i	Langmuir parameter, Pa^{-1}
C	constant used in eq (S37), $\mathrm{kg\ mol}^{-1}$
f_i	partial fugacity of species *i*, Pa
f_t	total fugacity of bulk fluid mixture, Pa
G^{excess}	excess Gibbs free energy, $\mathrm{J\ mol}^{-1}$
n	number of species in the mixture, dimensionless
p_i	partial pressure of species *i*, Pa
p_t	total system pressure, Pa
P_i^0	sorption pressure, Pa
q_i	molar loading of species *i*, $\mathrm{mol\ kg}^{-1}$
q_t	total molar loading of mixture, $\mathrm{mol\ kg}^{-1}$
$q_\mathrm{i,sat}$	molar loading of species *i* at saturation, $\mathrm{mol\ kg}^{-1}$
R	gas constant, 8.314 $\mathrm{J\ mol}^{-1}\ \mathrm{K}^{-1}$
S_ads	adsorption selectivity, dimensionless
T	absolute temperature, K
V_p	pore volume, $\mathrm{m}^3\ \mathrm{kg}^{-1}$
x_i	mole fraction of species *i* in adsorbed phase, dimensionless
y_i	mole fraction of species *i* in bulk fluid mixture, dimensionless

Nomenclature

Greek letters

γ_i	activity coefficient of component *i* in adsorbed phase, dimensionless
θ	fractional occupancy, dimensionless
Θ_i	loading of species *i*, molecules per unit cell
Λ_{ij}	Wilson parameters, dimensionless
μ_i	molar chemical potential, J mol^{-1}
ν	Freundlich exponent, dimensionless
π	spreading pressure, N m^{-1}
ρ	framework density, kg m^{-3}
Φ	surface potential, mol kg^{-1}

Subscripts

i,j	components in mixture
t	referring to total mixture
sat	referring to saturation conditions

Superscripts

0	referring to pure component loading
excess	referring to excess parameter

20 References

(1) Baerlocher, C.; Meier, W. M.; Olson, D. H. *Atlas of Zeolite Framework Types*. 5th Edition, Elsevier: Amsterdam, 2002; pp

(2) Baerlocher, C.; McCusker, L. B. Database of Zeolite Structures. http://www.iza-structure.org/databases/, International Zeolite Association, 10 January 2002.

(3) Krishna, R. Diffusion in Porous Crystalline Materials. *Chem. Soc. Rev.* **2012**, *41*, 3099-3118. https://doi.org/10.1039/C2CS15284C.

(4) Krishna, R. The Maxwell-Stefan Description of Mixture Diffusion in Nanoporous Crystalline Materials. *Microporous Mesoporous Mater.* **2014**, *185*, 30-50.

(5) Krishna, R. Describing the Diffusion of Guest Molecules inside Porous Structures. *J. Phys. Chem. C* **2009**, *113*, 19756-19781.

(6) Krishna, R.; van Baten, J. M. Investigating the Relative Influences of Molecular Dimensions and Binding Energies on Diffusivities of Guest Species Inside Nanoporous Crystalline Materials *J. Phys. Chem. C* **2012**, *116*, 23556-23568.

(7) Krishna, R.; van Baten, J. M. Investigating the Influence of Diffusional Coupling on Mixture Permeation across Porous Membranes *J. Membr. Sci.* **2013**, *430*, 113-128.

(8) Krishna, R.; van Baten, J. M. Influence of Adsorption Thermodynamics on Guest Diffusivities in Nanoporous Crystalline Materials. *Phys. Chem. Chem. Phys.* **2013**, *15*, 7994-8016.

(9) Krishna, R.; van Baten, J. M. Insights into diffusion of gases in zeolites gained from molecular dynamics simulations. *Microporous Mesoporous Mater.* **2008**, *109*, 91-108.

(10) Krishna, R.; van Baten, J. M. Diffusion of alkane mixtures in MFI zeolite. *Microporous Mesoporous Mater.* **2008**, *107*, 296-298.

(11) Krishna, R.; van Baten, J. M. In silico screening of metal-organic frameworks in separation applications. *Phys. Chem. Chem. Phys.* **2011**, *13*, 10593-10616.

(12) Krishna, R.; van Baten, J. M. In Silico Screening of Zeolite Membranes for CO_2 Capture. *J. Membr. Sci.* **2010**, *360*, 323-333.

(13) Krishna, R.; van Baten, J. M. Describing Mixture Diffusion in Microporous Materials under Conditions of Pore Saturation. *J. Phys. Chem. C* **2010**, *114*, 11557-11563.

(14) Krishna, R.; van Baten, J. M. Diffusion of alkane mixtures in zeolites. Validating the Maxwell-Stefan formulation using MD simulations. *J. Phys. Chem. B* **2005**, *109*, 6386-6396.

(15) Ryckaert, J. P.; Bellemans, A. Molecular dynamics of liquid alkanes. *Faraday Discuss. Chem. Soc.* **1978**, *66*, 95-106.

(16) Dubbeldam, D.; Calero, S.; Vlugt, T. J. H.; Krishna, R.; Maesen, T. L. M.; Smit, B. United Atom Forcefield for Alkanes in Nanoporous Materials. *J. Phys. Chem. B* **2004**, *108*, 12301-12313.

(17) Kumar, A. V. A.; Jobic, H.; Bhatia, S. K. Quantum effects on adsorption and diffusion of hydrogen and deuterium in microporous materials *J. Phys. Chem. B* **2006**, *110*, 16666-16671.

(18) Makrodimitris, K.; Papadopoulos, G. K.; Theodorou, D. N. Prediction of permeation properties of CO_2 and N_2 through silicalite via molecular simulations. *J. Phys. Chem. B* **2001**, *105*, 777-788.

(19) García-Pérez, E.; Parra, J. B.; Ania, C. O.; García-Sánchez, A.; Van Baten, J. M.; Krishna, R.; Dubbeldam, D.; Calero, S. A computational study of CO_2, N_2 and CH_4 adsorption in zeolites. *Adsorption* **2007**, *13*, 469-476.

(20) García-Sánchez, A.; Ania, C. O.; Parra, J. B.; Dubbeldam, D.; Vlugt, T. J. H.; Krishna, R.; Calero, S. Development of a Transferable Force Field for Carbon Dioxide Adsorption in Zeolites. *J. Phys. Chem. C* **2009**, *113*, 8814-8820.

(21) Krishna, R.; van Baten, J. M. Hydrogen Bonding Effects in Adsorption of Water-alcohol Mixtures in Zeolites and the Consequences for the Characteristics of the Maxwell-Stefan Diffusivities. *Langmuir* **2010**, *26*, 10854-10867.

(22) Krishna, R.; van Baten, J. M. Mutual slowing-down effects in mixture diffusion in zeolites. *J. Phys. Chem. C* **2010**, *114*, 13154-13156.

(23) Krishna, R.; van Baten, J. M. Highlighting Pitfalls in the Maxwell-Stefan Modeling of Water-Alcohol Mixture Permeation across Pervaporation Membranes. *J. Membr. Sci.* **2010**, *360*, 476-482.

(24) Kuhn, J.; Castillo-Sanchez, J. M.; Gascon, J.; Calero, S.; Dubbeldam, D.; Vlugt, T. J. H.; Kapteijn, F.; Gross, J. Adsorption and Diffusion of Water, Methanol, and Ethanol in All-Silica DD3R: Experiments and Simulation. *J. Phys. Chem. C* **2009**, *113*, 14290-14301.

(25) Rick, S. W. A Reoptimization of the Five-site Water Potential (TIP5P) for use with Ewald Sums. *J. Chem. Phys.* **2004**, *120*, 6085-6093.

(26) Chen, B.; Potoff, J. J.; Siepmann, J. I. Monte Carlo Calculations for Alcohols and Their Mixtures with Alkanes. Transferable Potentials for Phase Equilibria. 5. United-Atom Description of Primary, Secondary, and Tertiary Alcohols. *J. Phys. Chem. B* **2001**, *105*, 3093-3104.

(27) Kiselev, A. V.; Lopatkin, A. A.; Shul'ga, A. A. Molecular statistical calculation of gas adsorption by silicalite. *Zeolites* **1985**, *5*, 261-267.

(28) Frenkel, D.; Smit, B. *Understanding Molecular Simulations: From Algorithms to Applications*. 2nd Edition, Academic Press: San Diego, 2002; pp

(29) Rappé, A. K.; Casewit, C. J.; Colwel, K. S.; Goddard, W. A.; Skiff, W. M. UFF, A Full Periodic Table Force Field for Molecular Mechanics and Molecular Dynamics Simulations. *J. Am. Chem. Soc.* **1992**, *114*, 10024-10035.

(30) Mayo, S. L.; Olafson, B. D.; Goddard, W. A. DREIDING: A Generic Force Field for Molecular Simulations. *J. Phys. Chem.* **1990**, *94*, 8897-8909.

(31) Britt, D.; Furukawa, H.; Wang, B.; Glover, T. G.; Yaghi, O. M. Highly efficient separation of carbon dioxide by a metal-organic framework replete with open metal sites. *Proc. Natl. Acad. Sci. U.S.A.* **2009**, *106*, 20637-20640.

(32) Rosi, N. L.; Kim, J.; Eddaoudi, M.; Chen, B.; O'Keeffe, M.; Yaghi, O. M. Rod Packings and Metal-Organic Frameworks Constructed from Rod-Shaped Secondary Building Units. *J. Am. Chem. Soc.* **2005**, *127*, 1504-1518.

(33) Dietzel, P. D. C.; Panella, B.; Hirscher, M.; Blom, R.; Fjellvåg, H. Hydrogen adsorption in a nickel based coordination polymer with open metal sites in the cylindrical cavities of the desolvated framework. *Chem. Commun.* **2006**, 959-961.

(34) Dietzel, P. D. C.; Besikiotis, V.; Blom, R. Application of metal–organic frameworks with coordinatively unsaturated metal sites in storage and separation of methane and carbon dioxide. *J. Mater. Chem.* **2009**, *19*, 7362-7370.

(35) Caskey, S. R.; Wong-Foy, A. G.; Matzger, A. J. Dramatic Tuning of Carbon Dioxide Uptake via Metal Substitution in a Coordination Polymer with Cylindrical Pores. *J. Am. Chem. Soc.* **2008**, *130*, 10870-10871.

(36) Yazaydın, A. Ö.; Snurr, R. Q.; Park, T. H.; Koh, K.; Liu, J.; LeVan, M. D.; Benin, A. I.; Jakubczak, P.; Lanuza, M.; Galloway, D. B.; Low, J. J.; Willis, R. R. Screening of Metal-Organic Frameworks for Carbon Dioxide Capture from Flue Gas using a Combined Experimental and Modeling Approach. *J. Am. Chem. Soc.* **2009**, *131*, 18198-18199.

References

(37) Choi, H. J.; Dincă, M.; Long, J. R. Broadly Hysteretic H_2 Adsorption in the Microporous Metal-Organic Framework Co(1,4-benzenedipyrazolate). *J. Am. Chem. Soc.* **2008**, *130*, 7848-7850.

(38) Salles, F.; Maurin, G.; Serre, C.; Llewellyn, P. L.; Knöfel, C.; Choi, H. J.; Filinchuk, Y.; Oliviero, L.; Vimont, A.; Long, J. R.; Férey, G. Multistep N_2 Breathing in the Metal-Organic Framework Co(1,4-benzenedipyrazolate). *J. Am. Chem. Soc.* **2010**, *132*, 13782-13788.

(39) Zhang, C.; Yang, X. Molecular dynamics simulation of ethanol/water mixtures for structure and diffusion properties. *Fluid Phase Equilib.* **2005**, *231*, 1-10.

(40) Ruthven, D. M. *Principles of Adsorption and Adsorption Processes*. John Wiley: New York, 1984; pp 1-433.

(41) Myers, A. L.; Prausnitz, J. M. Thermodynamics of Mixed Gas Adsorption. *A.I.Ch.E.J.* **1965**, *11*, 121-130.

(42) Siperstein, F. R.; Myers, A. L. Mixed-Gas Adsorption. *A.I.Ch.E.J.* **2001**, *47*, 1141-1159.

(43) Streb, A.; Mazzotti, M. Adsorption for efficient low carbon hydrogen production: part 1—adsorption equilibrium and breakthrough studies for H_2/CO_2/CH_4 on zeolite 13X. *Adsorption* **2021**, *x*, xx. https://doi.org/10.1007/s10450-021-00306-y.

(44) Krishna, R.; Van Baten, J. M. Using Molecular Simulations to Unravel the Benefits of Characterizing Mixture Permeation in Microporous Membranes in Terms of the Spreading Pressure. *ACS Omega* **2020**, *5*, 32769−32780. https://dx.doi.org/10.1021/acsomega.0c05269.

(45) Krishna, R.; Van Baten, J. M. Elucidation of Selectivity Reversals for Binary Mixture Adsorption in Microporous Adsorbents. *ACS Omega* **2020**, *5*, 9031-9040. https://doi.org/10.1021/acsomega.0c01051.

(46) Krishna, R.; Van Baten, J. M. Using Molecular Simulations for Elucidation of Thermodynamic Non-Idealities in Adsorption of CO_2-containing Mixtures in NaX Zeolite. *ACS Omega* **2020**, *5*, 20535-20542. https://doi.org/10.1021/acsomega.0c02730.

(47) Krishna, R.; Van Baten, J. M. Water/Alcohol Mixture Adsorption in Hydrophobic Materials: Enhanced Water Ingress caused by Hydrogen Bonding. *ACS Omega* **2020**, *5*, 28393-28402. https://doi.org/10.1021/acsomega.0c04491.

(48) Krishna, R.; Van Baten, J. M. Investigating the Non-idealities in Adsorption of CO_2-bearing Mixtures in Cation-exchanged Zeolites. *Sep. Purif. Technol.* **2018**, *206*, 208-217. https://doi.org/10.1016/j.seppur.2018.06.009.

(49) Krishna, R. Occupancy Dependency of Maxwell−Stefan Diffusivities in Ordered Crystalline Microporous Materials. *ACS Omega* **2018**, *3*, 15743-15753. https://doi.org/10.1021/acsomega.8b02465.

(50) Talu, O.; Myers, A. L. Rigorous Thermodynamic Treatment of Gas-Adsorption. *A.I.Ch.E.J.* **1988**, *34*, 1887-1893.

(51) Talu, O.; Zwiebel, I. Multicomponent Adsorption Equilibria of Nonideal Mixtures. *A.I.Ch.E.J.* **1986**, *32*, 1263-1276.

(52) Krishna, R. Separating Mixtures by Exploiting Molecular Packing Effects in Microporous Materials. *Phys. Chem. Chem. Phys.* **2015**, *17*, 39-59.

(53) Krishna, R. Elucidation and Characterization of Entropy Effects in Mixture Separations with Micro-porous Crystalline Adsorbents. *Sep. Purif. Technol.* **2019**, *215*, 227-241. https://doi.org/10.1016/j.seppur.2019.01.014.

(54) Vlugt, T. J. H.; Zhu, W.; Kapteijn, F.; Moulijn, J. A.; Smit, B.; Krishna, R. Adsorption of linear and branched alkanes in the silicalite-1. *J. Am. Chem. Soc.* **1998**, *120*, 5599-5600.

(55) Vlugt, T. J. H.; Krishna, R.; Smit, B. Molecular Simulations of Adsorption Isotherms for Linear and Branched Alkanes and Their Mixtures in Silicalite. *J. Phys. Chem. B* **1999**, *103*, 1102-1118.

(56) Krishna, R.; Smit, B.; Calero, S. Entropy effects during sorption of alkanes in zeolites. *Chem. Soc. Rev.* **2002**, *31*, 185-194.

(57) Schenk, M.; Vidal, S. L.; Vlugt, T. J. H.; Smit, B.; Krishna, R. Separation of alkane isomers by exploiting entropy effects during adsorption on silicalite-1: A configurational-bias Monte Carlo simulation study. *Langmuir* **2001**, *17*, 1558-1570.

(58) Titze, T.; Chmelik, C.; Kärger, J.; van Baten, J. M.; Krishna, R. Uncommon Synergy Between Adsorption and Diffusion of Hexane Isomer Mixtures in MFI Zeolite Induced by Configurational Entropy Effects *J. Phys. Chem. C* **2014**, *118*, 2660-2665.

(59) Krishna, R.; van Baten, J. M. Segregation effects in adsorption of CO_2 containing mixtures and their consequences for separation selectivities in cage-type zeolites. *Sep. Purif. Technol.* **2008**, *61*, 414-423.

(60) Krishna, R.; van Baten, J. M. Separating n-alkane mixtures by exploiting differences in the adsorption capacity within cages of CHA, AFX and ERI zeolites. *Sep. Purif. Technol.* **2008**, *60*, 315-320.

(61) Krishna, R.; van Baten, J. M. Entropy-based Separation of Linear Chain Molecules by Exploiting Differences in the Saturation Capacities in Cage-type Zeolites. *Sep. Purif. Technol.* **2011**, *76*, 325-330.

(62) Krishna, R.; van Baten, J. M. Commensurate-Incommensurate Adsorption and Diffusion in Ordered Crystalline Microporous Materials. *Phys. Chem. Chem. Phys.* **2017**, *19*, 20320-20337.

(63) Krishna, R.; van Baten, J. M. A comparison of the CO_2 capture characteristics of zeolites and metal-organic frameworks. *Sep. Purif. Technol.* **2012**, *87*, 120-126.

(64) Krishna, R.; van Baten, J. M. Investigating cluster formation in adsorption of CO_2, CH_4, and Ar in zeolites and metal organic frameworks at sub-critical temperatures. *Langmuir* **2010**, *26*, 3981-3992.

(65) Costa, E.; Calleja, G.; Jimenez, A.; Pau, J. Adsorption Equilibrium of Ethylene, Propane, Propylene, Carbon Dioxide, and Their Mixtures in 13X Zeolite. *J. Chem. Eng. Data* **1991**, *36*, 218-224.

(66) Krishna, R.; van Baten, J. M. Highlighting a variety of unusual characteristics of adsorption and diffusion in microporous materials induced by clustering of guest molecules. *Langmuir* **2010**, *26*, 8450-8463.

(67) Herm, Z. R.; Wiers, B. M.; Van Baten, J. M.; Hudson, M. R.; Zajdel, P.; Brown, C. M.; Maschiocchi, N.; Krishna, R.; Long, J. R. Separation of Hexane Isomers in a Metal-Organic Framework with Triangular Channels *Science* **2013**, *340*, 960-964.

(68) Krishna, R.; van Baten, J. M. Screening of zeolite adsorbents for separation of hexane isomers: A molecular simulation study. *Sep. Purif. Technol.* **2007**, *55*, 246-255.

(69) Dubbeldam, D.; Krishna, R.; Calero, S.; Yazaydın, A. Ö. Computer-Assisted Screening of Ordered Crystalline Nanoporous Adsorbents for Separation of Alkane Isomers. *Angew. Chem. Int. Ed.* **2012**, *51*, 11867-11871.

(70) Krishna, R. Methodologies for Evaluation of Metal-Organic Frameworks in Separation Applications. *RSC Adv.* **2015**, *5*, 52269-52295.

(71) Krishna, R. Metrics for Evaluation and Screening of Metal-Organic Frameworks for Applications in Mixture Separations. *ACS Omega* **2020**, *5*, 16987−17004. https://doi.org/10.1021/acsomega.0c02218.

(72) Shen, J.; He, X.; Ke, T.; Krishna, R.; van Baten, J. M.; Chen, R.; Bao, Z.; Xing, H.; Dincă, M.; Zhang, Z.; Yang, Q.; Ren, Q. Simultaneous interlayer and intralayer space control in two-dimensional metal−organic frameworks for acetylene/ethylene separation. *Nat. Commun.* **2020**, *11*, 6259. https://doi.org/10.1038/s41467-020-20101-7.

(73) Ban, S.; van Laak, A.; de Jongh, P. E.; van der Eerden, J. P. J. M.; Vlugt, T. J. H. Adsorption Selectivity of Benzene and Propene Mixtures for Various Zeolites. *J. Phys. Chem. C* **2007**, *111*, 17241-17248.

(74) Jorgensen, W. L.; Madura, J. D.; Swenson, C. J. Optimized Intermolecular Potential Functions for Liquid Hydrocarbons. *J. Am. Chem. Soc.* **1984**, *106*, 6638-6646.

(75) Gautam, S.; Mitra, S.; Mukhopadhyay, R.; Chaplot, S. L. Diffusion of acetylene inside Na-Y zeolite: Molecular dynamics simulation studies. *Phys. Rev. E* **2006**, *74*, 041202.

References